Etude sur les dispositifs d'amélioration de SER inspirés des reflectarrays et des métamatériaux

Hussein Srour

THESE DE DOCTORAT DE

L'INSA RENNES
COMUE UNIVERSITE BRETAGNE LOIRE

ECOLE DOCTORALE N°601
Mathématiques et Sciences et Technologies
de l'Information et de la Communication
Spécialité : Eléctronique

Par

« Hussein SROUR »

« Investigation of RCS-enhancement devices inspired from reflectarrays and metamaterials »

« Thèse confidentielle jusqu'au 31 Mai 2021 »

Thèse présentée et soutenue à Rennes , le 29 Juin 2018
Unité de recherche : IETR
Thèse N° : 18ISAR 13 / D18 - 13

Rapporteurs avant soutenance :

Eric Lheurette, Professeur, IEMN Lille

Régis Guinvarc'h, Professeur, Centrale Supelec Gif-Sur_Yvette

Composition du Jury :

Jean Yves Dauvignac , Professeur, Université de Nice-Sophia Antipolis, Nice
Président

Eric Lheurette, Professeur, IEMN Lille

Régis Guinvarc'h, Professeur, Centrale Supelec Gif-Sur_Yvette

Raphaël Gillard, Professeur, INSA Rennes, directeur de thèse

Divitha Seetharamdoo, PhD,IFSTTAR Villeneuve D'Ascq, co-encadrante de thèse

Stéphane Méric, Maitre de Conférences HDR, INSA Rennes, co-encadrant de thèse

UNIVERSITE BRETAGNE LOIRE / MATHSTIC

INSA RENNES

Intitulé de la thèse :

Etude sur les dispositifs d'amélioration de SER inspirés des reflectarrays et des métamatériaux

Hussein Srour

En partenariat avec :

IETR INSTITUT D'ÉLECTRONIQUE ET DE TÉLÉCOMMUNICATIONS DE RENNES	IFSTTAR			

Remerciements

Firstly, I would like to express my sincere gratitude to my advisor Prof. Raphaël Gillard for the continuous support of my Ph.D study and related research, for his patience, motivation, and immense knowledge. His guidance helped me in all the time of research and writing of this thesis. I could not have imagined having a better advisor and mentor for my Ph.D study.

Besides my advisor, I would like to thank my thesis co-supervisors : Dr. Stéphane Méric and Dr. Divitha Seetharamdoo for their insightful comments and encouragement during this time.

I would like to express my gratitude to Prof. Eric Lheurette, Prof. Régis Guinvarc'h and Prof. Jean Yves Dauvignac for accepting being members in the jury of my phd defense. I thank you for your valuable comments and questions.

My sincere thanks also goes to Prof. Charles Tatkeu who provided me an opportunity to join his team as intern, and who gave me access to the laboratory and research facilities.

I thank my fellow labmates for the stimulating discussions and for all the fun we have had in the last three years. In particular, I am grateful to Dr. Mhamad Hassanein Rabah for enlightening me the first glance of research.

Last but not the least, I would like to thank my family : my parents and my sisters for supporting me spiritually throughout writing this thesis and my my life in general. The most special thanks go to my beloved wife who was always there for me and gave me the vital support so that I could accomplish my work. Finally, Julia, my little daughter, you have lighten up my life. Your presence has given me the extra motivation in the most needed time. Thank you my baby.

Table of Contents

Résumé de la Thèse

En milieu urbain, les aménagements ne sont pas toujours favorables à la cohabitation entre les modes de transport. En particulier, la cohabitation entre vélos et grands véhicules comme les bus augmente les risques d'accidents et peut causer des perturbations de la fluidité du trafic(Fig. 1, 2).

Dans le contexte du projet ANR CYCLOPE, l'objectif est de proposer des équipements de sécurisation pour les cyclistes en lien avec des dispositifs d'avertissement pour les conducteurs de bus. Les radar anticollision permettent d'apporter une réponse partielle à cette problématique. Toutefois, à cause de sa faible Surface Efficace RADAR (SER), le vélo est difficilement détectable par le RADAR.

Pour améliorer cette SER, on examine deux approches. La première approche est basé sur un réflecteur électromagnétique qui peut être installé sur le vélo pour maximiser la diffusion vers le RADAR. Il doit donc réfléchir le signal dans la direction dont il est issu sans connaissance préalable de la position du bus. Afin qu'un tel équipement soit intégrable sur un vélo, il doit être peu encombrant et faible coût.

Parmi les configurations possibles pour réaliser de tels réflecteurs rétrodirectifs passifs, les réseaux de Van Atta[37] sont bien connus. Toutefois, le réseau des lignes d'interconnexion utilisées pour relier les éléments conduit à des pertes importantes et s'avère très délicat à mettre en oeuvre en 2 dimensions. D'un autre côté, le réflecteur dièdre classique[19] (ou tétraédrique) fournit une bonne valeur de SER sur une large gamme d'angles d'incidence, mais il ne fournit pas une solution compacte de par sa configuration 3D. Par conséquent, le défi consiste à aplatir le dièdre tout en gardant le mécanisme qui assure son comportement rétrodirectif.

Figure 1 – Les angles morts où le conducteur du bus ne peut pas détecter visuellement les obstacles de la route en tant que les cyclistes

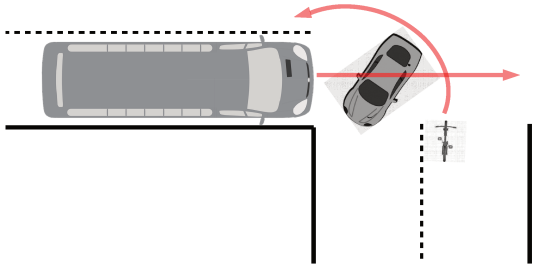

FIGURE 2 – Le scénario où le conducteur du bus est incapable de détecter le cycliste à un point d'intersection

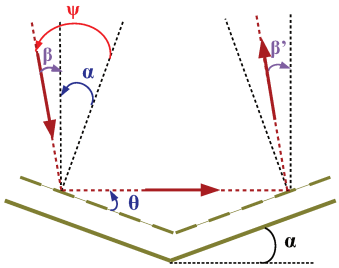

FIGURE 3 – Le mécanisme de réflexion entre panneau 1 et 2 dans le cas "vers l'avant"

Dans cette partie, une étude sur un dièdre aplati en utilisant l'approche reflectarray[63] est présentée. Plus précisément, une amélioration de la synthèse du réflecteur est proposée pour corriger les effets liés à l'incidence. Le dièdre, équipé par des cellules déphaseuses, obéit à la loi de phase rétrodirective pour rediriger l'onde dans la direction d'incidence. Comme il est montré sur la Fig. 3, les paramètres $\pi - 2\alpha$ et β correspondent à l'angle d'ouverture et l'angles d'incidence sur le panneaux gauche. Cette rétro-loi(γ_β) est dérivée en fonction des paramètres géométriques et de l'angle d'incidence de l'onde plane en utilisant des relations trigonométriques simples :

$$\gamma_\beta = k_0 d(\cos(\alpha + \arcsin[\frac{\sin(\beta)}{\tan(\alpha)}]) - \sin(\alpha - \beta))$$

En considérant que $\lambda_0 = 12.5mm$, $k_0 = 2\pi/\lambda_0$, l'espacement entre des éléments d=$\lambda_0/3$, et $\alpha = 22.5$, le loi de phase devient :

$$\gamma_0 = k_0 d(cos(\alpha) - sin(\alpha)) \approx 64.95$$

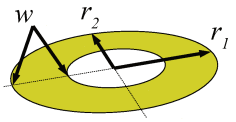

FIGURE 4 – La géométrie d'une cellule déphaseuse elliptique

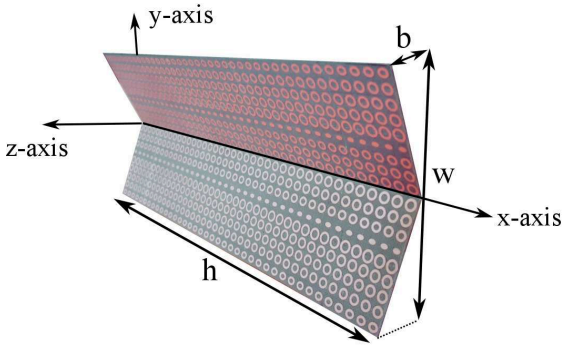

FIGURE 5 – Dièdre aplati formé des cellules elliptiques

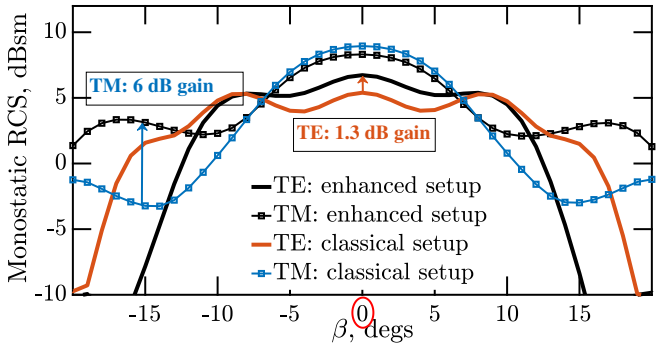

FIGURE 6 – Les résultats SER correspondants de la configuration amélioré de simulation en comparaison avec celle classique

Il est montré que le signal incident normalement(β=22.5°) à l'ouverture du panneau gauche atteint l'autre panneau avec un angle d'incidence très oblique. De ce fait, les réponses de phase des cellules, conçues à l'aide de la configuration classique d'incidence normale, se détériorent dans la mesure où elles ne respectent plus la loi de phase requise.

A partir de cette information, une nouvelle configuration de simulation est proposée en utilisant des cellules elliptiques (Fig. 4) comme un compromis pour améliorer la fonctionnalité des cellules et donc améliorer le comportement rétrodirectif du dièdre à 24 GHz. Des simulations utilisant le logiciel Ansoft HFSS ont été effectuées pour valider cette méthode. Fig. 5 montre le dièdre aplati simulé et ses dimensions sont données dans le Tab. 1. Fig. 6 montre l'amélioration introduite par la nouvelle configuration par rapport à celle classique pour les deux cas TE_x et TM_x respectivement. Les résultats des mesures sont données sur la Fig. 7. Les simulations sont bien validées par les mesures expérimentales.

Dans la deuxième partie de cette thèse, une solution basée sur les métamatériaux est étudiée. Les travaux sont consacrés à l'amélioration de la rétrodiffusion d'un cylindre diélectrique multi-couche modélisant le corps humain en utilisant une enveloppe de mé-

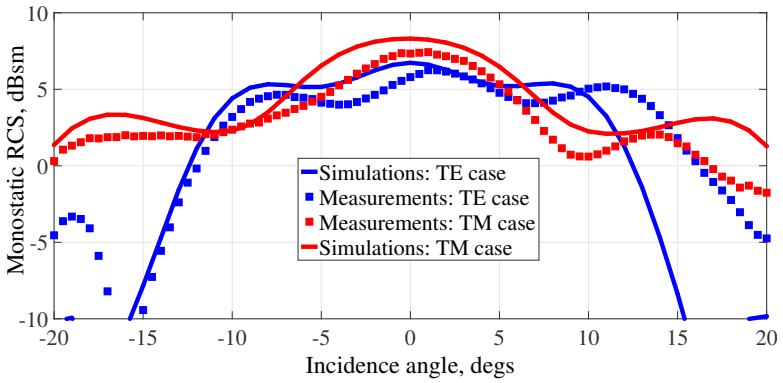

FIGURE 7 – Les résultats SER des mesures en comparaison avec ceux des simulations

TABLE 1 – Dimensions géométriques des dièdres classique et aplati

Structure	b, mm	h, mm	w, mm
Dièdre classique	34.65	162.5	69.29
Reflectarray	14.35	162.5	69.29

tamatériaux .

Dans un premier temps, cette problématique est envisagée en considérant les propriétés de rétrodiffusion d'un cylindre de longueur infinie. Le caractère infini du cylindre permet d'aborder le problème par une approche analytique sur la base de la théorie de Mie. Cette théorie est ensuite étendue au cas d'un cylindre bi-couche permettant de rendre compte de la réponse d'un corps homogène enveloppé dans un enrobage destiné à améliorer sa réflectivité. Ce problème, traité dans la littérature pour décrire la diffusion à partir d'une sphère est reformulé dans le cas présent à partir d'un système de coordonnées cylindriques. Le code numérique développé dans cette partie sur la base de la théorie de Mie est validé au moyen d'exemples de la littérature et de simulations full-wave réalisées à l'aide du logiciel HFSS.

L'analyse de la structure bi-couche considère tout d'abord le cas d'un noyau présentant une faible permittivité et un faible niveau de perte diélectrique pour évoluer vers des permittivités plus importantes tant au niveau des parties réelles qu'imaginaires. Pour ce qui concerne l'enveloppe, des valeurs de permittivités positives et négatives sont considérées. Les performances de l'enrobage sont quantifiées par un gain de rétrodiffusion qui correspond au quotient entre l'efficacité de rétrodiffusion du cylindre enrobé et celle du cylindre nu. Le recours à des valeurs de permittivité négative apparaît indiqué dans le cas où les parties réelle et imaginaire de permittivité du noyau sont importantes.

Dans une seconde partie, l'étude numérique considère un cylindre hétérogène incluant quatre couches. Les valeurs de permittivité sont choisies pour modéliser les tissus humains à partir de données référencées dans la littérature par C. Gabriel[98]. Cette étude est intéressante dans le sens où elle intègre des fluctuations de permittivités et d'épaisseurs relatives de couches à même de rendre compte des disparités rencontrées d'un individu

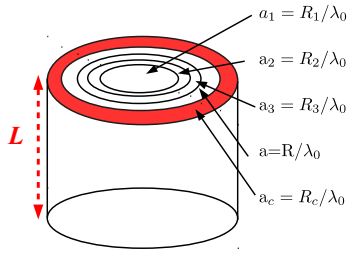

FIGURE 8 – La géométrie d'un cylindre fini multi-couche modélisant un corps humain

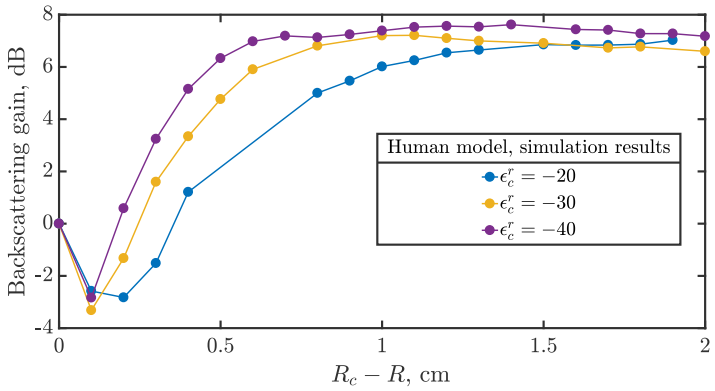

FIGURE 9 – Les résultats de gain rétrodiffusion (en dB) en fonction de l'épaisseur de l'enveloppe

à l'autre. Elle permet de démontrer que l'influence des fluctuations de permittivité reste faible. En revanche l'influence de la fluctuation des épaisseurs est plus déterminante. Néanmoins, dans l'hypothèse la plus défavorable considérée dans cette étude paramétrique, le gain de rétrodiffusion reste positif. Une étape supplémentaire est considérée vers la modélisation de la rétrodiffusion du corps humain en prenant en compte la longueur finie du cylindre multi-couche(Fig. 8). Pour ce faire, il n'existe pas de formulation exacte et on s'appuie dans un premier temps sur une formulation approchée issue de la littérature (modèle de Knott). Les premiers calculs effectués à partir de ce modèle donnent de bons résultats en comparaison des simulations par une méthode combinant les éléments finis et l'équation intégrale.

Ce point aurait mérité un commentaire. Pour l'étude du cylindre de dimension finie enrobé par une couche destinée à augmenter la rétrodiffusion, la situation d'un cylindre recouvert par une fine couche de conducteur parfait est considérée comme référence avec un gain en rétrodiffusion de 4 dB. La structure enrobée par une couche de permittivité relative égale à -15 est simulée pour différentes valeurs de permittivité complexe du noyau central (partie réelle égale à 3, partie imaginaire comprise entre 0 et 1). Cette étude permet de conclure à une augmentation du gain en rétrodiffusion pour toutes les valeurs

de permittivité considérées. Il convient également de souligner que ce gain majore celui d'un cylindre de dimension infini et que le gain obtenu en simulation est supérieur à celui que donne l'approximation analytique. Ce point illustre la contribution de la troncature du cylindre pour la rétrodiffusion de la puissance électromagnétique par diffraction. Les gains obtenus sont de l'ordre de 10 dB, ce qui est très supérieur au gain du cylindre enrobé par une fine couche de métal parfait, introduit comme structure de référence.

Enfin, comme noyau central, on considère un cylindre composé de quatre couches tel que défini sur la base des valeurs de permittivité répertoriées par C. Gabriel[98]. Les profils de gain en rétrodiffusion sont relativement monotones et témoignent de la présence d'un seuil d'épaisseur d'enrobage. Ce seuil est d'autant plus faible que la permittivité négative de l'enrobage est importante. Les valeurs de permittivité envisagées, comprises entre -20 et - 40 laissent entrevoir la possibilité d'une synthèse de la couche d'enrobage par métamatériaux avec un compromis nécessaire entre permittivité et épaisseur pour une fréquence de fonctionnement donnée (Fig. 9).

General introduction

Context

In the current context of energy transition, development of low energy-consuming transportation has become of public concern. Shifting to sustainable transportation modes has led to an increase of Utility Cycling. Urban policies are being deployed in order to facilitate this kind of transportation. However, urban development is not always favorable to the coexistence of different modes of transport. The sharing of public space between public transport and bicycles allows greater freedom for cyclists but also induces risks, especially in bus lanes. The impact of this increase in Utility Cycling should thus be the subject of intensive research particularly on safety issues and the feeling of insecurity of cyclists or even the other road users. Unfortunately, statistics do not lie, and they are pointing to one fact that cannot be ignored anymore : road safety nowadays is a major concern. Indeed, accident statistics show an increase of 12 % of deaths of cyclists since 2010 (ONISR, 2012). If this means anything, it is that more measures should be taken in order to prevent such fatalities on the road.

In the French national project CYCLO Protéction Éléctronique (CYCLOPE), the aim is to study technological solutions as well as their relevance in terms of acceptance and impact to enable a safer coexistence of bicycles and buses on the road. Indeed, cyclists hesitate in using the bus lanes because they are afraid of the large silent vehicles whose presence is difficult to detect. Also, the bus drivers see the bicycles as vulnerable and hard to detect obstacles. Therefore, there is a strong demand from bus drivers to have information on their immediate environment inorder to reduce their stress and eventually accident rates in urban areas.

Hence, one of the objectives of this project is to develop innovative low-cost technological solutions to facilitate the integration of cycling in urban traffic by improving both their safety and the comfort of bus drivers.

In the context of this thesis, the work will focus on the solutions to improve the detectability of the cyclist by vehicles equipped with a collision-avoidance radar. The objective is to improving the detectability of the bicycle-cyclist system such that the backscattered energy level is sufficient to cause alarm on the radar-equipped vehicle (*e.g.* bus).

Our subject of study

To reach the objective of improving the detectability of the bicycle-cyclist system, we propose to increase the Radar Cross-Section (RCS) of this system. In this thesis, two distinct approaches are investigated. The first one focuses on the design of a retrodirective device for the *bicycle* inspired on reflectarray antennas and the second one deals with a prospective proposal of a coat to increase the RCS of the *cyclist* based on the use of metamaterials.

Reflectarrays

In the first part of the thesis, the design of a retrodirective reflector inspired from reflectarray antennas is studied. A retrodirective reflector reflects the incident beam in the direction of incidence without a priori knowledge of this incidence direction. By attaching two metallic panels orthogonally, it is possible to steer the beam in a retrodirective manner. However, such geometry does not fit into compact spaces. A proposed solution is to flatten those panels while equipping them with a phasing mechanism so that to restore the retrodirective behavior.

First, a theoretical study on the potentials and limitations of utilizing a reflectarray as the required phasing mechanism is performed. Based on this study, a prototype operating at the frequency of interest (24 GHz for automotive RADARs) is designed, fabricated and tested. One can assume that by attaching this reflector to the bicycle frame, the overall RCS of the reflector-bicycle structure will be enhanced.

Metamaterials

In the second part of the thesis, the focus switches from the bicycle to the cyclist himself. The aim is thus to increase the RCS of the cyclist. Based on the assumption that the human torso can be modeled as a multi-layer dielectric cylinder, our theoretical problem reduces to increasing the backscattering of a multi-layered cylinder made of lossy dielectric materials. The backscattering of such a cylinder is then coated by a dielectric layer of variable permittivity and thickness. The variations are determined and optimised such that design rules for best coat characteristics in terms of permittivity and thickness can be defined.

The problem of scattering by a multilayered cylinder has an analytical solution based on Bessel and Hankel functions. This theoretical model is implemented and it is then validated with respect to current state-of-the-art configurations. The challenge here consists in the analysis of electrically large lossy bodies, which to the best of knowledge, has not been addressed before.

It is then applied to study the backscattering of a multi-layer cylinders with coats of different permittivity and thickness. Design rules for maximising the backscattering are then derived. It is shown that negative permittivity materials are very good candidates. Numerical simulations are then proposed to confirm these predictions. The main contributions in this part of the Ph. D. are (i) the extension of the theoretical scattering

analysis by electrically-large lossy bodies which enables simple prediction of adequate coats to enhance back-scattering and (ii) the theoretical demonstration of the relevance of negative permittivity metamaterial to enhance back-scattering of lossy cylindrical bodies.

Plan of the thesis

The thesis body consists of five chapters. Chapter one provides a literature review about the topic. Chapters two and three are dedicated for the analysis and design of a retrodirective flattened dihedral reflector. Chapters four and five are dedicated to the investigation of the backscattering of human torso based on a multi-layered cylinder model.

The first chapter starts with providing a literature review about the recent advances in systems deployed to improve the safety of vulnerable road users (VRU's) such as pedestrians and cyclists. Considering that CYCLOPE project investigates the applicability of the Radar systems to detect the VRU's and particularly cyclists, the next section in the chapter introduces the theoretical definition of the Radar Cross-Section. From there, the review focuses on the methods proposed to enhance the detectability of such targets. The solutions inspired from reflectarrays and metamaterials are discussed and put into critical examination as to what has been already done in literature.

In the second chapter, a detailed analytical study is provided to dissect the reflectarray phasing mechanism occurring between the panels of the dihedral. The retrodirective phase law is first formulated and the progressive phase shift required to retrodirectively steer the incident beam is obtained as a function of the beam incidence angle and the geometrical parameters. A complementary theoretical study would give predictions on the potentials and limits on the retrodirective performance influenced by those geometrical parameters and the incidence angle of the incoming wave, thus offering design guidelines to follow.

The third chapter discusses the design of a reflectarray-inspired retrodirective flattened dihedral operating at 24 GHz. This chapter is composed of three main parts : unit cell study, reflectarray construction and the design of the flattened dihedral. The unit cell study is first performed, and the reflection phase response is obtained with respect to the geometrical parameters and the incident wave characteristics. A reflectarray is hence constructed in a manner that its array cells obey the nominal retodirective phase law formulated in the previous chapter. Finally, a flattened dihedral prototype operating at 24 GHz is proposed. The prototype is fabricated and tested in an anechoic chamber using two horn antennas and a network analyzer.

In the fourth chapter, the possibility of the backscattering enhancement of the human torso is studied. A human torso can be approximately modeled as a lossy dielectric multi-layered cylinder of the human biological tissues. An exact solution of the scattering by a multi-layered lossy dielectric *infinitely long* cylinder exists.

Consequently, the problem is approached in a progressive manner. First, a numerical model is proposed for the solution of scattering by a double-layered infinitely long cylinder and then validated using examples found in literature. The model is then extended

to account for the solution of the scattering by a multi-layered cylinder. By assigning each layer to the corresponding biological tissue characteristics, it would be then possible to predict the backscattering efficiency of the human torso. To alter the backscattering intensity, the multi-layered cylinder is coated with a layer of negative permittivity medium. It would be then possible to predict the coat profile characteristics that optimally enhances the backscattering by a human torso.

Chapter five can be seen as an extension of chapter four. The chapter deals with the problem of backscattering by a *finite* multi-layered dielectric cylinder. To take into account the finiteness of the cylinder, a correction factor is introduced to the infinite model proposed in the previous chapter. Now, dealing with a finite structure, full-wave simulations are possible and they have been performed to test the backscattering model for the simpler case of double-layered cylinder. For the multi-layered cylinder emulating a human core, the theoretical model in this case is expected to provide guidelines to follow so that to obtain an enhanced backscattering. Full-wave simulations are hence performed to put those guidelines into practice. Finally, the backscattering enhancement performance of negative permittivity coats is assessed for variations of a human core.

The thesis context, scientific aspects and contributions are summed and wrapped up in a general conclusion together with a list of the perspectives.

Chapter 1

State of Art

1.1 Introduction

In this chapter, a literature review relevant to the context of this thesis is provided. This review takes into account the different aspects of the research work in terms of the general background and the specific applied scientific field. This chapter is divided into two major parts. In the first part, an overview is given about the Vulnerable Road Users (VRU) detection on roads. A description is given about the detection methods proposed and the advanced systems deployed nowadays.

In the second part, a review is provided on how the Radar cross section (RCS) tailoring problem has been tackled in the literature. VRUs present low reflective profiles and hence are difficult to detect using automotive Radars. Two approaches based on the concepts of retro-reflection and scattering maximization are investigated in order to enhance the RCS of VRUs. We go through each of the concepts and visit the methods and techniques relevant to each of the approaches.

1.2 Overview on the methods and techniques for Vulnerable Road Users (VRU) detection

1.2.1 Dangerous real life Scenarios : blind-spot, intersection point

Road is a dangerous place full of moving heavy vehicles driven by anxious and error-prone human beings[2],[3]. This agitated environment is in need for technology intervention to deal with its dangers and ease the anxiety of the drivers. Due to the fact that vehicles move with momentum, nearly any situation turn into a dangerous one. However, there are specific scenarios where the level of danger leading to accidents can be extremely high. Among those are the blind-spot and intersection point scenarios(Figs. 1.1 and . 1.2 respectively).[4],[5]

Blind-spot situation can be described as when the driver is visually or with the help of the mirrors is unable to detect or track the cyclist. Intersection point scenario is when the driver direct vision towards a cyclist is obstructed by the presence of a vehicle on the

FIGURE 1.1 – A sketch showing the blind spots where the bus driver cannot visually detect road obstacles as VRUs

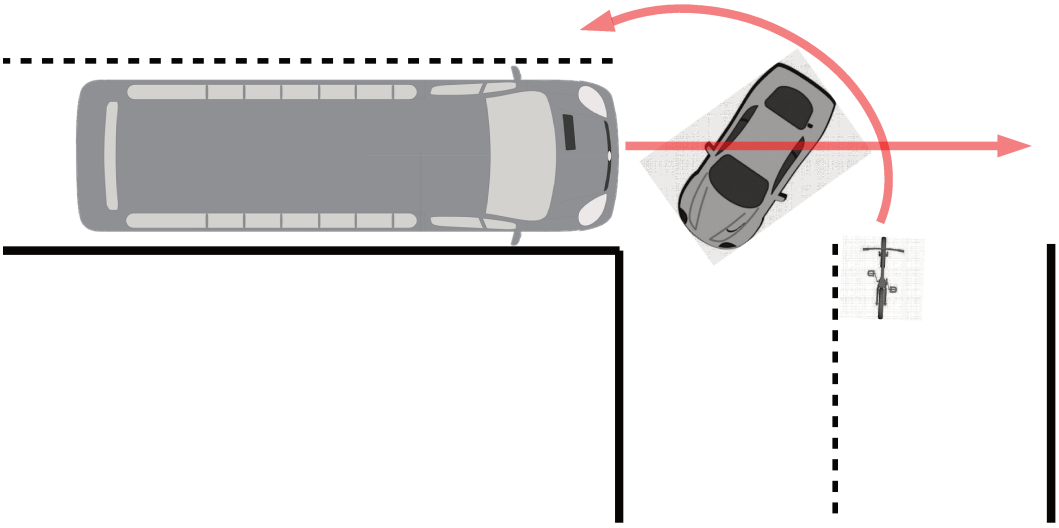

FIGURE 1.2 – A sketch of the scenario where the bus driver is visually unable to detect the cyclist at an intersection point

FIGURE 1.3 – sketch of a commercial camera system[10]

traffic intersection point. To overcome the human vision shortcomings, technology based systems are required to alert the driver and prevent a possible collision.

1.2.2 Sensor-based techniques

1.2.2.1 Vision based techniques using cameras

Vision based techniques using cameras[6] have always been seen as solutions (Fig. 1.3) to aid drivers on roads. A camera system scans its surrounding in order to detect a potential obstacle. However, it is not the problem of image scanning, but rather the processing of the visual data that makes it necessary to implement sophisticated processing units to handle the problem. Such difficulties even magnify due to the influence of external factors as lighting conditions and environmental clutter on the accuracy of the system [1].

Work is being done to improve the system detectability for VRU's as pedestrians [7] and cyclists [8],[9] but surely on the expense of additional complexity.

1.2.2.2 Detection using Lidar techniques

Lidar is a detection device that operates similarly to a Radar with the difference that beam emitted is a laser (Fig. 1.4). A Lidar sends a beam that that gets projected at a rotating mirror which scatters over the sensor's field of view. Via a photo diode receiver, the time it takes the reflected beam to return to the Lidar is measured. Based on the trip time and the mirror angle, it is then possible to precise the position of the obstacle. Utilizing multiple layers of rotating scanners it is possible to obtain a 3D cloud regarding the information from the reflected beams. This can be translated into a spatial shape formulation of the detected object. Also, Lidar systems are relatively robust against rain and snow conditions. All those features however come on the expense of production cost which is hindering the chances of mass deployment of such systems in the vehicles [1].

Specific work has been done on the purpose of enhancing the Lidar detectability of VRU's as pedestrians and cyclists using datasets and adaptive feature extractors [11] ,[12].

FIGURE 1.4 – An example of a commercial Lidar system[13]

FIGURE 1.5 – A photo of a commercial FMCW short range Radar operating at 24 GHz[17]

1.2.2.3 Detection using Radar techniques

A short range Radar sensor (Fig. 1.5) operates by transmitting an electromagnetic wave to scan its surrounding. Based on the frequency modulated continuous wave (FMCW) principle, it is possible to extract information regarding the obstacle radial range and its relative velocity[14], [15]. Most popular Radars operate in the 24 GHz or 77 GHz[16] frequency bands.

Radars are robust against weather conditions however have limited performance regarding the detection of VRUs due to their low reflectivity as compared to other vehicles on the road [1]. The core of this thesis is to investigate solutions that enhance the reflectivity of VRUs, in other words, their Radar cross section (RCS).

1.2.3 CYCLOPE project

CYCLO Protection Electronique (CYCLOPE) is a national project that targets the problem of cohabitation between transport modes as cycling and buses. The objective of this project is to propose novel securing equipment solutions to cyclists together with alerting systems to bus drivers. The project is organized in two parts, namely "Radio technology" and "Human and social sciences". The originality of the project resides in the strong interaction between the two parts to foresee the influence of the technical solutions chosen on the users behavior. Simulations should allow to test for the acceptability of the proposed solutions before experimental testing.

As a part of this project, we investigate in this thesis solutions based on Radar

technology. An automotive Radar operating at 24 GHz (or 77 GHz) is integrated on the bus in the purpose of scanning the surrounding and detecting possible VRU's as the cyclists. The main drawback of a Radar is its dependency on the target RCS. The objective is hence to improve the detectability of the cyclist by the Radar, in other words, to enhance the RCS of the bicycle-cyclist system.

1.3 Radar cross section (RCS) in automotive applications

1.3.1 RCS definition

Radar cross section (RCS) is qualitatively defined as the ability of a target to reflect the transmitter signal back in the same direction of incidence. Thus, RCS is directly related to the backscattering by the target [18].

The factors that impact the RCS are related to both the target itself and the electric field orientation and polarization. The target's electrical size, shape, surface and constituting material all impact its RCS.

For instance, retrodirective reflectors as the conventional dihedral corner possess high RCS values [19]. Usually, large structures as airplanes and ships also are good backscatterers. Other objects that have absorptive nature or are simply physically small don't possess such characteristic.

RCS reduction problem has been given a lot of attention especially with the impact the RADAR technology had on the international military balance of power. Quantitatively, RCS can be formulated as follow :

$$RCS = \lim_{r \to \infty} 4\pi r^2 \frac{|E_s|^2}{|E_i|^2} \tag{1.1}$$

where r is the distance between the Radar and the target (in meters), E_s and E_i are the intensities of the far field scattered and incident electric fields.

1.3.2 RCS measurement of automotive targets at 22-29 GHz and 76-81 GHz frequency bands

For the Radar processing unit, it is very important to have prior information about the RCS levels of the automotive targets. In this part, archived RCS measurement results are provided for pedestrian, bicycle-cyclist and different models of cars in the 22-29 GHz and 76-81 GHz frequency bands.

The measurement campaign was performed by Geary et *al.*[20] using a Anritsu ME7828A VectorStar VNA with measurement capability up to 110 GHz. Broadband K and W-band horn antennas were used and placed 17 m from a rotating platform that holds the targets.

Fig. 1.6 shows the RCS measurement results for the vehicle models Cadillac STS sedan, Chevrolet Avalanche truck and Chevrolet Express van in the horizontal polarization configuration (with respect to the ground). The results show highest RCS levels for

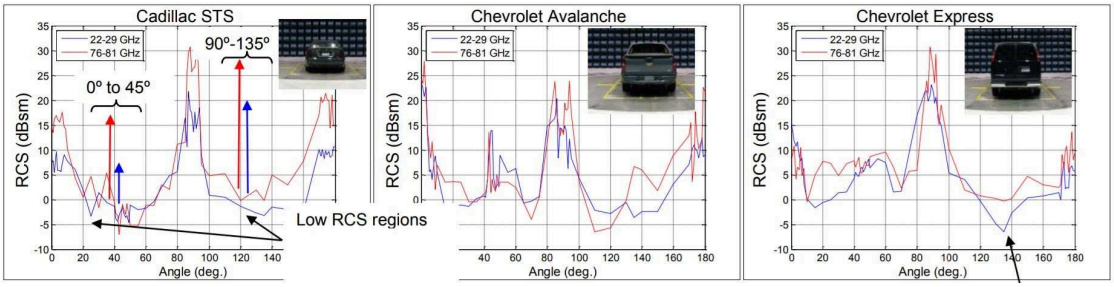

FIGURE 1.6 – Average RCS as a function of the azimuth angle of the Cadillac STS sedan, Chevrolet Avalanche truck and Chevrolet Express van for K-band and W-band in horizontal polarization configuration[20]

the scenario where the Radar faces the side of the vehicle (azimuth angle of 90°). For the 22-29 GHz frequency band, the vehicles average peak RCS levels vary from 20 to 23 dBsm. For the 76-81 GHz frequency band, the vehicles average peak RCS levels vary from 24 to 30 dBsm.

The pedestrian peak RCS levels given in Fig. 1.7 do not exceed -2 dBsm for both frequency bands. Significant increase in the RCS level occurs for the case of a cyclist-bicycle system. Fig. 1.8 shows that the peak RCS in the 22-29 GHz band goes up to nearly 6 dBsm and 15 dBsm for the 76-81 GHz band.

Those result clearly show that the RCS signature level of a vehicle is much higher than that of a pedestrian or a cyclist-bicycle system.

Using a 24 GHz automotive Radar, it is clear that an enhancement in the RCS levels of the pedestrian and the bicycle-cyclist is crucial to improve their detectability by a short range automotive Radar.

1.4 Approaches to enhance the backscatter RCS

1.4.1 An overview

Several methods and techniques have been proposed in the aim of altering the backscattering by a target. Due to its importance in military applications, RCS reduction topic has been the most studied in the past decades as compared to RCS maximization[18]. The structures that require its backscattering to be maximized are usually large and hence such a problem does not come as a real challenge. Simple metallic tetrahedral or dihedral corner reflectors possess high RCS values and can be easily mounted on structures as ships or airplanes[21]. However, this is not the case for decreasing the RCS. Lot of efforts has been focused on stealth technology. In this term, several techniques have been utilized as purpose-shaping, frequency selective surface (FSS) scatterers and Radar absorbent materials.

In this thesis, the challenge rises to enhance the backscatter RCS of structures of small physical size. It is then required to propose new simple, compact, low cost and effective

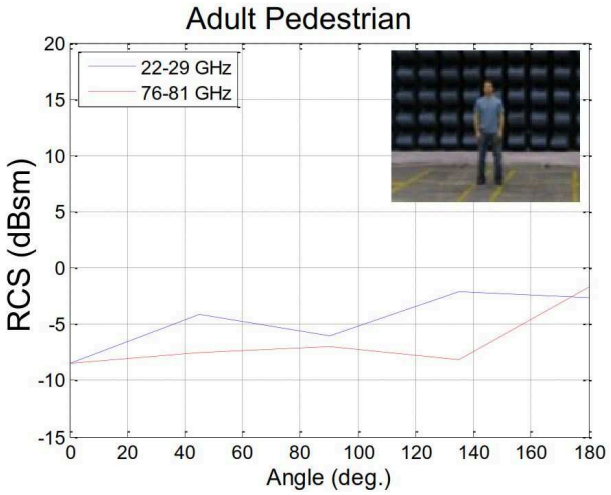

FIGURE 1.7 – Average RCS as a function of the azimuth angle of an adult pedestrian for K-band and W-band in horizontal polarization configuration[20]

FIGURE 1.8 – Average RCS as a function of the azimuth angle of bicycle-cyclist for K-band and W-band in horizontal polarization configuration[20]

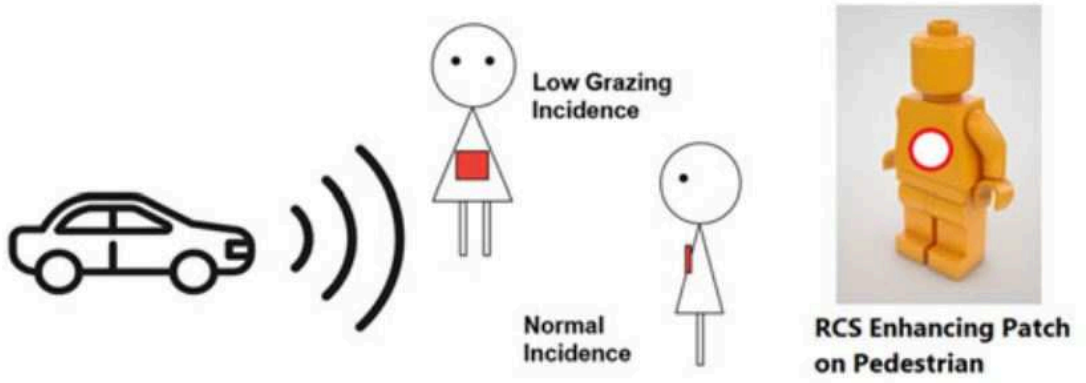

FIGURE 1.9 – A sketch showing the possible incidence scenarios on a pedestrian RCS enhancing patch[22]

solutions that can be applicable for automotive targets. Such solutions were investigated in the letter entitled as "*Radar Cross Section Enhancing Structures for Automotive Radars*"[22]. The authors propose a reflector that can be attached to a pedestrian or a bicycle to enhance its backscattering. An illustration is given in Fig. 1.9. The main contribution in their work is the design of a low-profile dihedral corner metallic web ridge with a good frequency broadband performance. The design is less sensitive to incidence angle as compared to a flat patch and can invariantly operate for any polarization. A fabricated prototype of size 20 cm by 20 cm is shown in Fig. 1.10. The reflectivity comparison between the ridge design and a metallic patch of the same dimensions is provided in Fig. 1.11. The results for both polarizations show an improvement over the simple patch reflector.

The proposed designs can be interesting solutions as RCS enhancing structures for an automotive Radar. However, a web ridge design cannot be a realistic solution for the case of a pedestrian or a cyclist due to its bulky size. Also, comparing the angle sensitivity of the proposed design to that of a metallic disk is not very convincing knowing that a flat patch is the worst-case scenario reflector in terms of incidence angle sensitivity.

In our thesis, two approaches are investigated as RCS enhancing solutions : retro-reflection property and scattering maximization using artificial materials. For the first approach, the design of a retrodirective flattened dihedral is investigated with its RCS performance being compared to a dihedral corner. This is a much better reference than a flat patch ; in fact the dihedral corner is the retro-directive reflector best-case scenario in terms of polarization and incidence angle performance as well as simplicity. In the second approach, the possibility of designing wearable reflective jackets based on artificial materials is investigated.

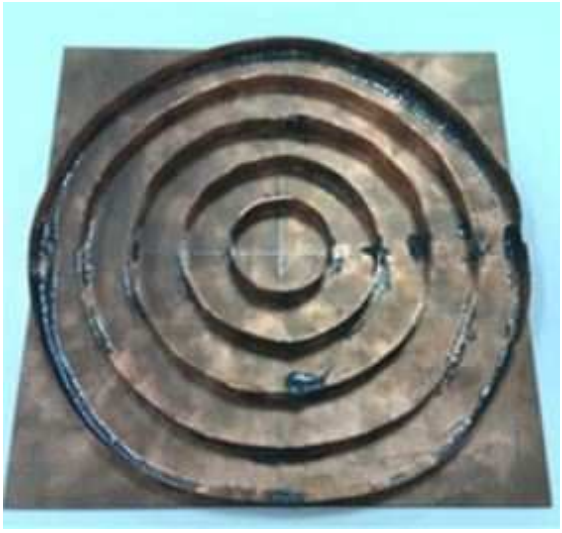

FIGURE 1.10 – A prototype of a low profile dihedral corner web ridge of patch size 20 cm by 20 cm[22]

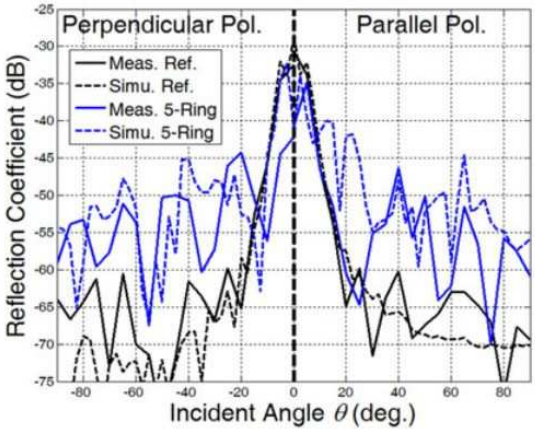

FIGURE 1.11 – Reflection coefficient versus the incidence angle of the web ridge patch as compared to a flat patch for both polarization configurations[22]

FIGURE 1.12 – A depiction of a diamond tetrahedral fixed on the mast of a yacht[23]

1.4.2 Utilizing the retro-reflection property

As previously stated, RCS is defined as the ratio of backscatter power per steradian (unit solid angle) to the power density that is intercepted by the target. Therefore, not only an electrically large object can possess a high RCS, but more definitely this is characteristic possessed by a target that can specifically redirect the incident energy back in the same direction of the Radar. Such objects are called retrodirective reflectors. A relatively small and simple metallic dihedral corner possesses high RCS due to its ability to efficiently redirect the incident beam back in the same direction of incidence [19]. For example, such type of reflectors have been a long time servants in maritime navigation systems on ships and lifeboats to enhance their detectability by marine Radars operating in the X-band. A depiction of a diamond tetrahedral fixed on the mast of a yacht is given in Fig. 1.12.

As illustrated in Fig. 1.13, the dihedral principle of operation is very simple. The beam hits the first panel and is reflected to the second panel with a certain angle of reflection. Due to the orthogonality of the structure, the beam on the other is reflected with an additional 180° with respect to the incidence angle and back in the same direction of incidence. The tetrahedral corner operates in a similar fashion.

In this thesis, simple and compact design based on the concept of retro-reflection is investigated. The proposed reflector is a flattened version of the dihedral corner. The study is hence focused on the compensating phasing mechanism that re-ensures the flattened dihedral behaves retrodirectively again.

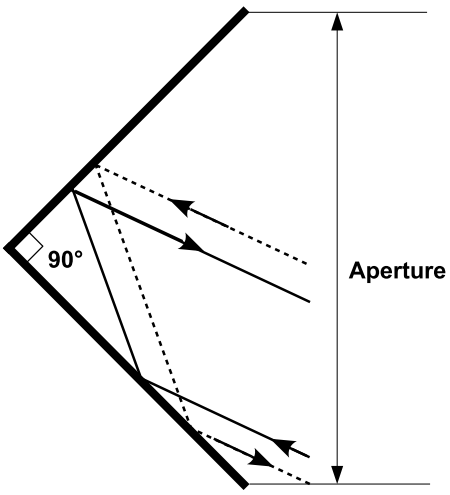

FIGURE 1.13 – An illustration of te dihedral corner reflection principle of operation

1.4.3 Scattering maximization using artificial materials

Artificial materials have been long used in the purpose of engineering the scattering by Radar targets. Radar absorbent materials have been heavily investigated as a possible stealth technology. Those materials are mainly classified as either impedance match surfaces or resonant absorbers.[24],[25] As the weight reduction and optimization of the operating bandwidth are two important issues, new techniques based on carbonaceous materials have been recently proposed.[26] Such materials offer a large flexibility for design and properties control.

Metamaterials have been also investigated as possible Radar absorbent materials. Using their extraordinary capabilities, absorbents of ultrathin thickness[27] and operating on a broadband of frequencies [28], [29] have been designed.

In our thesis, the aim is to use metamaterials in the purpose of scattering maximization. The investigation is concentrated on the possibility of designing a reflective jacket that enhances the backscattering by the cyclist or pedestrian. Such metamaterial jacket can be implemented using mechanically flexible textiles. This is a simpler solution as compared to wearable and on-body antennas that require antenna excitation systems [30],[30],[31],[32],[33].

1.5 Retro-directive reflectors

1.5.1 Phase conjugation systems

A retrodirective reflector reflects the incident signal back in the direction of incidence [34], [35],[36] by conjugating the phase of the wave along the receiving axis.

Several techniques have been proposed to realize analog as well as digital phase conjugation systems. For analog systems, the most common techniques are based on either

passive Van Atta array [37] or on active heterodyne technique using phase conjugate mixer (Pon array) [38], phase detection and Phase-Locked Loop (PLL) technique [39]. Van Atta array uses a network of transmission lines to pair arrays of distinct antennas with each other (Fig. 1.14). The incoming plane wave is first received by the antennas at one end. It then propagates along the transmission lines where its initial phase is conjugated, and is finally re-radiated by the antennas at the other end of the pair. The resultant of the interference of all the re-radiated waves along the axis of the array is a reconstructed wave traveling back in the direction of the source. Despite being simple and reliable over a wide range of incidence angles, this topology suffers from losses in transmission lines. Modified versions of Van Atta array have been proposed with the possibility of bi-directional amplification [40], albeit, at the expense of high cost and added complexity. In [41], a passive circularly polarized Van Atta array has been proposed at 25 GHz for the use in automotive Radar applications.

Heterodyne techniques use phase conjugation mixers to reverse the incoming wave. This can be done by two main methods, either heterodyne technique using a local oscillator (LO) (Fig.1.15) at twice the radio frequency (RF) [42], or heterodyne technique using intermediate frequency (IF) [43]. Phase detection and PLL techniques use more expensive and complicated systems to obtain better performance [39]. In digital systems, the signal is first down-converted using A/D converter, and is then processed by a digital signal processing system. At that stage, the carrier gets recovered and the digital signal gets demodulated, modulated and up converted [44].

Retroreflection property is being recently researched as for possible utilization in modern applications. In [45], a retrodirective antenna array (RDA) for wireless power transmission (WPT) has been presented. The idea behind this system is illustrated in Fig. 1.16. A RDA based on Pon array configuration offers far-field transmission of electromagnetic energy to serve as a charging pad for the electronic devices in its nearby. In [46], a low-complexity WPT scheme has been presented based on the new retrodirective beamforming technique in a multi-user massive MIMO WPT system. Another low complexity WPT system has been proposed in [47] by combining large antenna retrodirectivity at the transmitter part with signal backscattering at the receiver side.

Investigating compactness, a novel concept for electrically compact retrodirective antenna arrays with super-resolution radiation patterns and auto-pointing has been presented in [48].

1.5.2 Beam steering using non low-profile configuration : Dihedral corner

Those above mentioned active retrodirective reflectors suffer from high complexity and cost. Hence, such solutions are not attractive for mass-market applications where cost and simplicity are major concerns such as for the automotive RADAR industry where backscattering is also a very desirable feature.

For automotive RADARs, a methodology based on passively redirecting waves using simple conventional metallic corner dihedral [19] can prove to be attractive due to its

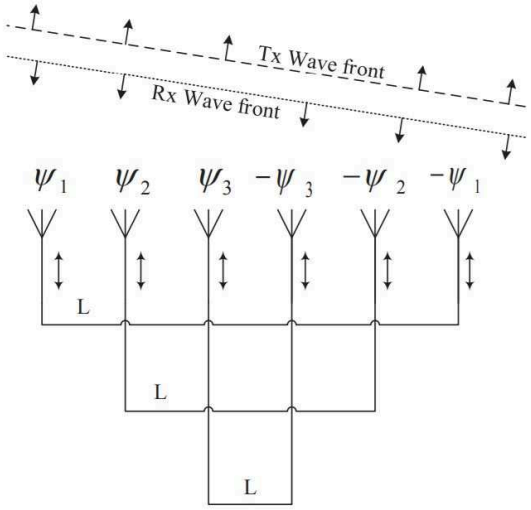

FIGURE 1.14 – A schematic of a Van attay transmission lines network array

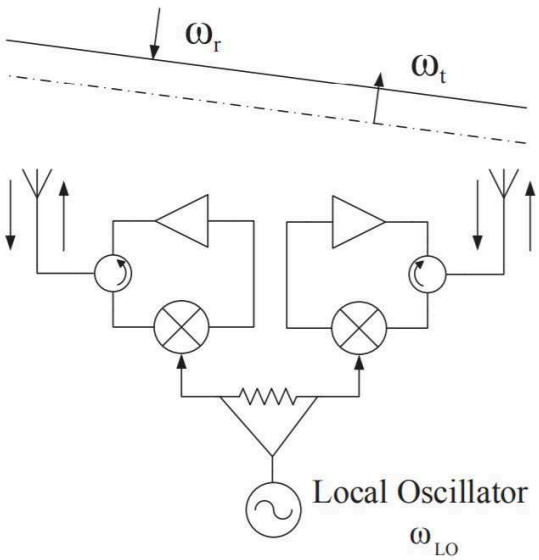

FIGURE 1.15 – A schematic of a Pon array utilizing a local oscillator and conjugate mixers

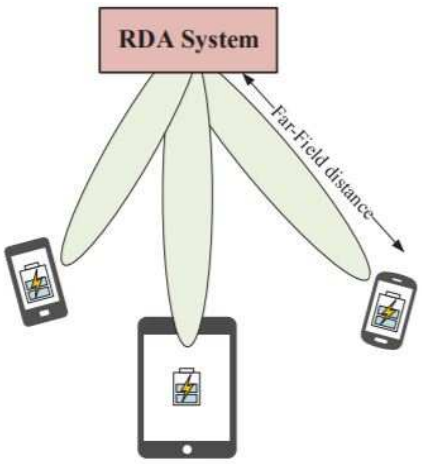

FIGURE 1.16 – An RDA system with farfield energy transmission capabilities [45]

passive nature and the characteristic retrodirective profile it proposes for a wide range of incidence angles. However, because of its bulky structure, there is a growing interest in finding solutions to lower its profile while preserving its performances. In the next part, solutions based on flattened dihedral corner configuration are presented and a critical examination of those methods and techniques is provided.

1.6 Retrodirective flattened dihedral configurations

1.6.1 Compact dihedral corner based on transformation optics

Transformation Optics (TO) technique has been proposed to reach low profile metallic corner dihedral. By applying an adequate linear coordinate transformation, a TO domain can be realized using anisotropic homogeneous dielectric layers[49], [50], [51].

In [52], a new approach is proposed to flatten the dihedral corner. The proposed method enables compact reflectors via Transformation Optics combined with Surface Impedance Modulation (SIM). This combination permits to relax the constraints on the anisotropic material resulting from the TO. Phase gradient approach is generalized to be used within anisotropic media and is implemented with SIM. An illustration is given in Fig. 1.17. The RCS results are shown in Fig. 1.18. Configuration 1 represents the case where the retrodirective mechanism only depends on the surface impedance modulation. Configuration 4 is the extreme case where the anisotropic factor is not relaxed at all. These results show that a small amount of SIM can significantly relax the anisotropic factor without affecting the performance too much, especially when skipping from configuration 4 to 3, in which 1.5 reduction factor in the anisotropy is induced.

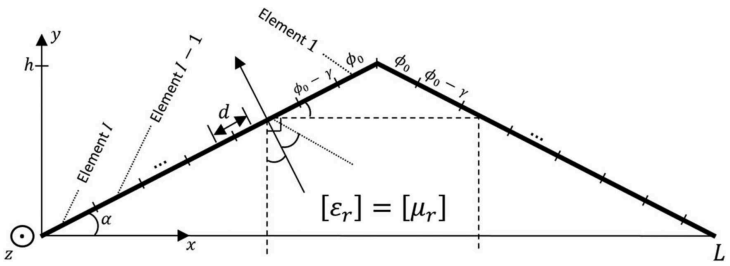

FIGURE 1.17 – The design of a low profile dihedral corner based on Transformation Optics combined with Surface Impedance Modulation [52]

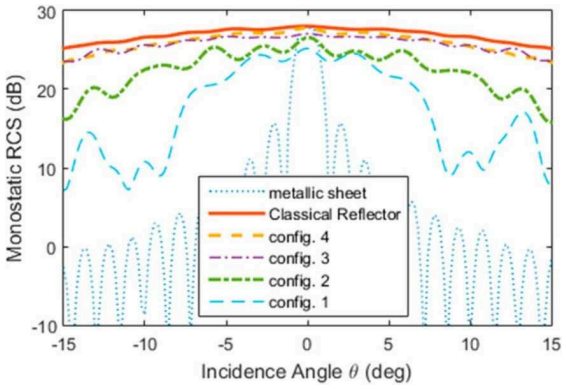

FIGURE 1.18 – A comparison between the monostatic RCS profiles of the dihedral corner, metallic sheet and the proposed low profile reflector for different anisotropy-SIM combination configurations [52]

1.6.2 Panels equipped with frequency selective surfaces

In this part, the techniques based on implementing frequency selective surfaces (FSS) on the panels of the flattened dihedral panels are examined. The FSS's operate as a phasing mechanism that directs the beam from one panel to the other and back in the direction of incidence.

1.6.2.1 Method based on continuously shaped metasurfaces

The reformulation of the generalized laws of reflection and refraction laid the foundation for the rise of phase gradient metasurfaces [53],[54]. Metasurfaces are classically constructed using discrete array elements of sub-wavelength spacing. Such discretization introduces errors to the gradient phase formulated and hence degrades the overall performance of the surface.

In [55], Guo Yinghui et *al* have proposed the principle of a scattering-harness mechanism by utilizing continuous gradient phase stemming from the spin-orbit interaction via sinusoidal metallic strips. By adjusting the amplitude and period of the sinusoidal metallic strip it is possible to efficiently control the scattering characteristics of the metasurface.

Inspired from this principle of operation, a retrodirective flattened dihedral has been proposed. On each of the panels is attached a phasing mechanism constructed from sinusoidal metallic strips so that the overall dihedral virtually behaves as a dihedral corner. Fig. 1.19 shows the associated prototype along with the frequency-RCS enhancement profiles with to respect to the bare dihedral for both TE and TM configurations. The simulation ((c) and (d) and measurement ((e) and (f)) results show that significant RCS enhancement can be obtained over the frequency range 8 to 12 GHz. The authors did not provide results regarding the reflector sensitivity to incidence angle.

1.6.2.2 Method based on fractal-based patches

Since their mathematical definition by Benoît Mandelbrot [56], fractal geometry patterns have gained attention due to their potential applicability in various fields of science.

The synthesis of retrodirective flattened dihedral using fractal-based patch geometry has been studied in [57]. Fig. 1.20 shows a scheme of the reflector designed using square metallic patches. The associated monostatic RCS for a design operating at 9.55 GHz is given in Fig. 1.21. The RCS profiles of the TE and TM configurations show significant enhancement as compared to a bare flattened dihedral. However, the result show that the reflector is very sensitive to incidence angle.

1.6.2.3 Method based on discrete periodic array

Periodic arrays offer the capability of steering an electromagnetic beam to a predefined direction. Whenever a plane wave impinges on an infinite array of periodic elements, currents of same amplitude are induced. The current phase on each of the elements should match the phase velocity of the incident signal in the direction within the array is

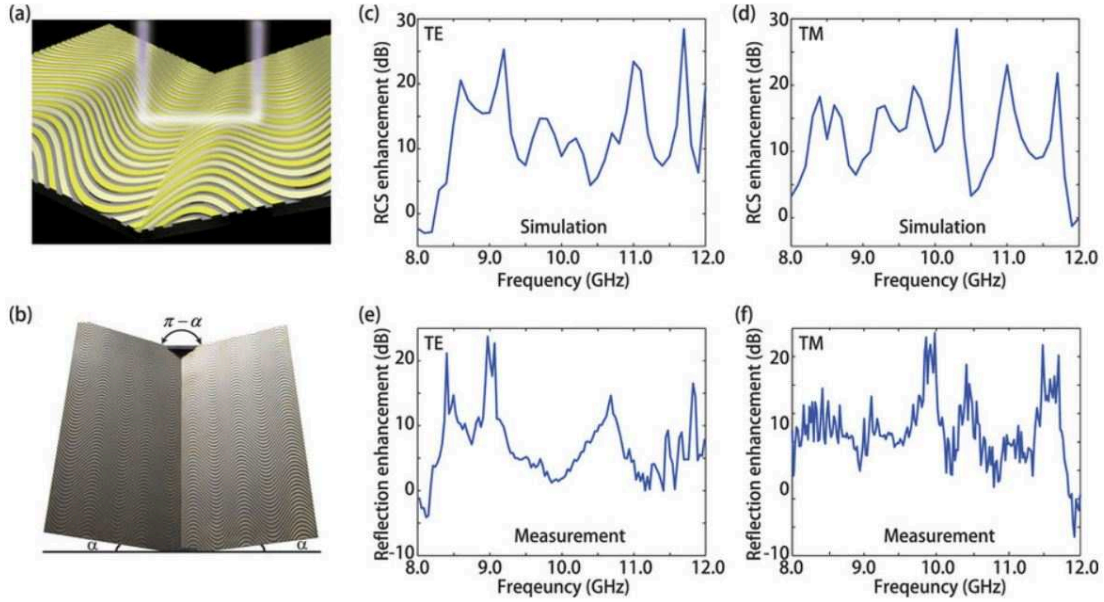

FIGURE 1.19 – (a) shows the depiction of the retrodirective flattened dihedral based on the continuous sinusoidal metasurfaces, (b) gives the associated reflector prototype, (c,d) and (e,f) show the simulation and measurement results of the RCS enhancement versus frequency for TE and TM configurations respectively [55]

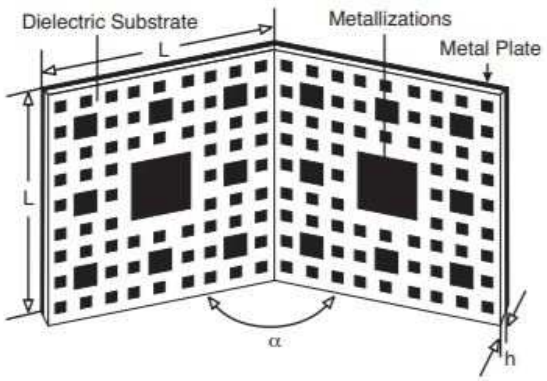

FIGURE 1.20 – A depiction of the retrodirective flattened dihedral using fractal-based patch geometry [57]

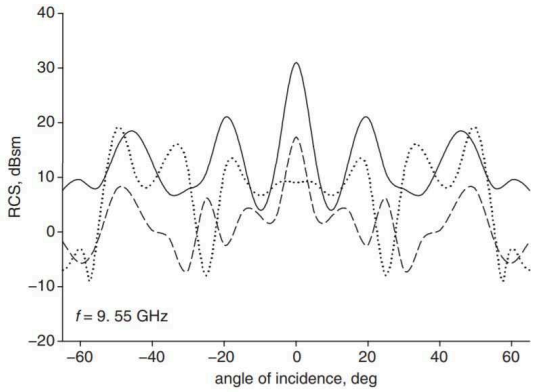

Fig. 3 *Variation of RCS with angle of incidence*
Corner angle = 80°, $h = 3$ mm
—— MDS loaded, TM polarisation
– – – MDS loaded, TE polarisation
..... plain dihedral corner reflector

FIGURE 1.21 – RCS versus incidence angle comparison between a fractal-based reflector and the associated bare flattened dihedral [57]

placed. Gaston Floquet addressed the mathematical parallel of the problem. In his work, he solves the problem of differential equations with periodic coefficients. By expressing the problem of periodic array in the appropriate form, Floquet theory can be exploited to analytically obtain the elements current phases[58].

By engineering the phase response from each array element it is possible to reproduce the current phase profile associated with the scattered beam in the desired direction.

Utilizing this property, it is possible to construct a phase law on the panels of dihedral in a manner that the incident beam is directed from the first panel to the other one and back in the same direction of incidence. In the next section, an approach based on reflectarrays is introduced.

1.7 Flattened dihedral inspired by reflectarrays

Theory of operation

The emergence of reflectarrays [59] stems from the fact they combine the characteristics of a parabolic reflector [60], [61] and an antenna array [62] while getting rid of their bulky volume and complexity respectively. As shown in Fig. 1.22, the parabolic reflector requires only a feed horn antenna to excite its surface. By utilizing the array properties, a low profile low cost reflectarray is born. Shown in Fig. 1.23 is the configuration of a reflectarray with a feed antenna in its proximity.

Inspired by this concept, a retrodirective flattened dihedral utilizing reflectarrays is proposed. However, in this case here, the excitation is considered distant from the

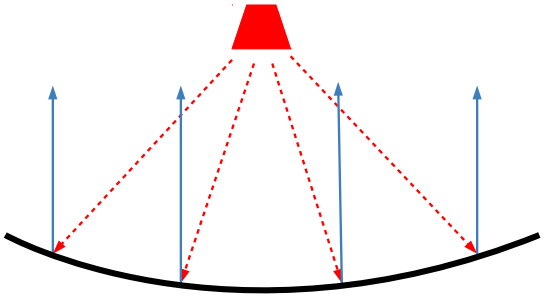

FIGURE 1.22 – A depiction of a parabolic reflector fed by a horn antenna

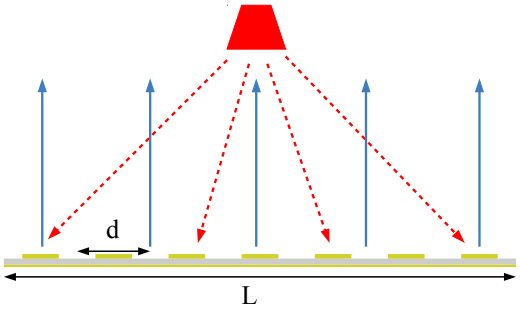

FIGURE 1.23 – A depiction of a reflectarray of size L and periodicity d fed by a horn antenna

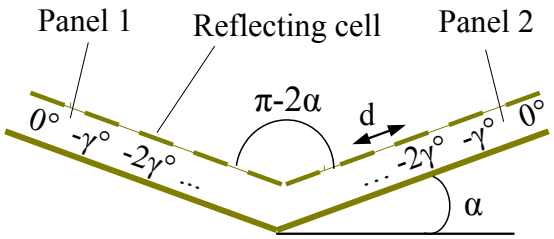

FIGURE 1.24 – The configuration of a flattened dihedral using reflectrray ; the phasing cells obey a global retrodirective phase law (γ) to steer the beam from panel 1 to 2 and back in the direction of incidence

reflector and hence treated as a plane wave. Our structure consists of two patch arrays assembled on a dihedral reflector with an opening angle equal to $\pi - 2\alpha > \pi/2$ as shown in Fig. 1.24. The distance between each two patches is equal to d. The electromagnetic beam is steered from one panel to the other and then reflected back in the direction of arrival. This is achieved by tuning the cells dimensions in order to obtain a linear phase variation in the plane of incidence. This variation or the phase law can be secured and governed by selecting an appropriate phase shift (γ) between two consecutive cells as illustrated in Fig. 1.24.

Design at 9 GHz

In [63], a prototype using annular patches and operating at 9 GHz has been designed, fabricated and tested to prove the concept. Fig. 1.25 shows a schematic of the proposed prototype. The dihedral flattening degree is set to $\alpha = \pi/8$. The inter-element spacing is set to $d = \lambda_0/3$ where λ_0 is the free space wavelength. Measured RCS profiles versus incidence angle for the transverse electric (TE) configuration are shown in Fig.1.26. The results show that the obtained RCS profile is flat as compared to a flat plate while the RCS level is till comparable to that of a dihedral corner over the range of incidence angles. Also, RCS results corresponding to the TM configuration show better performance as compared to the TE configuration (Fig. 1.27). Tab. 1.28 shows that this promising performance was possible while still being able to shrink the dihedral corner thickness by half.

Those results persuaded us to further investigate the limits and potentials of this design. In the first part of the thesis, two objective are identified. The first is to design a prototype operating at 24 GHz for applications of automotive Radars. The second is to perform an analytical study to understand the impact of the different geometry factors on the performance of the dihedral.

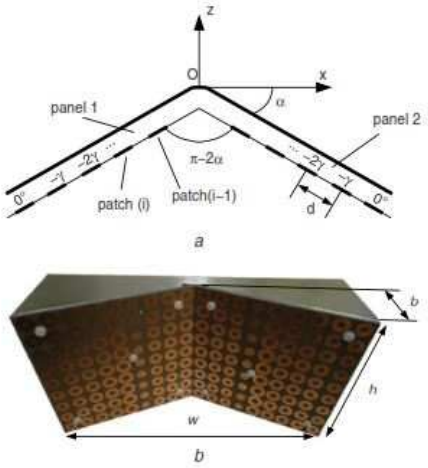

FIGURE 1.25 – A prototype of a flattened dihedral inspired by reflectarrays operating at 9 GHz [63]

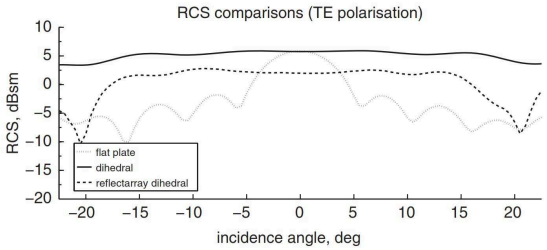

FIGURE 1.26 – Measured RCS comparison between a flat plate, retrodirective flattened dihedral and classic dihedral corner in TE configuration (E-field along y-axis) [63]

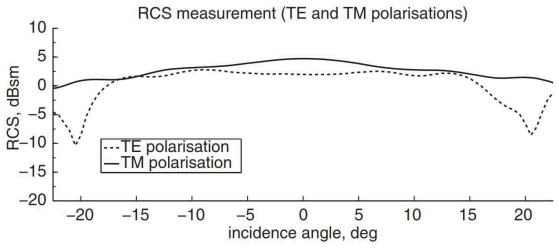

FIGURE 1.27 – Measured RCS of the retrodirective flattened dihedral in both TE and TM configurations (E-field along y-axis and x-axis respectively) [63]

Structure	b (mm)	h (mm)
Flat plate	0	100
Dihedral	70.7	100
Reflectarray dihedral	38.3	100

FIGURE 1.28 – Dimensions of the flattened dihedral as compared to the equivalent classical dihedral corner [63]

1.8 Scattering maximization using artificial materials : Metamaterials

In this section, a review is given on the works related to the scattering manipulation using metamaterials.

The parameter which determines if a substance is homogeneous and can have bulk electromagnetic properties is the wavelength of the incident wave. The nature of the atoms and their arrangement determines the macroscopic electric permittivity and magnetic permeability of the medium. This is how things are in nature[64].

It is possible then to synthesize artificial materials of certain permittivity and permeability inspired by the same concept. By constructing a cell sensible to electric and magnetic fields and arranging it in a periodic array of sub-wavelength periodicity, it is possible to build a medium of arbitrary electric permittivity and magnetic permeability[65]. The choice of the cells is crucial to obtain this rich response. Classically, a cell consisting of a wire dipole and a split ring resonator synthesize an effective double negative medium (i.e., both permittivity and permeability are negative) as shown in Fig. 1.29.

When the synthesized permittivity and/or permeability have a negative value, then the material constructed can be called a metamaterial. Such artificial material is extraordinary and cannot be found in nature when the incident wavelength is in the millimeter range.

Now, that it is possible to construct materials of such negative values, this had a dramatic impact on the fields of optics, physics and consequently engineering communities, and led to the rise of numerous applications that were impossible in the near past.

Metamaterials are used nowadays to enhance the radiation and matching properties of electrically small antennas. Zero-index metamaterials can be used to improve the directivity of an antenna [67]. Metamaterials can be used as perfect absorbers[68], superlenses [69] and are capable of enhancing the performance of sensors in biomedical or agricultural applications [70].

However, the one application existing in the human fantasy is cloaking. It is the ability to manipulate the wave-front of an incident beam and bend it around an object as to totally conceal it. Cloaking techniques fit into two main categories : transformation-based metamaterial cloaking [71] and scattering cancellation-based cloaking [72],[73].

In our work, we deal with cylindrical objects. Several works have been done on the

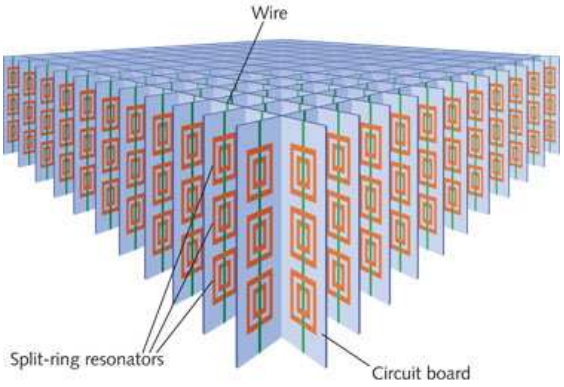

FIGURE 1.29 – sketch of a metamaterial synthesize using wires and double ring resonators[66]

topic of cloaking or scattering of cylindrical objects [74] [75] [76]. However, attention has been rarely given for the problem of enhancing the scattering or backscattering by cylinderical objects. One of the few works on the enhancement of the backscattering by a finite conducting cylinder is presented in [77], [92]. The paper proposes a technique based on gradient metasurfaces to manipulate the beam and redirect it back in the same direction of incidence. An illustration is given in Fig. 1.30. Another suggestion was the use of a coat of negative permittivity or permeability or both to tailor the scattering of the cylinder[93], [94].

Remarkably, to the knowledge of the authors, few works have dealt with applications relating to the scattering or backscattering by a dielectric cylinder. The main works are concentrated in the field of modeling of vegetation components for remote sensing applications. Actually, for certain range of frequencies, a tree can be approximated to an infinite lossy dielectric cylinder[91]. In this work, some numerical results of the backscattering width have been presented.

The interest in our work is in using single negative permittivity materials to assess their performance in enhancing the backscattering of dielectric cylinders. The concept of plasmonic cloaking has been already utilized in the aim to reduce of the scattering by a dielectric cylinder[97]. The concept is based on pairing double positive material with a single negative coat to cancel the scattering by an electrically small cylinder.

Our methodology is somehow similar, however, there are fundamental differences in the manner it is implemented as compared to the work in [97]. Our final objective is to enhance the backscattering by a multi-layered cylinder (not a single cylinder) as you'll see in the next section. Also, the electrical size in our case is in the moderate Mie region (cylinder radius comparable to wavelength) which is more complicated than the problem of an electrically small cylinder, where the fundamental mode is the main contributor in the overall scattering. Add to that the fact that dielectric properties of the human tissue layers possess high permittivity values and losses as compared to the simple dielectric examples given in [89].

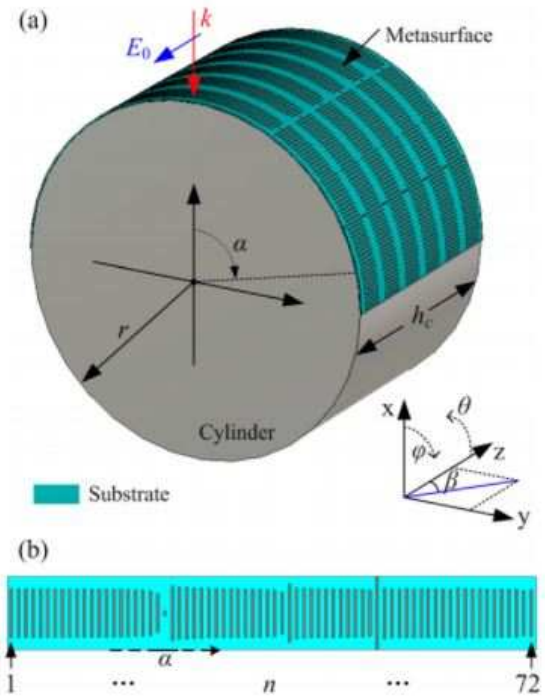

FIGURE 1.30 – (a) depicts the conducting cylinder coated with a dielectric substrate-metasurface repeated 6 times along the length of the cylinder and (b) provides a zoom in on the conformal metasurface consisting of 72 strips [77]

Specifically, in [89], the case of an electrically small coated cylinder (outer radius is small compared to the wavelength) was considered. The cylinder was normally illuminated by a plane wave whose electric field is parallel to the axis of the cylinder (TM configuration). In this small electrical regime, conditions of the overall scattering can be simply given in the form of closed loop equations as a function of the radius and the permittivity of the inner and outer cylinders. Using these equations, it is easy to obtain the coat size and permittivity that leads to the required scattering reduction. With the core permittivity being fixed to $\epsilon = 3$, it was predicted that the scattering reducing shell should have a value of $\epsilon_c^r \approx -8.5$. In our work, the objective lies in the opposite direction. It is desired to find the coat profile characteristics that can enhance the backscattering by the dielectric cylinder.

Chapter 2

Analytical Study on the retrodirective performance of a flattened dihedral using periodic arrays

2.1 Introduction

Regarded as the conventional, simple and effective solution, dihedral corner configuration have always captured attention due to naturally possessing high cross section. Despite being used extensively in civil applications, where usually there's a need to enhance the target RCS, few analysis had been performed on the backscattering -of such reflectors. This can be interpreted by the trivial retro-directive mechanism such reflectors possess. However, the unwanted inadvertent formation of dihedral corner by the military ships or vehicles pushed towards putting more efforts on understanding the physics behind its retrodirective mechanism.

In fact, it was interesting at that time to study the impact of non-orthogonality on the backscattering properties of the dihedral reflector for two main reasons. The first is to assess the impact of fabrication inaccuracies regarding the orthogonality of the dihedral on its performance. While the other was to investigate whether slight alteration in the corner shape would be sufficient to produce the wanted dramatic reduction in its RCS. It was found that non-orthogonality may introduce deep interference nulls depending on the electrical size of dihedral panels and the opening angle, in other words, the flattening degree. Those nulls along the axis of symmetry of the dihedral can lead to significant deterioration in its retrodirective mechanism.

In the context of the project here, the need arises to design a compact retrodirective flattened dihedral. However, once a dihedral corner is flattened, it loses its congenital retrodirective properties. As explained previously in the state of art, it has been shown that by tuning the array cells to follow a predefined phase law, a phasing mechanism can

be constructed on the dihedral panels to redirect the incoming wave back in the same direction of incidence. A reflector prototype at 9 GHz had been designed, fabricated and tested as a proof of concept. The results had shown flat RCS response for wide range of incidence angles compared to a flat plate. However, no explicit study had been performed on the potentials and limits of this configuration.

In this chapter, a detailed analytical study is presented to dissect the reflectarray phasing mechanism occurring between the panels. Based on this study, it will be possible to predict the potentials and limits on the retrodirective performance influenced by the geometrical parameters of the configuration and the incidence angle of the incoming wave. First, a detailed derivation of the phase law is offered as a function of the configuration parameters as well as the incidence angle. Based on this derivation, complementary formulations are defined to study the two critical elements influencing the retrodirective performance : the impact of flattening degree and the phase law dependence on incidence angle. From those studies, final conclusions are drawn in form of guidelines predicting the overall performance of the reflector.

2.2 Analytical derivation of the phase law

2.2.1 Theoretical background

Arranging radiating elements in a periodic pattern to steer beams is nothing new. The scattering and impedance properties of periodic structures have been extensively studied throughout the past century. Assuming currents of same amplitude as shown in Fig. 2.1, the current phase on each of the elements should enable a coherent combination of all radiated waves in the desired direction. This leads the current to be expressed in the form :

$$I_m = Ie^{-jk_0 dmcos(\theta)} \tag{2.1}$$

where k_0 is the wave number, d is the inter-element spacing, m corresponds to the number of the element and θ describes the direction of maximum radiation. This form is easy to accept because it well expresses the straightforward understanding of this electromagnetic propagation problem. Gaston Floquet addressed the mathematical parallel of the problem. In his work, he solves the problem of differential equations with periodic coefficients. By expressing the problem of periodic array in the appropriate form, Floquet theory can be exploited and the same form of equation 2.1 can be obtained for the fundamental mode. Higher order modes can be avoided, provided d is lower than $\lambda_0/2$.

Assuming the currents are produced by an incident wave, it can be hypothesized that by tuning the dimensions of equally distant conducting cells, the impinging beam can be steered into a predefined desired direction as illustrated in Fig. 2.2. The array elements will follow a predefined phase law to produce an incremental phase shift (γ) :

$$\gamma = k_0 d\cos(\theta) \tag{2.2}$$

As an extension to this definition, the phase law can be defined for the case where

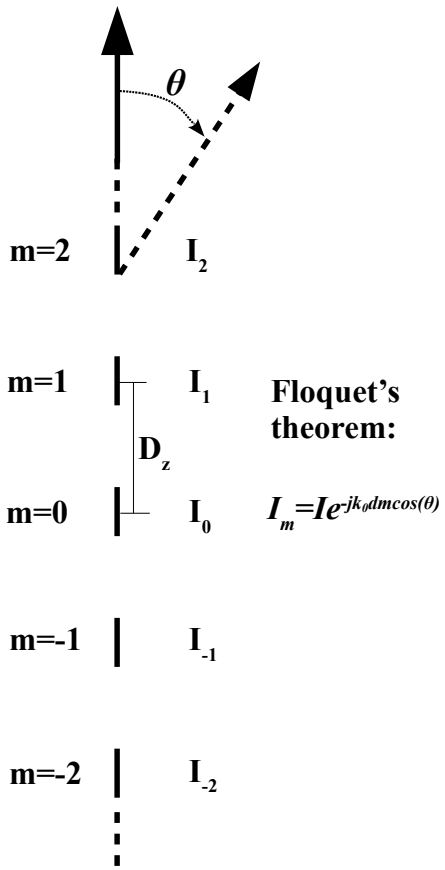

FIGURE 2.1 – The presentation of current phases on m-number of elements as expressed by Floquet's theorem

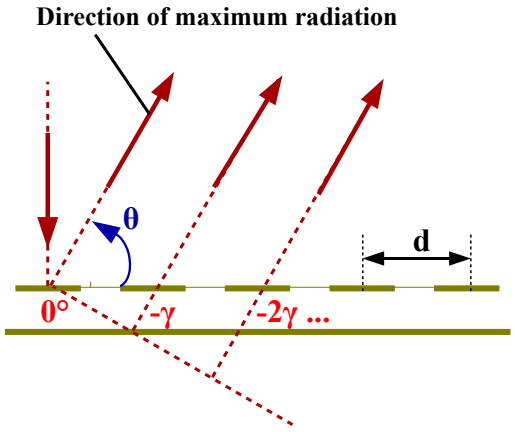

FIGURE 2.2 – Assignment of incremental phase shift (γ) for the periodic array of inter-element spacing d

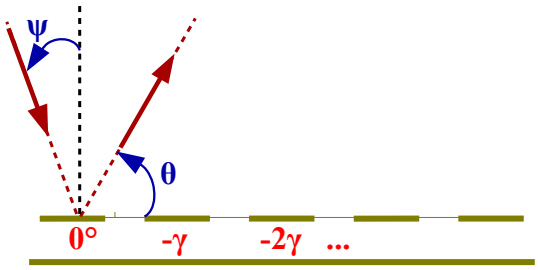

FIGURE 2.3 – Periodic array excited by a plane wave of angle of incidence in retard to the normal

the incidence is non-normal, meaning that the beam hits the array axis in retard (as illustrated in Fig. 2.3) or in advance (as illustrated in Fig. 2.4) to the normal. This can be represented by the angle ψ, which possesses a positive value in the retard case and negative value in the advance case. The consequent phase law can be expressed as following :

$$k_0 d\cos(\theta) = \gamma + k_0 d\sin(\psi) \tag{2.3}$$

$$\gamma = k_0 d\cos(\theta) - k_0 d\sin(\psi) \tag{2.4}$$

2.2.2 Derivation

In the work here, the structure of flattened dihedral is composed of the complex geometry of two attached metallic panels. Each panel is equipped with a periodic finite

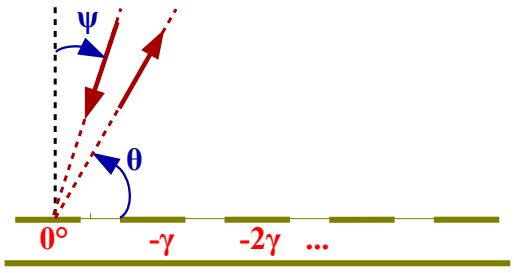

FIGURE 2.4 – Periodic array excited by a plane wave of angle of incidence in advance to the normal

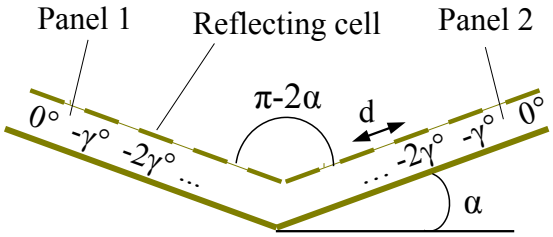

FIGURE 2.5 – The proposed structure of the flattened dihedral with the incremental phase shift (γ) on both panels

array of metallic cells. Theoretically, the problem can be best approximated as being two semi-infinite arrays positioned obliquely one to the other.

The solution of this problem is two reflectarray steering mechanisms on proximity of each other. Each mechanism is characterized by the incremental phase law depending on the angle of incidence (ψ) and the desired angle of reflection (θ).

The desire in this project is to obtain a retrodirective reflection using the combination of the two steering mechanisms on each of the dihedral panels as illustrated in Fig. 2.5. For this sake, a global phase law can be defined by relating the two phase laws using the appropriate parameters.

Fig. 2.6 illustrates the reflection process between the two panels of the flattened dihedral (flattened till a certain degree α). The beam intercepts the panel 1 with an angle β, which represents the deviation from the normal to the horizontal of the radiating aperture. It gets reflected to panel 2 with an angle θ and is expected to leave theoretically with an angle β' equal to β. Upon formulating the global phase law, three reflection configurations can be distinguished. The nominal case as illustrated in Fig. 2.7 is defined when the beam is normally incident to the horizontal radiating aperture of the reflector ($\beta = 0°$). For the second configuration, the beam intercepts panel 1 first with any incidence angle ($\beta \neq 0°$) and leaves the reflector from panel 2. An illustration is given in Fig. 2.6. The third configuration refers to the reverse case of the second one. An illustration is given in Fig. 2.8.

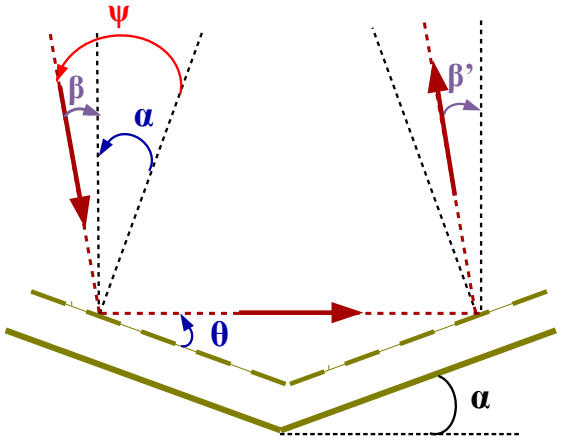

FIGURE 2.6 – The reflection mechanism of any beam of incidence angle β from panel 1 to panel 2 in the forward case

Let's consider the nominal case. Here, the condition to have retrodirective reflection is simply :

$$\theta = \alpha \tag{2.5}$$

Hence, to obtain the global phase law in this case it would be sufficient to apply the retard phase law on panel 1. The incidence angle here is $\psi = \alpha$ and with substituting equation 2.5 in 2.4, the global phase law becomes :

$$\gamma_0 = k_0 d(\cos(\alpha) - \sin(\alpha)) \tag{2.6}$$

This is consistent with the previous work in [63], where the phase law had been derived only dependent on the flattening degree.

Here, taking into consideration the incidence angle, the general case is illustrated in Fig. 2.6. The phase law, materialized in the form of phase shift, is derived in function of the incidence angle of the incoming wave β, the flattening degree α, inter-element spacing d, and the wave number k_0. γ^{β}, the phase gradient between two consecutive cells, can be formulated using simple trigonometric formulations that describe the reflection from one panel to the other.

The beam intercepts panel 1 with an angle β with respect to the vertical and leaves with angle θ with respect to the panel. The combination of the imposed phase shift, γ_β, in addition to the delay resulting from the oblique incidence angle $\alpha - \beta$ can be represented by the following equation :

$$\gamma_\beta = k_0 d\cos(\theta) - k_0 d\sin(\alpha - \beta) \tag{2.7}$$

Then, the beam intercepts panel 2 and leaves by angle $\beta^{'}$:

$$-\gamma_\beta + k_0 d\cos(2\alpha - \theta) = k_0 d\cos(\pi/2 - \alpha - \beta^{'}) \tag{2.8}$$

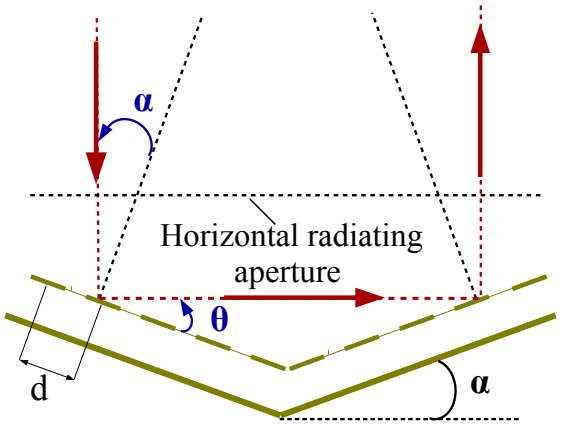

FIGURE 2.7 – The reflection mechanism from panel 1 to panel 2 in the nominal case ($\beta = 0$)

The condition so that the beam is redirected back in the direction of incidence is :

$$\beta^{'} = \beta \tag{2.9}$$

Hence, the equation becomes :

$$\gamma_\beta = k_0 d\cos(2\alpha - \theta) - k_0 d\sin(\alpha + \beta) \tag{2.10}$$

By substituting equation 2.10 in 2.9, a system of two equations and two unknowns is obtained, which can be solved using simple trigonometric relations as following :

$$k_0 d\cos(\theta) - k_0 d\sin(\alpha - \beta) = k_0 d\cos(2\alpha - \theta) - k_0 d\sin(\alpha + \beta) \tag{2.11}$$

$$k_0 d\cos[(\theta - \alpha) + \alpha] - k_0 d\cos[(\theta - \alpha) - \alpha] = k_0 d\sin(\alpha - \beta) - k_0 d\sin(\alpha + \beta) \tag{2.12}$$

Using the trigonometric relations :

$$\cos(a - b) - \cos(a + b) = 2\sin(a)\sin(b) \tag{2.13}$$

and

$$\sin(a + b) - \sin(a - b) = 2\cos(a)\sin(b) \tag{2.14}$$

the equation becomes :

$$\sin(\theta - \alpha)\sin(\alpha) = \cos(\alpha)\sin(\beta) \tag{2.15}$$

This leads to :

$$\theta = \alpha + \arcsin[\frac{\sin(\beta)}{\tan(\alpha)}] \tag{2.16}$$

Finally, by substituting equation 2.16 in 2.7 the phase law is materialized in a phase shift of the following form :

$$\gamma_\beta = k_0 d(\cos(\alpha + \arcsin[\frac{\sin(\beta)}{\tan(\alpha)}]) - \sin(\alpha - \beta)) \tag{2.17}$$

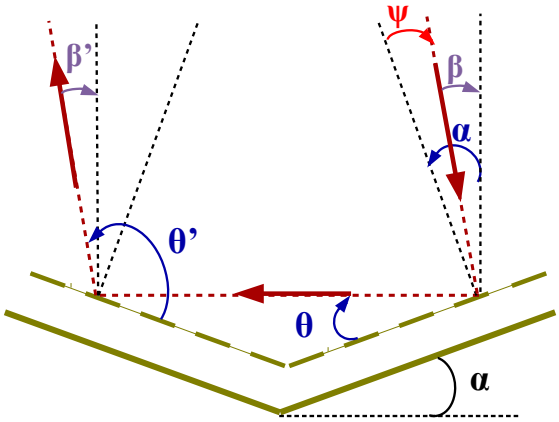

FIGURE 2.8 – The reflection mechanism from panel 2 to panel 1 in the reverse case

The formulation of the nominal case can be obtained by enforcing $\beta = 0$ in the above equation.

The reverse case is illustrated in Fig. 2.8.

Similar steps to those of the forward case are followed to obtain the global phase law in the reverse case.

The beam here intercepts panel 2 with an angle β with respect to the vertical and leaves with angle θ. Phases combination on the panel can be obtained using 2.4 as follows :

$$\gamma_\beta = k_0 d\cos(\theta) - k_0 d\sin(\alpha + \beta) \tag{2.18}$$

On panel 1, again using the same equation in2.4 :

$$-\gamma_\beta + k_0 d\cos(2\alpha + \theta) = k_0 d\cos(-\pi/2 + (\alpha - \beta^{'})) \tag{2.19}$$

Condition of retrodirective reflection is :

$$\beta^{'} = \beta \tag{2.20}$$

The equation becomes :

$$\gamma_\beta = k_0 d\cos(2\alpha + \theta) - k_0 d\sin(\alpha - \beta) \tag{2.21}$$

Substituting 2.21 in 2.18 and using the trigonometric relations of equations 2.13 and 2.14, the global phase law for the reverse case is :

$$\gamma_\beta = k_0 d(\cos(\alpha - \arcsin[\frac{\sin(\beta)}{\tan(\alpha)}]) - \sin(\alpha + \beta)) \tag{2.22}$$

It can be shown that this is an even equation β-wise, in other words : $\gamma_\beta = \gamma_{-\beta}$. This means that a unique formulation of the global phase law is sufficient for both configurations. Now, the phase law has been formulated as a function of the incidence angle β and the geometrical parameters of the configuration. Through this chapter, separate studies on those factors are conducted to analyze their influence on the performance of the reflector.

2.3 Ideal and attainable reflections

Before going deeper in this study, there is a necessity to distinguish between what are going to be called the attainable and ideal reflections.

2.3.1 Ideal reflection

The reflection is assumed ideal when the cells can be reconfigured to match the phase shift (equation 2.17) required for any incidence angle. This means that the reflector should be able to sense the direction from which the beam is coming and reconfigure its cells to adjust to the phase law for this specific angle. This is of course not feasible in this case. However, this ideal situation is of notable importance because it can help in the analysis of some aspects of the study while totally neglecting the effects of phase law inaccuracies.

2.3.2 Attainable reflection

The attainable case is the one where cells are tuned to realize the progressive phase shift corresponding to a specific and unique incidence angle. In other words, the cells are assigned predefined dimensions regardless of the incoming beam incidence angle. This actually emulates the real case scenario where the objective is to design a simple reflector using simple patches. An analytical study dedicated for this case should theoretically provide all the required materials to know how the fabricated prototype might perform.

2.4 Study on the flattening degree

2.4.1 Introduction

In this section, the effect of the flattening degree, the most critical geometrical factor, on the retrodirective performance of the flattened dihedral is studied. To do so, a new parameter β_l is defined as a function of the flattening degree α for both the ideal and attainable cases. The angle β_l describes the limiting range in which the reflected beam from the first panel is intercepted by the second panel. The value of $\beta_l(0)$ corresponds to the lower limit where $\theta = 0°$ and $\beta_l(2\alpha)$ corresponds to the upper limit where $\theta = 2\alpha$. An illustration is provided in Fig. 2.9. As seen in the figure, all waves of incidence angles less than $\beta_l(0)$ will be reflected by the reflector in the invisible range. On the other hand, all beams of incidence angle more than $\beta_l(2\alpha)$ will not intercept the other panel at all and all the energy will be lost. At the end of this section, it should be possible to define the theoretical visible range of the reflector upon which it operates.

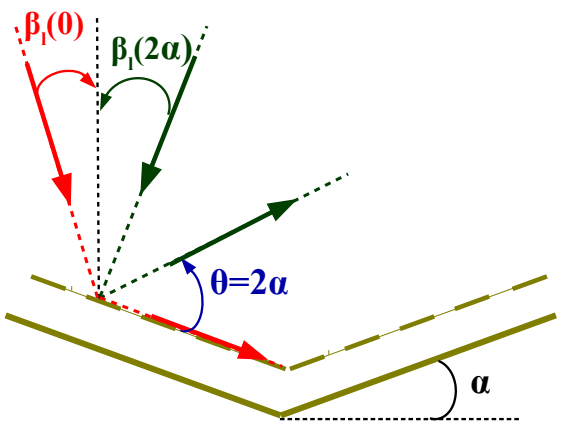

FIGURE 2.9 – Illustration of the limiting range using β_l and θ angles

2.4.2 Analytical derivation

In the process of formulating the global phase law, the angle θ for the ideal case has been deduced in (2.16) as following :

$$\theta = \alpha + \arcsin[\frac{\sin(\beta)}{\tan(\alpha)}] \tag{2.23}$$

The angle β can be written in function of angle θ as following :

$$\beta(\theta) = -\arcsin[\sin(\theta - \alpha)\tan(\alpha)] \tag{2.24}$$

By substituting angles 2α and $0°$ it is clear that $\beta_l(2\alpha)$ = -$\beta_l(0)$ with the latter being obtained by forcing θ to $0°$ as following :

$$\beta_l(0) = -\arcsin[\sin(\alpha)\tan(\alpha)] \tag{2.25}$$

For the attainable case, θ can be obtained from equation (2.7) by locking the phase shift to a nominal incidence angle β_0. θ can be hence written in this form :

$$\theta = \arccos[\frac{\gamma_{\beta_0}}{k_0 d} + \sin(\alpha - \beta)] \tag{2.26}$$

Here, $\beta_l(0)$ and $\beta_l(2\alpha)$ have different values and can be obtained from θ as following :

$$\beta_l(0) = \alpha - \arcsin(1 - \frac{\gamma_{\beta_0}}{k_0 d}) \tag{2.27}$$

$$\beta_l(2\alpha) = \alpha - \arcsin[\cos(2\alpha) - \frac{\gamma_{\beta_0}}{k_0 d}] \tag{2.28}$$

As explained earlier, in the ideal case, the phase shift is automatically reconstructed by the reconfigurable cells so that redirect the beam of any incidence angle in a retrodirective manner. On the other hand, for the attainable case, it is necessary to specify the

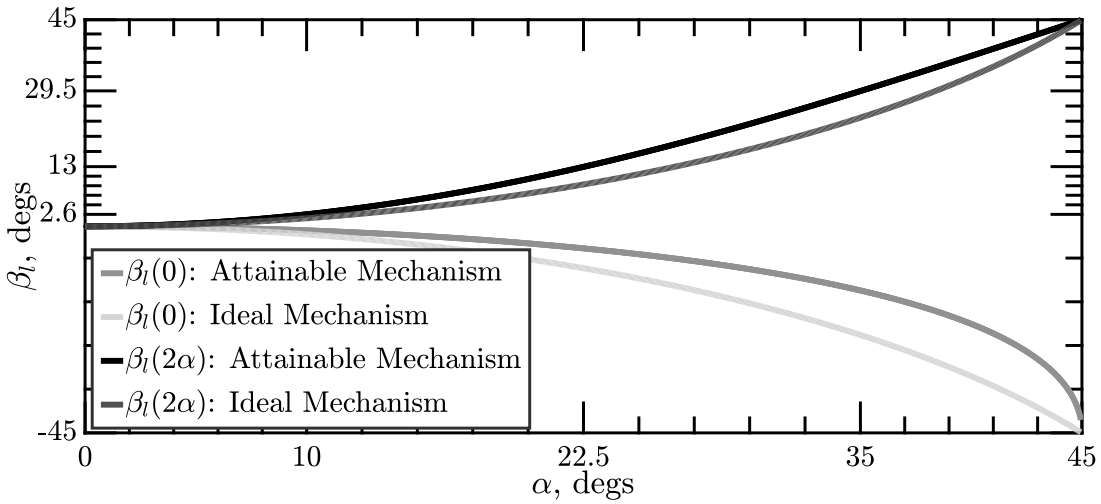

FIGURE 2.10 – -β_l versus α for the ideal and attainable cases

progressive phase shift which the dihedral cells are going to implement. Here, the phase shift is obtained for the nominal case ($\beta = 0°$) and the inter-element spacing over wavelength ratio d/λ is fixed to 1/3. Using equation 2.6, the phase shift becomes :$\gamma_{\beta_0} \approx 65°$. In Fig. 2.10, $\beta_l(0)$ and $\beta_l(2\alpha)$ are plotted in function of α for the ideal and the attainable cases. As expected, $\beta_l(0) = -\beta_l(90) = -45°$ is obtained for $\alpha = 45°$ (classical dihedral). Both $\beta_l(0)$ and $\beta_l(2\alpha)$ decrease whenever the dihedral is flattened, in other words, as α decreases. It is interesting to find out that even for the ideal case the limiting range decreases quite rapidly with α. The curves also show that the absolute value of $\beta_l(0)$ for the ideal case is greater than that of the attainable case. The difference goes up to as much as 20° degrees for certain flattening degrees. However, the upper limit $\beta_l(2\alpha)$, is greater for the attainable case. Also, $\beta_l(2\alpha)$ of the attainable case is always greater than the absolute value of the lower limit $\beta_l(0)$ of the ideal case.

For the reverse configuration, following similar derivation, the reverse β_l formulations have been obtained. They can be written as a function of those of the forward configuration as following : $\beta_l^r(0) = -\beta_l(2\alpha)$ and $\beta_l^r(2\alpha) = -\beta_l(0)$ for both the attainable and ideal cases.

2.4.3 Discussion on the visible range

2.4.3.1 Definition of the visible range per configuration and the total visible range

Before getting into this discussion, the visible range should be well defined. Two notions can be distinguished here :the visible range per configuration (VRC) and the total visible range (TVR). The visible range per configuration can be simply defined as :

$$| \beta_l(0) - \beta_l(2\alpha) | \text{ for the forward case}$$

TABLE 2.1 – List of attainable and ideal dihedrals of certain flattening degree and their corresponding visible range limits for the forward configuration

$\alpha(°)$	Attainable$\beta_l(0)$ (°)	Attainable $\beta_l(2\alpha)$ (°)	Ideal $\beta_l(0)(°)$	Ideal $\beta_l(2\alpha)$ (°)
10	-0.9	2.6	-1.8	1.8
22.5	-5	13	-9	9
35	-14	29	-24	24

TABLE 2.2 – List of attainable dihedrals of certain flattening degree and their corresponding visible range limits for the forward and reverse configurations

$\alpha(°)$	$\beta_l(0)$ (°)	$\beta_l^r(2\alpha)$ (°)	$\beta_l(2\alpha)(°)$	$\beta_l^r(0)$ (°)
10	-0.9	0.9	2.6	-2.6
22.5	-5	5	13	-13
35	-14	14	29	-29

and $\mid \beta_l^r(0) - \beta_l^r(2\alpha) \mid$ for the reverse case.

Furthermore, the total visible range can be defined as the difference between the maximum absolute value of the set $(\beta_l(0), \beta_l(2\alpha))$ and the maximum absolute value of the pair $(\beta_l^r(0), \beta_l^r(2\alpha))$. It can be written in this form :

$$\max(\mid \beta_l(0) \mid ; \mid \beta_l(2\alpha) \mid) + \max(\mid \beta_l^r(0) \mid ; \mid \beta_l^r(2\alpha) \mid)$$

This describes that the dihedral is still operating in at least one of the reverse or forward configurations. In other words, the beam incidence angle falls in at least one visible range per configuration.

2.4.3.2 Comparison on the visible range per configuration (VRC)

A comparison of β_l is performed in this part to show the difference in performance between the ideal and attainable cases as a function of the flattening degree, in other words, to compare the ideal and attainable VRCs. Three different cases of flattening degrees are put under study : $\alpha = 10°$, $22.5°$ and $35°$.

For better comparison, only the forward configuration is considered. Tab. 5.1 gives a summary showing the β_l values obtained for those three specified cases. Using the formulations given in the previous part it is possible to calculate the resulting VRCs. For $\alpha = 10°$, the VRC obtained is $3.5°$ and $3.6°$ for the attainable and ideal cases respectively. For $\alpha = 22.5°$, the values are quite similar at $18°$. The values show some divergence for $\alpha = 35°$. The range rises to $48°$ for the ideal case while the attainable one manages $43°$. Hence, it is clear that as the dihedral gets less flattened the ideal visible range per configuration becomes more significantly wider for the ideal case over the attainable one.

It is concluded that per one configuration, the ideal case shows better performance in terms of visibility range. The difference in performance gets more negligible as the dihedral gets flattened.

2.4.3.3 Total visible range (TVR) for the forward and reverse configurations

In the part, the forward and reverse configurations are both considered. Now, it is noticed from Tab. 5.1 that for the ideal case $\beta_l(0) = -\beta_l(2\alpha)$, in other words, the visible ranges per forward and reverse configurations are identical. This mean that the ideal TVR is equal to VRC for any flattening degree.

However, this is not the case for the attainable case. Tab. 3.2 summarizes the β_l values for the attainable case in both the forward and reverse configurations. The TVR for $\alpha = 10°$ records $5.2°$ which is higher than that of the ideal case ($3.6°$). The same runs for the other flattening degrees. For $\alpha = 22.5°$, attainable TVR obtained is $26°$ as compared to $18°$ of the ideal case. Also, for $\alpha = 35°$, the attainable TVR scores $58°$ compared to $48°$ of the ideal reflection.

Thus, it can be concluded, that whatsoever the flattening degree is, the TVR of the attainable case is always wider than that of the ideal case.

2.4.3.4 Conclusion : modes of operation

These observations hide some interesting results. The visible range of incidence angles upon which the dihedral operates in principle is wider for that of the attainable mechanism in comparison with the ideal one. In other words, regardless of the fact that the ideal mechanism would perfectly steer the beam inside its visible range, the attainable mechanism would engage incident beams more than that the ideal one can do, despite the fact that it might not offer that perfect steering over the whole range of incidence angles. Actually, it is those additional errors in the attainable phasing mechanism produced by the inaccuracies in phase law that served in widening the range of visible incidence angles. This can be seen as similar to the case where the additional losses in a dispersive medium enhance its frequency band of operation.

A classical dihedral ($\alpha = 45°$) theoretically possesses a TVR equal to $90°$. In comparison, a dihedral flattened to the half of the flattening degree ($\alpha = 22.5°$) still possesses a TVR equal to $26°$. Also, a dihedral of $\alpha = 35°$ operates over a TVR of $58°$. Those are nearly 29% and 65% of the optimum visibility range of the classical dihedral. Taking into consideration the massive deterioration in the retrodirective performance of the classical dihedral even with the slightest degrees of flattening, we consider such restored TVR values very acceptable.

Finally, in the ideal case, there is only unique mode of operation which is when both configurations operate simultaneously.

However, in the attainable case, three modes of operation can be distinguished. Those modes cover the total range of visibility of the dihedral reflector.

1. The simultaneous visible range is when both configurations operate simultaneously. Mathematically, it can be expressed as following :
$\min(\mid \beta_l(0) \mid ; \mid \beta_l(2\alpha) \mid) + \min(\mid \beta_l^r(0) \mid ; \mid \beta_l^r(2\alpha) \mid)$.
2. The visible range per forward configuration describes when the reflector only operates in the forward configuration and can be represented by the following expression : $\beta_l(2\alpha) - \beta_l^r(2\alpha)$.

3. The visible range per reverse configuration describes when the reflector only operates in the forward configuration and can be represented by the following expression : $\beta_l(0) - \beta_l^r(0)$.

2.5 Study on the phase law dependence on incidence angle

2.5.1 Introduction

In the previous section, the modes of operation by the reflector for the attainable case have been defined . In this section, the impact of phase law inaccuracies over the visible range of incidence angles is assessed. As illustrated in Fig. 2.2, the metric $\beta^{'}$ is defined as the angle which describes the direction of maximum radiation of the reflected beam with respect to the normal of horizontal aperture.

In the ideal case, $\beta^{'}$ is simply equal to β, while for the attainable case, $\beta^{'}$ can be deduced from equation 2.8 upon fixing a predefined nominal phase shift.

2.5.2 Derivation

Following the angle definitions in Figs. 2.6 and 2.8, angle $\beta^{'}$ can be written for the forward and reverse reflections respectively as :

$$\beta^{'} = -90^{\circ} - \alpha - \arccos[\frac{\gamma_{\beta_0}}{k_0 d} + \cos(\alpha - \arccos(\frac{\gamma_{\beta_0}}{k_0 d} + \sin(\alpha - \beta)))] \quad (2.29)$$

and

$$\beta^{'} = -90^{\circ} + \alpha + \arccos[-\frac{\gamma_{\beta_0}}{k_0 d} + \cos(\alpha - \arccos(\frac{\gamma_{\beta_0}}{k_0 d} + \sin(\alpha + \beta)))]. \quad (2.30)$$

2.5.3 Discussion

In this study, the inter-element spacing is fixed to $d/\lambda = 1/3$. The global phase law is constructed for the nominal case ($\beta = 0^{\circ}$)The same three cases as in the previous section are considered here.

In Fig. 2.11, the ideal $\beta^{'}$ corresponding to the case of the classical dihedral and the attainable $\beta^{'}$ assuming that $\alpha = 10^{\circ}$ are plotted. As expected, the reflector theoretically behaves perfectly for incidence angle $\beta = 0^{\circ}$. The attainable $\beta^{'}$ still manages a deviation less than 1° for the range of incidence angles where both configurations operate simultaneously $-0.9^{\circ} < \beta < 0.9^{\circ}$. For the range of angles where only one configuration is operating, the error does not exceed 2°. Fig. 2.12 gives the same results for $\alpha = 22.5^{\circ}$. In the simultaneous visible range $-5^{\circ} < \beta < 5^{\circ}$, the error stays in the range of 5°. The error only increases significantly at the edges of the visible range in the unique configuration operation modes. Referring to Fig. 2.13, similar conclusions can be drawn from the results obtained for $\alpha = 35^{\circ}$.

Based on those results, it can be said that the phase law inaccuracies do not result in significant impact of the retrodirective performance of the dihedral. The deterioration

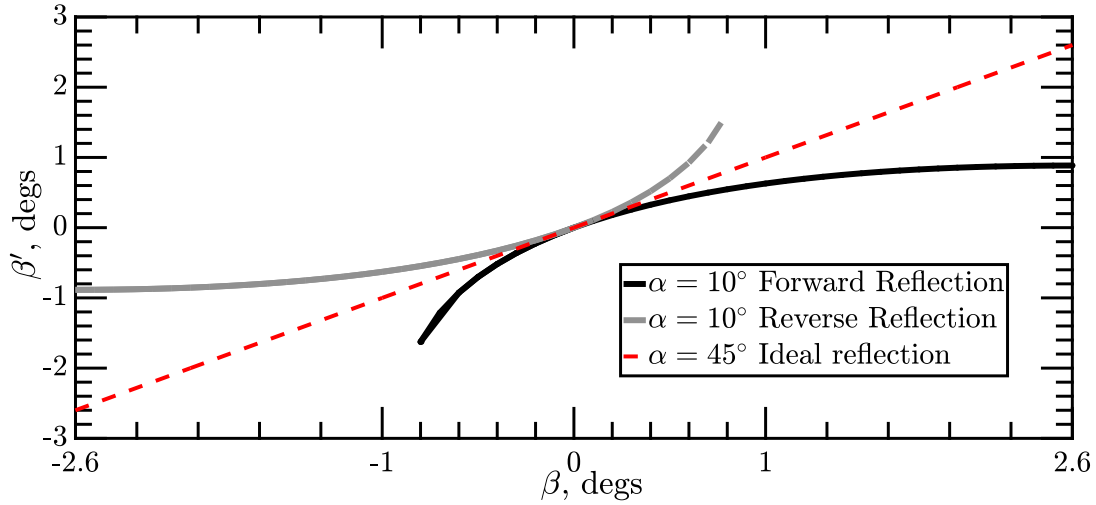

FIGURE 2.11 – β' versus β of dihedral $\alpha = 10°$ for the forward and reverse configurations

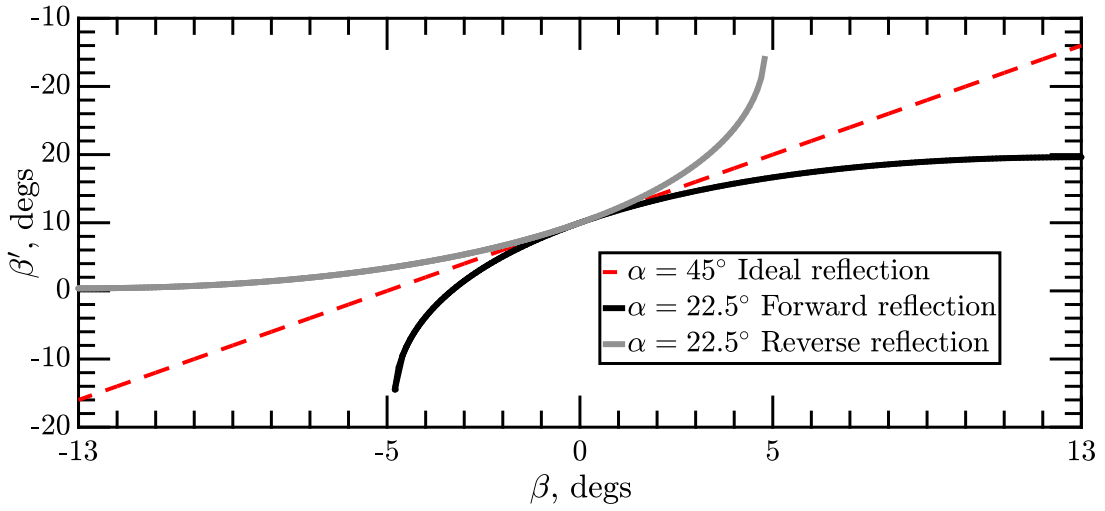

FIGURE 2.12 – β' versus β of dihedral $\alpha = 22.5°$ for the forward and reverse configurations

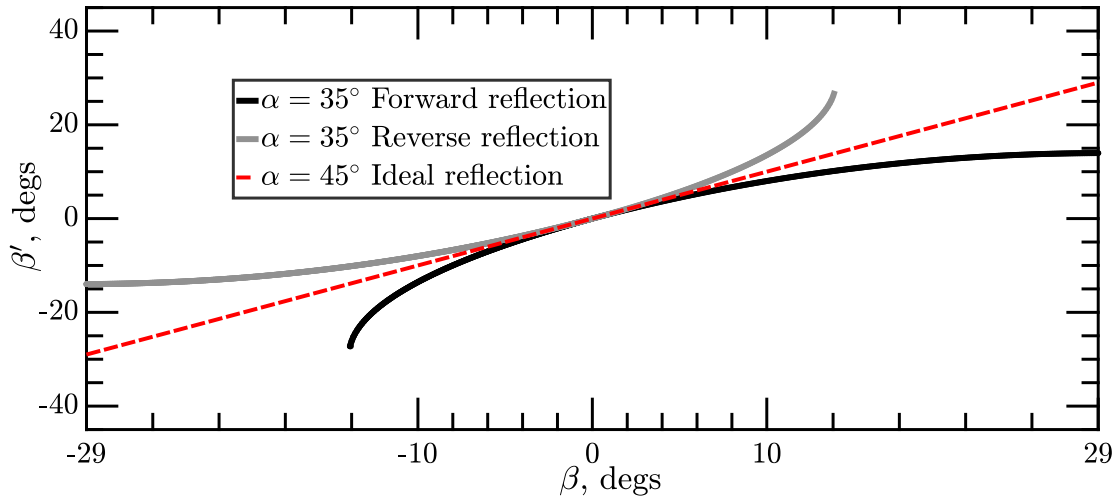

FIGURE 2.13 – β' versus β of dihedral $\alpha = 35°$ for the forward and reverse configurations

in the phasing mechanism can only be noticed when the visible range is large enough, specifically for high values of α.

2.6 Illustrations using Matlab

As an illustration to the findings of the previous sections, a scenario is established to follow the path of a plane wave that intercepts the reflector at a certain incidence angle β and leaves it with an angle β' as shown in Fig. 2.14. A Matlab code is used to simulate the reflection of an incident beam by an array of specific number of elements and inter-element spacing. The array elements in this case are assigned a predefined incremental phase shift. Two stages are needed here to simulate the incidence on and reflection from the one panel to the other. It is worth noting that it is sufficient to simulate the forward configuration ; simulating the reverse configuration will lead to similar results anyway.

The aim here is to show the beam path direction resulting in the attainable case for several angles of incidence, hence, a large number of elements is considered so that to have a very directive main lobe. The dihedral is made flattened till degree $\alpha = 22.5°$ and the inter-element spacing is chosen at $d = \lambda/3$ so that to avoid grating lobes. In the first scenario, the nominal case is simulated with the phase law specifically defined for incidence angle $\beta = 0°$. With the array being assigned the same phase law, different angles of incidence $\beta = 5°$ and $13°$ are simulated.

The first beam hits the array with angle $\psi_1 = \alpha = 22.5°$ equivalent to $\beta = 0°$. According to equation 2.6, the required phase shift to enforce the retrodirective phase law is $\gamma_0 \approx 65°$. Fig. 2.15 shows the directivity pattern of the reflected wave corresponding to the incident beam on panel 1. It is observed that the beam leaves panel 1 with an angle $\theta 1 = 22.5°$, which is in agreement with the theoretical formulation. This beam then

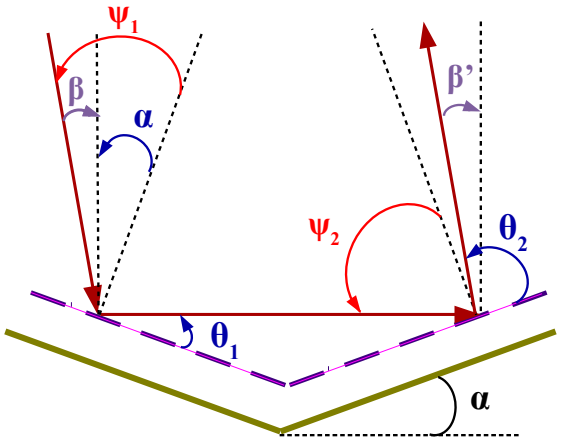

FIGURE 2.14 – Sketch showing the used angle notations in the Matlab simulations

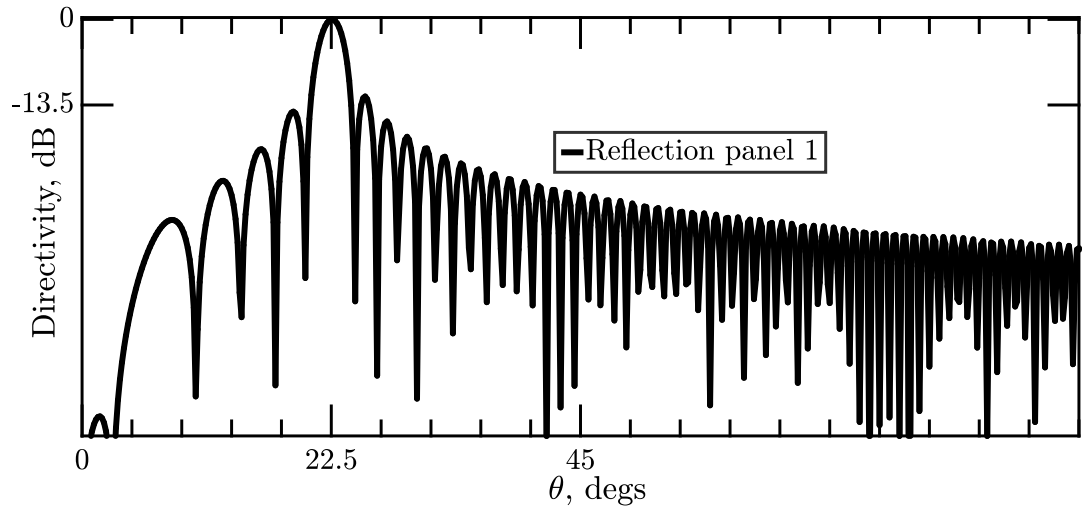

FIGURE 2.15 – Directivity pattern of the reflected beam from panel 1 for beam of incidence angle $\beta = 0°$ in the nominal case

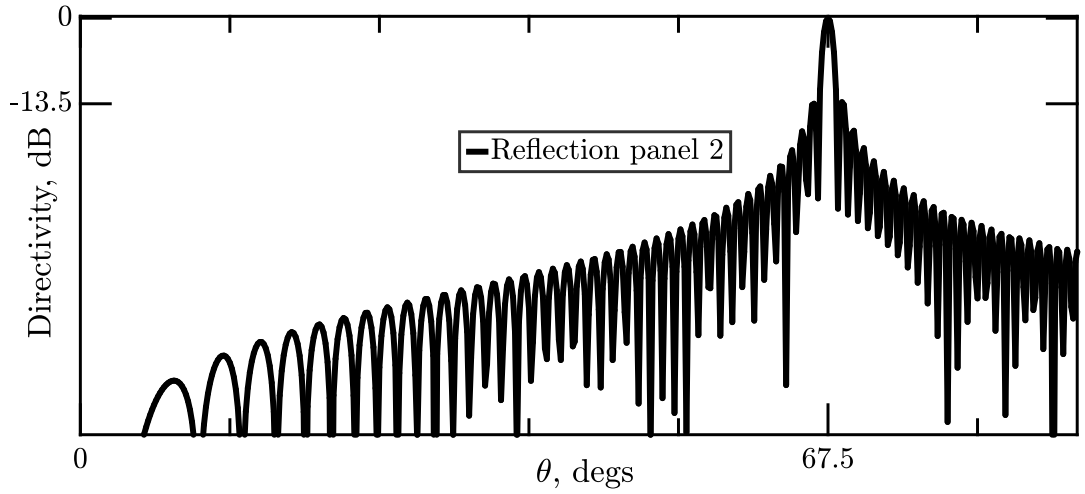

FIGURE 2.16 – Directivity pattern of the reflected beam from panel 2 for beam of incidence angle $\beta = 0°$ in the nominal case

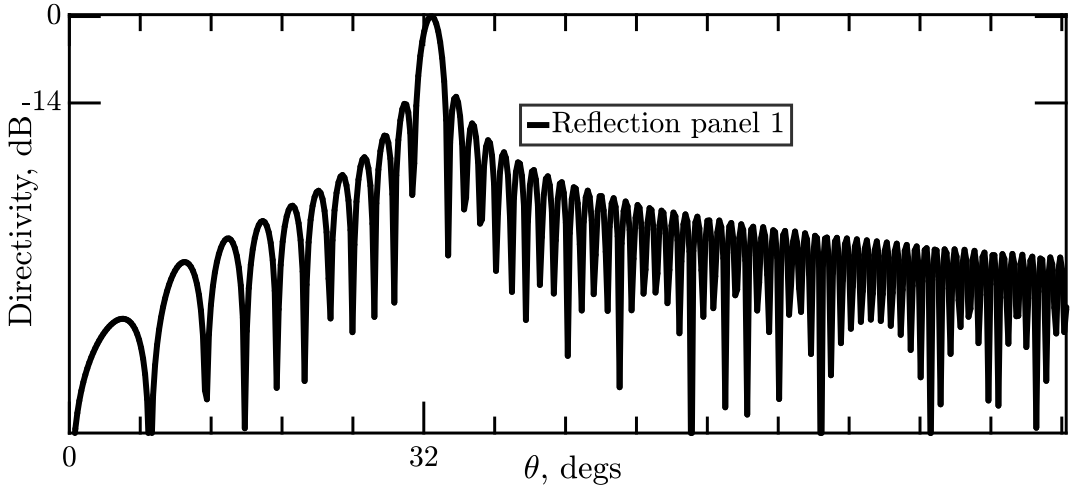

FIGURE 2.17 – Directivity pattern of the reflected beam from panel 1 for beam of incidence angle $\beta = 5°$ in the nominal case

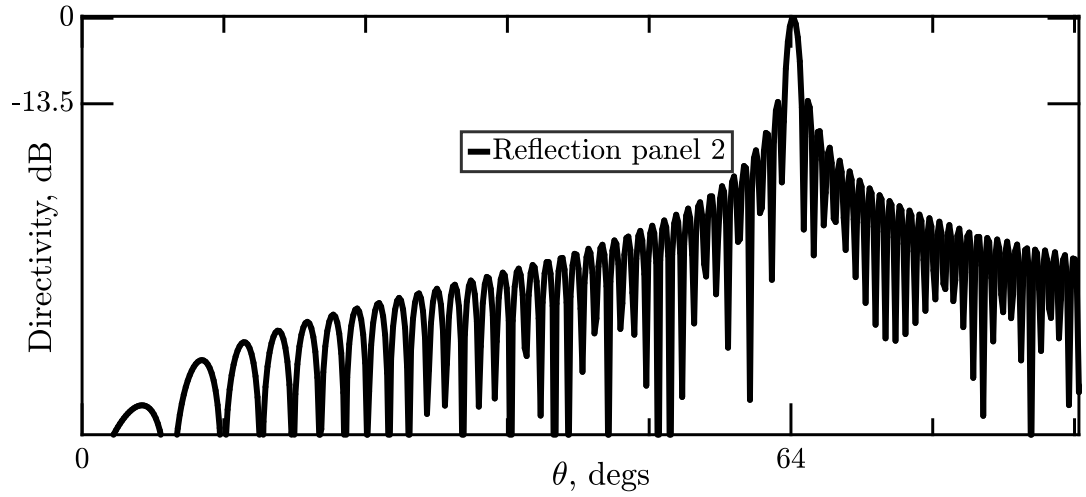

FIGURE 2.18 – Directivity pattern of the reflected beam from panel 2 for beam of incidence angle $\beta = 5°$ in the nominal case

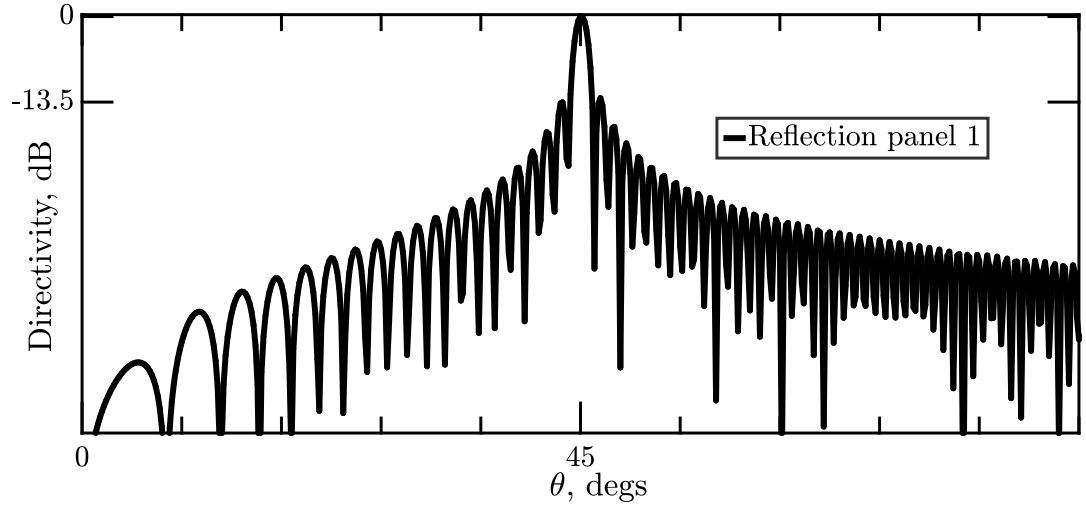

FIGURE 2.19 – Directivity pattern of the reflected beam from panel 1 for beam of incidence angle $\beta = 13°$ in the nominal case

hits the next panel with an angle of incidence $\psi_2 = \pi/2 - (2\alpha - \theta) = 67.5°$. Fig. 2.16 shows the directivity pattern of the reflected wave from panel 2. It is observed that the beam leaves panel 2 and the reflector with an angle $\theta = 67.5°$, in other words with angle $\beta' = \beta = 0°$. This demonstrates that the beam is ideally reflected from one panel to the other and back in the same direction of incidence.

The second simulation is performed in the first scenario to observe what happens when a beam of another incidence angle $\beta_2 = 5°$ hits the same flattened dihedral whose cells follow the global phase law predefined for the nominal incidence angle $\beta = 0°$. From Fig. 2.17 that shows the directivity pattern of the reflected wave, the beam leaves panel 1 with angle $\theta_1 \approx 32°$. This wave hits panel with incidence angle $\psi_2 \approx 77°$. From the directivity pattern in Fig. 2.18, it is seen that the beam leaves the panel with angle $\theta_2 \approx 64°$ and the reflector with angle $\beta' \approx 3°$. Obviously, the beam is not ideally retrodirected by the reflector, however the margin of error is only 2°. This confirms the theoretical predictions done in the previous section which suggests that the phase law inaccuracies do not affect the retrodirective in a severe manner.

The third simulation in the first scenario is when a beam of $\beta = 13°$ hits the reflector. Fig. 2.19 shows the directivity pattern of the reflected wave corresponding to the incident beam on panel 1. The beam actually leaves the panel with an angle $\theta_1 = 45°$ which is equivalent to 2α. Hence, this beam lies on the edge of the invisible range and won't intercept the second panel. This is with absolute agreement with the theoretical work.

In the second scenario, the array elements follow the phase law defined for incidence angle $\beta = 5°$. The incremental phase shift required in this case is $\gamma_0 \approx 63°$. Similarly, the paths of the beams corresponding to incidence angles $\beta = 0°$ and 5° are simulated in this scenario. For $\beta = 5°$, Fig. 2.20 shows that the beam leaves panel 1 with angle $\theta_1 = 35°$. The beam intercepts panel 2 with angle $\psi_2 \approx 80°$. It can be observed from Fig. 2.21 that the reflected beam is perfectly retrodirected with angle $\theta_2 = 62.5°$, in other words, $\beta' = \beta = 5°$.

For the same scenario, the beam of incidence angle $\beta = 0°$ leaves the first panel with angle $\theta_1 = 25°$ as illustrated in Fig. 2.22. The beam hits panel 2 with angle $\psi_2 \approx 70°$ and leaves it with angle $\theta_2 = 65°$. This is equivalent to say that $\beta' \approx 2.5°$. An illustration is given in Fig. 2.23. Again, the error margin is very small.

In the third scenario, the array elements follow the phase law defined for incidence angle $\beta = 15°$. Here, the path of the beam corresponding to incidence angle $\beta = 15°$ is simulated. Fig. 2.24 shows that the beam leaves panel 1 with angle $\theta_1 = 61°$ which is way larger than 2α. Hence, the beam would never intercept the second panel. And the dihedral won't establish a retrodirective mechanism. This illustrates the idea that even tuning the dimensions of the cells to operate at a certain incidence angle won't be sufficient to make the dihedral properly perform. The targeted angle of incidence should be necessarily chosen inside the visible range of the ideal case depending on the desired flattening degree α.

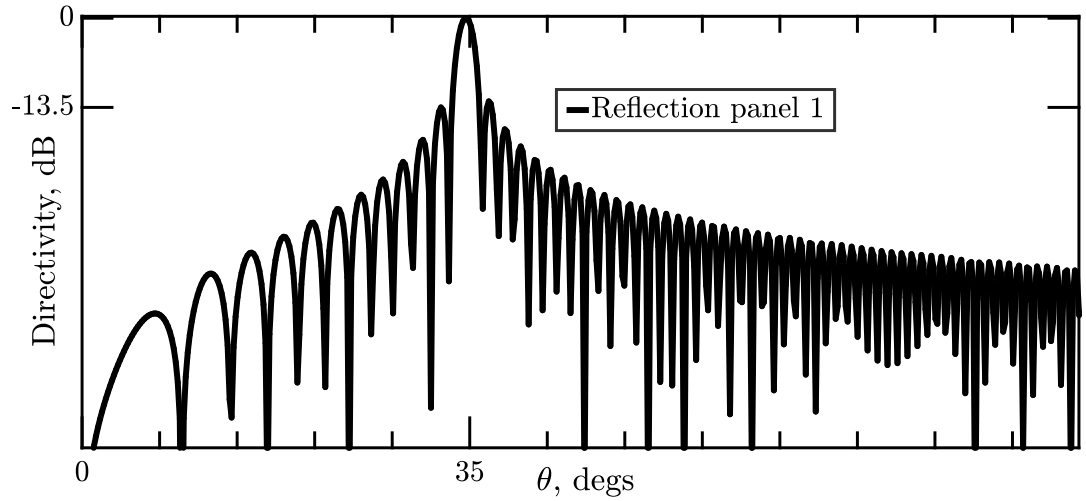

FIGURE 2.20 – Directivity pattern of the reflected beam from panel 1 for beam of incidence angle $\beta = 5°$ on an array following phase law at $\beta = 5°$

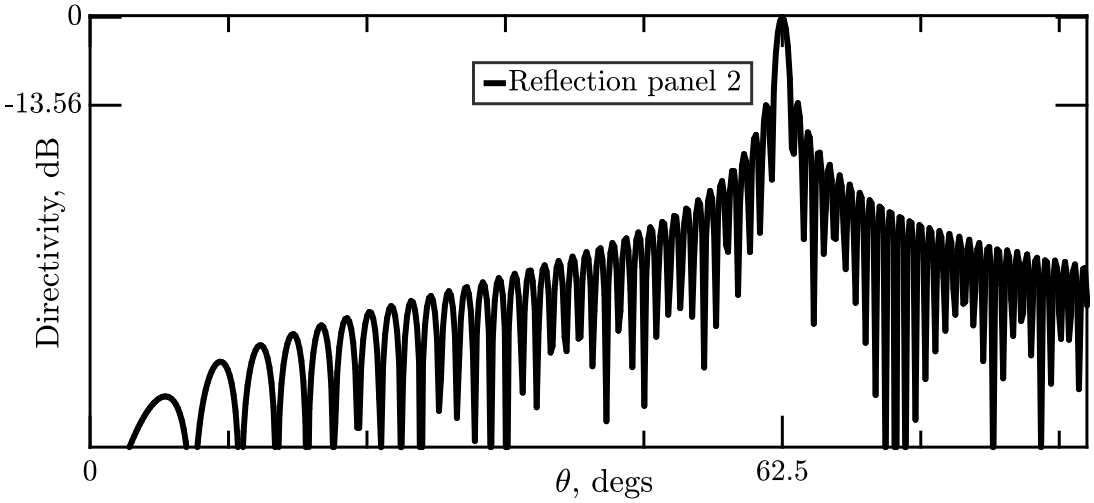

FIGURE 2.21 – Directivity pattern of the reflected beam from panel 2 for beam of incidence angle $\beta = 0°$ on an array following phase law at $\beta = 5°$

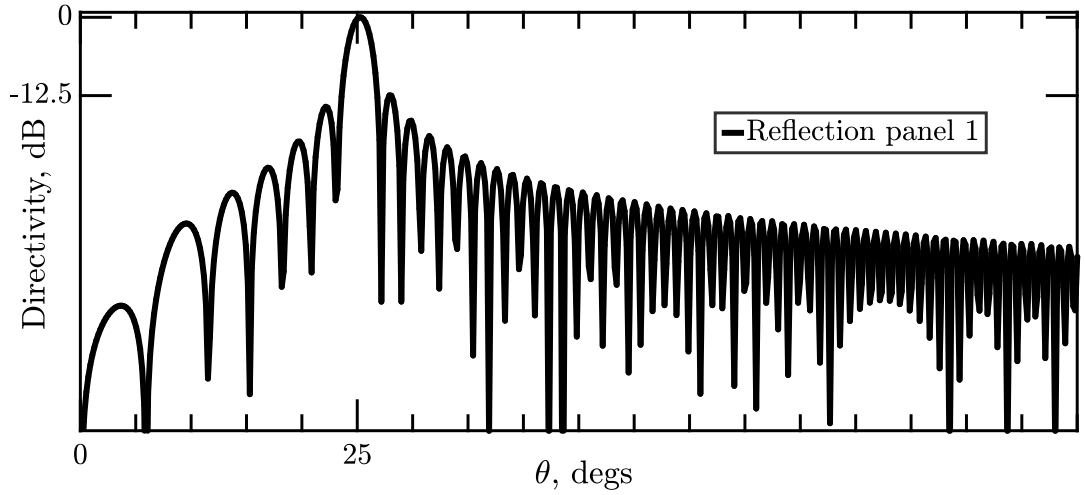

FIGURE 2.22 – Directivity pattern of the reflected beam from panel 1 for beam of incidence angle $\beta = 0°$ on an array following phase law at $\beta = 5°$

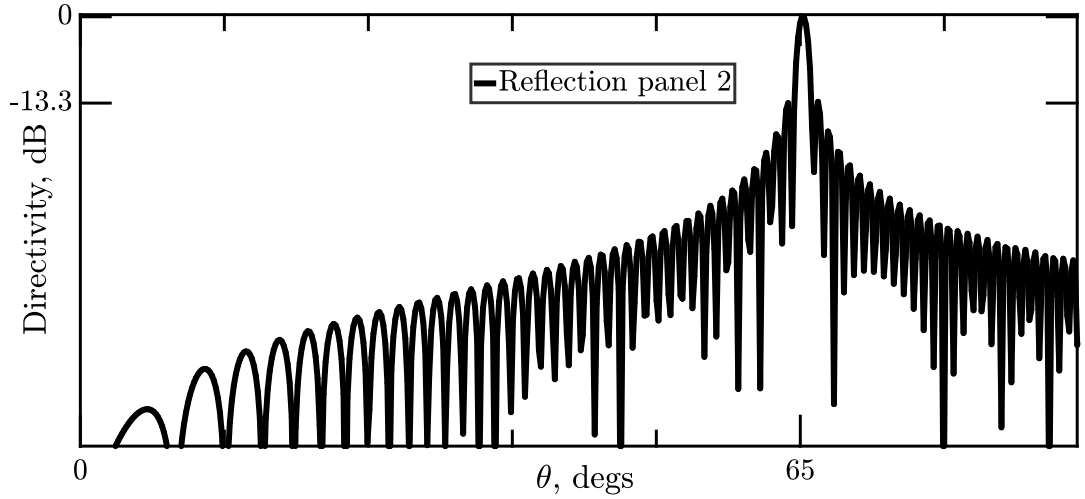

FIGURE 2.23 – Directivity pattern of the reflected beam from panel 2 for beam of incidence angle $\beta = 0°$ on an array following phase law at $\beta = 5°$

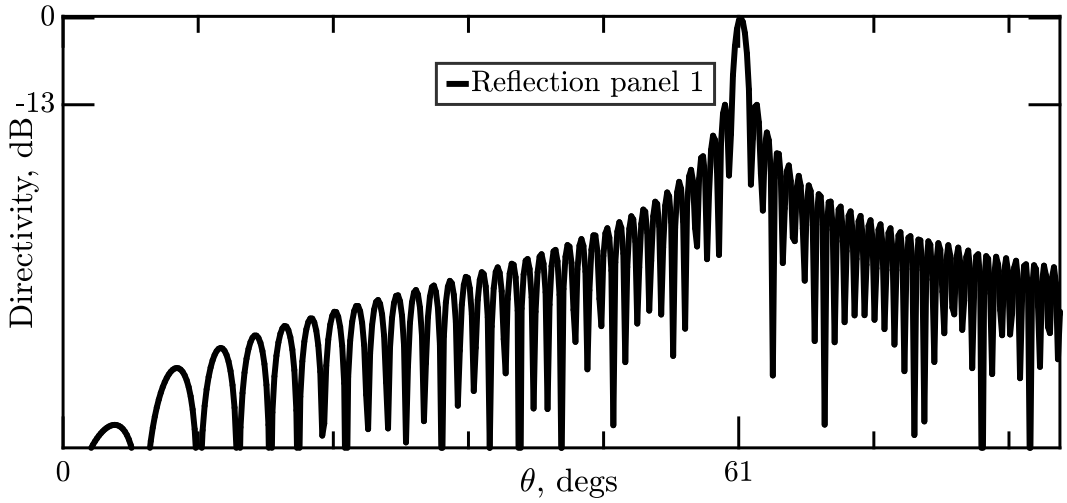

FIGURE 2.24 – Directivity pattern of the reflected beam from panel 1 for beam of incidence angle $\beta = 15°$ on an array following phase law at $\beta = 15°$

2.7 Conclusion

In this chapter, a detailed analysis on the retrodirective performance of a flattened dihedral using periodic arrays have been presented. First, the global phase governing has been analytically derived in function of the incidence angle and the geometrical parameters of the configuration. Using complementary formulations, the critical factors affecting the dihedral reflection mechanism have been studied and their impact on the retrodirective performance has been assessed. In the process, the ideal case of reflection has been distinguished from the attainable one as the case where the cells phase responses can be re-tuned to construct a global phase law corresponding to any incidence angle of the incoming wave.

It is found that the degree of the flattening of the dihedral influences the visibility of the beam by the second panel. As the dihedral gets flattened, the range of incidence angles upon which the beam intercepts the second panel of reflection becomes narrower.

On the other hand, it is known that the cells are tuned to construct a phase law for a unique incidence angle. This introduces inaccuracies in the retrodirective performance over the visible range of incidence angles. It has been shown that deviation from the ideal retrodirective axis increases as the angle of incidence becomes more distant from the targeted incidence angle. However, the margin of error remains generally non-influential on the retrodirective performance of the dihedral.

Taking into account the forward and reverse configurations, three regions of operation could be identified. The first is when both configuration are operating simultaneously around the targeted incidence angle. In the second and third, only one of the configurations is operating while the other lies in the invisible region.

Finally, the impact of degree of flattening can be seen as the most critical as having

the beam not intercepting the other panel meaning that all energy is lost. The phase law inaccuracies produce deviation errors that are tolerable especially around the targeted angle of incidence. Those conclusions give the needed physical insight to understand the reflection mechanism and serve as guidelines to follow in the design of such type of reflectors.

Chapter 3

Realization of retrodirective flattened dihedral using metallic patches

3.1 Introduction

In the previous chapter, the theoretical aspects of the retrodirective mechanism had been extensively studied. The impact of critical factors on the reflector performance has been assessed. It has been shown theoretically that the phase law inaccuracies do not have a major impact on the retrodirective phasing mechanism. However, the optimum performance of a phasing mechanism can get easily deteriorated as a function of the degree of flattening. It could be seen that the range of incidence angles upon which the dihedral operates decreases drastically whenever flattening the dihedral. With the complementary analysis on the forward and reverse cases, a mono-static RCS profile can be predicted for a retrodirective flattened dihedral of a certain phase law constructed on its panels.

Following this analytical study, the purpose of this chapter would be to validate the analytical predictions obtained. For this sake, a prototype of a flattened dihedral operating at 24 GHz has been designed, fabricated and tested. The RCS results obtained are analyzed to validate that they comply with the theoretical predictions.

This chapter is composed of three main parts : unit cell study, reflectarray construction and design of a flattened dihedral inspired from this reflectarray functionality. In the unit cell part, after justifying the choice of the cell type, a study is conducted to obtain the reflection phase response by the unit cell with respect to different parameters including the correlated geometrical parameters and incident wave characteristics. This is done by numerically simulating the infinite environment in which a unit cell belongs to.

In the second part, based on this unit cell study, a reflectarray is constructed neglecting the effects of the finiteness of the array and also the fact that the cells are not

identical.

In the last part, a prototype of retrodirective flattened dihedral is proposed. The dihedral functions as a combination of two reflectarrays symmetrically attached to each other. Using the simulation results of the second part, the reflection mechanism between the two panels is dissected and a method is proposed to enhance the retrodirective performance of the dihedral.

Complementary studies are included in this part to investigate several related subjects of interest. Using the unit cell study done in the first part, a comparison is performed over the design of a flattened dihedral using cells of different periodicities. Also, the dispersive nature of the flattened dihedral is discussed based on the study done on the dispersive nature of the used unit cell. Another aspect to be given attention is the impact the flattening degree can have on the performance of the dihedral. For this sake, dihedrals with different flattening degrees are simulated and their results are analyzed to have a conclusion. Those aspects are going to be discussed explicitly in this chapter.

To back this whole study, a prototype operating at 24 GHz is fabricated and tested. The measurements are held in an anechoic chamber using two horn antennas operating as a transmitter and a receiver and a Virtual Network Analyzer (VNA) to calculate the monostatic RCS of the reflector. After having validated the simulation results, an overall conclusion could be drawn on the potentials and limits of the flattened dihedral configuration inspired by reflectarray.

3.2 Unit cell analysis

3.2.1 Introduction

The effective design of a reflectarray that performs well relies on the phase response of the array cells forming it. Normally, reflectarrays are composed of a large number of elements that makes it exhaustive and tedious to analyze. To reduce the study time, an effective approach is based on modelling the reflectarray as an infinite array[78]. By doing so, a reflectarray element can be visualized as a unit cell in this infinite environment. This permits to evaluate its response based on Floquet theory which takes into account the mutual coupling between the elements. In this section, the unit cell structure is proposed and the critical parameters of design are defined. Later, the phase response of the cells is studied in terms of these parameters along with the characteristics of the incident plane wave.

3.2.2 Unit cell structure

Fig. 3.1 shows the structure of the unit cell used in this study. The unit is composed of three layers. The first layer consists of a metallic patch of certain shape. The second layer is a dielectric substrate that supports the patch. The third is the ground plane that ensures that the energy is totally reflected back. In this study, the unit cell is part of an infinite environment upon which cells interact and couple to produce a collective response that scatters an incident beam of certain incidence angle and polarization. The result is

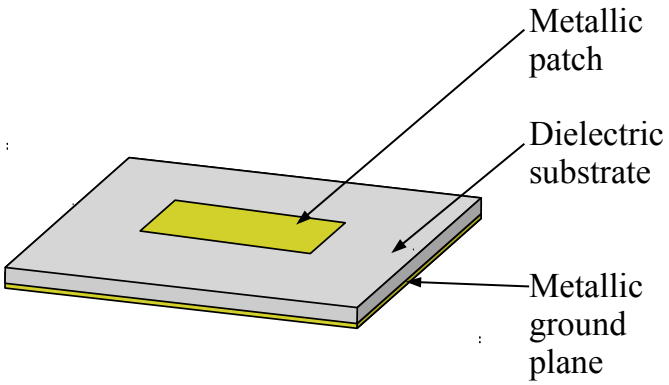

FIGURE 3.1 – The description of the layers composing a unit cell

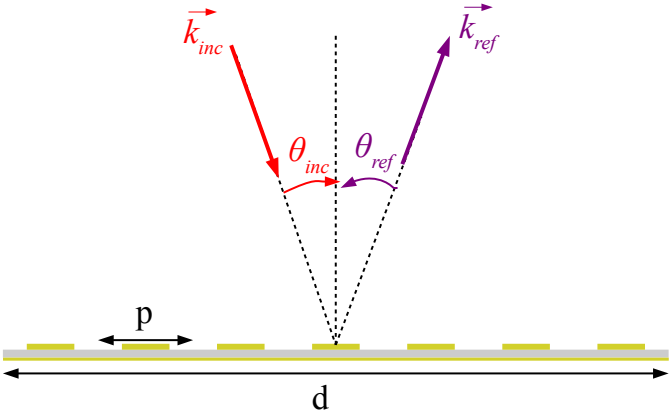

FIGURE 3.2 – The reflection mechanism on a reflectarray of certain length d and periodicity p

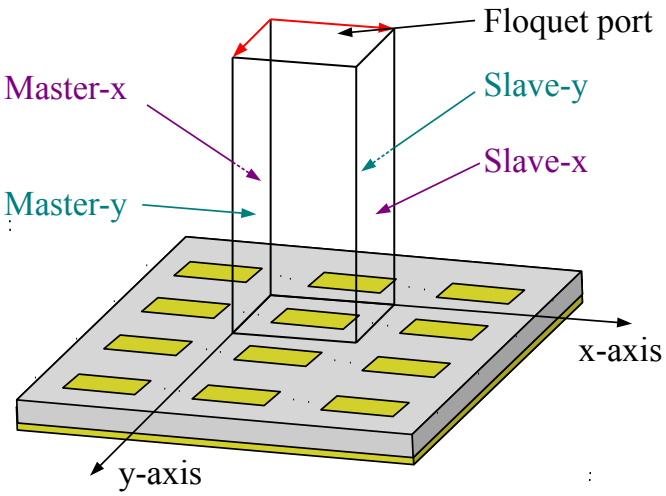

FIGURE 3.3 – A description for the Floquet setup upon which the unit cell is numerically modeled

a reflected beam with certain angle of reflection and polarization. As an approximation, a large finite array -known as reflectarray- can be characterized as an infinite array and is considered to have the same scattering behavior. An illustration is provided in Fig. 3.2.

3.2.3 Infinite array solver

Numerically modeling an infinite array is possible using HFSS commercial software. A unit cell is modeled by appropriately defining a Floquet port and the master/slave boundaries as illustrated in Fig. 3.3. The corresponding periodic array can support one or more Floquet modes depending on the scanning angle and the chosen periodicity of the lattice. Each Floquet mode is a plane wave of either Transverse Electric (TE) or Transverse Magnetic (TM) polarization. The dominant modes denoted TE00 and TM00 correspond to the main lobe created by the array while the higher modes can be seen as the result of the appearance of grating lobes. The master/slave boundaries are there to match the electric field amplitude between the array cells while forcing a phase shift in function of the lattice periodicity and the scanning angle.

3.2.4 Reflection phase response

The reflection phase response of a unit cell is of great importance in our study due to being focally used in the design of the reflectarray elements. For a given unit cell, this response varies based on the polarization of the Floquet mode and the delay of the incident beam with respect to the normal. An illustration is given in Fig. 3.4. By de-embedding the distance between the Floquet port and the unit cell, it would be possible

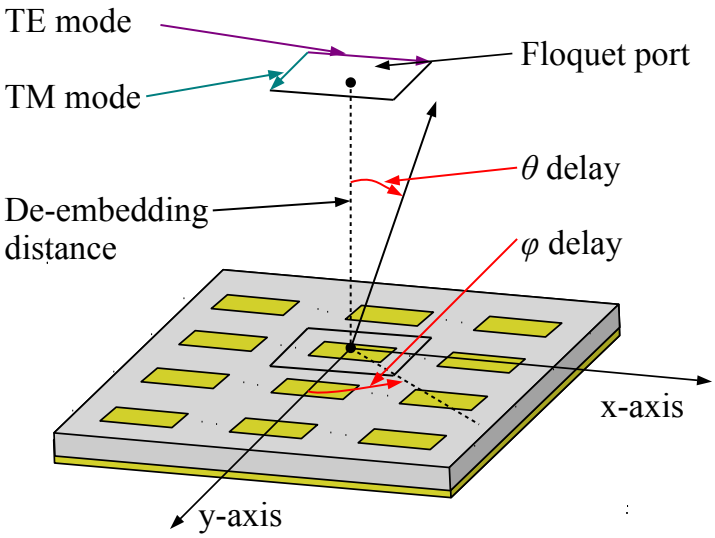

FIGURE 3.4 – A definition of the Floquet excitation polarization and the scanning angle in polar coordinates along with the precision of the de-embedding distance that helps in the calculation of the reflection phase response

to numerically obtain the corresponding S-parameter reflection phase. The curve is hence constructed by correlating this reflection phase with the geometrical parameters of the unit cell.

3.2.5 Cell type choice

The desired cell has to be compact since the periodicity must be small enough to avoid grating lobes. But also, enough space is needed if a wide phase range is to be achieved. Hence, the interest is in cells that can act as folded resonators. Several types of patches exist in literature that can offer the characteristics desired in our work [79],[80].

Annular cell provides a wide phase response and due to its folded geometry is ap-

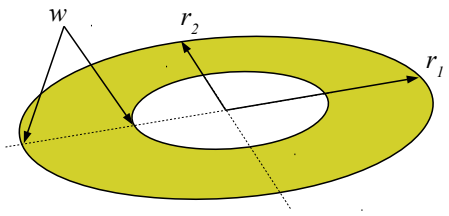

FIGURE 3.5 – A representation of the geometrical parameters of an elliptical annular cell

propriate for the usage in the construction of the phasing mechanism operating in dual polarization configuration. Annular cell in its most general case is an elliptical cell of a certain width w and major and minor radii denoted $r1$ and $r2$ respectively. An illustration is given in Fig. 3.5.

In this work, the width will be fixed into a certain value. The major and minor radii are correlated to the reflection phase response of the unit cell in the TE and TM cases respectively. By tuning those geometrical parameters it would be possible to create a phased array that follows a predefined certain law for both polarizations. Throughout this chapter, the substrate height is fixed to nearly $\lambda_0/16$ and its relative permittivity to $\epsilon_r = 2.2$.

3.2.6 Periodicity choice

The most critical parameter in the design of an array is its periodicity. Referring to array theory [81], the combination of having certain periodicity with a certain scan angle would mean the presence of grating lobes or not. In this work here, it is required from the array to stimulate solely the appearance of the fundamental Floquet mode (TE00 or TM00) that corresponds to the main lobe. In this case, according to array theory, the condition so that only the main lobe appears is having periodicity $p < \lambda_0/2$ regardless of the scanning angle. Very small periodicity would mean richer coupling between the array elements. However, in the case of geometrically tuned phased arrays this would also provide less room to maneuver and hence narrower range of reflection phase.

To obtain the reflection phase profile, a circular unit cell ($r = r_1 = r_2$) has been simulated using Floquet setup in TE configuration mode. The frequency of operation is chosen at 24 GHz. The incidence of the incoming wave is $\phi = 0°, \theta = 50°$. The substrate height is fixed to $0.787mm$. Fig. 3.6 shows the reflection phase curve of unit cells of different periodicities for two given cell widths $0.5mm$ and $0.8mm$ correlated to the outer radius r. The maximum outer radius is equal to 1.55, 2.05 and $3.1mm$ for the periodicities equal to $\lambda_0/4$, $\lambda_0/3$ and $\lambda_0/2$ respectively. The reflection phase curves for $p = \lambda_0/2$ show wide phase range for both widths with a steeper resonance for the case where $w = 0.5mm$. Regardless, the appearance of grating lobes for certain scanning angles in this case is not a desired feature in this work. For width $w = 0.8mm$, the phase range corresponding to $p = \lambda_0/3$ is significantly wider than that corresponding to $p = \lambda_0/4$. Even for $p = \lambda_0/4$ and thinner width of $0.5mm$, still the phase range is quite wider for the case where $p = \lambda_0/4$ and $0.8mm$.

Using the unit cell structure of a periodicity $p = \lambda_0/3$, it would be possible to obtain a relatively wide range of reflection phase (about 340°) with no additional grating lobes. Thus, it is the most appropriate choice based on this work requirements.

3.2.7 Width choice

In the previous section, a study about the unit cell periodicity has been conducted. The study on the cell width in this section is correlated to that of the periodicity. Consequent to the choice of $p = \lambda_0/3$ at frequency of operation 24 GHz, three potential

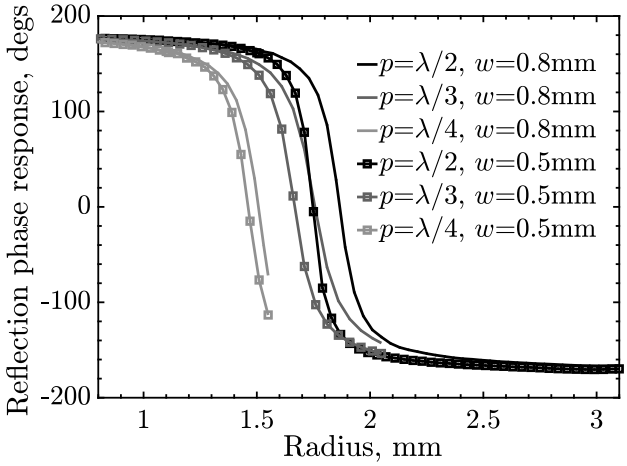

FIGURE 3.6 – The reflection phase response versus outer radius for unit cells of different periodicities($p = \lambda_0/4$, $\lambda_0/3$ and $\lambda_0/2$) and widths(0.5 and $0.8mm$) operating at 24 GHz and excited by a Floquet port at an oblique incidence of $\theta = 50°$ in TE mode configuration

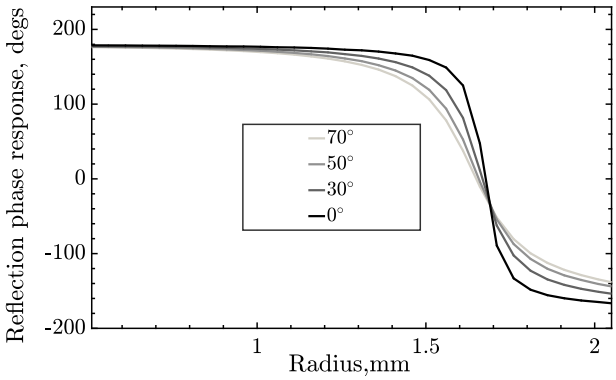

FIGURE 3.7 – The reflection phase response versus outer radius for a unit cell of $w = 0.5mm$ operating at 24 GHz for different incidence angles in TE mode configuration

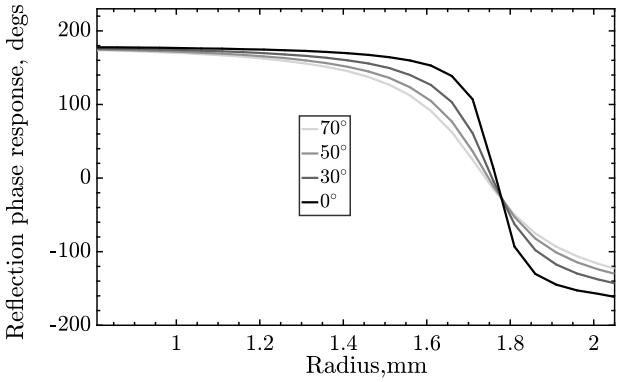

FIGURE 3.8 – The reflection phase response versus outer radius for a unit cell of $w = 0.8mm$ operating at 24 GHz for different incidence angles in TE mode configuration

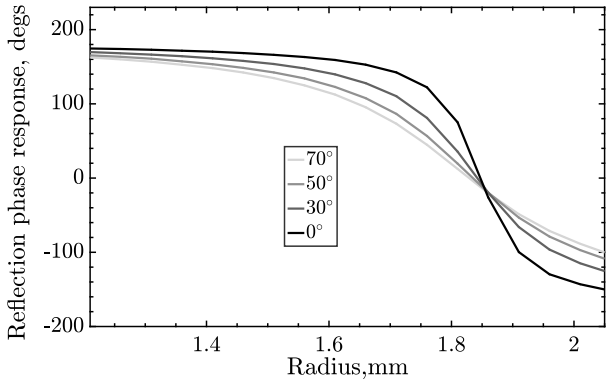

FIGURE 3.9 – The reflection phase response versus outer radius for a unit cell of $w = 1.2mm$ operating at 24 GHz for different incidence angles in TE mode configuration

widths are studied here : 0.5, 0.8 and $1.2mm$. For this sake, a unit cell is simulated using a Floquet setup with different incidences, $(\phi;\theta)$: $(0°;0°)$, $(0°;30°)$, $(0°;50°)$ and $(0°;70°)$ for both TE and TM mode configurations. The results for TE configuration are presented in Fig. 3.7, 3.8 and 3.9 for widths of 0.5, 0.8 and $1.2mm$ respectively. From those results, some observations can be seen :

1. For a given width, the resonance gets less steeper whenever the incidence gets more oblique.
2. Whenever the width increases, the phase range shrinks especially when the delay get more oblique.

In the case of TM configuration, similar observations are made from Fig. 3.10, 3.11 and 3.12. From these observations, a circular cell of $w = 0.8mm$ is the most appropriate for the design of the reflectarray. Although the unit cell of $w = 0.5mm$ possesses the widest phase range, however its steep resonant behavior makes it more sensitive in terms of fabrication tolerances and thus produces errors that degrades the performance of the

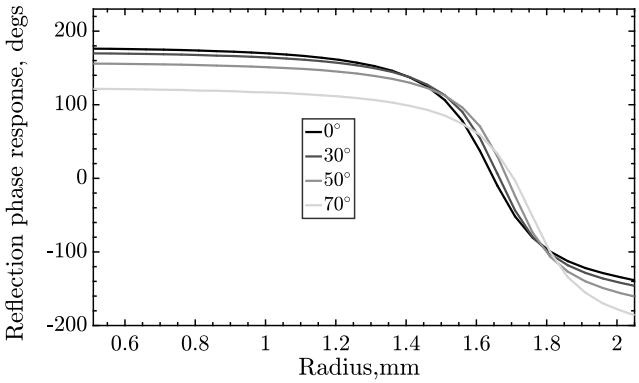

FIGURE 3.10 – The reflection phase response versus outer radius for a unit cell of $w = 0.5mm$ operating at 24 GHz for different incidence angles in TM mode configuration

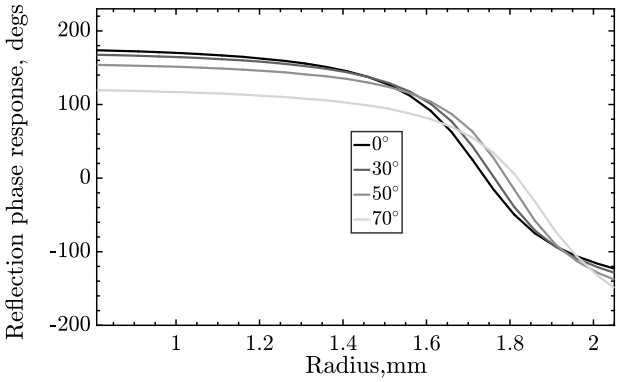

FIGURE 3.11 – The reflection phase response versus outer radius for a unit cell of $w = 0.8mm$ operating at 24 GHz for different incidence angles in TM mode configuration

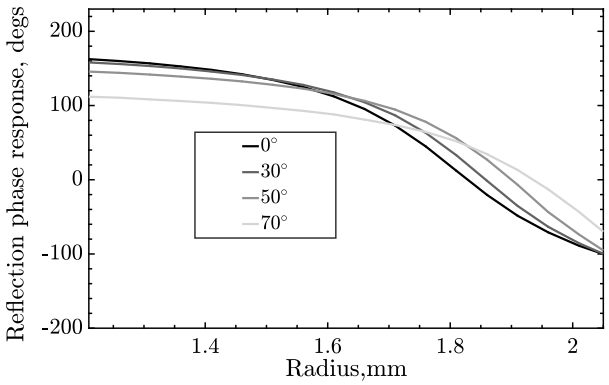

FIGURE 3.12 – The reflection phase response versus outer radius for a unit cell of $w = 1.2mm$ operating at 24 GHz for different incidence angles in TM mode configuration

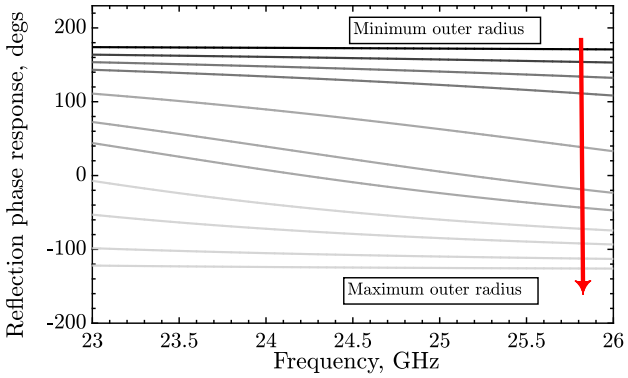

FIGURE 3.13 – The reflection phase response versus frequency for a unit cell of $w = 0.8mm$ having its outer radius ranging from the minimum to the maximum possible value and excited at normal incidence

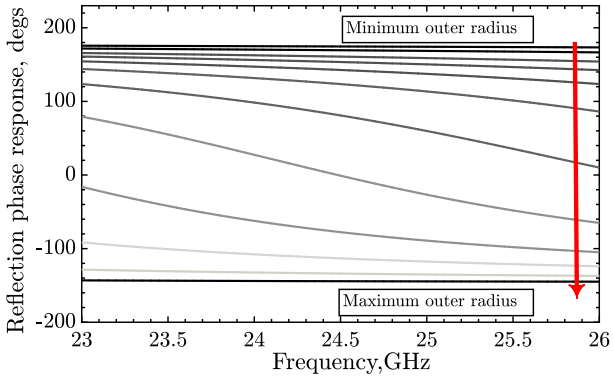

FIGURE 3.14 – The reflection phase response versus frequency for a unit cell of $w = 0.8mm$ having its outer radius ranging from the minimum to the maximum possible value and excited at oblique incidence $\theta = 50°$ in TE mode configuration

reflectarray.

3.2.8 Study on the dispersive nature of the cells

In this section, the dispersive nature of the phasing cell is discussed. This is an interesting study for the later parts of this chapter where the frequency band of operation of the reflectarray is under study.

A cluster of circular cells of different outer radii is simulated over frequencies ranging from 23GHz to 26GHz. The periodicity of the unit cell is $p = \lambda_0/3$ at a central frequency of operation equal to 24 GHz while the width is fixed to $w = 0.8mm$.

Fig. 3.13 shows the reflection phase curves for the case where the incidence is set to $\theta = 0°$. In this case, the same response can be obtained in TE and TM configurations due

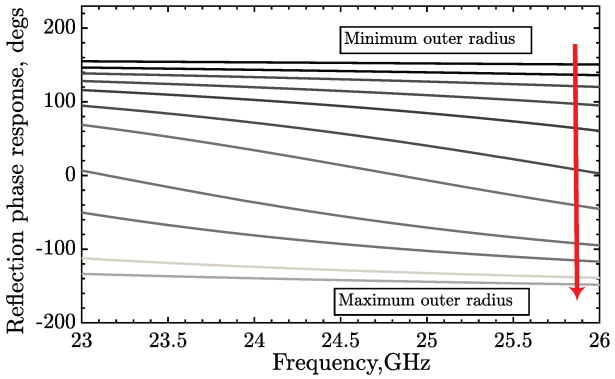

FIGURE 3.15 – The reflection phase response versus frequency for a unit cell of $w = 0.8mm$ having its outer radius ranging from the minimum to the maximum possible value and excited at oblique incidence $\theta = 50°$ in TM mode configuration

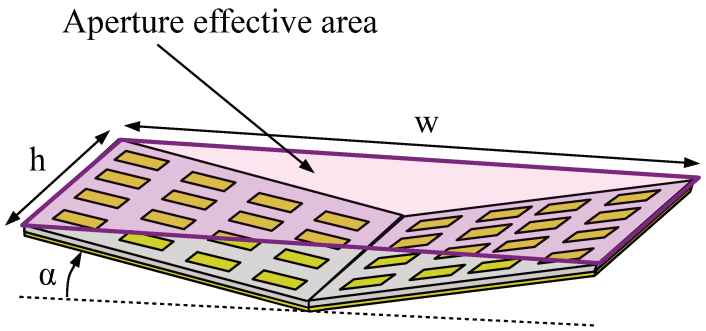

FIGURE 3.16 – A sketch illustrating the aperture effective area $(h * w)$ of a flattened dihedral of a certain flattening degree (α)

to the structure symmetry. On the other hand, Fig. 3.14 and 3.15 show the phase curves corresponding to the oblique excitation delay of $\theta = 50°$ for TE and TM configurations respectively.

From those results, it is observed that the phase curves possess smooth profile over the frequency band. Also, the curves keep a nearly constant phase difference between each other around the frequency of interest in a region where the phasing array might still properly perform.

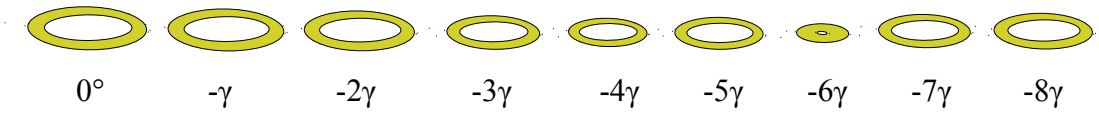

FIGURE 3.17 – Caption of the circular cells used in the design of the reflectarray

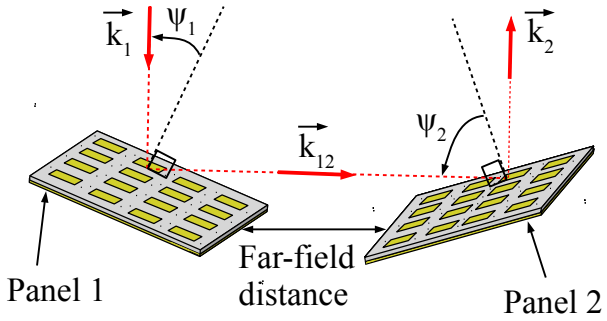

FIGURE 3.18 – An illustration of the reflection mechanism between the panels 1 and 2 constructing the flattened dihedral : Angles ψ_1 and ψ_2 represent the angle of incidence on panel 1 and 2 respectively. Vector $\vec{k}_1$ corresponds to the wave vector of the incident beam, $\vec{k}_{12}$ corresponds to the reflected wave vector by panel 1 and $\vec{k}_2$ corresponds to the wave vector of the reflected beam by panel 2.

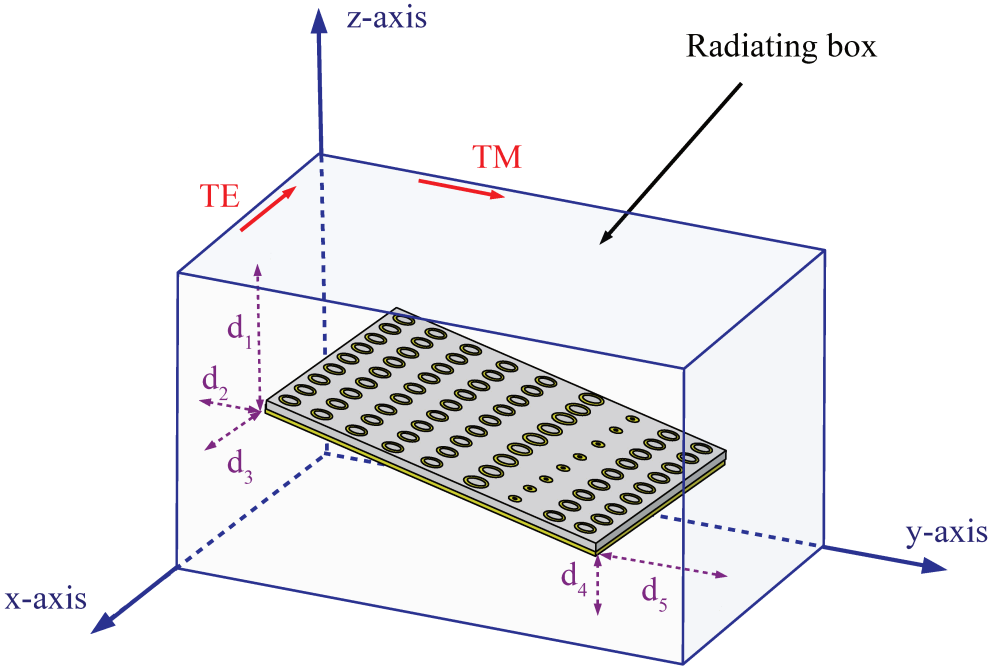

FIGURE 3.19 – Illustration of the simulation setup of the reflectarray panel which is immersed in the radiating box with d_1, d_2, d_3, d_4 and d_5 all should be greater than $\lambda_0/4$

3.3 Reflectarray design based on annular Cells

3.3.1 Introduction

In this section, the retrodirective reflection mechanism of a retrodirective flattened dihedral using annular cells is discussed. The section can be divided into several parts. The first discusses the general design specifications and requirements. In the second, a reflectarray is designed based on the results of the cell study performed in the previous section. In the process, the retrodirective phase law enforced by the cells is defined and the correlated cells dimensions are specified. Two identical reflectarrays are simulated to emulate the reflection mechanism between the two panels of the dihedral in both TE and TM configurations. The simulation results will provide the needed physical insight to understand the occurring reflection phenomenon.

3.3.2 General design specifications

For the reflector-RADAR system, the minimum required level of backscattering by the reflector should be set to a certain value dBsm. In the case of a flattened dihedral, this value can be theoretically related to the aperture effective area as illustrated in Fig. 3.16. The backscattering by a dihedral possessing this effective area is equivalent to that of a metallic flat plate of the same area.

The frequency of operation is bound to the RADAR application itself. In this project, a short-range RADAR operating at 24 GHz is used. The dihedral hence should operate at this specific frequency.

Being required to fit into compact volume, the dihedral flattening degree is set to $\alpha = 22.5°$.

3.3.3 Phase law

Following the most-likely scenario, the dihedral would be designed to operate for the nominal case as defined in the previous chapter. The corresponding incremental phase shift γ_0 is obtained using the theoretical formulation in previous chapter. Considering $\lambda_0 = 12.5$mm, $k_0 = 2\pi/\lambda_0$, $d = \lambda_0/3$ and $\alpha = 22.5°$, the phase shift becomes :

$$\gamma_0 = k_0 d[\cos(\alpha) - \sin(\alpha)] \approx 65°$$

. Hence, enforcing this incremental phase shift on the dihedral panels should be sufficient to obtain a retrodirective reflection for the nominal case.

3.3.4 Array construction

Following the performed cell study, simple annular patches can possess phase reflection response that provides phase control of sufficiently wide range to achieve the required phase law. The corresponding phase shift at a certain unit cell is obtained by tuning the patch dimension to a specific radius while keeping its width fixed.

TABLE 3.1 – List of the cells dimensions corresponding to each required phase shift using the classical cell setup

Phase-shift(deg.)	Classical setup(mm)
130	1.5
65	1.66
0	1.75
-65	1.84
-130	2.05
165	1.01
100	1.59
35	1.7
-30	1.78

In a classical design, the cells dimensions are usually obtained assuming a plane wave at normal incidence to the panel. In other words, the incidence as defined in the cell study is set to 0°.

Based upon this assumption, the cells dimensions for an array of 9 elements ensuring an incremental phase shift $\gamma_0 \approx 65°$ can be obtained using the phase profile in Fig. 3.11.

The obtained cells are depicted in Fig. 3.17.

The corresponding dimensions can be found in Tab. 5.1.

3.3.5 Simulation setup

In this section, the setup of the simulation emulating the reflection by a flattened dihedral is described. Each panel consists of the defined array repeated 9 times in the x-direction. Thus, the total dimension of the panel becomes $3\lambda_0$ by $3\lambda_0$. In this scenario, the dihedral panels are assumed to be in the far-field of each other. Fig. 3.18 illustrates the reflection path simulation of an electromagnetic beam from one panel to the other where the beam intercepts panel 1 with an angle of incidence ψ_1 and panel 2 with angle ψ_2. Angle ψ_2 can be deduced from the information gathered about the angle upon which the beam leaves panel 1.

This scenario can be emulated by simulating each of the panels alone. In this simulation setup, each of the panels is deeply immersed in a radiating box with its edges distant by at least $\lambda_0/4$ from the box facets as illustrated in Fig. 3.19. The radiating box facets are assigned radiation boundaries so that absorb to the electromagnetic far-field scattering. This setup will permit for the calculation of far-field metrics as cross section and directivity.

3.3.6 Directivity Results for TE and TM configurations

In this section, the simulation results of the reflection mechanism on the panels of the dihedral are presented for both TE and TM configurations. The far-field scattering is

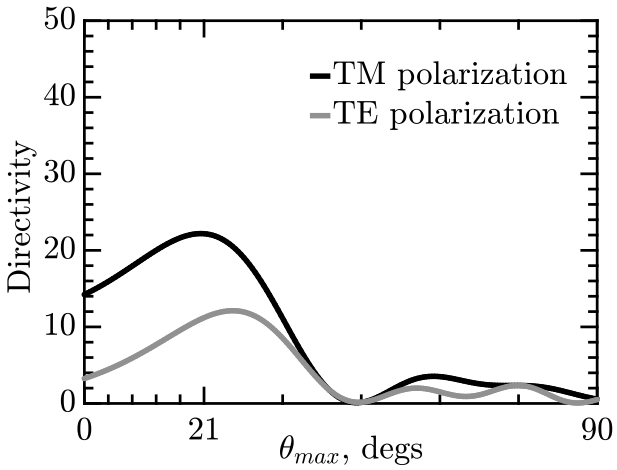

FIGURE 3.20 – The directivity of the reflected beam of incidence angle $\beta = -5°$ by panel 1 in TE and TM configurations

quantized here in terms of directivity, which is the ratio of the scattering intensity by the reflector in a given direction to the scattering intensity averaged over all directions. With its unit being dimensionless, this quantity serves as an information about the direction of the main lobe created by the array. Scenarios of incidence angles of significant importance are simulated here : $\beta = -5°, 0°, 11°, 22.5°$ and $38°$. The angle notations used in this part are the same ones used in the previous chapter. Please, revisit Fig. 2.6.

3.3.6.1 Reflection on panel 1

Starting with the scenario of $\beta = -5°$, theoretically, this is the case where the reflected beam from panel 1 grazes the surface of the array ($\theta_{max} = 0°$). Fig. 3.20 shows the directivity results in this case for both TE and TM configurations. From the curves, it could be seen that the main lobe is wide with a peak around angle $\theta_{max} = 21°$ in TM configuration with the peak being slightly shifted upwards in TE configuration. Two major observations can be made. The first is the remarkable difference between the theoretical and simulated θ_{max}. While the second is that the directivity in the TM configuration possesses higher intensity with respect to that of TE, this observation being common in all the following scenarios.

The $\beta = 0°$ scenario is of significant importance because it is the nominal case for which the array elements have been specifically designed to work upon. Fig. 3.21 shows the directivity results corresponding to this scenario. From the resulting curves and expected θ_{max}, it can be observed that the simulated main lobe peaks in TM and TE configurations($\theta_{max} = 30°$ and $32°$ respectively) are shifted from the theoretical one ($\theta_{max} = 22.5°$) by not more than $10°$. Next is the scenario of $\beta = 11°$. From the resultant curves in Fig. 3.22, the main lobe peaks at angle $\theta_{max} = 45°$ in both TE and TM configurations. This angle is equivalent to 2α, hence, geometrically, the reflected

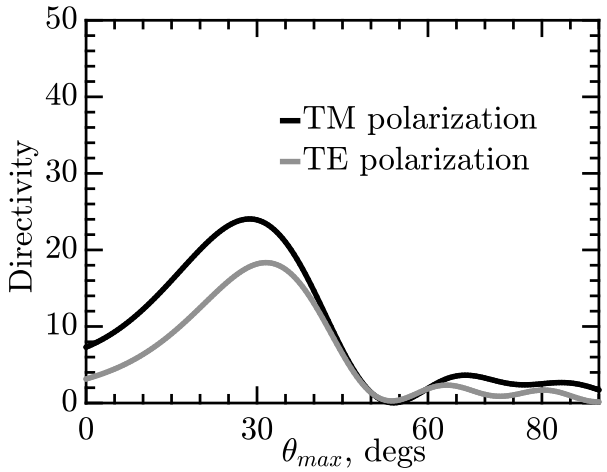

FIGURE 3.21 – The directivity of the reflected beam of incidence angle $\beta = 0°$ by panel 1 in TE and TM configurations

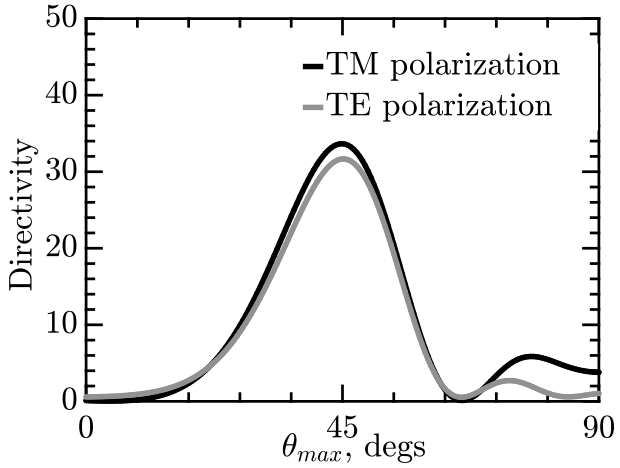

FIGURE 3.22 – The directivity of the reflected beam of incidence angle $\beta = 11°$ by panel 1 in TE and TM configurations

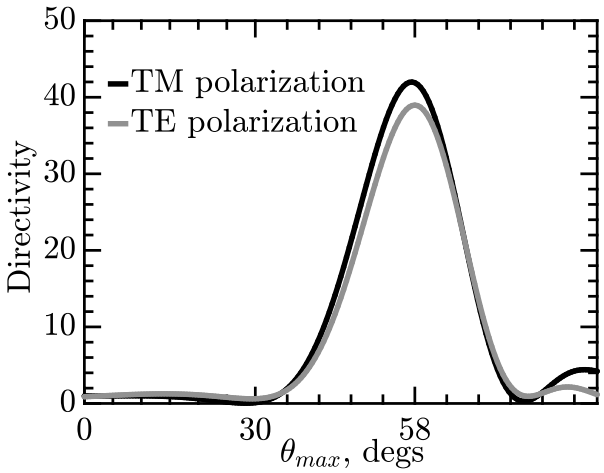

FIGURE 3.23 – The directivity of the reflected beam of incidence angle $\beta = 22.5°$ by panel 1 in TE and TM configurations

TABLE 3.2 – A presentation of the scenarios and the corresponding angles of incidence and reflection on panel 1

Scenario	$\beta(°)$	$\psi_1(°)$	Theoretical $\theta_{max}(°)$	Simulated TM $\theta_{max}(°)$	Simulated TE $\theta_{max}(°)$
1	-5	27.5	0	21	26
2	0	22.5	22.5	30	32
3	11	11.5	42	45	45
4	22.5	0	57	58	58
5	38	-15.5	74	75	75

beam would never intercept panel 2. The significance of the $\beta = 22.5°$ scenario lies in the fact the cells here are simulated with the same angle upon which the unit cell design has been conducted, in other words, the beam being normally incident on the cells. The directivity results shown in Fig. 3.23 show excellent agreement with the theoretical predictions ($\theta_{max} = 57°$). In the last scenario, a beam of incidence angle $\beta = 38°$ is simulated. The resultant simulated θ_{max} is in excellent agreement with the theoretical formulation for both TE and TM configurations as shown in Fig. 3.24. The significance of obtaining $\theta_{max} = 75°$ lies in the fact that the reflected beam from panel 1 is redirected back in the same direction of incidence. Also, the obtained main lobe can be seen as the most directive with respect to the cases of other incidence angles.

Tab. 3.2 summarizes those scenarios and their corresponding theoretical and simulated reflection direction represented by the angle θ_{max}, noting that the theoretical formulation is independent of the polarization configuration.

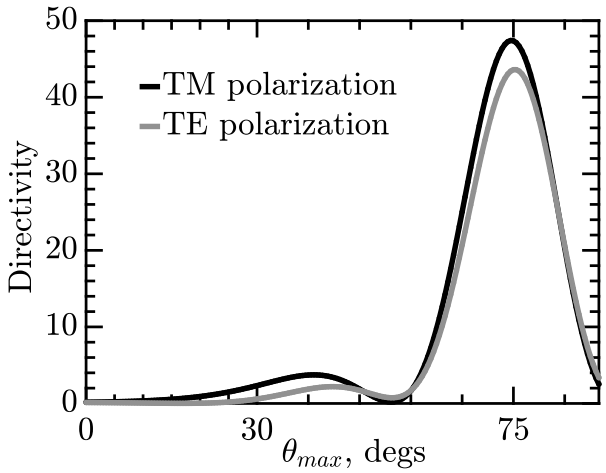

FIGURE 3.24 – The directivity of the reflected beam of incidence angle $\beta = 38°$ by panel 1 in TE and TM configurations

3.3.6.2 Reflection on panel 2

In this section, the scenarios where the reflected beams from panel 1 intercept panel 2 will be simulated, in other words, those incident beams whose corresponding θ_{max} fall in the visible range ($0° < \theta_{max} < 45°$). This relates to the scenarios of incident beams $\beta = -5°$ and $0°$.

Using the analytical formulations in the previous chapter, ψ_2 can be written as a function of ψ_1 :

$$\psi_2 = \arcsin[\frac{\gamma_0}{k_0 d} - \sin(\psi_1 - 2\alpha)] \tag{3.1}$$

Tab. 3.3 presents a comparison on the angle ψ_2 based on the afore-mentioned theoretical formulation and the simulations performed on panel 1. In the ideal case, $\beta' = \beta$ for every angle β.

In Fig. 3.25, the directivity with respect to angle β' is shown in the scenario of $\beta = -5°$ for both TE and TM configurations. Again, the main lobe in both polarization configurations peak at the same angle $\beta' = 0°$ which is $5°$ shifted in advance from the theoretical one. In Fig. 3.26, the absolute value of E-field resulting from the scattering by panel 2 is plotted in the yoz plane cutting through panel 2 for the TE configuration. The plot shows a main traveling wave in the retrodirective direction. The high concentration of the E-field around the array patches indicates to possible losses and this justifies the drop of the directivity level as compared to the TM case.

Fig. 3.27 plots the absolute E-field in the TM configuration. Similar to the TE case, the main traveling wave is scattered in the retrodirective direction. The wavefront is constructed in a better manner as compared to the TE case.

Concerning $\beta = 0°$ scenario, the results presented in Fig. 3.28 show that the slight deviation of β' from the theoretical value of $0°$ by $2°$ for TE case and $5°$ for TM case.

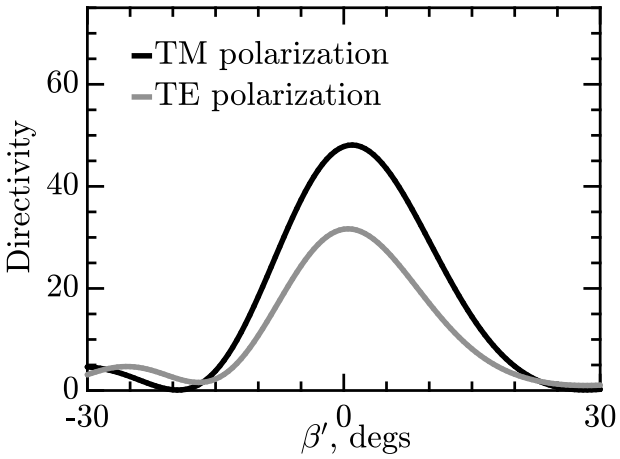

FIGURE 3.25 – The directivity of the reflected beam of incidence angle $\beta = -5°$ by panel 2 in TE and TM configurations

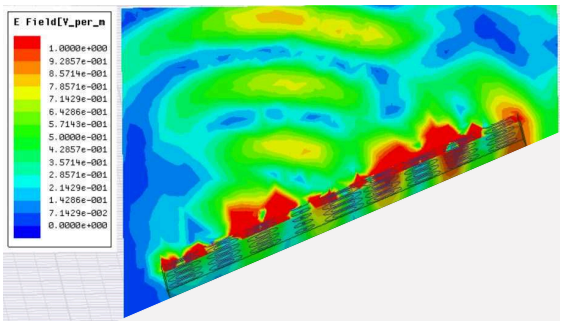

FIGURE 3.26 – The plot of E-field in the (YoZ) plane scattered by panel 2 for the scenario of incidence angle $\beta = -5°$ in TE configuration

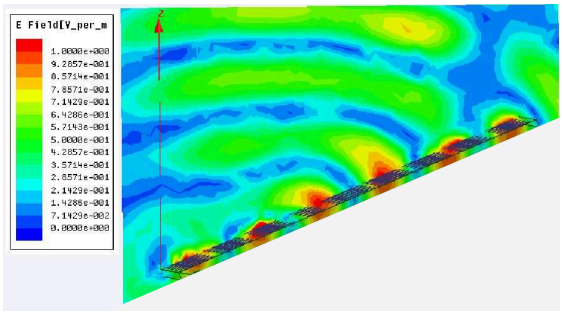

FIGURE 3.27 – The plot of E-field in the (YoZ) plane scattered by panel 2 for the scenario of incidence angle $\beta = -5°$ in TM configuration

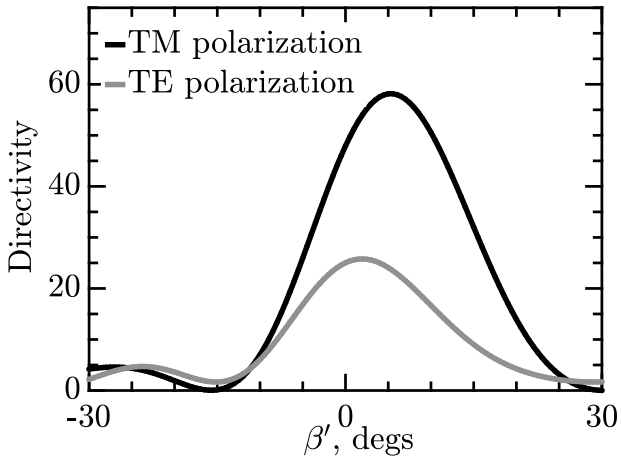

FIGURE 3.28 – The directivity of the reflected beam of incidence angle $\beta = 0°$ by panel 2 in TE and TM configurations

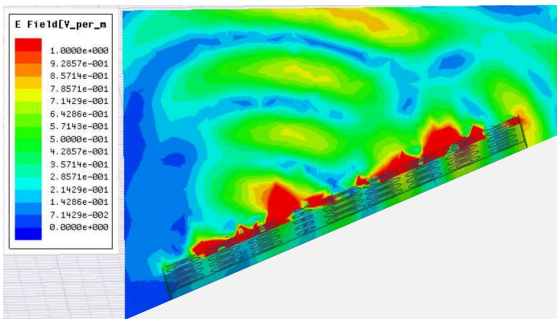

FIGURE 3.29 – The plot of E-field in the (YoZ) plane scattered by panel 2 for the scenario of incidence angle $\beta = 0°$ in TE configuration

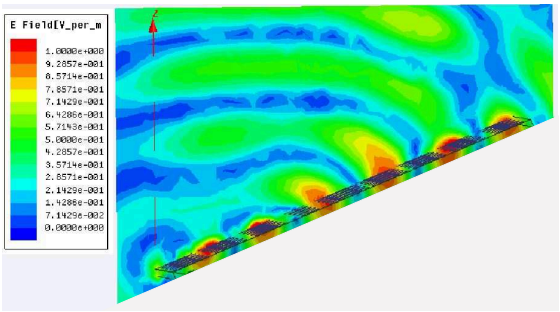

FIGURE 3.30 – The plot of E-field in the (YoZ) plane scattered by panel 2 for the scenario of incidence angle $\beta = 0°$ in TM configuration

TABLE 3.3 – A presentation of the scenarios and the corresponding angles of incidence on panels 1 and 2

Scenario	$\beta(°)$	$\psi_1(°)$	Theoretical $\psi_2(°)$	Simulated TM $\psi_2(°)$	Simulated TE $\psi_2(°)$
1	-5	27.5	45	66	71
2	0	22.5	67.5	75	77

TABLE 3.4 – A presentation of the scenarios and the corresponding angles of incidence on panel 1 compared with that of reflection on panel 2

Scenario	$\beta(°)$	Theoretical $\beta'(°)$	Simulated TM $\beta'(°)$	Simulated TE $\beta'(°)$
1	-5	-5	0	0
2	0	0	5	2

Figs. 3.29 and . 3.30, the absolute E-field is plotted for TE and TM configuration respectively. Similar observations and interpretations to that of the $\beta = -5°$ scenario can be given.

3.3.6.3 conclusion

In this section, panel-to-panel reflection scenarios of beams of different incident angles were simulated. The panel 1 reflection comparison results are summarized in Tab. 3.2. Using the information obtained about θ_{max}, the reflection scenario on panel 2 is simulated as summarized in Tab. 3.3. Finally, Tab. 3.4 summarizes the comparison between β and β' angles. Those results show that the phasing mechanism operates properly with slight deviation from the theoretical retrodirection.

3.4 Design and realization of a retrodirective flattened dihedral prototype

3.4.1 Design description

In this section, a design of a flattened dihedral using annular cells is proposed. Operating at 24 GHz, this dual-polarized reflector can be of great interest for collision avoidance systems. As shown in Fig. 3.31, the dihedral array is composed of the same 9 annular cells obtained in the previous section. However, here, those 9 cells are repeated 39 times in the x-axis direction, and the reason is to obtain an aperture effective area equivalent to that of a classical dihedral theoretically possessing a maximum RCS of $10dBsm$.

As a summary, Tab. 3.5 shows the full description of the designed flattened dihedral and the relevant classical dihedral corner.

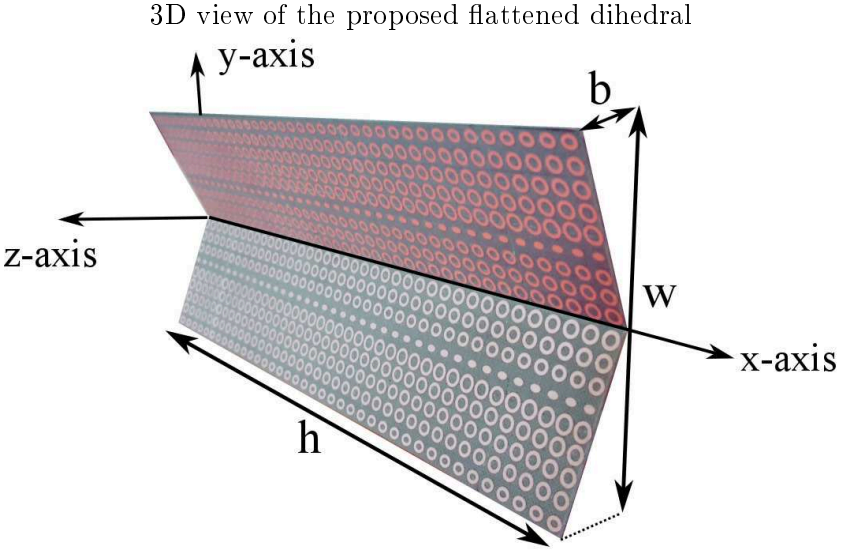

FIGURE 3.31 – 3D view of the proposed flattened dihedral

TABLE 3.5 – Geometrical dimensions of reference corner dihedral and flattened dihedral

Structure	b, mm	h, mm	w, mm
Classical dihedral	34.65	162.5	69.29
Flattened dihedral	14.35	162.5	69.29

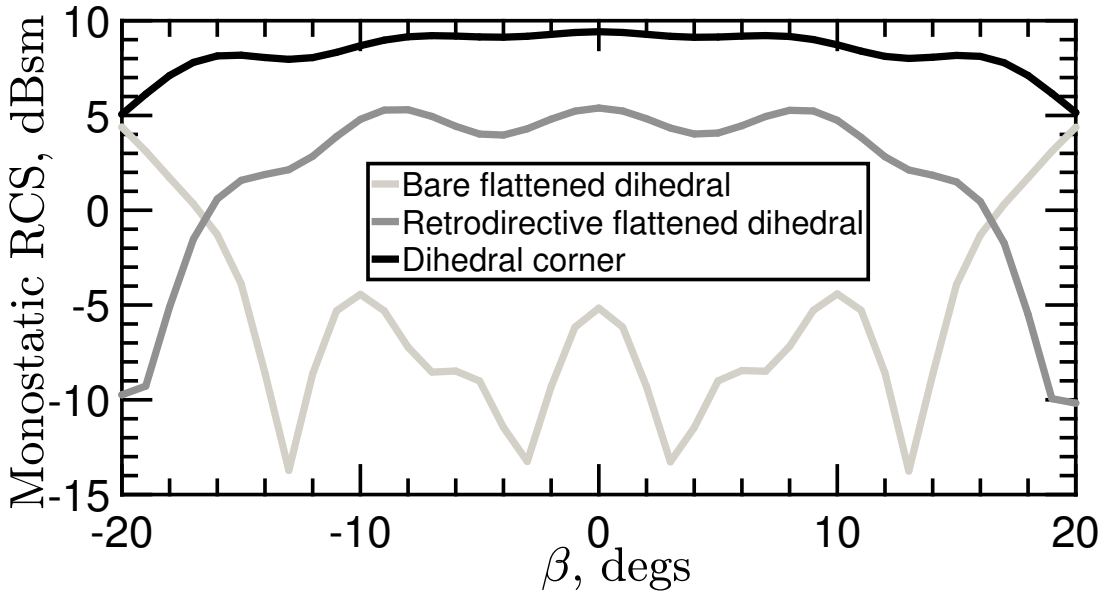

FIGURE 3.32 – RCS profiles of bare, classical dihedral corner and retrodirective flattened dihedral in TE configuration

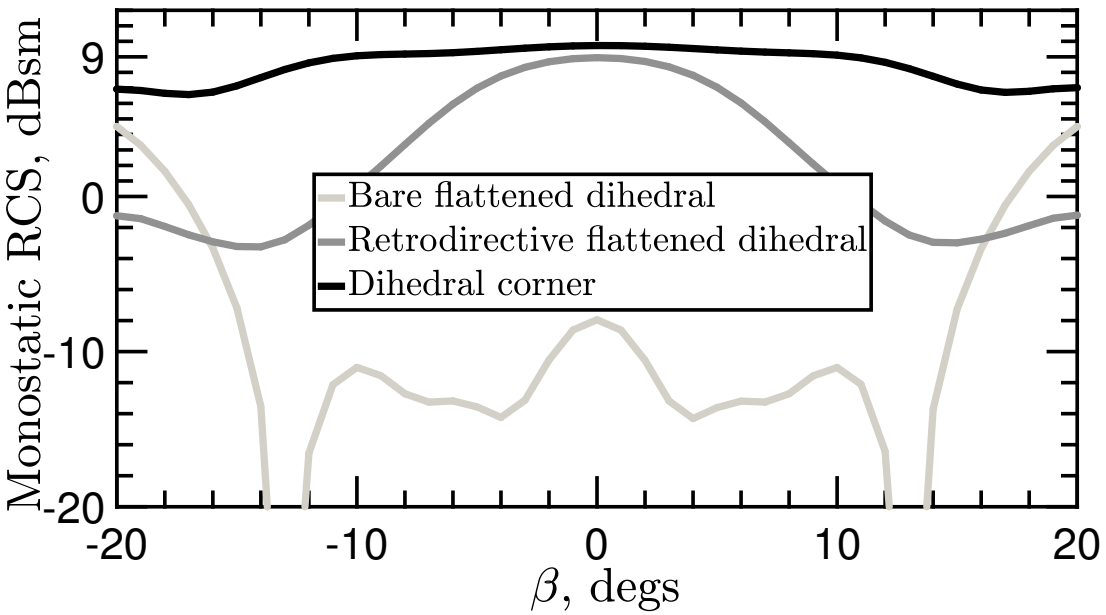

FIGURE 3.33 – RCS profiles of bare, classical dihedral corner and retrodirective flattened dihedral in TM configuration

3.4.2 Simulation

For better understanding of the performance of the retrodirective flattened diherdal using reflectarray, the structures of bare flattened dihedral (without phasing cells) and dihedral corner have been simulated also. Each of the above targets has been immersed in a radiating box and excited by an incident wave ranging from $-20°$ till $20°$ with respect to the z-axis in the (YOZ) plane. The radiating box is surrounded by perfectly matched layers to absorb the scattered wave similar to the simulation setup of one panel in Fig. 3.19. Here, the farfield quantity used is the monostatic RADAR cross section (RCS) as defined in chapter state of art.

Fig. 3.32 shows the monostatic RCS level of the above-mentioned structures for the TE configuration (E field along x-axis). First to notice is the massive enhancement the phasing mechanism introduces to a bare flattened dihedral specifically at normal incidence with an increase of more than 10 dB. The RCS profile sustains a nearly constant value around $5dBsm$ for a respected range of incidence angles. However, a significant difference of RCS can be observed for $\beta = 0°$ as compared to a dihedral corner signaling a possible problem in the overall retrodirective mechanism.

Similarly, the same structures have been simulated this time in TM configuration (E field along y-axis). Fig. 3.33 shows the corresponding monostatic RCS results. For angle $\beta = 0°$, the obtained RCS level is very close to the theoretical maximum. Around the nominal angle, the RCS level remains high, however, this level decreases sharply afterwards.

3.4.3 Design based on enhanced Floquet setup

Following the RCS profile results obtained in the previous section an investigation has been committed to understand the reason behind the significant difference between the theoretical RCS maximum value at $\beta = 0°$ (especially in TE configuration), for which the mechanism has been specifically constructed. For this sake, the work of the cell study and the reflectarray panel construction has been carefully read. The first thing to observe

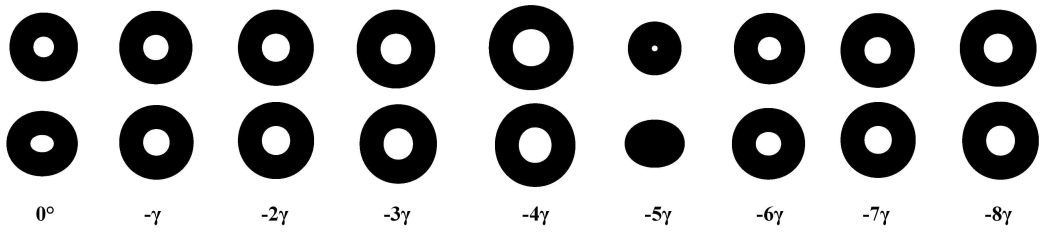

FIGURE 3.34 – Caption of the circular and elliptical cells used for the design of the retrodirective flattened dihedral

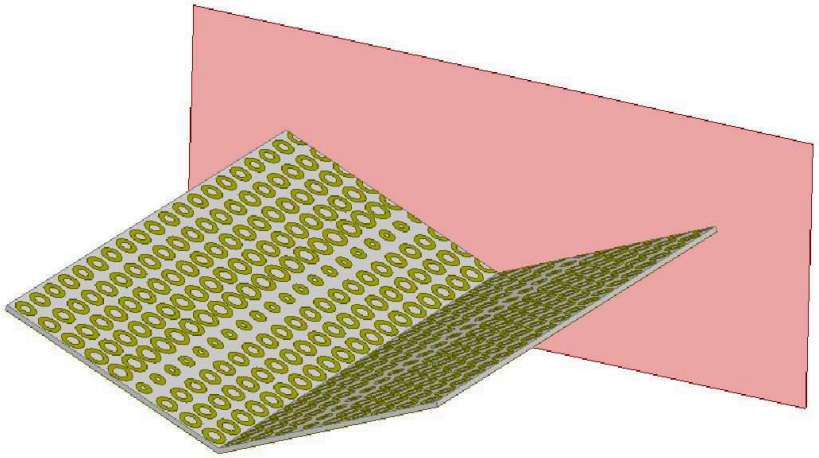

FIGURE 3.35 – 3D view of the proposed flattened dihedral of circular cells designed based on the enhanced Floquet setup in TE configuration

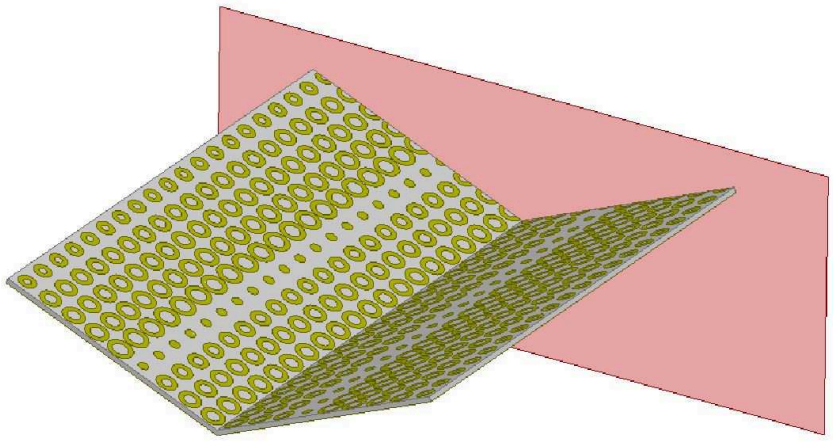

FIGURE 3.36 – 3D view of the proposed flattened dihedral of circular cells designed based on the enhanced Floquet setup in TM configuration

is that the reflector is a complex structure composed of two attached panels. In such a topology, the beam hits the two panels with two very different incidence angles ψ_1 and ψ_2 as shown in Tab. 3.3. The difference gets even more severe when comparing ψ_1 with the simulated ψ_2.

With this first evidence in hand, a cautious revision to the cell study is effectuated, especially to the curve of Fig. 3.11. It can be seen from the curves that the selection of the appropriate radius for a given phase law on the panels is highly related to the expected incident angle. This was not taken into account in previous work [63]. In fact, the cells on both panels were tuned based on the same classical setup assuming normal incidence on both panels.

To solve this problem, an average-angle setup is proposed to simultaneously enhance the cell response on each of the two panels so that to obtain better reflection mechanism between them. The new setup considers an average angle as a trade-off between the incidence angle on panel 1, $\psi_1 = \alpha = 22.5°$ (nominal case), and the corresponding incidence angle on panel 2, ψ_2. Following equation 3.1, the corresponding theoretical ψ_2 is equal to 67.5°.

Hence, the average incidence angle is set to $(67.5°+22.5°)/2 = 45°$. Since the incidence is non-normal, hence the reflection phase profiles are different for TE (E field along x-axis) and TM (H field along x-axis) polarizations leading to non-identical cells along both axes. Here, one can simply design two separate reflectors using different arrays of circular cells. Other possibility which seems more feasible is to use elliptical cells upon which each of its axes corresponds to a polarization. The dimensions of the required radii for TE and TM configurations are listed in Tab. 3.6. The cell dimension corresponding to phase shift 165.15° could not be covered by the obtained phase range and hence is set to the closest value which is 0.81mm.The proposed elliptical cells are captured in Fig. 3.34.

To finally assess the improvement the enhanced Floquet setup adds to the overall retrodirective performance, three different structures has been simulated. The first is the flattened dihedral designed using circular cells specifically for TE configuration depicted in Fig. 3.35, while the second is that of circular cells designed for TM configuration depicted in Fig. 3.36. The third one is the design using elliptical cells that should theoretically provide kind of trade-off for both TE and TM configurations simultaneously which is depicted in Fig. 3.31.

The obtained results are presented in Fig. 3.37. First, by comparing the RCS profiles of those corresponding to the classical and enhanced Floquet setups in TE configuration, an obvious enhancement is seen at the nominal angle. Although the RCS level at $\beta = 0°$ had been already high using the classical setup in TM configuration, however, an additional overall enhancement of the RCS profile is obtained over wide range of incidence angles using the enhanced setup.

Second, for what relates to the enhanced setup, by comparing the designs using circular and elliptical cells the results show slightly better profiles for those of elliptical cells in both TE and TM configuration which is very good news as there will be no need to utilize two independent designs.

TABLE 3.6 – List of the cells dimensions corresponding to each required phase shift using the enhanced cell setup in TE and TM configurations

Phase-shift(deg.)	45° TE (mm)	45° TM (mm)
130	1.6	1.39
65	1.7	1.7
0	1.76	1.78
-65	1.8	1.86
-130	1.91	2.0
165	1.22	0.81
100	1.66	1.6
35	1.73	1.74
-30	1.78	1.81

3.4.4 Results interpretation and discussion

Using the simulation results in this chapter along with the analytical work done in previous chapter, the possibility of interpreting the obtained RCS profiles -in terms of the range of incidence angles and the intensity level- is discussed in this section.

First, to understand why the flat RCS profile suddenly deteriorates at a certain angle, the answers can be found in the analysis done on the limiting range. The limiting

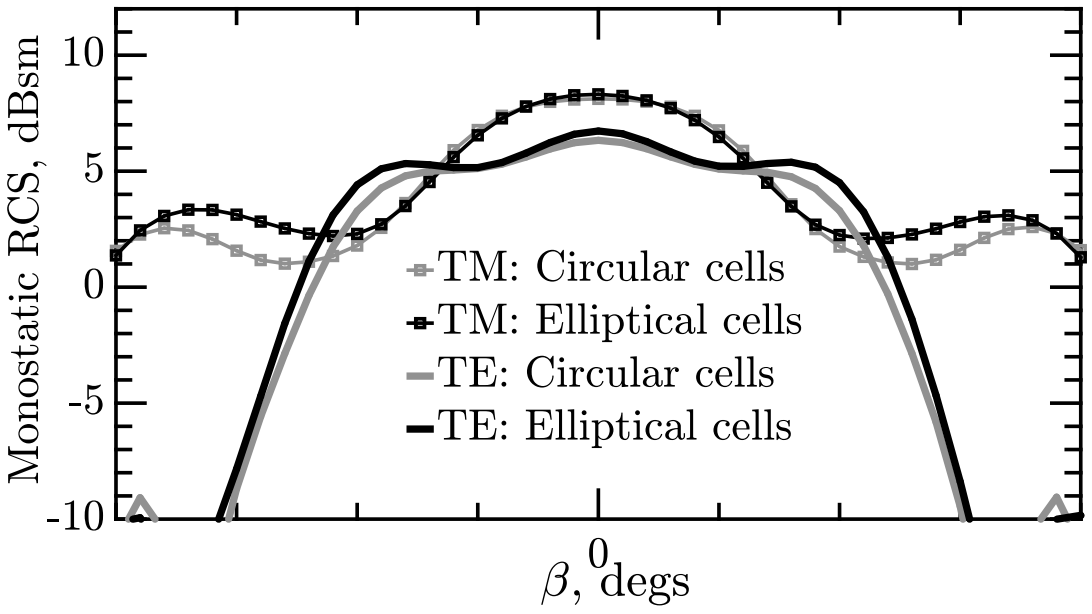

FIGURE 3.37 – Comparison of RCS profiles of retrodirective flattened dihedrals using circular and elliptical cells designed based on the enhanced Floquet setup in TE and TM configurations

range in the forward configuration of the attainable case has been already plotted in the previous chapter. For this case where $\alpha = 22.5°$, it can be found that $\beta_l(0) \approx -5°$ and $\beta_l(45) \approx 13°$. Similarly, for the reverse configuration, it can be deduced that $\beta_l(0) \approx -13°$ and $\beta_l(45) \approx 5°$. This means that theoretically at least one of the two forward and reverse configurations is operating for $-13° < \beta < 13°$. From the simulation results of a panel in the previous section, the simulated upper end of the limiting range $\beta_l(45) \approx 11°$, which is in good agreement with the theoretical predictions. For the lower end of the limiting range, things become a bit complicated. In fact, not a definite lower end could be obtained from the simulation results. However, the reflected beam intensity tends to diminish as angle β decreases beyond a value $-5°$. Following this explanation, the angle $\beta = -5°$ can be excusably assumed as the simulated $\beta_l(0)$. Based on all what has been aforementioned, the simulated limiting range can be predicted to be $-11° < \beta < 11°$ which is in excellent agreement with the simulation results of the monostatic RCS profile especially for in TE configuration.

On the other hand, the three regions discussed in previous chapter can be clearly visualized in the RCS profile in TE configuration. Again, the analytical formulations for the attainable case predict maximum performance intensity-wise for incidence angles $-5° < \beta < 5°$ for the first region due to the forward and reverse reflection mechanisms being active simultaneously. For regions two ($-11° < \beta < -5°$) and three ($5° < \beta < 11°$), either forward or reverse reflection function is active, and acceptable RCS is obtained. It can be observed that the RCS intensity peaks again at $\beta \approx 9 and - 9°$. This can be explained by the fact that the reflected beam by panel 1 possesses a directivity that intensifies as beta increases or decreases in the forward and reverse configurations respectively. Beyond those angles, the incident beams start to fall outside the limiting angles which explains the sudden drop in the RCS values afterwards.

Despite that the interpretations mentioned above are not so evident in the results of TM configurations, the RCS profile sustains high values for incidence angles around the nominal angle as compared to a dihedral corner.

Overall, the full wave simulations do validate the predictions obtained using the analytical formulations. Those findings can be seen as guidelines designers can follow in order to engineer the desired RCS using the flattened dihedral reflector.

3.5 Study on the Frequency band of operation of the reflector

The same flattened dihedral designed using elliptical cells to operate at 24 GHz is simulated for frequencies ranging beteen 23 to 26 GHz to assess the performance deterioration that might result from the additional phase law inaccuracies in both TE and TM configurations.

Fig. 3.38 shows the monostatic RCS for the TE case. It can be observed that the for the lower frequencies, a drop in the RCS occurs at $\beta = 0°$. Fig. 3.39 plots the maximum RCS value as a function of the frequency range, in other words, those corresponding to

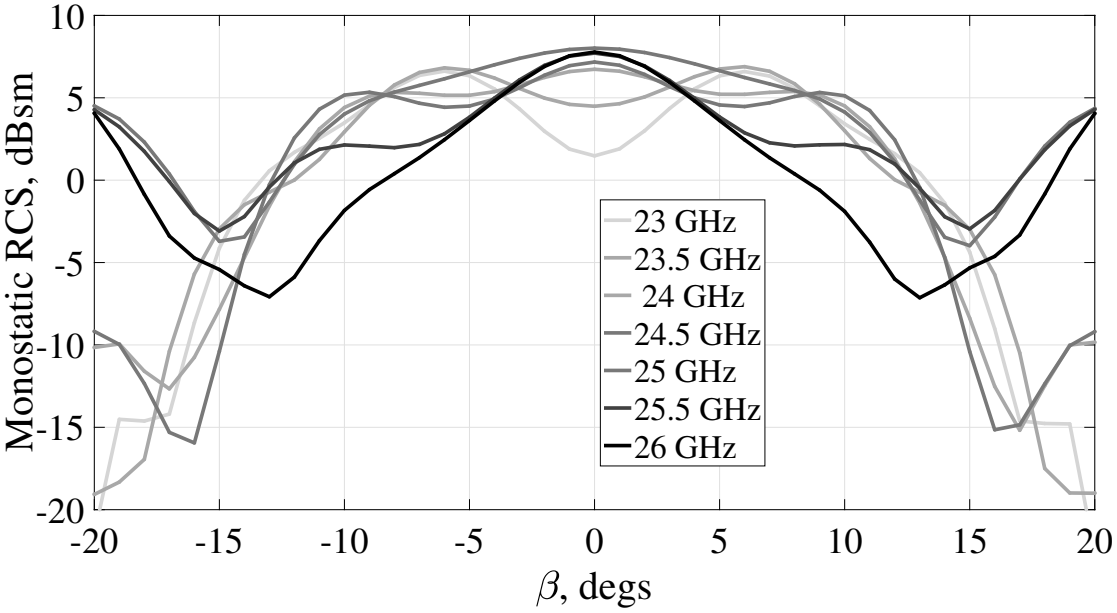

FIGURE 3.38 – RCS profile of a flattened dihedral for range of frequencies around the operating frequency in TE configuration

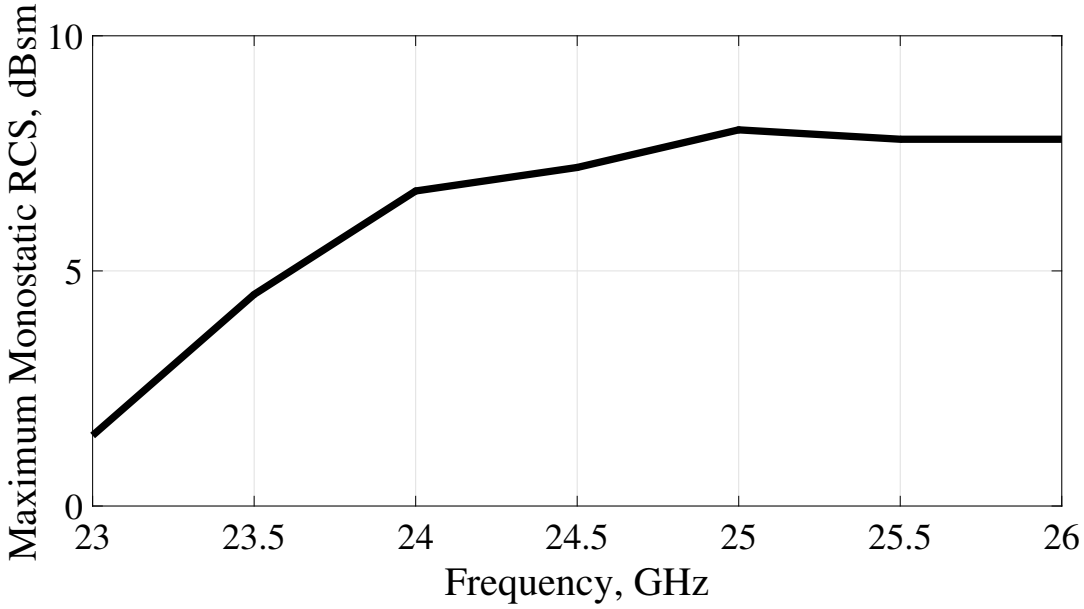

FIGURE 3.39 – RCS values corresponding to $\beta = 0°$ over the simulated range of frequencies

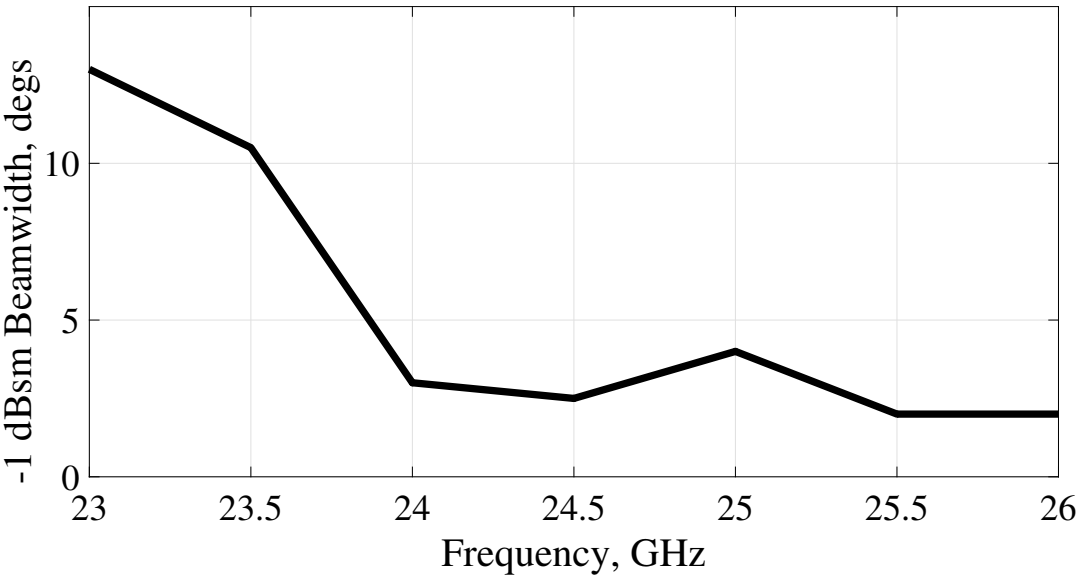

FIGURE 3.40 – The -1 dBsm beamwidth centered at the RCS value corresponding to $\beta = 0°$ over the simulated range of frequencies

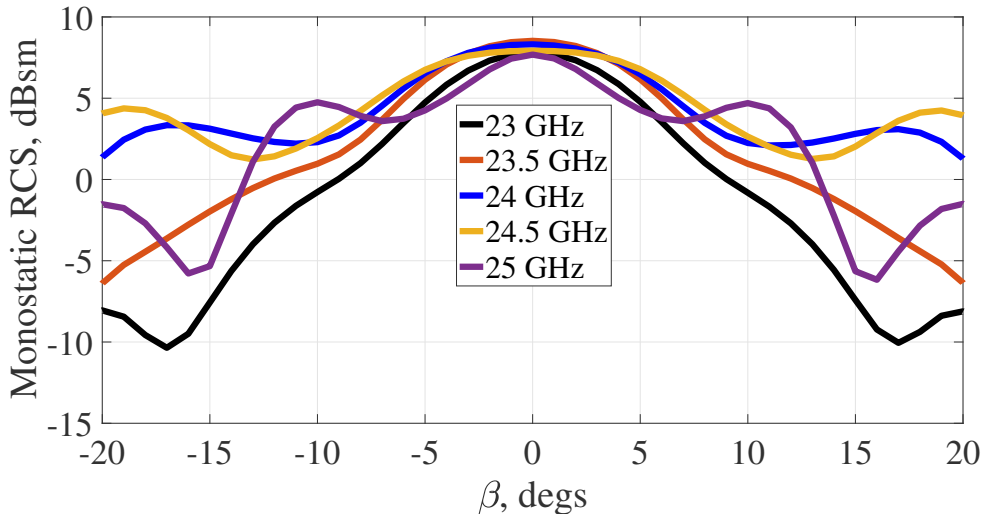

FIGURE 3.41 – RCS profile of a flattened dihedral for range of frequencies around the operating frequency in TM configuration

TABLE 3.7 – List of the cells dimensions corresponding to the required phase shifts in the case of $\alpha = 10°$ using the enhanced cell setup in TE configuration

Phase-shift(deg.)	Enhanced setup (mm)
-39	1.79
-136	2.02
127	1.59
29	1.73
-68	1.82
195	0.81
97	1.65
0	1.75
-97	1.87

beam of incidence angle $\beta = 0°$. The curve plot shows that for higher frequencies, the RCS sustains even higher RCS values compared with that at the operating frequency. This value drops down when reaching towards the lower end of the frequency range. The reflection phase profile versus frequency for a range of radii has been already included in the unit cell study. Fixing the frequency at 23 GHz, it is observed that the phase values can shift up to 50° from those at 24 GHz. Those additional errors can explain the significant deterioration in the retrodirective performace. On the other hand, despite this drop at $\beta = 0°$, the RCS for lower frequencies sustains a similar profile to that at the operating frequency. This flatness in the RCS profile gets significantly deteriorated going towards the upper end of the frequency range. To illustrate, the angle beamwidth upon which the value of RCS drops by -1 dBsm from the maximum value is plotted in Fig. 3.40 The plot clearly shows the beamwidth shrinks as the frequency increases.

Fig. 3.41 shows the RCS profiles for the TM case for frequency band ranging from 23 till 25 GHz. Here, there is no noticeable drop at $\beta = 0°$, however, the overall profile is more deteriorated for the frequencies in the lower end of the range. There is no interest in investigating higher frequencies due to the fact that there's no enhancement in the maximum RCS value despite obtaining flatter profile at 25 GHz.

3.6 Study on the flattening degree

In this section, the effect of flattening degree on the retrodirective performance is studied. In the previous chapter, it has been hypothesized that the RCS profile loses its flatness as the dihedral gets more flattened. To investigate this assumption, new flattened dihedrals based on the enhanced Floquet setup have been designed and simulated in TE configuration for $\alpha = 10°$ and 35° in order to be compared with the already obtained results of the corner dihedral and the flattened dihedral of $\alpha = 22.5°$ operating at 24 GHz. The design procedure is exactly the same as explained earlier. The nominal phase shift obtained for the case of $\alpha = 10°$ is $\gamma_0 \approx 97°$ and 29° for $\alpha = 35°$. The number of

TABLE 3.8 – List of the cells dimensions corresponding to the required phase shifts in the case of $\alpha = 35°$ using the enhanced cell setup in TE configuration

Phase-shift(deg.)	Enhanced setup (mm)
177	0.81
147	1.49
118	1.61
88	1.67
59	1.7
29	1.73
0	1.75
-29	1.78
-59	1.81

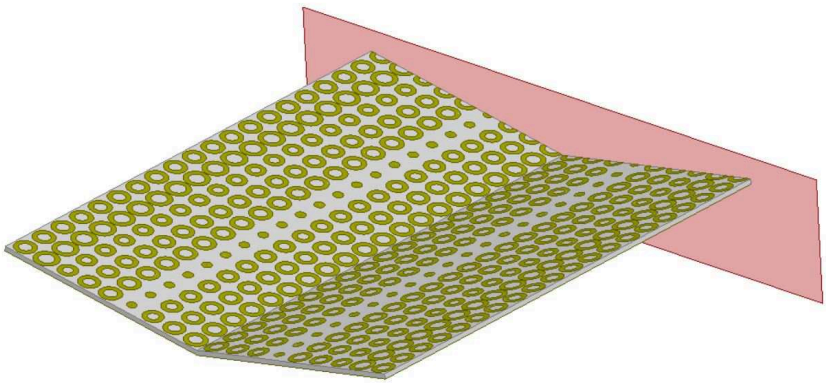

FIGURE 3.42 – Sketch of the simulated flattened dihedral of $\alpha = 10°$ being cut in the middle by an E-symmetry plane to reduce simulation time

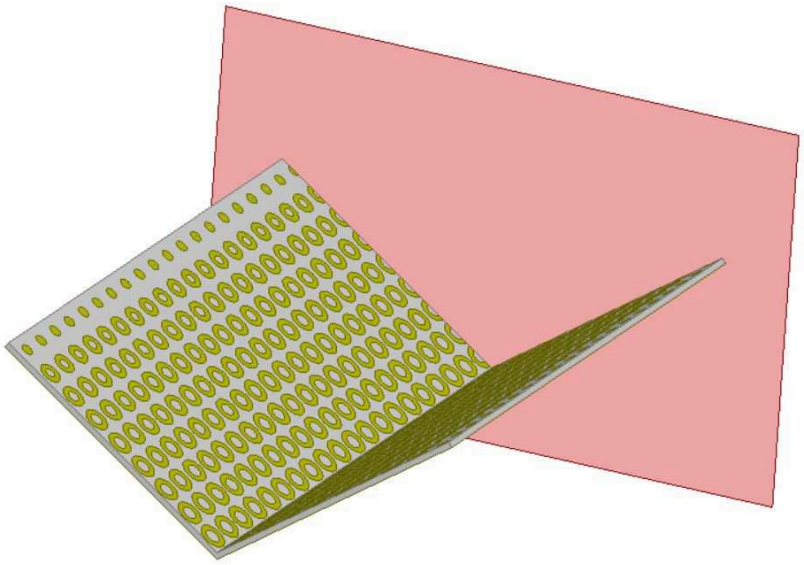

FIGURE 3.43 – Sketch of the simulated flattened dihedral of $\alpha = 35°$ being cut in the middle by an E-symmetry plane to reduce simulation time

cells in both directions is the same as that of the design of $\alpha = 22.5°$ with the inter-element spacing being fixed to $d = \lambda_0/3$. The obtained circular cells dimensions are listed in Tab. 3.7 and 3.8 for the cases $\alpha = 10°$ and $35°$ respectively. The resulting flattened dihedral designs are depicted in Fig. 3.42and . 3.43.

Before discussing the results it is important noting the effective areas of the apertures of the dihedrals of different α are not identical. Only the area of each of the panels is identical in all cases. This means that the effective area in the case of $\alpha = 10°$ is larger than that of the case of $\alpha = 35°$. To make the comparisons more reasonable, two new classical dihedral corners have been designed whose aperture effective areas match those reflectors of flattening degrees $\alpha = 10°$ and $35°$.

Fig. 3.44 shows the comparison between the obtained RCS profiles of the retrodirective flattened dihedral reflectors for $\alpha = 10°, 22.5°$ and $35°$. From the curves, it is observed that as α decreases the less flattened the RCS profile becomes. In other words, the range of incidence angles upon which the reflector operates retrodirectively shrinks as the dihedral flattens. Those results approve the theoretical predictions relating the limiting range represented by the value of β_l to the flattening degree α.

For $\alpha = 10°$, theoretically the limiting range extends from nearly $-2.5°$ to $2.5°$. From the obtained RCS profile, the drop in the RCS value starts instantaneously around angle $\beta = 0°$, which is in good agreement with the theoretical work.

While for $\alpha = 35°$, it is expected that the reflector would possess a constant RCS profile. The limiting range is expected to be from nearly $-30°$ to $30°$. Using the simulation results, the RCS profile seems to possess no steep drop over the simulated range of incidence angles. This is sufficient to say that the simulated limiting range well agrees

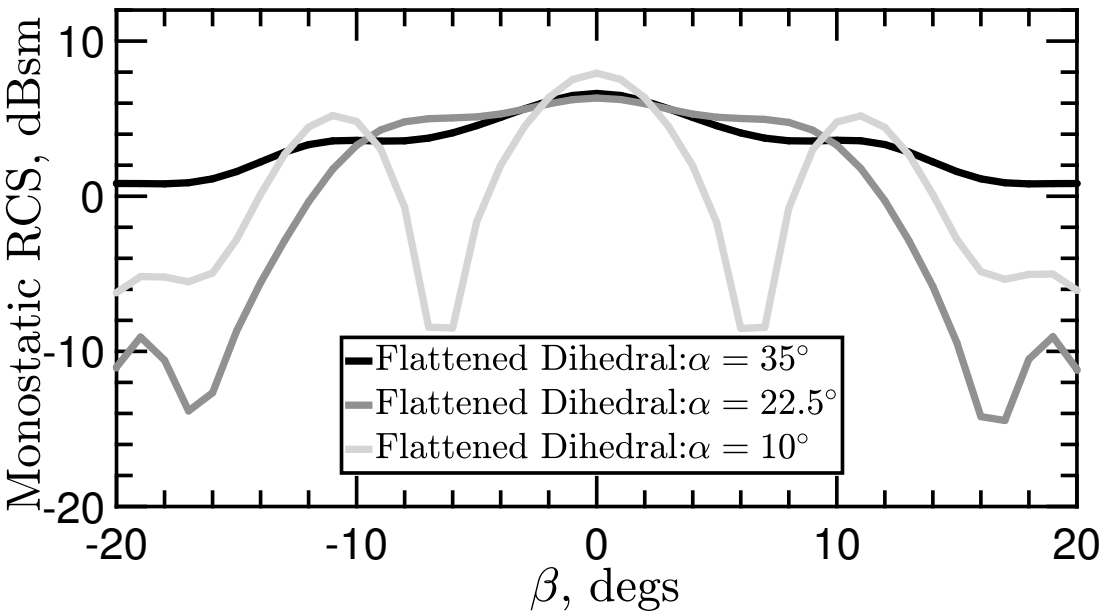

FIGURE 3.44 – RCS profiles comparison for flattened dihedrals of $\alpha = 10°, 22.5° and 35°$ in TE mode

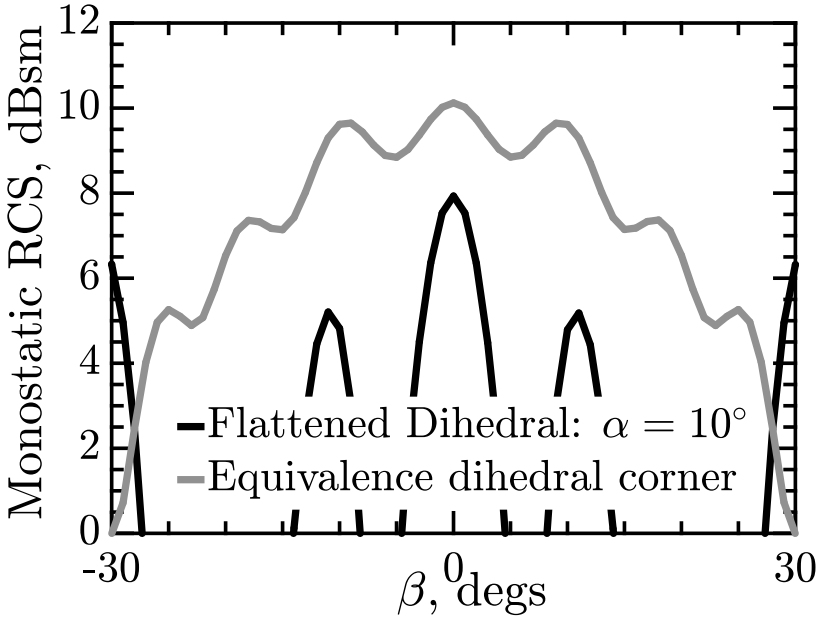

FIGURE 3.45 – RCS profiles comparison between the flattened dihedral of $\alpha = 10°$ and its equivalent dihedral corner in TE configuration

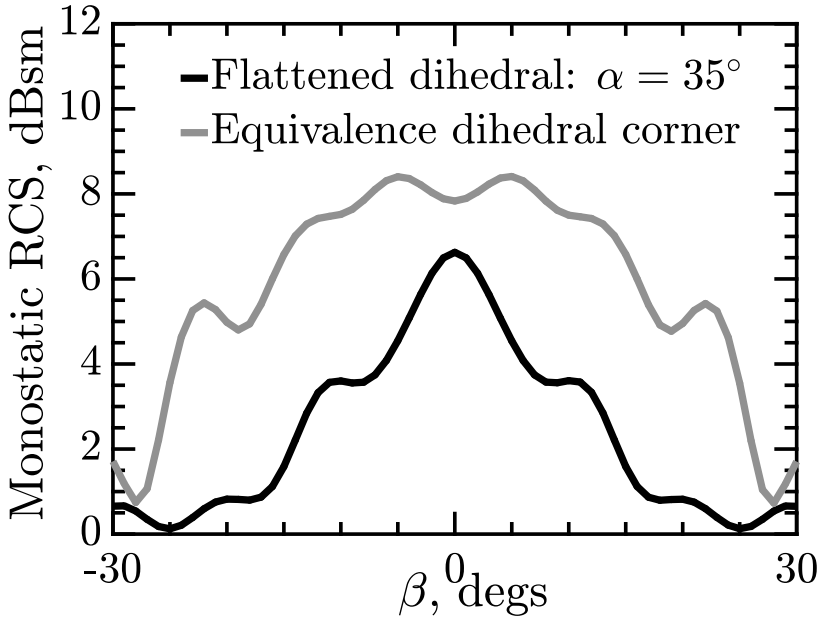

FIGURE 3.46 – RCS profiles comparison between the flattened dihedral of $\alpha = 35°$ and its equivalent dihedral corner in TE configuration

with the theoretical one.

Fig. 3.45 and 3.46 show the RCS profiles of the flattened dihedrals compared to those of the equivalent dihedral corners for $\alpha = 10°$ and $35°$ respectively. The results demonstrate the fact that the reflection intensity remains quite satisfying at the nominal incidence angle $\beta = 0°$ for whatsoever flattening degree chosen.

3.7 Study on the periodicity choice

In this section, a study is conducted to assess the dihedral performance using unit cells of different periodicities. Here, the dimensions related to the unit cell remain the same as chosen in previous sections : same substrate height and material and cell width. The corresponding dihedral reflectors are designed for a fixed flattening degree $\alpha = 22.5°$ and are set to operate in TE configuration.

Here, the comparison is performed for three periodicities $p = \lambda_0/2$, $\lambda_0/3$ and $\lambda_0/4$. Based on those unit cells, the aim is to design three distinct flattened dihedrals that operate retrodirectively in the nominal case($\beta = 0°$). The panel dimensions are set to $2\lambda_0$ by λ_0 for two reasons : the first is to reduce the simulation time and the second is to obtain equivalent panel area in the three periodicity cases.

The required phase shift to enforce the retrodirective phase law is obtained as $\gamma_0 \approx 97°$ for $p = \lambda_0/2$ and $\gamma_0 \approx 49°$ for for $p = \lambda_0/4$. Using the reflection phase profiles from the cell study, the correlated circular cells dimensions are obtained and listed in the following

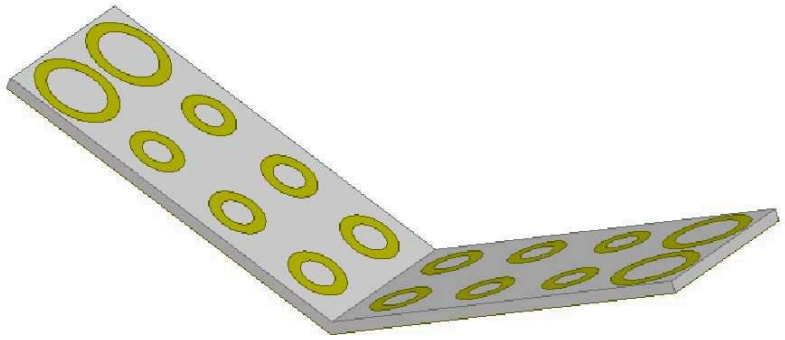

FIGURE 3.47 – Sketch of the flattened dihedral using unit cell of $p = \lambda_0/2$

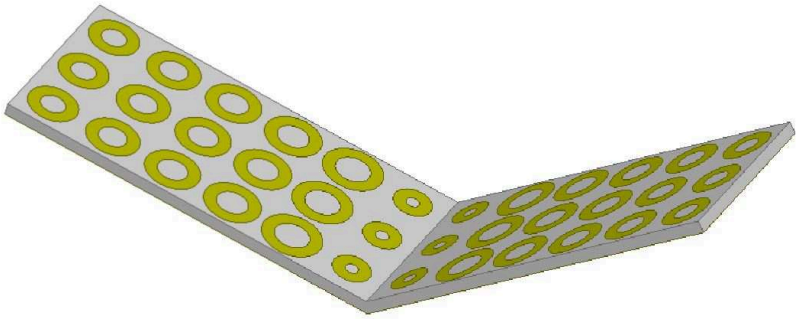

FIGURE 3.48 – Sketch of the flattened dihedral using unit cell of $p = \lambda_0/3$

Tab. 3.9, Tab. 3.10 and Tab. 3.11 for $p = \lambda_0/2, \lambda_0/3 and \lambda_0/4$ respectively.

Fig. 3.47, 3.48 and 3.49 depict the resultant flattened dihedral designs. Using similar simulation setup in the previous sections, the monostatic RCS profiles can be obtained. Fig. 3.50 shows those results for the three case studies. The first surprise is that the bare flattened dihedral possesses a better RCS at $\beta = 0°$ than that of retrodirective flattened dihedral of $p = \lambda_0/2$. This shows how severe the impact of appearance of grating lobes is on the overall performance of the reflector. As expected, the RCS profile corresponding to $p = \lambda_0/3$ possesses the best performance regarding the range of incidence angles as well as the RCS level in the nominal case. For $p = \lambda_0/4$, the drop in the RCS level at $\beta = 0°$ can be explained by the need to approximate the dimensions of two of the used cells due to the narrow phase range offered by the unit cell study. In general, those findings cement the optimality to design and fabricate a reflector using unit cell of $p = \lambda_0/3$.

3.8 Experimental Validation

In order to validate the simulation results, a prototype of a flattened dihedral using elliptical cells has been fabricated using laser technology to engrave the cells on the

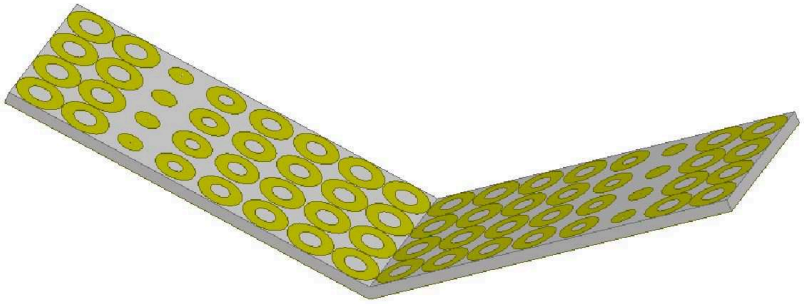

FIGURE 3.49 – Sketch of the flattened dihedral using unit cell of $p = \lambda_0/4$

TABLE 3.9 – List of the cells dimensions corresponding to the required phase shifts in the case of $p = \lambda_0/2$ using the enhanced cell setup in TE configuration

Phase-shift(deg.)	Enhanced setup (mm)
195	2.81
97	1.8
0	1.87
-97	1.94

TABLE 3.10 – List of the cells dimensions corresponding to the required phase shifts in the case of $p = \lambda_0/3$ using the enhanced cell setup in TE configurations

Phase-shift(deg.)	Enhanced setup (mm)
130	1.6
65	1.7
0	1.76
-65	1.8
-130	1.91
165	1.22

TABLE 3.11 – List of the cells dimensions corresponding to the required phase shifts in the case of $p = \lambda_0/4$ using the enhanced cell setup in TE configuration

Phase-shift(deg.)	Enhanced setup (mm)
-68	1.55
-116	1.6
195	.81
146	1.3
97	1.43
49	1.48
0	1.52
49	1.54

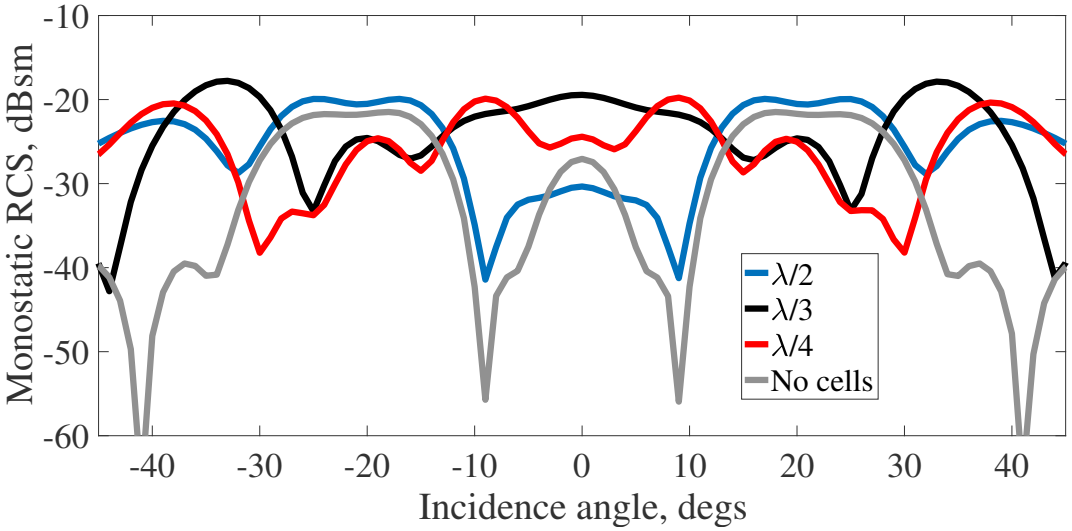

FIGURE 3.50 – RCS profiles comparison for flattened dihedrals of periodicities $p = \lambda_0/4, \lambda_0/3 and \lambda_0/2$ in TE configuration

substrate. The reflector cells are designed based on the enhanced Floquet setup and operate at 24 GHz. Fig. 3.31 shows a sketch of the proposed prototype.

The measurements were performed in the IETR facility CACENDRA (ChAracterization in CENtimeter band of RAdiating devices) chamber shown in Fig. 3.51. The measurement setup is composed of two horn antennas and a network analyzer as illustrated in Fig. 3.52. Those antennas are fixed in the farfield region of the target. While the target is placed on a rotating platform. This permits to measure the monostatic RCS for the whole range of incidence angle. Time gating method is incorporated in the measurements procedure. First, it transforms the frequency domain response to a time domain one. Then, by imposing a time gate, the multi-path interferences can be suppressed. The resultant time domain signal is re-transformed into frequency domain and processed.

To mount the retrodirective flattened dihedral on the rotating platform, a bare metallic dihedral is fabricated and attached to the platform as shown in Fig. 3.53. Then, the dihedral reflectarray panels are carefully glued to the bare dihedral as shown in Fig. 3.54.

Fig. 3.55 shows the comparison between the simulation and measurement results for the flattened dihedral using elliptical cells for TE and TM cases. The measurement results are in very good agreement with those of the simulation. In general, the measurement results validate the concept behind using a phasing mechanism based on phasing cells. And specifically, they show that the simple method of using an average-angle unit cell setup has improved its retrodirective performance.

3.9 Conclusion

In this chapter, a flattened dihedral using reflectarray approach has been designed, fabricated and tested. During this journey, the work has been divided into three main parts : unit cell study, reflectarray array construction and retrodirective flattened dihedral design based on reflectarray approach.

The unit cell study has been considered the corner stone of this work. In fact, the reflectarray design procedure relies solely on the reflection phase profiles obtained in this part. In this part, the phase profiles versus radius have been provided for different

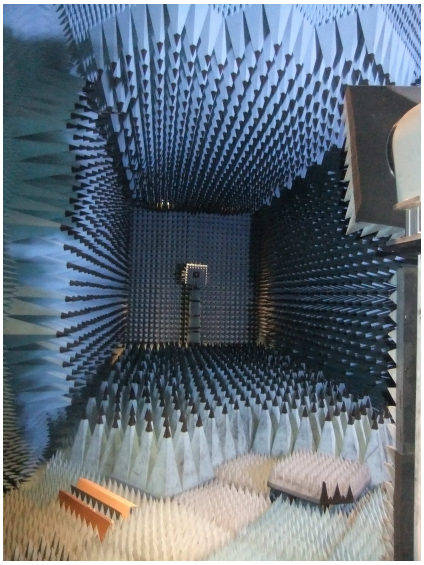

FIGURE 3.51 – The anechoic chamber in CACENDRA facility

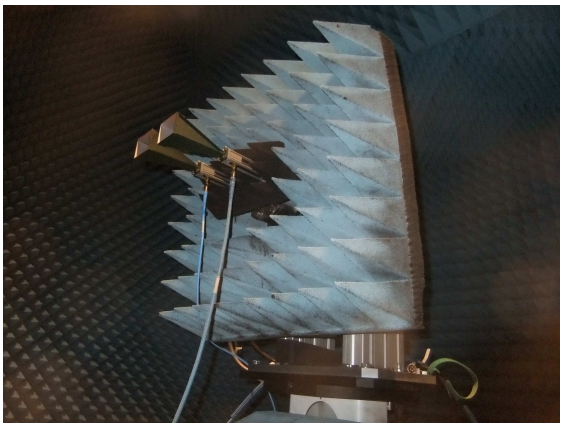

FIGURE 3.52 – The transmitting and receiving horn antennas attached to the network analyzer system

widths and periodicities. In addition, the phase profile vs frequency have been provided for various radii. Each of those profiles has been independently used as part of the studies included in the chapter.

Based on the phase profiles obtained in the unit cell study, a reflectarray and its Siamese twin were designed to obey a predefined global phase law that ensures retro-directive behavior of the whole flattened dihedral system at a specific incidence angle (nominal case here). The reflection mechanism between the panels of the dihedral was dissected by simulating a scenario of two stages. The first stage is when the beam hits the first panel and leaves it with a certain angle. In the second one, the beam reflected by the first panel intercepts the second panel and hence the beam reflected from the whole dihedral would correspond to that leaving the second panel. By simulating scenarios of incidence angles of certain significance, a primary vision has been built about the way the reflector operates over a certain range of incidence angle. The physical insight brought

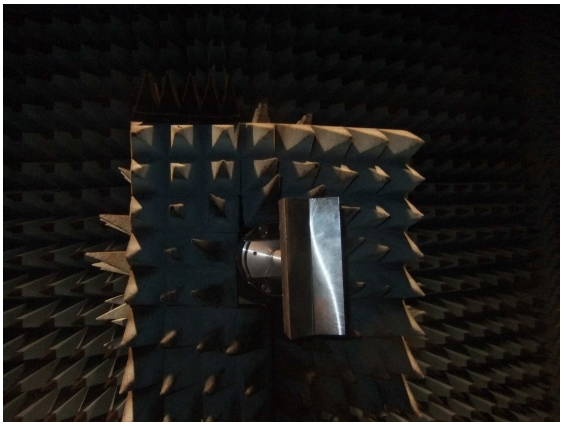

FIGURE 3.53 – The bare metallic dihedral fixed to the rotating platform

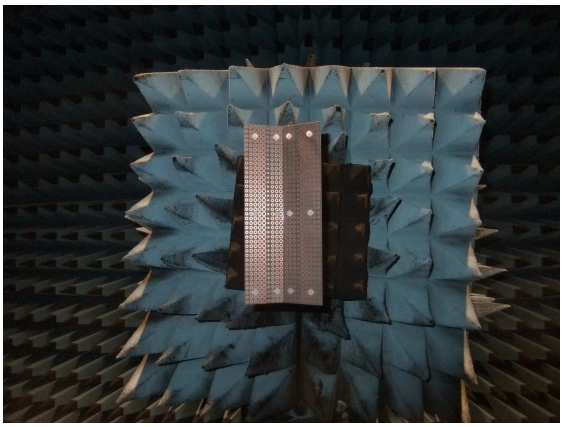

FIGURE 3.54 – The placement of the elliptical cells panels on the bare metallic dihedral which is fixed to the rotating platform

by this study will be helpful in interpreting and understanding the results obtained in the following part of work.

The purpose of the first two parts was to pave the way for the third part which is the concentration of this work. Along with a classical dihedral corner, a flattened dihedral using reflectarray approach has been designed and simulated. To assess the retrodirective performance of the reflector,the monostatic RCS profile in both TE and TM configurations has been obtained. For TM configuration, the results showed a high return in energy for the nominal angle of incidence. For TE configuration, the RCS profile sustains a constant value for a relatively wide range of incidence angles. To compensate for the significant drop in RCS level at the nominal angle of incidence with respect to the maximum attainable RCS level, a method based on average-angle Floquet cell setup has been proposed. The results did show an improvement on the performance for the nominal case in TE configuration. Finally, the theoretical work performed in the previous chapter was combined with the physical insight on the reflection mechanism to form an interpretation about the obtained monostatic RCS profile. Those interpretations served as a validation for the theoretical work done in the previous chapter.

Afterwards, necessary studies were performed to complete this study. First, the dispersive nature of the flattened dihedral was discussed. The results showed that the reflector can still operate properly for respectable range of frequencies around the frequency of operation (bandwidth percentage not less than 10%) . Then, aspect of the degree of flattening was targeted. By designing and simulating dihedrals of several flattening degrees, the impact on the retrodirective performance of the dihedral could be assessed. The simulation results were in good agreement with the theoretical work that predicted that as the dihedral gets flattened the range of incidence angles upon which the reflector

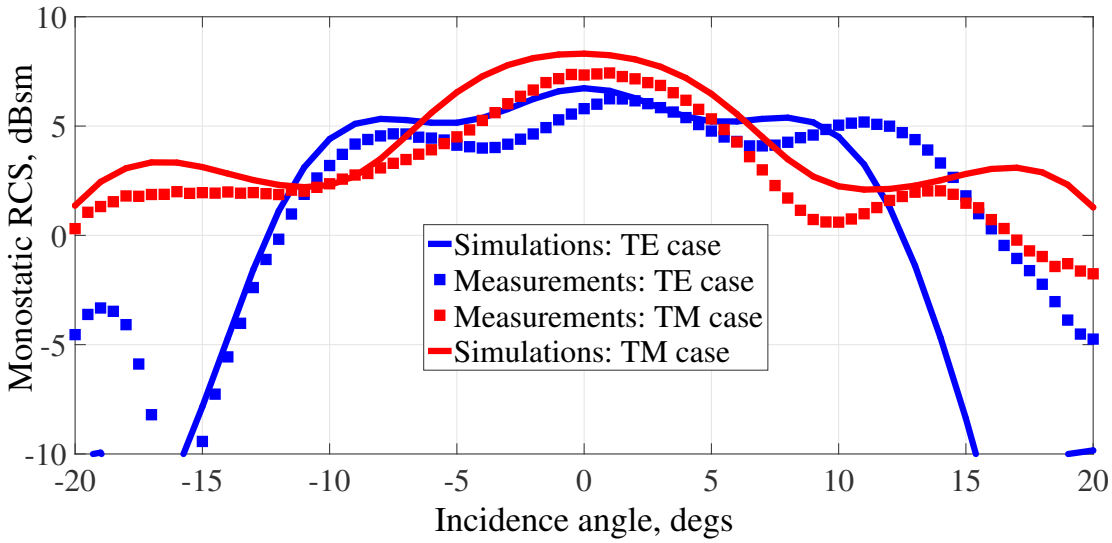

FIGURE 3.55 – Comparison between RCS profiles of the simulations and measurements of retrodirective flattened dihedral using elliptical cells in TE and TM configuration

operates shrinks significantly. Later, the choice of periodicity was put under the microscope. Simplified flattened dihedrals using unit cells of different periodicities have been designed and simulated. The results showed that the usage of a unit cell of periodicity equal to $\lambda_0/3$ offers the optimum retrodirective performance.

To validate the aspects of this study, a prototype using elliptical cells and operating at 24 GHz in TE and TM configurations simultaneously is fabricated and tested. The measurements was performed in an anechoic chamber using two horn antennas operating as a transmitter and a receiver and a Virtual Network Analyzer (VNA) to calculate the monostatic RCS of the reflector. The measurement results were in relatively good agreement with those of simulations. By that, the theoretical study backed by the performed simulations were satisfactorily validated.

Chapter 4

Backscattering enhancement of a long Multi-layered cylinder emulating a human core using dielectric coat

4.1 Introduction

The objective in the context of this work is to intensify the electromagnetic response of the bicycle-cyclist system. In the first part of the thesis, a reflector based on reflectarray approach has been proposed as a solution to enhance the backscattering of the bicycle and system in general. In the second part of this thesis, the possibility of enhancing the backscattering by a human being is investigated. As a first approximation, the human body can be modeled as multi-layered finite cylinder composed of lossy dielectric materials. Hence, the problem can be formulated as following : having a multi-layered finite cylinder of known size, length and constitutive parameters, what will be the size and the constituent of a coat that improves the backscattering of this cylinder.

This problem will be investigated on the coarse of the next two chapters. In this chapter, we only investigate the possibility of enhancing the backscattering by an infinitely long multi-layered lossy dielectric cylinder emulating a human body using a coat of dielectric medium. The next chapter tackles a more complicated problem : the possibility of enhancing the backscattering by a finite multi-layered lossy cylinder emulating a human body.

This chapter is divided into three main parts. In the first, a theoretical background is built around the problem of scattering by a long dielectric cylinder. This problem has been extensively studied throughout the past century. An exact rigorous mathematical model to the scattering problem has been given by Mie. The Mie solution is hence presented here with all the necessary related explanations. Based on this method, a solution expressed in the cylindrical coordinates is given for the problem of scattering

by a single layered dielectric cylinder illuminated normally with respect to the axis of the cylinder. An extension for this solution is provided afterwards for the problem of scattering by double-layered dielectric cylinder. Based on the scattering coefficients and using far-field approximations, it becomes possible to quantize the far-field scattering utilizing well-defined metrics as the backscattering efficiency and gain.

In the second part of this chapter, the theoretical results of the scattering by single and double-layered cylinders are presented. First, our numerical code is validated for both single and double-layered cylinders by comparing its obtained results with ones found in literature. Using this code, some examples of the scattering profiles are obtained for the single layered case. In those profiles, valuable information regarding the scattering characteristics can be extracted as a function of the material electromagnetic properties and size. Using these informations, it would be possible to form a concrete comprehension about the scattering by a dielectric cylinder. Afterwards, the results for the case of a double-layered cylinder are presented. The analysis of those results is basically classified based on the size of the cylinder and then on the nature of the material used in the cylinder coat. The effect of utilizing coats of negative permittivity on the backscattering of the cylinder is hence investigated.

The third part discusses the backscattering enhancement by a long multi-layered cylinder model emulating a human core. First, the characterization models of the dielectric properties of the human tissues are presented as given in literature. Distinctly afterwards, a part is dedicated to present the numerical model utilized to calculate the scattering coefficients for the case of a infinite multi-layered cylinder illuminated under normal incidence. Based on this model, the backscattering profile of a coated multi-layered cylinder emulating a human core is obtained as a function of the coat size and permittivity. This profile is obtained for a specific frequency upon which the electrical size of the human core is in order of wavelength. The conclusions drawn from those results will serve as guidelines in the pursuit to obtain a coat that theoretically enhances the backscattering by a real human core modeled as a finite multi-layered lossy dielectric cylinder.

4.2 Formulation of the problem of scattering by an infinitely long cylindrical body

4.2.1 Introduction

The work of this thesis is concerned with the so-called direct problem of scattering, where the objective is to determine the scattering properties of a body of known size, shape and electromagnetic properties. The aim is hence to obtain the electromagnetic field in all points of space resulting from the action of the body being illuminated by a polarized electromagnetic wave. This kind of problems has been usually studied at the optical level and has been applied in various fields like chemistry, biology, physics [82].

In this section, a conceptual idea about how the electromagnetic wave interacts with a body of given dielectric properties is first given. Then, the rigorous mathematical Mie solution is introduced. The aim of this hybrid physical-mathematical presentation here is

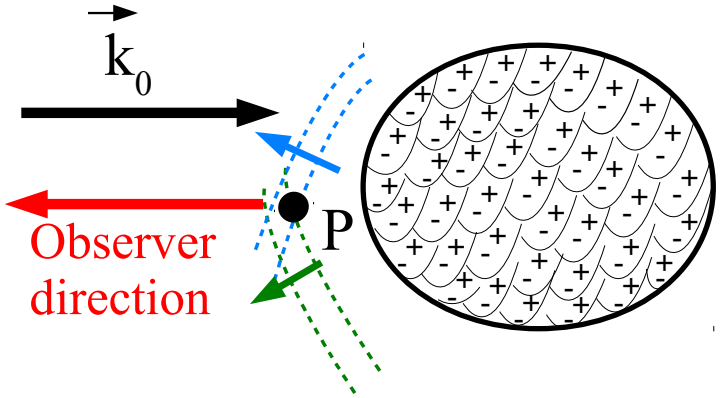

FIGURE 4.1 – Illustration of the local scattering by the dipoles conceptually forming the scatterer and the superposition of their corresponding wavelets at a certain P in the space

to create a primary taste to the problem. As a matter of fact, the scattering problem by a dielectric medium is a complex phenomenon that needs lot of effort and engagement to comprehensively understand. This can be underlined by counting the numerous attempts that had been performed by scientists to address and revisit this problem [83, 84, 85, 86].

4.2.2 Interaction of the electromagnetic radiation with the illuminated medium

4.2.2.1 Factors influencing the resultant overall scattering

In this section, a brief qualitative characterization of the wave-body interaction is offered. When a monochromatic electromagnetic wave illuminates a homogeneous dielectric medium, this induces dipole moments on the scale of the subdivisions that conceptually form the medium. Those dipoles oscillate and re-radiate local wavelets depending on the frequency of the incident beam [84]. With those wavelets being coherent, only the phase differences count in their superposition at a certain point. This superposition results in the electric and magnetic fields in all points of space.

For example, the fields at a certain point P are considered to be the actual result of the total scattering by the body in the direction of the observer. An illustration is offered in Fig. 4.1 where the observer is fixed in the opposite direction of incidence.

So, the phase relationship between the interacting scattered wavelets actually depends on several factors :
1. Electrical size,

2. Body shape,
3. Nature of the material, which solely determines the phase and amplitude of the scattered wavelet,
4. Direction of the scattered wavelet by the dipole moment.

Each one of the above factors can play a significant role in determining the phase superposition. An electrically large scatterer would mean more wavelets construction and destruction and the size variation in that region can lead to very different total scattered amplitudes at a certain fixed point. In an electrically small particle, the dipole moments will be polarized in a similar way and the overall scattering obtained will not differ significantly.

The phase relationship depends on the above mentioned factors. However, the phase and amplitude of the wavelet themselves are intrinsic properties of the bulk material nature. Those properties can be characterized by the electric permittivity which measures the resistance encountered by the electric field when propagating through the material, and the permeability which measures the degree of magnetization that the material reaches when a certain magnetic field is applied to it.

Accepting the fact that scattering phenomenon is very complex, it is safe to say that the mathematical solution and formulations can never be sufficient to fully understand the scattering profile obtained for an illuminated body of specific shape, size and material. Hence, it will be always useful to keep those factors in mind while progressing in the chapter. This will make a qualitative interpretation of the resultant scattering profiles an easier task.

4.2.2.2 Scattering, backscattering and absorption

Given in Fig. 4.2 a body of homogeneous medium being illuminated by an electromagnetic beam of wavenumber k_0. This interaction results in the scattering of the wave in all directions. However, there's one sub-phenomenon of particular significance that can be distinguished from this overall scattering : the back-scattering.

It's based on the factors mentioned earlier that a dielectric body tends to efficiently back-scatter or not. Particularly speaking, usually, spheres and cylinders of media found in nature tend to efficiently forward scatter rather than back-scatter [84]. Hence, by modeling the human core as multi-layered dielectric cylinder, this makes it quite a challenge to enhance its back-scattering especially taking into consideration the absorptive nature of the materials constituting human organs and tissues.

4.2.3 Brief overview about Mie theory

In the previous parts, the terms of scattering have been conceptually introduced. Complementing this presentation, a rigorous mathematical tool is introduced in this part that has been used for decades to describe the phenomena resulting from the wave-medium interaction.

Mie or Lorentz-Mie theory gives an exact solution for the scattering by a dielectric body. It is a rigorous solution of Maxwell's equations applied to the scattering of plane

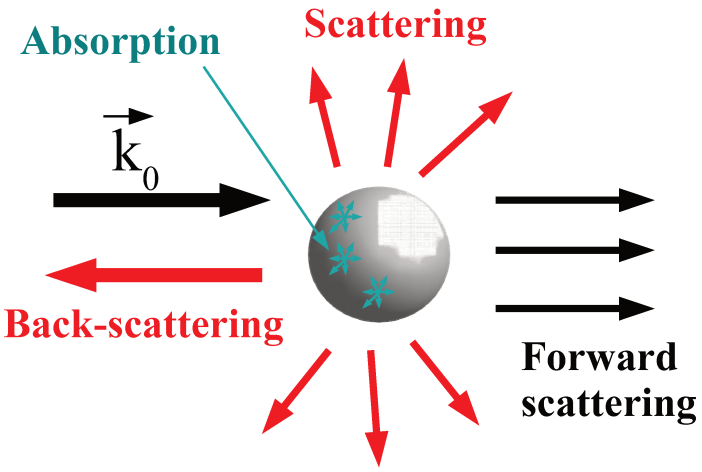

FIGURE 4.2 – Illustration of the phenomena resulting from the interaction of an incident beam of wavenumber k_0 with a dielectric body

waves mainly by a dielectric sphere [87] but also can be applied on any body shape that has a surface that corresponds to a coordinate system which is complete and in which the wave equation is separable. It was demonstrated by Gustav Mie in 1908 despite being first studied by Lorentz in 1891 [88].

The way to mathematically solve this problem is to start with the Helmholtz wave vector equation. Based on some assumptions, this vector wave equation can be reduced to a scalar one which is easier to handle. The solutions of this scalar equations are actually the generating functions of the Spherical Vector Harmonics (SVH). The incident and scattered fields can be expressed in terms of weighted vector harmonics. For the incident wave, those weights can be simply obtained by applying the orthogonality conditions of those harmonics. The weights of the scattered vector harmonics, in other words, the scattering coefficients are obtained by applying the continuity boundary conditions on the interface between the sphere and the outer medium. Those coefficients will be used to obtain the *extinction*, *scattering* and *absorption* efficiencies, gain and cross sections[87].

Similar derivation procedure can be extended to the case of a cylindrical body by expressing the fields in terms of Cylindrical Vector Harmonics and solving the cylindrical scalar equation. The following section deals with the mathematical derivation of the solution for this specific problem.

4.3 Solution of scattering by an infinitely long cylinder

4.3.1 Introduction

In this part, the derivation of the scattering expansion coefficients (a_n and b_n) resulting from the scattering by a normally illuminated infinitely long dielectric cylinder is reminded. The derivation is explicitly given for the case of a single layered cylinder. The incident, internal and scattered fields ($\mathbf{E}_{inc}, \mathbf{E}_{int}$ and $\mathbf{E}_s$ respectively) are expressed in terms of cylindrical Bessel functions weighted by the expansion coefficients. The boundary conditions are then applied on the interface separating the cylinder medium from the outer medium to obtain those coefficients.

A brief part is dedicated afterwards to discuss the extension of the derivation to a double layered cylinder. Based on these derivations, we have developed a numerical code to calculate the scattering expansion coefficients for the cases of single and double layered cylinders of arbitrary size and dielectric properties. It is important to note that the optical convention ($e^{-i\omega t}$) is used throughout this derivation to stick to the formalism used in the reference publications for the ease of comparison when validating the code.

4.3.2 Solving for a single layer cylinder

In this section, the solution for the scattering problem by an infinitely long cylinder is presented. The latter can be described in the coordinate system of the same geometry upon which the wave equation can be separable. Thus, by solving Maxwell differential equations, an exact mathematical solution based on Lorentz-Mie theory is possible.

4.3.2.1 Vector wave equation

Consider a non-dispersive, homogeneous, and isotropic medium, the $\mathbf{E}$ and $\mathbf{H}$ fields that propagate in such a medium satisfy the following wave equations :

$$\nabla^2\mathbf{E} + k^2\mathbf{E} = 0 \qquad \nabla^2\mathbf{H} + k^2\mathbf{H} = 0 \tag{4.1}$$

where $k^2 = \omega^2\epsilon\mu$ is the frequency of the incident field, ϵ and μ are the electric permittivity and the magnetic permeability of the medium respectively.

With no charge density, the electric and magnetic fields are divergence free :

$$\nabla.\mathbf{E} = 0, \qquad \nabla.\mathbf{H} = 0, \tag{4.2}$$

Considering $e^{-i\omega t}$ time harmonic fields, Faraday's and Ampère's laws can be written as following :

$$\nabla \times \mathbf{E} = i\omega\mu\mathbf{H}, \qquad \nabla \times \mathbf{H} = -i\omega\epsilon\mathbf{E} \tag{4.3}$$

where ω is the angular frequency. Now, with the vector wave equation being stated and the relations governing the fields being given, a solution for this equation is still not obvious. Hence, an intermediate stage should be established so that to simplify the

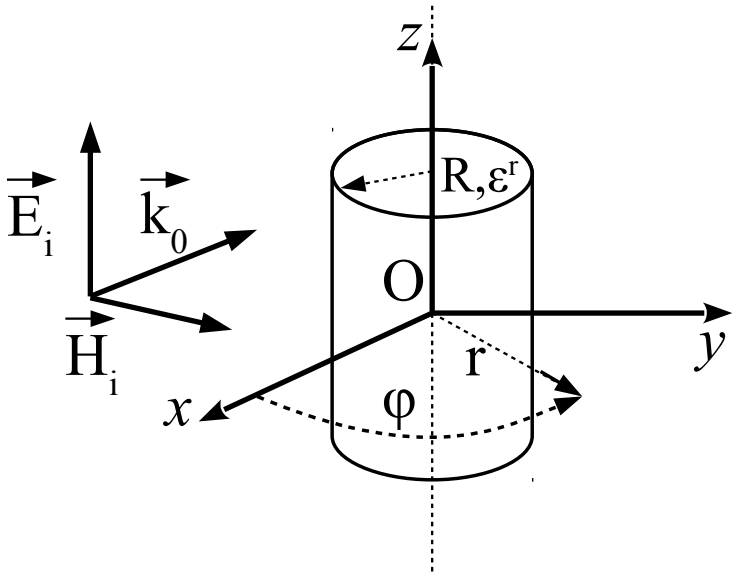

FIGURE 4.3 – A scheme showing an infinite single-layered cylinder (R, ϵ^r) whose axis is placed along the z-axis normally illuminated by a plane wave whose electric field is aligned along the axis of the cylinder

problem and to find an acceptable and expressible form of solution in different coordinate systems. For this sake, let the following function be first defined as :

$$\mathbf{M} = \nabla \times (\mathbf{c}\psi), \tag{4.4}$$

where $\mathbf{c}$ is a constant vector and ψ is a scalar function. Since $\mathbf{M}$ is written as a function of a curl, hence, it is divergence free :

$$\nabla.\mathbf{M} = 0. \tag{4.5}$$

Applying the operator$\nabla^2 + k^2$ in equation 4.4, the following equation is obtained :

$$\nabla^2\mathbf{M} + k^2\mathbf{M} = \nabla \times [\mathbf{c}(\nabla^2\psi + k^2\psi)]. \tag{4.6}$$

From equations 4.1 and 4.6, $\mathbf{M}$ verifies being a wave function if and only if ψ is the solution of the scalar equation :

$$\nabla^2\psi + k^2\psi = 0. \tag{4.7}$$

Now, $\mathbf{M}$ can be seen as an equivalent to an electric or magnetic field. Another divergence free vector can be generated in a manner to verify the vector wave equation :

$$\mathbf{N} = \frac{\nabla \times \mathbf{M}}{k} \tag{4.8}$$

or in other words,

$$\nabla \times \mathbf{M} = k\mathbf{N} \tag{4.9}$$

. Based upon this, it is sufficient now to solve the scalar equation 4.7 to solve the wave vector equation. The scalar ψ can be called the *Generating function* and $\mathbf{c}$ the *pilot vector*.

4.3.2.2 Scalar wave equation in cylindrical coordinates

In the previous part, the vector wave equation has been reduced into a scalar wave equation. In this part, the scalar wave equation is expressed in cylindrical coordinates and solutions expanded as a function of the cylindrical vector harmonics are investigated. Consider a cylindrical coordinate system (r, ϕ, and z) as shown in Fig. 4.3. For the case where the hosting medium is free space, the scalar wave equation in 4.7 can be written in cylindrical coordinates in the following form :

$$\frac{1}{r}\frac{\partial}{\partial r}(r\frac{\partial \psi}{\partial r}) + \frac{1}{r^2}\frac{\partial^2 \psi}{\partial \phi^2} + \frac{\partial^2 \psi}{\partial z^2} + k_0^2\psi = 0 \tag{4.10}$$

The solution of this equation can be written in the following form[84] :

$$\psi_n = Z_n(\rho)e^{in\phi}e^{ihz} \tag{4.11}$$

where $\rho = r\sqrt{k_0^2 - h^2}$, $Z_n(\rho)$ is a solution to the Bessel equation and h is a factor to be deduced through derivation later on.

As stated earlier, the solutions of scalar wave equation 4.10 are the functions that generate the vector harmonics that in turn are a form of the solution of the vector wave equation. By considering the pilot vector to be along the z-direction, the modal cylindrical harmonics can be deduced from equations 4.4 and 4.8 as following :

$$\mathbf{M}_n = \nabla \times (\hat{\mathbf{e}}_z\psi_n), \qquad \mathbf{N}_n = \frac{\nabla \times \mathbf{M}_n}{k_0} \tag{4.12}$$

By substituting the scalar equation solution in the above equations, the vector harmonics can be written in the following form :

$$\mathbf{M}_n = \sqrt{k_0^2 - h^2}\left(in\frac{Z_n(\rho)}{\rho}\hat{\mathbf{e}}_r - Z_n'(\rho)\hat{\mathbf{e}}_\phi\right)e^{i(n\phi+hz)}, \tag{4.13}$$

$$\mathbf{N}_n = \frac{\sqrt{k_0^2 - h^2}}{k_0}\left(ihZ_n'(\rho)\hat{\mathbf{e}}_r - hn\frac{Z_n(\rho)}{\rho}\hat{\mathbf{e}}_\phi + \sqrt{k_0^2 - h^2}Z_n(\rho)\hat{\mathbf{e}}_z\right)e^{i(n\phi+hz)}. \tag{4.14}$$

4.3.2.3 Expansion of incident field as a function of the cylindrical harmonics

Consider an infinitely long dielectric cylinder whose axis is placed along the z-axis as shown in Fig. 4.3. The cylinder material is considered non-magnetic : $\mu = \mu_0$. The cylinder is normally illuminated by an electric field parallel to the cylinder axis (transverse magnetic, TM case). The incident electric field can be now written as a weighted expansion of the cylindrical harmonics. The generating function (ψ_n) has the form of $J_n(k_0 r)e^{in\phi}$. The factor h is set here to zero due to the fact that the problem is z-invariant when the electric field is normally incident to the axis of the cylinder. Finally, the **E** can be expressed as :

$$\mathbf{E}_{inc} = \sum_{n=-\infty}^{\infty} [A_n \mathbf{M}_n^{(1)} + B_n \mathbf{N}_n^{(1)}] \tag{4.15}$$

where the (1) superscript symbolizes the vectors being generated by Bessel functions of first kind. The aim is now to find the expansion coefficients A_n and B_n. This can be obtained by applying the orthogonality property of the vectors **M** and **N** [84]. By solving the resultant integrals and using the properties of Bessel functions, the expansion coefficients in this case are finally obtained as[84] :

$$A_n = 0, \qquad B_n = \frac{E_0(-i)^n}{k_0}; \tag{4.16}$$

$$\mathbf{E}_{inc} = \sum_{n=-\infty}^{\infty} E_n \mathbf{N}_n^{(1)}, \qquad \mathbf{H}_{inc} = \frac{-ik_0}{\omega\mu_0} \sum_{n=-\infty}^{\infty} E_n \mathbf{M}_n^{(1)}, \tag{4.17}$$

where $E_n = \frac{E_0(-i)^n}{k_0}$.

Hence, the z-component of the incident electric field can be written as following :

$$\mathbf{E}_{inc}^z(k_0 r) = E_0 \sum_{n=-\infty}^{\infty} [i^n J_n(k_0 r)e^{in\phi}] \tag{4.18}$$

4.3.2.4 Obtaining the scattering coefficient

In a similar fashion, the internal and scattered fields can be expanded as a function of the cylindrical vector harmonics. For the internal fields, those harmonics are generated by the function $J_n(\sqrt{\epsilon^r}kr)e^{in\phi}$ where ϵ^r is the relative permittivity of the cylinder medium. The internal electric field is written as :

$$\mathbf{E}_{int}^z(\sqrt{\epsilon^r}k_0 r) = -E_0 \sum_{n=-\infty}^{\infty} [i^n d_n J_n(\sqrt{\epsilon^r}k_0 r)e^{in\phi}] \tag{4.19}$$

where d_n is the expansion coefficient. For the scattered fields, the cylindrical harmonics are generated by Hankel functions of the first kind : $H_n^{(1)}(\sqrt{\epsilon^r}k_0 r)e^{in\phi}$. The scattered

electric field can be formulated as :

$$\mathbf{E}_s^z(k_0 r) = -E_0 \sum_{n=-\infty}^{\infty} [i^n b_n H_n^{(1)}(k_0 r) e^{in\phi}] \tag{4.20}$$

where b_n is the scattering coefficient to be calculated. The scattered and internal magnetic fields can be obtained using the conditions of tangential continuity are applied at the interface between the cylinder and the outer medium ($r = R$) as following [86] :

$$[\mathbf{E}_{inc}(R) + \mathbf{E}_s(R) - \mathbf{E}_{int}(R)] \times \hat{\mathbf{e}}_r = 0 \tag{4.21}$$

and

$$[\mathbf{E}_{inc}(R) + \mathbf{H}_s(R) - \mathbf{H}_{int}(R)] \times \hat{\mathbf{e}}_r = 0 \tag{4.22}$$

where R is radius of the cylinder. Finally, the scattering expansion coefficient is obtained as following :

$$b_n = \frac{J_n(k_0 R\sqrt{\epsilon^r}) J_n'(k_0 R) - \sqrt{\epsilon^r} J_n'(k_0 R\sqrt{\epsilon^r}) J_n(k_0 R)}{J_n(k_0 R\sqrt{\epsilon^r}) H_n^{(1)'}(k_0 R) - \sqrt{\epsilon^r} J_n'(k_0 R\sqrt{\epsilon^r}) H_n^{(1)}(k_0 R)} \tag{4.23}$$

where J_n' and Y_n' are the derivatives pf the Bessel functions with respect to their arguments. Similar procedure can be followed to obtain the scattering expansion coefficient for the case where the E-field is perpendicular to the axis (transverse electric, TE case) of the cylinder :

$$a_n = \frac{\sqrt{\epsilon^r} J_n'(k_0 R) J_n(k_0 R\sqrt{\epsilon^r}) - J_n(k_0 R) J_n'(k_0 R)\sqrt{\epsilon^r}}{\sqrt{\epsilon^r} J_n(k_0 R\sqrt{\epsilon^r}) H_n^{(1)'}(k_0 R) - J_n'(k_0 R\sqrt{\epsilon^r}) H_n^{(1)}(k_0 R)}. \tag{4.24}$$

By obtaining those scattering coefficients, it would be possible to perform a comprehensive study on the scattering properties of cylinders of certain size and permittivity. As it will be seen later on, the scattering efficiency, gain and cross section are all metrics based on the scattering coefficients.

4.3.3 Scattering by a long double-layered dielectric cylinder

In this section, the problem of scattering by an infinitely long double-layered cylinder is introduced and solved.

Consider an infinitely long cylinder of radius R, permittivity ϵ axially placed along the z-axis. The cylinder is coated with a dielectric shell of an outer radius R_c and permittivity ϵ_c. The incident electric field propagates in the direction perpendicular to the axis of the cylinder and has a wavenumber k_0 in the outer medium, k in the core cylinder and k_c in the shell medium. The geometry is depicted in Fig. 4.4. This problem has been targeted by Kerker in his work [86]. In this case where the incident beam is perpendicular to the cylinder axis, the problem becomes very similar to that of a sphere. Hence, solutions to this problem can be obtained based on the extension of Mie theory in the cylindrical coordinates.

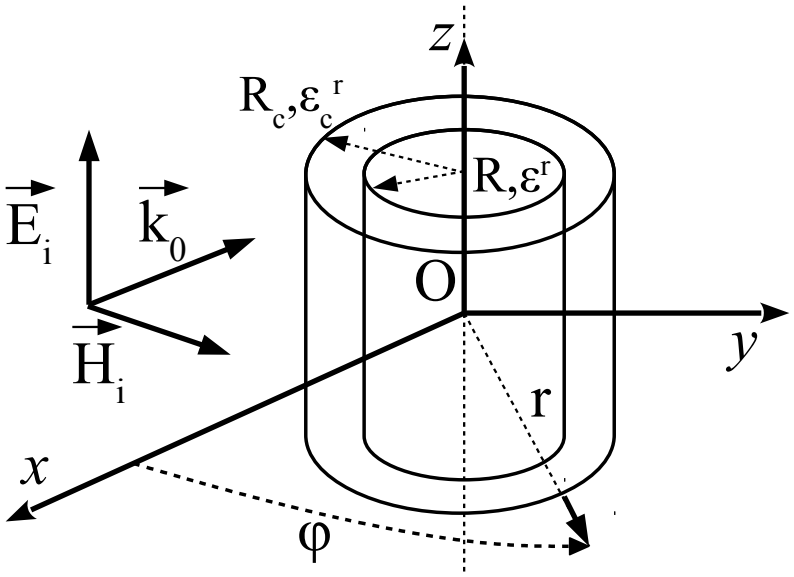

FIGURE 4.4 – A scheme showing an infinite double-layered cylinder of coat profile(R_c, ϵ_c^r) whose axis is placed along the z-axis normally illuminated by a plane wave whose electric field is aligned along the axis of the cylinder

By applying the conditions of tangential continuity at $r = R$ and $r = R_c$, set of four equations are obtained and solved. In [89, 90], the scattering coefficients have been reformed in a manner to provide with more room for physical explanations and interpretations.

The cylinder material is considered non-magnetic, in other words, $\mu_c^r = \mu^r = 1$. The relative permittivity of the coat (ϵ_c^r) can have any value.

For the case where the electric field is parallel to the cylinder axis (TM case), the corresponding scattering coefficient can be written in the following form[89] :

$$b_n = \frac{-U_n}{U_n + iV_n} \tag{4.25}$$

U_n and V_n are 4×4 determinants and can be expressed as following :

$$U_n = \begin{vmatrix} J_n(k_0 R\sqrt{\epsilon^r}) & J_n(k_0 R\sqrt{\epsilon_c^r}) & Y_n(k_0 R\epsilon_c^r) & 0 \\ \frac{\sqrt{\epsilon^r}}{\eta_0} J_n'(k_0 R\sqrt{\epsilon^r}) & \frac{\sqrt{\epsilon_c^r}}{\eta_0} J_n'(k_0 R\sqrt{\epsilon_c^r}) & \frac{\sqrt{\epsilon_c^r}}{\eta_0} Y_n'(k_0 R\sqrt{\epsilon_c^r}) & 0 \\ 0 & J_n(k_0 R_c\sqrt{\epsilon_c^r}) & Y_n(k_0 R_c\sqrt{\epsilon_c^r}) & J_n(k_0 R_c) \\ 0 & \frac{\sqrt{\epsilon_c^r}}{\eta_0} J_n'(k_0 R_c\sqrt{\epsilon_c^r}) & \frac{\sqrt{\epsilon_c^r}}{\eta_0} J_n'(k_0 R_c\sqrt{\epsilon_c^r}) & \frac{1}{\eta_0} J_n'(k_0 R_c) \end{vmatrix} \tag{4.26}$$

and

$$V_n = \begin{vmatrix} J_n(k_0R\sqrt{\epsilon^r}) & J_n(k_0R\sqrt{\epsilon_c^r}) & Y_n(k_0R\epsilon_c^r) & 0 \\ \frac{\sqrt{\epsilon^r}}{\eta_0}J_n'(k_0R\sqrt{\epsilon^r}) & \frac{\sqrt{\epsilon_c^r}}{\eta_0}J_n'(k_0R\sqrt{\epsilon_c^r}) & \frac{\sqrt{\epsilon_c^r}}{\eta_0}Y_n'(k_0R\sqrt{\epsilon_c^r}) & 0 \\ 0 & J_n(k_0R_c\sqrt{\epsilon_c^r}) & Y_n(k_0R_c\sqrt{\epsilon_c^r}) & Y_n(k_0R_c) \\ 0 & \frac{\sqrt{\epsilon_c^r}}{\eta_0}J_n'(k_0R_c\sqrt{\epsilon_c^r}) & \frac{\sqrt{\epsilon_c^r}}{\eta_0}J_n'(k_0R_c\sqrt{\epsilon_c^r}) & \frac{1}{\eta_0}Y_n'(k_0R_c) \end{vmatrix} \tag{4.27}$$

where η_0 is the free space characteristic impedance. The scattering coefficient for the case where E is perpendicular to the cylinder axis (TE case) can be obtained by electromagnetic duality, in other words, swapping ϵ_i by μ_i.

4.3.4 Analytical metrics

The scattering coefficients formulated in the previous parts are considered raw and need more processing to become more useful in performing a satisfying comprehensive study. In this part, the scattering efficiency, gain and width are defined as a function of the scattering coefficient in the TM configuration. A careful attention is given for the formulation of the backscattering efficiency as well as gain. The latter can be very useful for predicting the intensity of energy a transmitting RADAR might intercept at its receiving end.

4.3.4.1 Scattering width

For the case of a single cylinder of infinite length, a $3D$ cross section formulation is obviously not possible. Instead, the scattering width is defined as the ratio of the power density scattered per unit length to the incident field power density. The scattered power density is obtained by integrating the scattering function over the whole domain of azimuth angle. The scattering width is measured in meters and can be expressed in function of the scattering coefficient as following[85] :

$$W_{sca} = \frac{4}{k_0}\Big[|b_0|^2 + 2\sum_{n=1}^{\infty}|b_n|^2\Big]. \tag{4.28}$$

Same formulation can be used for the case of double-layered cylinder.

4.3.4.2 Scattering efficiency and gain

When comparing cylinders of different sizes, it becomes a necessity to define a universal metric that is irrelevant to the electrical size. For this sake, the scattering efficiency is defined as a dimensionless ratio of the scattering width to the electrical size(k_0R) of the cylinder as following[84] :

$$Q_{sca} = \frac{2}{k_0R}\Big[|b_0|^2 + 2\sum_{n=1}^{\infty}|b_n|^2\Big] \tag{4.29}$$

For the case of a double-layered cylinder the scattering efficiency can be obtained simply by replacing R by R_c to account for the overall diameter of the scatterer.

Scattering gain can be defined as the ratio of the scattering efficiency by a coated cylinder over the scattering efficiency of that of the core cylinder. A representation can be given as[89] :

$$G_{sca} = \frac{Q_{sca}}{Q^0_{sca}} \tag{4.30}$$

where the 0 superscript symbolizes the single layered case. Those metrics have been extensively used in literature and will be used in the next section in the purpose of validating our numerical code.

4.3.4.3 Backscattering

In RADAR applications, the far-field scattered quantity is the one that a receiver actually senses. In this part, formulations predicting the far-field backscattering are given.

In the far-field region, in other words, when kr is very large, the Hankel functions of first kind can be approximated by their asymptotic form :

$$H^{(1)}_n(k_0 r) \sim (\frac{2}{\pi k_0 r})^{1/2} e^{ik_0 r - i(2n+1)\pi/4} \tag{4.31}$$

Based on this approximation, the relation between the scattered and incident fields in the two polarization cases (TE and TM) can be described by the Amplitude Scattering Matrix as following[84] :

$$\begin{pmatrix} E_z^{\parallel s} \\ E_z^{\perp s} \end{pmatrix} = e^{i3\pi/4}\sqrt{\frac{2}{\pi k_0 r}} e^{ik_0 r} \begin{pmatrix} T_1 & 0 \\ 0 & T_2 \end{pmatrix} \begin{pmatrix} E^{\parallel 0} \\ E^{\perp 0} \end{pmatrix} \tag{4.32}$$

where

$$T_1(\Theta) = \sum_{n=-\infty}^{\infty} b_n e^{-in\Theta} = b_0 + 2\sum_{n=1}^{\infty} b_n cos(n\Theta) \tag{4.33}$$

and

$$T_2(\Theta) = \sum_{n=-\infty}^{\infty} a_n e^{-in\Theta} = a_0 + 2\sum_{n=1}^{\infty} a_n cos(n\Theta). \tag{4.34}$$

The angle Θ is equal to $\pi - \phi$ where ϕ is the azimuth angle as represented in Fig. 4.4. And the nulls in the matrix appear due to the fact that the beam hits the cylinder perpendicularly, thus, no cross polarized terms result from this scattering. Using the scattering amplitude function T_1, backscattering efficiency is formulated in a similar fashion to that of the sphere case [84]. There's no claim that the formulation methodology can be similar for both the sphere and cylinder cases due to the latter being an infinite structure. However, the concept is similar for the case where the incidence is normal to cylinder axis. The formulation can be written as following :

$$Q_{backsca} = (\frac{2}{k_0 R}|T(180°)|)^2. \tag{4.35}$$

The scattering efficiency relates to the scattering coefficients which weigh the contributing scattering modes in all directions. Here, by relating the backscattering efficiency to the scattering amplitude functions, it is possible to isolate the scattering contribution in a single direction, which is the backward direction in our case. Similar formulation can be given for the double-layered case with substituting R by R_c. The backscattering gain is defined as the ratio between the double-layered backscattering efficiency over that of the single one as following :

$$G_{backsca} = \frac{Q_{backsca}}{Q^0_{backsca}} \tag{4.36}$$

where the 0 superscript symbolizes the single layered case. Also, the backscattering width can be given as :

$$W_{backsca} = \frac{4}{k_0}(|T(180°)|)^2. \tag{4.37}$$

The scattering metrics are mainly used in this chapter for validation purposes and also to relate to the theoretical aspects of scattering that have been studied extensively in the literature. However, the context of our work does not deal with the scattering problem but rather with the far-field backscattering one. The results obtained using the backscattering formulations are the ones that will be explicitly analyzed. It is through these formulations that we aim to analytically predict and investigate the backscattering enhancement by a multi-layered model emulating a human being.

4.4 Validation of our numerical code

Before generating any results, our numerical code should be tested and validated using examples found in literature.

4.4.1 case of a single-layered cylinder

In this part, the case of a single cylinder is examined. The code generates the same results obtained by Bohren in his book[84]. In this example, a single infinite cylinder of dielectric permittivity $\epsilon^r = 2.4$ (which is equivalent to an index of refraction $m = 1.55$ as given by Bohren) is normally illuminated by a plane wave of wavelength $\lambda = 0.6328\mu m$ in the TM configuration. This non-absorbing cylinder is surrounded by medium of free space.

Bohren computed what he has defined as the scattering cross section per unit particle volume. In our work, we have not defined the scattering cross section but rather the scattering width. In fact, the metric used by Bohren is equivalent to the scattering width (W_{scat}) per unit area of the cylinder. This ratio, in cm^{-1}, can be deduced as following :

$$\frac{W_{sca}}{S} = \frac{4}{k_0(\pi R^2)}\left[|b_0|^2 + 2\sum_{n=1}^{\infty}|b_n|^2\right] \tag{4.38}$$

where S is the traversal surface of the cylinder. Fig. 4.5 shows a scan of the corresponding plot as given in [84]. The scattering metric is plotted as a function of the varying diameter where the dashed plot refers to the asymptotic limit.

Using our code, we have plotted the ratio W_{sca}/S similarly as a function of the diameter of the cylinder. Fig. 4.6 shows that the results obtained by our code are identical to those obtained by Bohren. A close look shows that the curve profiles are exactly the same where the peaks occur at the same diameter value approximately equal to $0.5\mu m$. Using this comparison, it is safe to say that our code generates results corresponding to that of the exact mathematical formulation of the problem of a single cylinder.

To elaborate more on the plotted curve, a brief analysis is offered on the profile of the obtained curve. Actually, three main observations can be identified :
1. The electrically small region where the scattering cross section increases monotonically versus the size of the diameter.
2. The interference region, which is visualized as a pattern of maxima's and minima's over the range of diameter. Those maxima's and minima's can be qualitatively interpreted due to the constructive and destructive interference between the incident beam and the scattered waves by the scatterer. Those specific positions could be analytically approximated depending on the size and properties of the particle.
3. The ripples that occur on the microscopic level, that result from the resonance phenomena that occur over the range of the size of the cylinder. The resonances are related to the "virtual modes" of the cylinder that appear when the denominator of the scattering coefficient b_n hits its minima. This interesting issue has been extensively analyzed in [84].

4.4.2 Case of a double-layered cylinder

In this part, a verification procedure of the numerical code is presented for the case of a double-layered cylinder. The choice of the example of validation should be relevant to the context of our work. For this sake, the work on cylinder cloaks in [89] is revisited and examined. In this work, the objective was to reduce the overall scattering by a dielectric cylinder utilizing a coat of negative permittivity medium.

In this part, some results of Alu work are replicated to validate the code extended to apply for the case of a double-layered cylinder. Two stages are attempted to validate the numerical code. In the first, a comparison is performed only to account for the theoretical numerical results. In the second, a specific example of a cylinder of certain material and coat is studied and accompanied with validating full wave simulations.

4.4.2.1 Numerical code validation

For the first stage, the case of an electrically small coated cylinder (outer radius is small compared to the wavelength) is considered. The cylinder is normally illuminated by a plane wave whose electric field is parallel to the axis of the cylinder (TM configuration). The electrical size of the cylinder is $k_0 R_c = 0.1$ where $R_c = 1.1R$. In this electrical regime, conditions of the overall scattering can be simply given in the form of closed loop equations as a function of the radius and the permittivity of the inner and outer

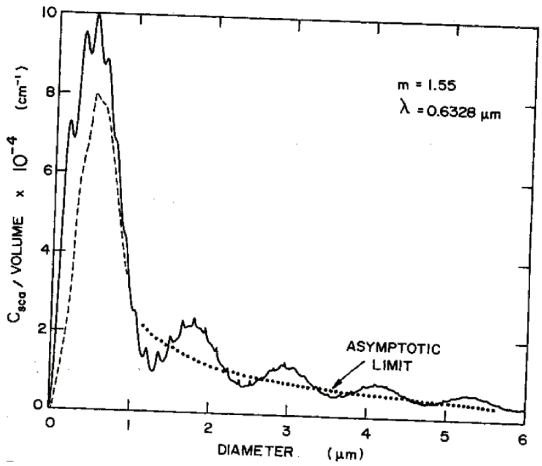

FIGURE 4.5 – Scattering cross section per unit volume versus the diameter dimensions as given in Bohren book[84]

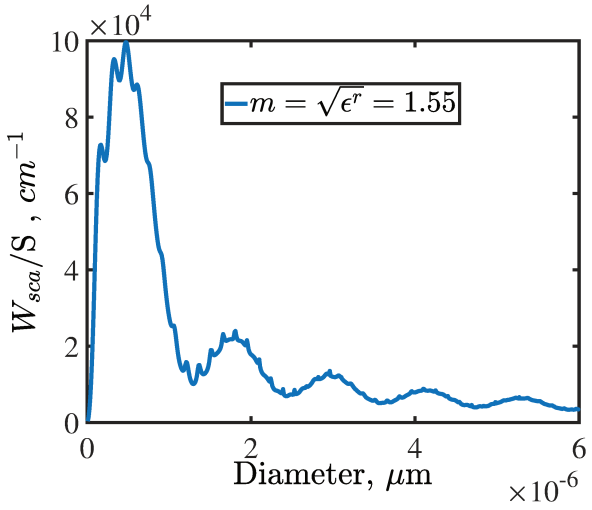

FIGURE 4.6 – Scattering width per azimuthal area of an infinite cylinder of permittivity $\epsilon = 2.4$ versus its radius

cylinders [89]. Using these equations, it is easy to obtain the coat size and permittivity that leads to the required scattering reduction. With the core permittivity being fixed to $\epsilon = 3$, it is predicted that the scattering reducing shell should have a value of $\epsilon_c^r \approx -8.5$.

Fig. 4.7 shows the profile of scattering efficiency as a function of the coat permittivity fo different incidence angles as given in Alu paper. This validation is only concerned with the normal incidence, in other words, tilt of 90° from the axis of the cylinder. Observing the referred curve, as predicted, the efficiency drops drastically at the specified permittivity (-8.5). Using our code, the same scenario is simulated. The results in Fig. 4.8 are identical to those obtained by Alu with the overall scattering reduction occuring at the same value $\epsilon_c^r \approx -8.5$.

4.4.2.2 Verification of the analytical model using full wave simulations

Those obtained results are sufficient to approve on the validation of our numerical code. However, we are not going to stop here. In the second stage of the validation, the case of a long cylinder of finite length is considered. This is logical especially knowing that our analytical work on infinite cylinders will be applied later on the case of a finite cylinder.

The verification procedure is based on full wave simulations of a finite cylinder that have been performed utilizing Ansys HFSS commercial software. In the simulation setup, the cylinder is immersed in a radiating box surrounded by perfectly matching layers that absorb the far-field scattering by the cylinder. The procedure is divided into four stages :
1. The first step is to consider a particular case of a coated cylinder. In this case, it is chosen in the electrically small regime where there are only few contributing modes, thus, making it easier to design a coat that is effective in canceling its overall scattering. Using the proposed analytical model, it is predicted that an infinite cylinder of radius $R = \lambda/8$ and permittivity $\epsilon^r = 3$ can have its scattering reduced when coated by a shell whose permittivity is $\epsilon_c^r = -13.55$ where the outer radius is $R_c = 1.1R$[89].
2. The next step is to perform full wave simulations to validate those predictions. The operation is decomposed into two stages. In the first, a finite cylinder of radius $R = \lambda/8$, length $L = \lambda = 10cm = 8R$ and permittivity $\epsilon^r = 3$ is simulated. The operating frequency $f_0 = 3$ GHz. In the second, the same cylinder gets coated with the appropriate shell to reduce its scattering. The cylinder coat dielectric dispersive properties are been modeled based on a Drude model such that the dielectric permittivity is $\epsilon = -13.55$ at f_0.
3. Now, the far-field results of the scattering by the single and coated have been obtained. It is time to process those results and make the needed comparisons. Here, the analytical and simulated overall scattering gains are plotted versus frequency. The latter is defined as the ratio of the total RCS ratio obtained for the coated cylinder to that obtained for the single cylinder. The total RCS at a single frequency is calculated by integrating the obtained simulated bi-static RCS over the whole azimuth range (2π). On the other hand, the analytical gain is obtained by integrating the same Drude model in the analytical infinite cylinder model to account for the dispersive nature of the coat. Fig. 4.9 plots the analytical overall scattering gain as compared to the simulated one on a linear scale

similar to what have been produced in [89]. The results show that the simulated and analytical scattering gains comply with each other. The simulated gain curve shows a significant reduction at the frequency of design 3 GHz. Also, the curve profile is similar to that of the analytical infinite cylinder.
4. In the final stage, the total RCS is plotted versus frequency for the single and coated cylinders. The RCS values have been normalized to the highest value obtained in the frequency range. Fig. 4.10 shows the plot of the dimensionless normalized RCS versus frequency. The results again demonstrate the fact that coating the cylinder with a shell of a negative dielectric as predicted using the analytical model has indeed reduced its overall scattering.

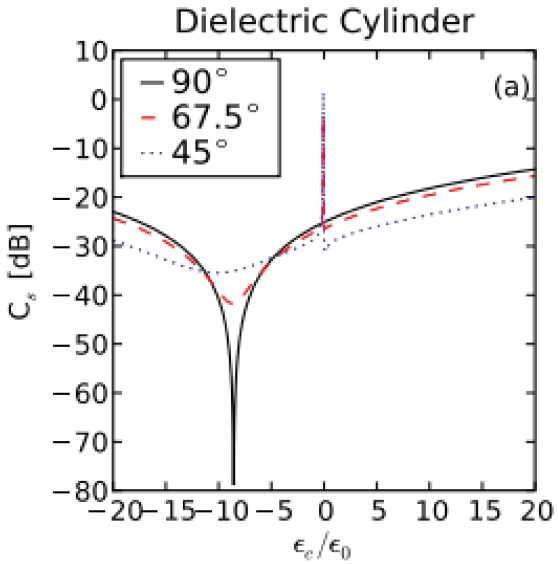

FIGURE 4.7 – Scattering efficiency of coated cylinder of permittivity $\epsilon^r = 3$ and electrical size $k_0 R_c = 0.1$ where $R_c = 1.1R$ as given in Alu work [89] as a function of the shell permittivity

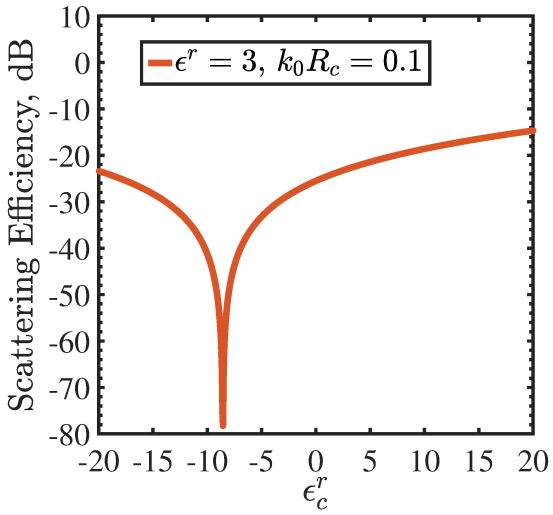

FIGURE 4.8 – Scattering efficiency of a coated cylinder of permittivity $\epsilon^r = 3$ and electrical size $k_0 R_c = 0.1$ and $R_c = 1.1R$ as a function of the shell permittivity

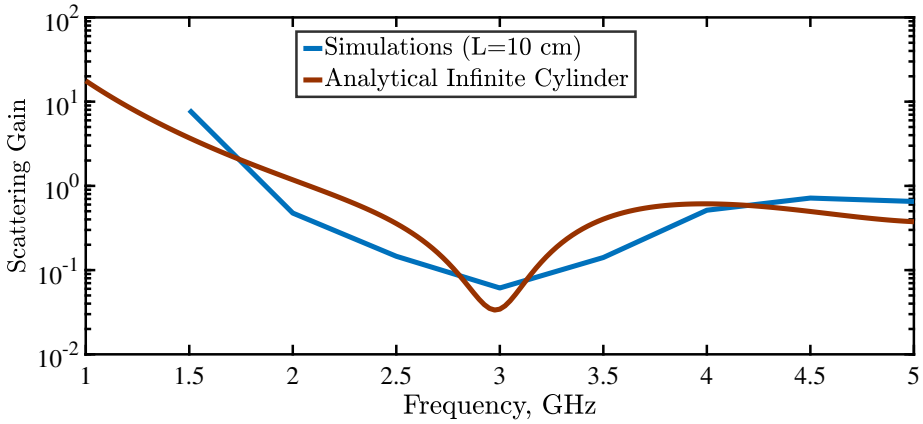

FIGURE 4.9 – Comparison between the analytical and simulated scattering gain corresponding to a finite cylinder of length of 10 cm

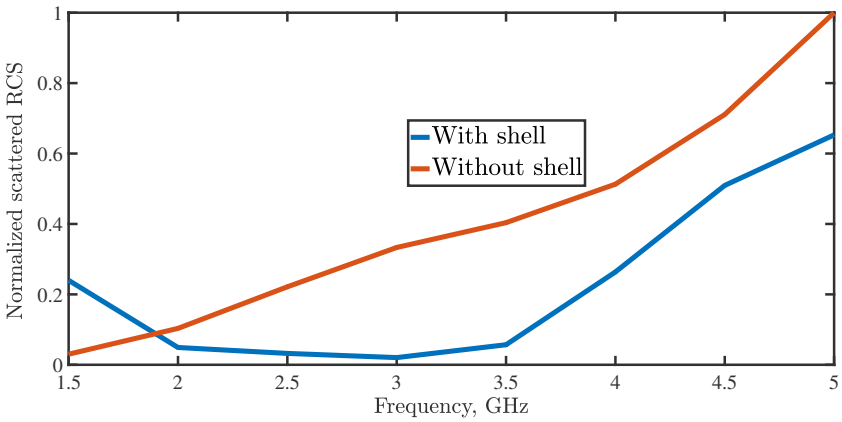

FIGURE 4.10 – Comparison between the normalized total RCS for the single and coated dielectric cylinders ($L = 10$ cm) versus the frequency range centered at the design frequency 3 GHz

Finally, by reproducing similar numerical and full wave simulation results to those found in literature, it is safe to say that our numerical code is valid for the cases of single and coated cylinders, and hence can be relied on for producing further results that serve the analysis to follow in this chapter.

4.5 Numerical results for the backscattering by a double-layered cylinder

4.5.1 Introduction

In the literature, few works have dealt with applications relating to the backscattering by a dielectric cylinder. The main works actually are concentrated in the domain of modeling vegetation components for remote sensing applications. Actually, for certain range of frequencies, a tree can be approximated to an infinite lossy dielectric cylinder[91]. In this work, some numerical results of the backscattering width (W_{sca}) have been presented. In our work, the aim is not to obtain the backscattering by single cylinders independently, hence using the metric backscattering width is not the optimal choice. But rather, the aim is to measure how a coat of certain dielectric material might tailor the backscattering of a single cylinder, specifically, enhancement-wise. For this sake, the numerical results in this section are given in the form of backscattering efficiency and gain as defined in section 4.3.4.

Remarkably, no work has been done before on enhancing the backscattering by a dielectric cylinder. But rather, the works targeted enhancing or reducing the backscattering by conducting cylinders [92]. One of the suggested approaches has been the use of a coat of negative permittivity or permeability or both to tailor the scattering of the cylinder[93], [94]. Also, there have been interest in numerically modeling the scattering by metamaterial cylinders to assess its scattering characteristics [95], [96].

On the same track, the interest in our work is in using single negative permittivity materials to assess their performance in enhancing the backscattering of dielectric cylinders. The concept of plasmonic cloaking has been already utilized in the aim to reduce of the scattering by a dielectric cylinder[97]. The concept is based on pairing double positive material with a single negative coat to cancel the scattering by an electrically small cylinder.

Our methodology is somehow similar, however, there are fundamental differences in the manner it is implemented as compared to the work in [97]. Our final objective is to enhance the backscattering by a multi-layered cylinder (not a single cylinder) as you'll see in the next section. Also, the electrical size in our case is in the moderate Mie region (cylinder radius comparable to wavelength) which is more complicated than the problem of an electrically small cylinder, where the fundamental mode is the main contributor in the overall scattering. Add to that the fact that dielectric properties of the human tissue layers possess high permittivity values and losses as compared to the simple dielectric examples given in [89].

Throughout the study in this section, the electrical size of the radius of the cylinder is defined as $R = 0.5\lambda_0$. The backscattering efficiency and gain are calculated in dB. A gain of null dB means the coat has introduced neither enhancement nor reduction to the backscattering of the cylinder. Positive gain signifies backscattering enhancement while negative gain signifies backscattering reduction.

The study is decomposed in a manner that the dielectric properties of the core cylin-

der progressively complicates, in other words, the permittivity, in the beginning of the study, is assigned low values with no losses ; at the end of the study, is assigned a high permittivity value with high losses too. This progression will help tackle the problem in an easier manner before reaching the problem of multi-layered cylinder emulating a human core, where at the operation frequency the tissue dielectric properties are of high permittivity and losses. Fig. 4.11 gives the intended plan of the progressive study.

From the results obtained in this section, it will be possible to draw important conclusions on the possibility of enhancing the backscattering by a cylinder using single negative coats as compared to double positive coats. And knowing that the human core layers are composed of media of high permittivity and losses, the backscattering obtained for the scenario of single-layered cylinder of such complex medium will give a glimpse about the possible coat permittivity ;size profile that might optimally enhance the backscattering by a cylinder model emulating a human core.

4.5.2 Numerical results for a core cylinder of lossless medium and low permittivity

4.5.2.1 Backscattering efficiency of single cylinder

As given in part 4.3.4, backscattering efficiency is defined as :

$$Q_{backsca} = (\frac{2}{k_0 R}|T(180°)|)^2. \tag{4.39}$$

Fig. 4.12 plots the backscattering efficiency for permittivity values $\epsilon^r = 3, 5$ and 10 as a function of the electrical size of the cylinder ($a = R/\lambda_0$). The curves show that the backscattering efficiency peaks in the electrically small regime with higher values obtained for higher values of permittivity. The profile is of ripple nature. This rippling behavior gets more intense with the electrical size of the cylinder. This shows that the backscattering efficiency is dependent on the cylinder size even in the electrically large region.

4.5.2.2 Backscattering gain results for coated cylinders

Coat permittivity : positive versus negative ϵ_c^r In this part, the core cylinder considered is of permittivity $\epsilon^r = 3$ and size $a = 0.5$. The possibility of enhancing the backscattering of this cylinder using coats of positive and negative ϵ_c^r is studied. Before, as a reminder, the backscattering gain is defined in part 4.3.4 as following :

$$G_{backsca} = \frac{Q_{backsca}}{Q^0_{backsca}} \tag{4.40}$$

where $Q_{backsca}$ is the backscattering efficiency of the coated cylinder and $Q^0_{backsca}$ is the backscattering efficiency of the single cylinder. Fig. 4.13 plots the backscattering gain versus a_c for different values of positive permittivity. The curves show that the backscattering can be enhanced using materials of permittivity as low as $\epsilon_c^r = 2$. However,

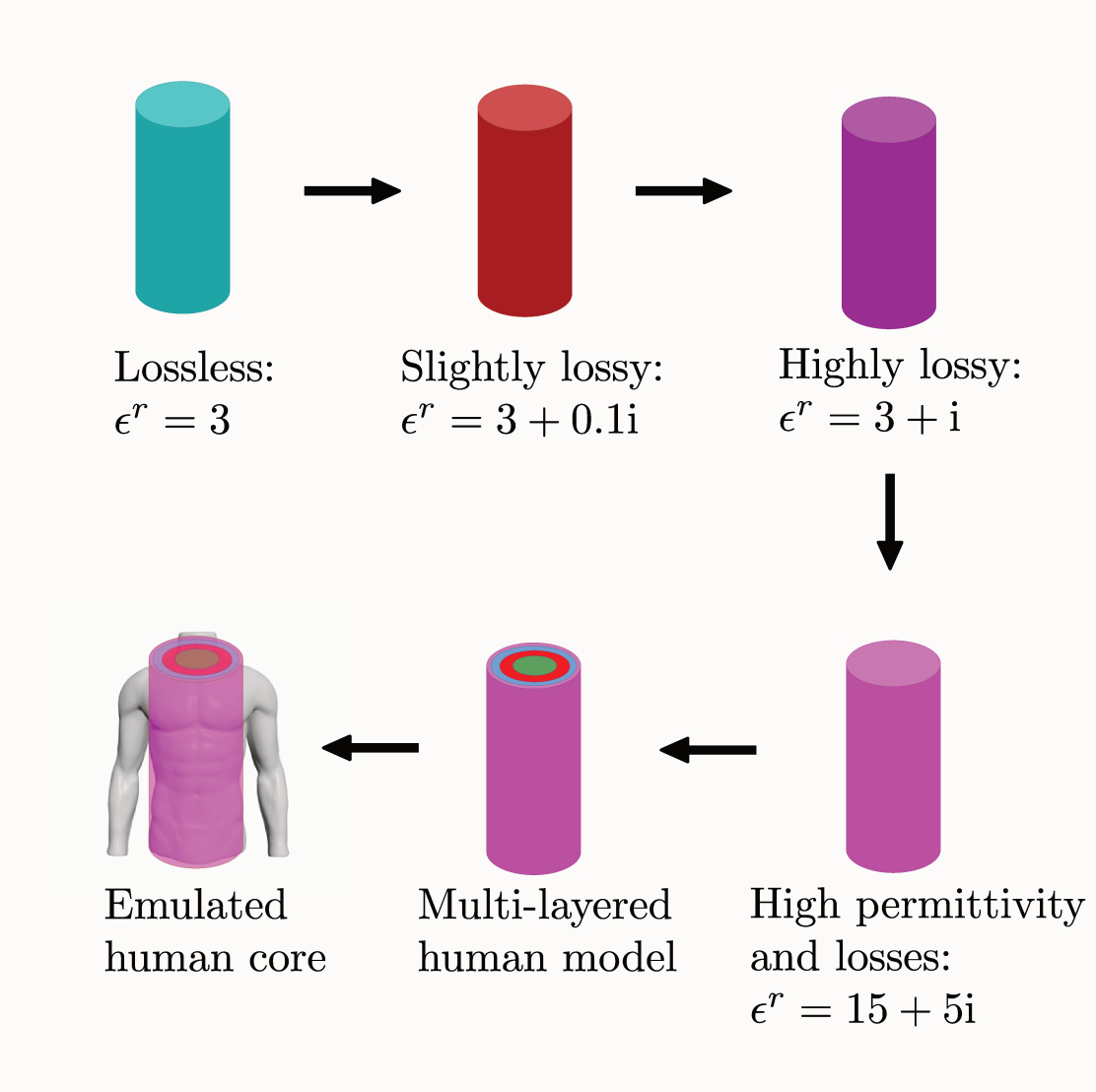

FIGURE 4.11 – Plan of the progressive study on the cylinder dielectric properties

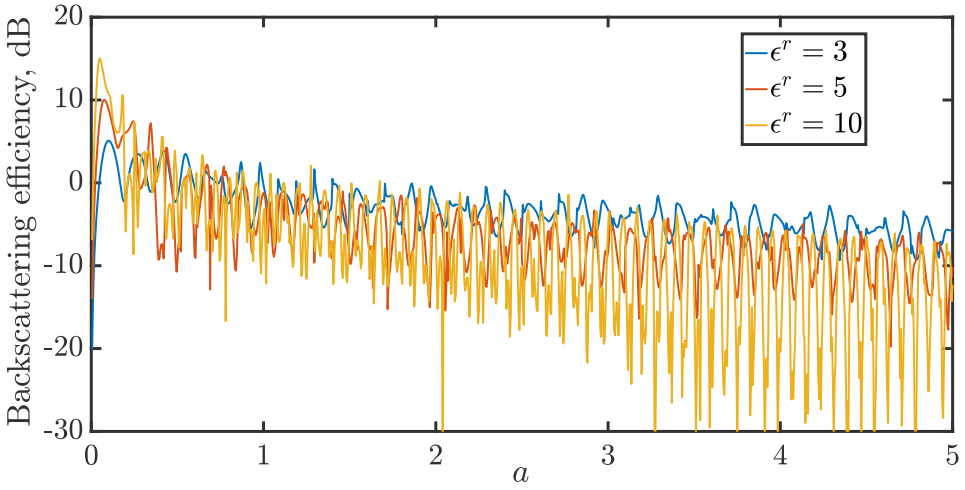

FIGURE 4.12 – Backscattering efficiency (in dB) for cylinders of positive permittivity values $\epsilon^r = 3, 5$ and 10 as a function of the radius size a

what's intended is to achieve this feat using thin coats, and this can only be achieved using coats of higher ϵ_c^r. USing a coat of $\epsilon_c^r = 20$, it is possible to obtain 6.7 dB gain for a coat of thickness $(0.505 - 0.5)\lambda_0 = 0.005\lambda_0$. Similar results are obtained for negative coats. Fig. 4.14 plots the backscattering gain versus coat radius a_c for several values of negative permittivity. It is shown that a gain of 6.6 dB can be obtained using a coat of $\epsilon_c^r = -20$ and thickness $(0.51 - 0.5)\lambda_0 = 0.01\lambda_0$. The significant difference between the profiles of the negative and positive coats is the fact that the negative coats profiles are smoother and steadier with respect to the electrical size of the cylinder.

The backscattering gain profiles actually show similarities to the profiles of backscattering efficiency of single cylinders having same negative permittivity values (ϵ^r) as those of the coat. Fig. 4.15 plots the corresponding curves versus the cylinder size a.

Using Fig. 4.15 and Fig. 4.14, it can be observed that the gain and efficiency profiles for negative permittivity case are similar, starting with a peak and then decreasing smoothly as the electrical size of the cylinder or coat increases. The main difference is in the location of the peak value. As the coat negativity decreases, it seems to get relaxed with the respect to the coat thickness. Also, it is noticeable that for coats of $\epsilon_c^r = -5, -10$ and -20, nearly identical peak values are obtained.

Contour plot As an extension for the previous part, the contour plot of the backscattering gain is plotted for each coat profile combination of sizes and permittivity values ranging between $0.5 > a_c > 0.7$ and $-20 > \epsilon_c^r > 20$ respectively. The plot shows the regions upon which significant backscattering gain can be obtained with reddish color.

A gain of 3 dB can be obtained using a shell as thin as $(0.505 - 0.5)\lambda_0 = 0.005\lambda_0$ for a coat of negative permittivity $\epsilon_c^r = -20$. On the other end, a positive coat of thickness $0.002\lambda_0$ is sufficient to obtain the 3 dB gain at $\epsilon_c^r = 20$.

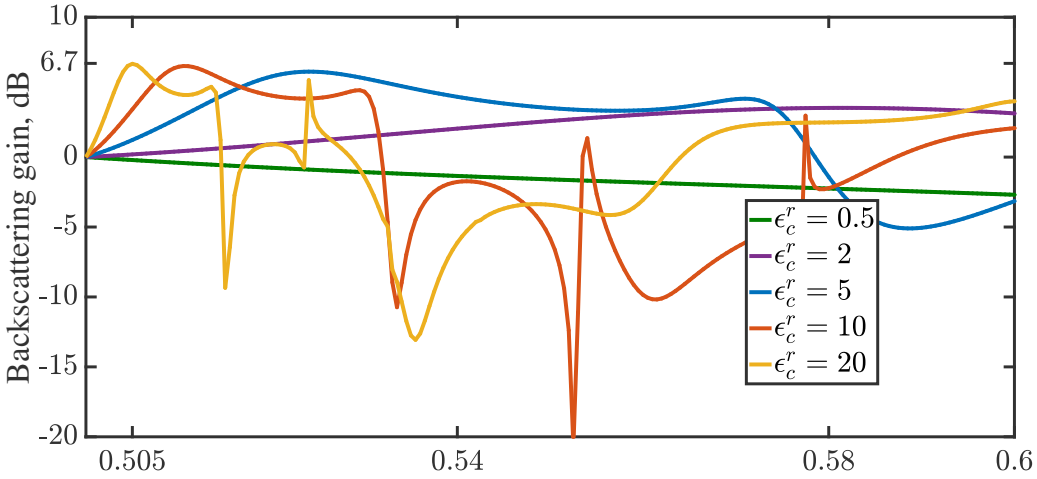

FIGURE 4.13 – Backscattering gain (in dB) of cylinder of permittivity $\epsilon^r = 3$ and electrical size $a = 0.5$ versus coat radius a_c for different values of $\epsilon_c^r = 0.5, 2, 5, 10$ and 20

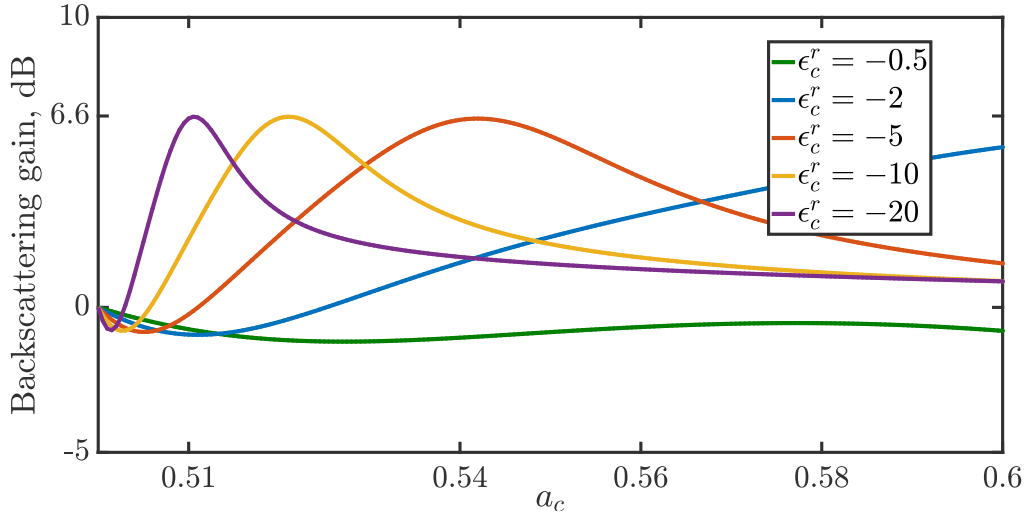

FIGURE 4.14 – Backscattering gain (in dB) of cylinder of permittivity $\epsilon^r = 3$ and electrical size $a = 0.5$ versus coat radius a_c for different values of $\epsilon_c^r = -0.5, -2, -5, -10$ and -20

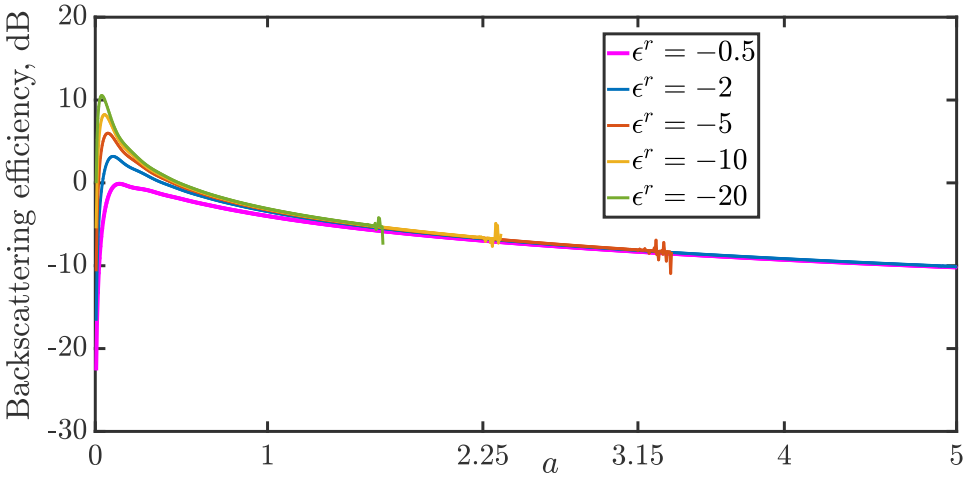

FIGURE 4.15 – Backscattering efficiency (in dB) for cylinders of negative permittivity values $\epsilon^r = -0.5, -2, -5, -10$ and -20 as a function of the radius size a

What's better demonstrated in this part is the fact that such enhancement can be obtained for a wide range of size ; permittivity coat profiles. This means respectable tolerances regarding the material synthesis and fabrication in both size and permittivity senses.

4.5.3 Numerical results for a core cylinder of lossy medium and low permittivity

4.5.3.1 Backscattering efficiency for a single cylinder

In this part, losses are brought into the picture. Fig. 4.17 shows the backscattering efficiency of a cylinder of permittivity values : $\epsilon^r = 3$, $\epsilon^r = 3 + 0.1\mathrm{i}$ and $\epsilon^r = 3 + \mathrm{i}$. The results show that the efficiency peak occur at the same $a \approx 0.1$. The value of this peak decreases upon adding losses with approximately -2 dB reduction for the case of $\epsilon^r = 3 + \mathrm{i}$. Concerning the curve profile, the ripples maximums for all three cases occur at similar positions. The period of the ripples is consistently at $0.15\lambda_0$ with $\pm 0.01\lambda_0$ shift over the range of the electrical size. The asymptotic limit corresponding to that of a lossless material actually seems to diverge from those of lossy materials. For the case of $\epsilon^r = 3 + \mathrm{i}$, the backscattering curve gets gradually damped and completely loses its rippling behavior at $a \approx 1$.

4.5.3.2 Backscattering gain for a coated cylinder

In this part, the cylinder electrical size is fixed to $a = 0.5$. Fig. 4.18 shows the backscattering gain contour plot versus the coat profile, $a_c; \epsilon_c^r$, for the case where the core permittivity is $\epsilon^r = 3 + 0.1\mathrm{i}$. The plot shows similar results for those obtained for

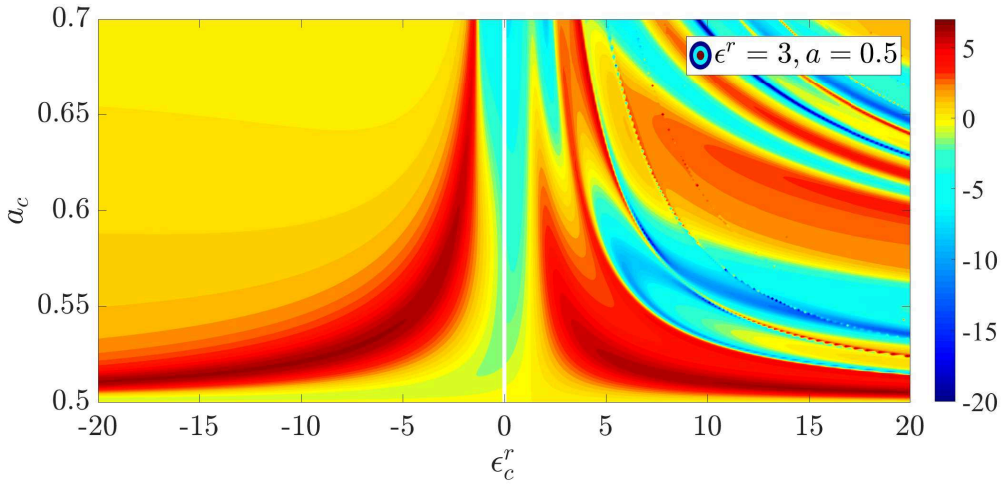

FIGURE 4.16 – Contour plot of the backscattering gain (in dB) of a double-layered cylinder of a core profile($\epsilon^r = 3, a = 0.5$) versus the outer coat radius a_c and coat permittivity ϵ_c^r

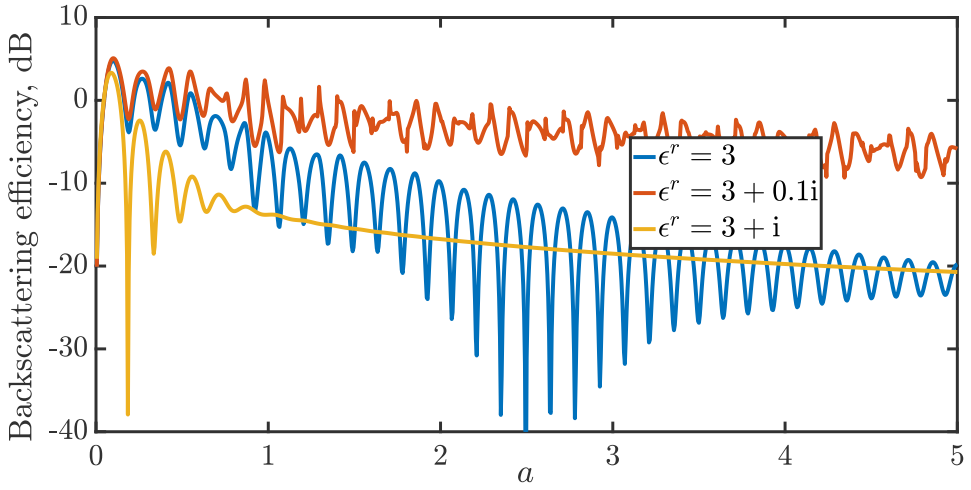

FIGURE 4.17 – Backscattering efficiency (in dB) for lossy dielectric cylinders of permittivity values $\epsilon^r = 3 + 0.1\mathrm{i}$ and $\epsilon^r = 3 + \mathrm{i}$ as a function of the radius size a

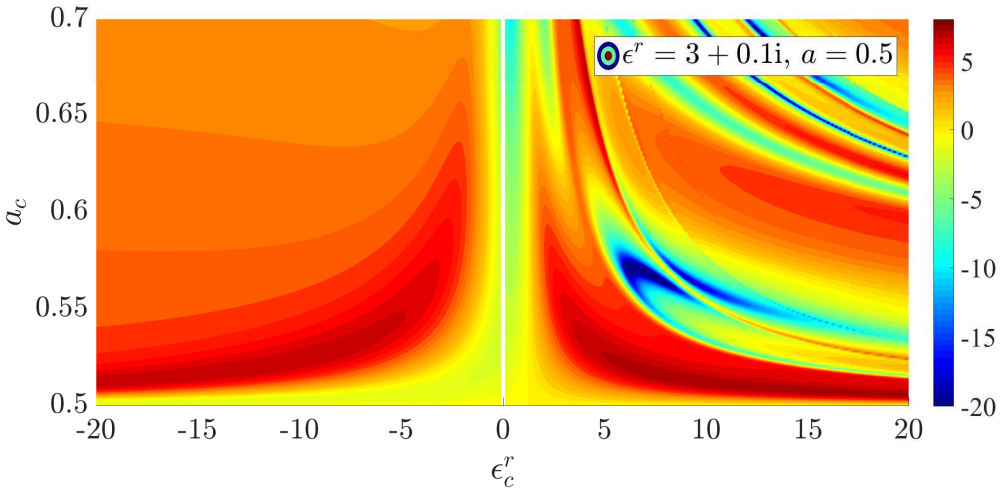

FIGURE 4.18 – Contour plot of the backscattering gain (in dB) of a double-layered cylinder of a core profile($\epsilon^r = 3 + 0.1\text{i}, a = 0.5$) versus the outer coat radius a_c and coat permittivity ϵ_c^r

the case of $\epsilon^r = 3$. The main observation to see is that the gain is positive for wider regions of $\epsilon_c^r < 0$.

Now, the core cylinder losses are intensified such that $\epsilon^r = 3 + \text{i}$. Fig. 4.19 shows the contour plot of the backscattering gain. Two main things are observed. The first is that the overall gain level is much higher than that of the case of $\epsilon^r = 3$. The second and the more important is that it is possible to significantly enhance the backscattering nearly using any coat of negative permittivity.

4.5.4 Numerical results for a core cylinder of highly lossy medium and high permittivity

4.5.4.1 Backscattering efficiency of the single cylinder

In the part, the scenario of a cylinder of permittivity $\epsilon^r = 15 + 5\text{i}$ is simulated. This medium properties are actually similar to that of the outer human skin-fat layer at 870 Mhz. Thus, the results obtained here might give some basic indications about how things will go with the real human model.

But before rushing into this complex permttivity, the case of lossless media $\epsilon^r = 15$ is considered. Fig. 4.20 shows the plot of the corresponding backscattering efficiency. Similar profile to those in Fig. 4.12 is obtained. The peak gain turns to be 17.5 dB at $a = 0.04$.

Fig. 4.21 shows the plot of the backscattering efficiency for the case of $\epsilon^r = 15 + 5\text{i}$. From the previous parts, one would have easily predicted this curve to have a high peak in the electrically small regime and a drastic dampening of the profile due to high losses.

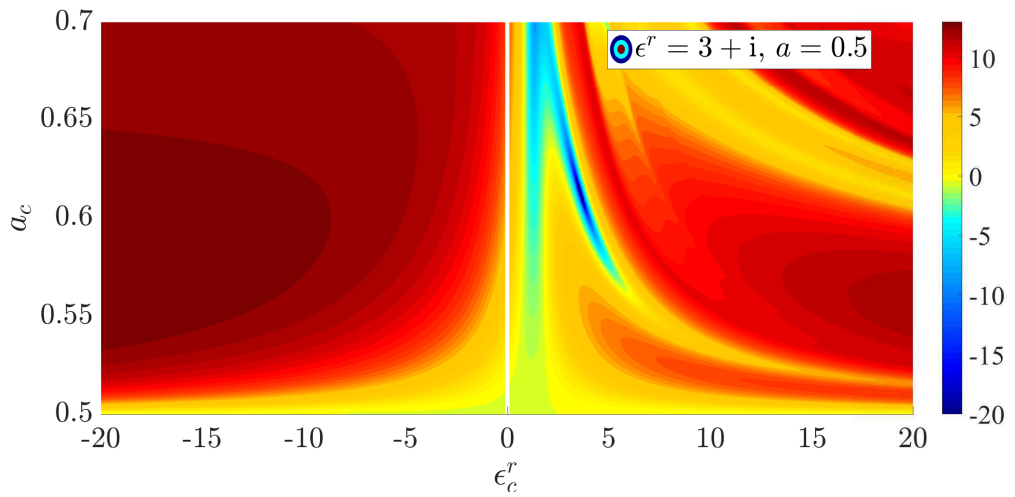

FIGURE 4.19 – Contour plot of the backscattering gain (in dB) of a double-layered cylinder of a core profile($\epsilon^r = 3 + \mathrm{i}, a = 0.5$) versus the outer coat radius a_c and coat permittivity ϵ_c^r

The peak of 14.6 dB occurs at radius $a = 0.035$. For the cylinder size $a = 0.5$, the efficiency drops to -4.35 dB.

4.5.4.2 Backscattering gain of the coated cylinder

In this part, the backscattering gain is plotted in form of a contour graph for the cases of $\epsilon^r = 15$ and $\epsilon^r = 15 + 5\mathrm{i}$.

Fig. 4.22 shows the contour for the case $\epsilon^r = 15$. Comparing this plot with that of $\epsilon^r = 3$ shows major profile differences. In the case of the higher permittivity, it becomes more difficult to theoretically enhance the backscattering using either positive or negative coats. Despite the fact that significant enhancement can be obtained for low positive permittivity values, however, the corresponding permittivity and thickness size ranges are very thin. Also, it is not possible to obtain backscattering enhancement using negative coats for $\epsilon_c^r \approx> -11.5$. Negatively high values are needed to obtain significant backscattering enhancement for thin coats.

The case of a lossy cylinder of permittivity $\epsilon^r = 15 + 5\mathrm{i}$ is now considered. The backscattering gain obtained for the coated cylinder is plotted in Fig. 4.23 as a function of the coat profile (a_c, ϵ_c^r). Several important observations can be noted :

1. In contrast to the contour plots for the cases of lossy media $\epsilon^r = 3 + 0.1\mathrm{i}$ and $\epsilon^r = 3 + \mathrm{i}$, the contour plot shows here that no significant backscattering enhancement can be obtained using positive permittivity coats whatsoever the thickness is.
2. Using coats of negative permittivity, backscattering gain can be enhanced, however, with less intensity than in the case of $\epsilon^r = 3 + \mathrm{i}$. To obtain at least 3 dB gain, there's a need to use a material of $\epsilon_c^r < -7$. In the region of permittivity plotted, the thinnest

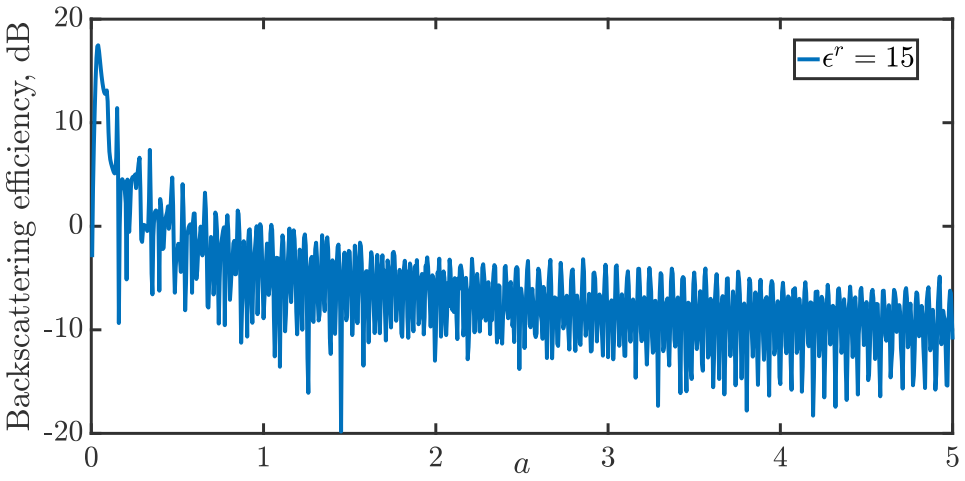

FIGURE 4.20 – Backscattering efficiency (in dB) for dielectric cylinder of permittivity value $\epsilon^r = 15$ as a function of the radius size a

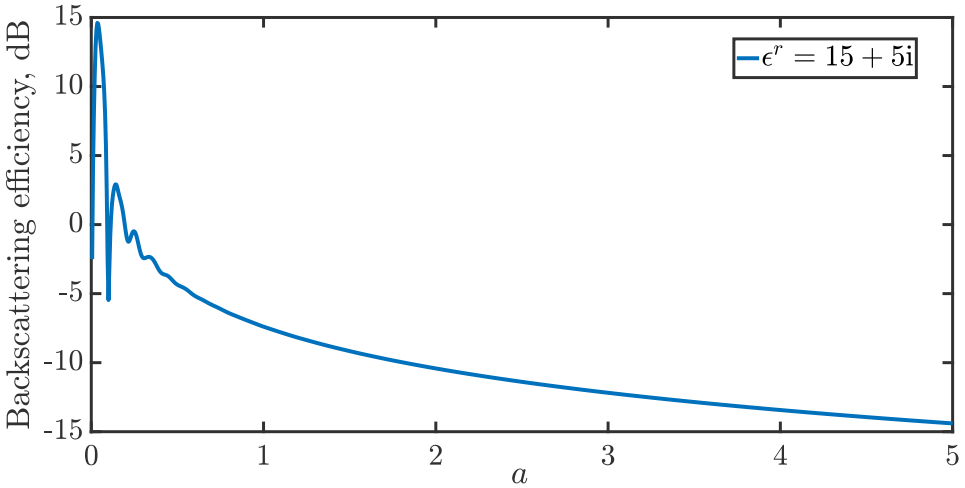

FIGURE 4.21 – Backscattering efficiency (in dB) for dielectric cylinder of permittivity value $\epsilon^r = 15 + 5\mathrm{i}$ as a function of the radius size a

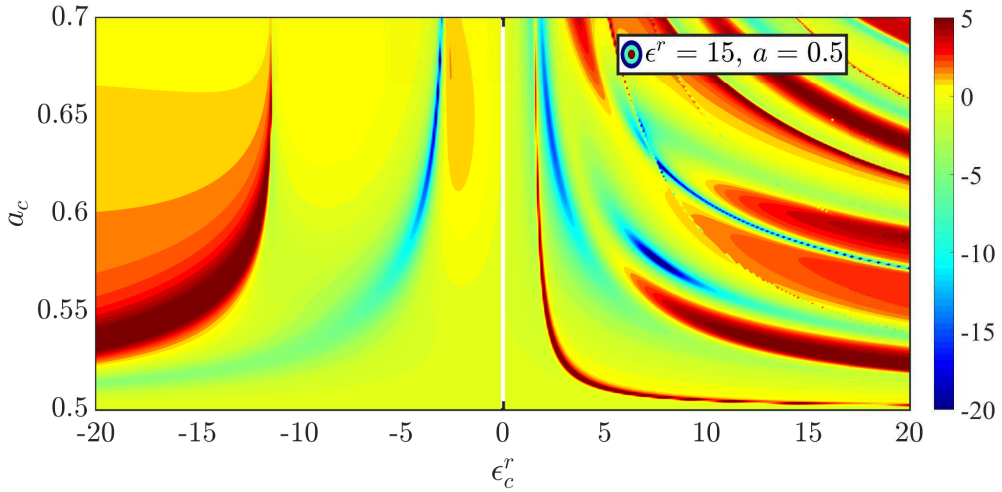

FIGURE 4.22 – Contour plot of the backscattering gain (in dB) of a cylinder of profile $(\epsilon^r = 15, a = 0.5)$ versus the coat permittivity ϵ_c and outer radius a_c

coat that results in 3 dB gain is $(0.534 - 0.5)\lambda_0 = 0.034\lambda_0$ using permittivity $\epsilon_c^r = -20$.

For more insight, Fig. 4.24 plots the backscattering gain for negative permittivity values ranging between -40 and -20. The contour plot shows that it is possible to obtain 3 dB gain using thinner coats, despite the fact that not much improvement in the backscattering gain level is obtained relative to using coats of really negatively high values. Again, the results show numerical instabilities when $a_c \times \epsilon_c^r$ product is large.

4.5.5 Summary

In this section, an analytical study has been performed on the backscattering enhancement of cylinders of lossless and lossy dielectric media using positive and negative dielectric coats. The idea was to progressively complicate the medium in terms of real permittivity value and losses so that make insightful observations on the manner the coats impact the backscattering by the cylinder. Here are the two most important conclusions drawn from this analysis :
1. The cylinder geometry is different from that of a slab. A slab of positive permittivity is known to backscatter based on the level of mismatch between the slab medium and free space. In the case of a cylinder, things are different. A coat of low permittivity can enhance the backscattering better than that of high permittivity for a fixed coat thickness. Similar conclusions can be drawn for the case of negative coats. Hence, it requires a well-defined coat profile (a_c, ϵ_c^r) to enhance the backscattering by a cylinder.
2. For lossless media of high permittivity values, it becomes more of a difficult task to obtain a thin coat profile to enhance the cylinder backscattering. The range of profiles to achieve this enhancement is very narrow for positive coats. On the other hand, backscat-

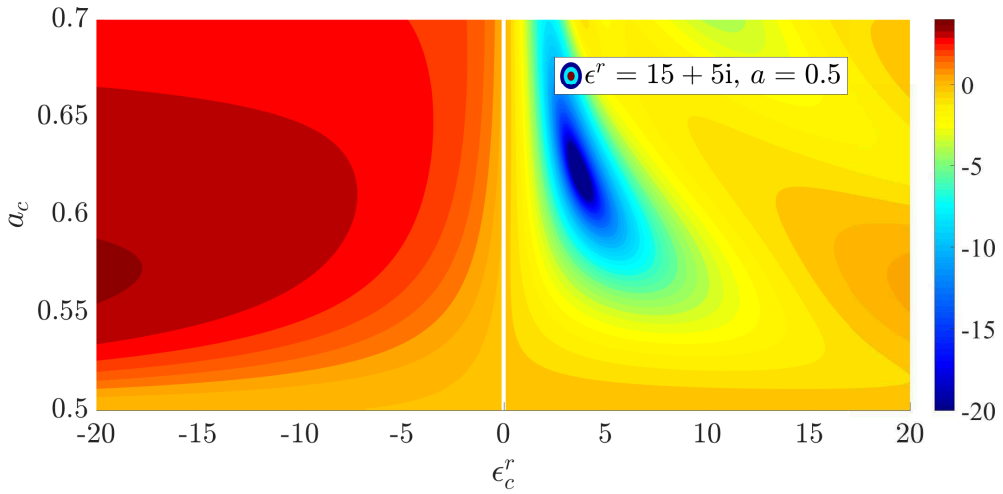

FIGURE 4.23 – Contour plot of the backscattering gain (in dB) of a cylinder of profile ($\epsilon^r = 15 + 5\mathrm{i}, a = 0.5$) versus the coat permittivity ϵ_c and outer radius a_c

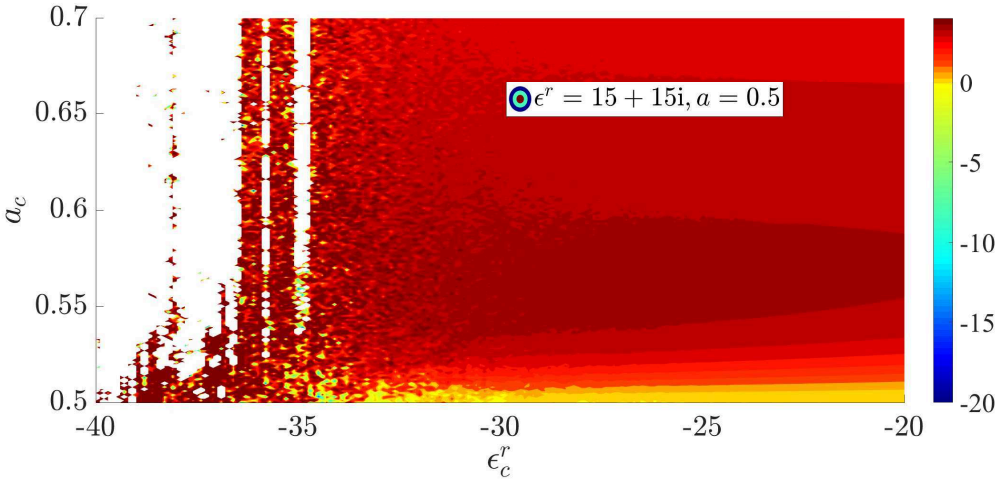

FIGURE 4.24 – Extended contour plot of the backscattering gain (in dB) of a cylinder of profile ($\epsilon^r = 15 + 5\mathrm{i}, a = 0.5$) for coat permittivity $-40 < \epsilon_c < -20$ and outer radius a_c

tering enhancement can be only obtained using negative thin coat profiles that require highly negative values.
3. The takeaway message of this section is that a cylinder of highly lossy medium and high permittivity value requires a coat of negative permittivity to enhance its backscattering. This cannot be achieved using coats of positive permittivity. Actually, the negative coats seem to reduce the absorptive effect of cylinder's lossy media .

4.6 Backscattering by a multi-layered lossy dielectric cylinder emulating a human core

4.6.1 Introduction

In section 4.5.2, the results of backscattering by a single cylinder have been obtained for lossless and lossy dielectric media. The objective in section 4.5 was to investigate the possibility of enhancing a lossy dielectric cylinder by a coat of dielectric medium. Particularly, in the last part of this section, backscattering gain results have been obtained for the case where the core cylinder possesses real and imaginary permittivity parts of high values. This progression actually served in the build-up of our complex problem dealing with the human core.

In this section, the backscattering enhancement by a multi-layered lossy dielectric cylinder emulating a human core is investigated. The size of the human core is assumed to be electrically moderate, in other words, of order of wavelength. Hence, the dielectric properties of the biological tissues have been obtained at a frequency of 870 MHz based on well-known models found in literature[98]. Obviously, the biological tissues are of dispersive nature and different dielectric properties are obtained at 24 GHz (frequency upon which an automotive radar operates). The reason behind not pushing towards higher frequencies is due to numerical instabilities. Bessel function tend to increase exponentially as its argument imaginary part increases. Regardless of the electrical size of the cylinder, the concept remains the same, if it is valid for low frequencies, then theoretically it should also be valid for higher frequencies.

4.6.2 Human core modeling and characterization

There have been several distinct attempts to model a human core in various fields as the study on the human thermal response[99], medical imaging[100] and body area network (BAN)[101], [102].

The human body is usually modeled in simple canonical forms as spheres and cylinders to emulate the human parts as head, torso, arms and legs. In one interesting study on the thermal exchange of the human body with the environment, the human torso is modelled as a multilayered cylinder to consider the different tissues characterized with different thermal properties[99].

Specifically in electromagnetics field, different types of studies are accompanied with the need to model the human body parts :

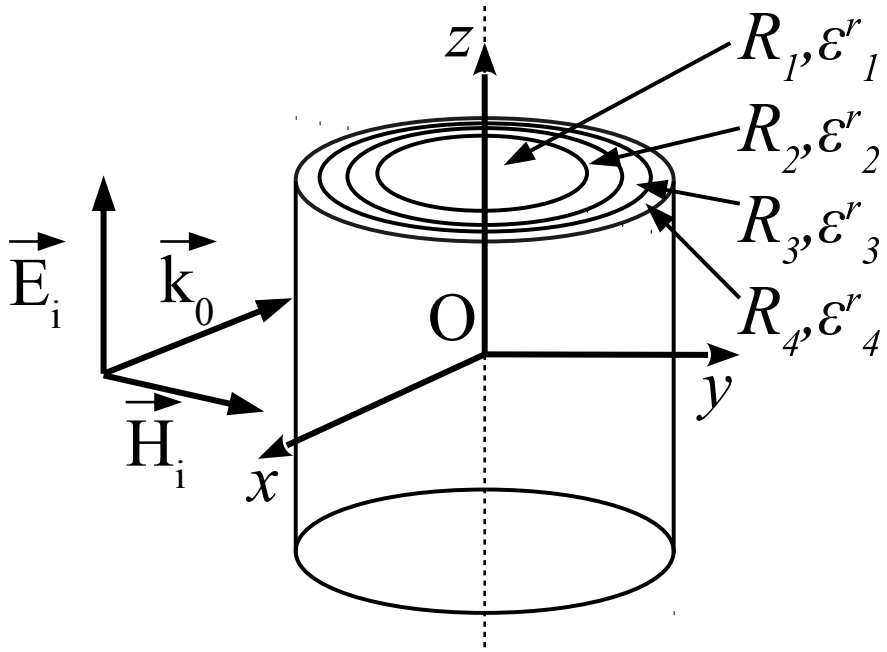

FIGURE 4.25 – Geometry of a four-layered cylinder emulating a human core normally illuminated by plane wave whose electric field is aligned along the axis cylinder

1. Human head exposure to electromagnetic radiation by cell-phones characterized by the Specific Absorption Rate (SAR).
2. Wearable antennas : the effect of the impedance mismatch (produced by the human body) on the performance of the antenna.
3. Scattering by human body : tumors diagnosis by analyzing the scattering obtained by the tissues.

For example, the basic human head model is a multi-layered sphere comprising the tissues found in the head. However, these days, standard models as [80] have been specified by the commercial softwares to be used directly by the costumers, making performing full wave simulations tempting for various applications. This means that less attention is given to the analytical study on the scattering behavior of the human body.

Regarding the context of our work here, few work can be found in the literature on modeling the human core or torso. Such interest can be mainly found in the domain of wearable antennas[103]. In one of the works[101], the human core has been modeled as a multi-layered elliptical cylinder consisting of internal organs, bone, muscle, and skin-fat layers. The dielectric properties of the tissues are based on the tissue library created by C. Gabriel et al. Full wave simulations have been performed to study the antenna characteristics (matching, radiation) when placed on the skin layer and in the proximity of the complex medium of the human body.

In our work, we take a similar path. The human torso is modeled here as a circular multi-layered cylinder rather than elliptical to simplify the analytical study. A scheme describing the geometry is given in Fig. 4.25. At the frequency of interest ($870MHz$), the layers sizes and dielectric properties are given as following :
1. $R_1 = 13.6cm \approx 0.39\lambda_0, \epsilon_1^r = 52.1 + 18.8\text{i}$
2. $R_2 = 14.2cm \approx 0.41\lambda_0, \epsilon_2^r = 20.8 + 6.82\text{i}$
3. $R_3 = 15.5cm \approx 0.45\lambda_0, \epsilon_3^r = 55.1 + 19.2\text{i}$
4. $R_4 = 16.75cm \approx 0.49\lambda_0, \epsilon_4^r = 14.5 + 5.16\text{i}$.

4.6.3 A multi-layered lossy dielectric cylinder model

In section 4.3, a derivation of the scattering coefficients was presented for the single and coated cases. The solution for a coated cylinder can be straightforwardly extended to the case of a multi-layered stratified cylinder as demonstrated by Kerker in his book[104]. Based on his theoretical model, we have developed a numerical code to obtain the scattering coefficients for a multi-layered cylinder of arbitrary number of layers and dielectric properties. The scattering coefficients are similarly obtained by expanding the fields in terms of cylindrical functions and finally applying the boundary conditions on the interfaces separating each two layers. The resulting set of equations is then solved to obtain the expansion coefficients in each layer as well as as the scattering coefficients. The metrics formulated in section 4.3 are all the same here for the case of a multi-layered cylinder.

4.6.4 Study on the optimum coat profile enhancing the backscattering

4.6.4.1 Coat permittivity : positive and negative ϵ_c^r

As previously stated, the multi-layered cylinder has an outer radius of approximately $0.49\lambda_0$. The layers materials complex permittivity values are characterized for frequency 870 MHz. Hence, from now on, $a = \frac{R}{\lambda_0}$ and $a_c = \frac{R_c}{\lambda_0}$ where λ_0 is the wavelength at frequency 870 MHz.

The numerical results of backscattering gain of a coated multi-layered cylinder emulating a human core are presented. Fig. 4.26 plots the backscattering gain versus a_c for different values of positive permittivity. The results show that it requires a very high positive permittivity to obtain any significant backscattering enhancement. A gain of 2.47 dB is obtained using a coat of permittivity $\epsilon_c^r = 50$ and thickness $0.02\lambda_0 \approx 0.7cm$.

Fig. 4.27 plots the backscattering gain versus coat radius a_c for several values of negative permittivity. It is shown that a gain of 2.7 dB can be obtained using a coat of $\epsilon_c^r = -25$ and thickness $0.02\lambda_0 \approx 0.7cm$. The most significant difference between the positive and negative coats profiles is in the thin coat region ($a_c < 0.54$). Profiles of negative coat tend to exponentially increase as the permittivity gets negatively higher. This is an indication that it is possible to obtain nearly 3 dB gain for thinner shells by increasing the negativity of the coat. This cannot be achieved using a positive coat.

Actually, in the thin coat region, the positive coat tends to reduce the backscattering rather than enhancing it.

4.6.4.2 Contour plot

The contour plot in Fig. 4.28 shows the backscattering gain versus the coat profile (a_c, ϵ_c^r). The obtained plot is similar to that of Fig. 4.23 produced in part 4.5.4.2 where the core cylinder has a permittivity of $\epsilon^r = 15 + 5\mathrm{i}$ and size $a = 0.5$. This can be due to fact that the outer fat-skin layer has a similar dielectric medium. The plot show that positive backscattering gain can only be achieved using coats of negative permittivity. For thinner shells, the gain intensity increases as the negativity of the coat increases.

4.6.5 Study on the tissues dielectric properties error margin

In this part, a study on the impact of the material permittivity fluctuations on the backscattering gain profile is done. The coat permittivity is fixed here to $\epsilon_c^r = -20$.

To perform the study, the real and imaginary parts of the complex permittivity of each of the layers are set to fluctuate by $\pm 5\%$ around their central values given in part 4.6.2. The backscattering gain is then plotted for all possible combinations of the layers dielectric complex permittivity values. This results in a beam of backscattering gain profiles. Fig. 4.29 plots this beam versus the coat radius a_c. The plot shows that for a coat or $a_c = 0.53 \approx 1.1a$, the least value obtained by any combination is 2.5 dB while the maximum value obtained is 2.9 dB. Hence, fluctuations by $\pm 5\%$ in the layers media dielectric results in maximum backscattering gain difference not more than 0.4 dB. This is a very acceptable margin.

4.6.6 Study on the layers radii error margin

In this part, the impact of the cylinder size fluctuations on the backscattering profile is studied. As in the previous part, ϵ_c^r is set to -20. The dielectric properties of the tissues are fixed to their central values.

The radius size fluctuation of each of the layers is set at $\pm 2\%$. The backscattering gain profiles corresponding to each possible combination are hence plotted versus the coat radius a_c. Fig. 4.30 plots the corresponding profiles. The combinations related to the outer radius $a_4(1-2\%)$ are plotted in red, while those of radius $a_4(1+2\%)$ are plotted in blue. For $a_4(1-2\%)$ radius, the lowest gain value obtained by any combination is still positive (1 dB) at $a_c = 1.1a_4(1-2\%)$, while the highest gain value obtained is nearly 2.8 dB. For $a_4(1+2\%)$ radius, the lowest gain value obtained by any combination is close to 2.7 dB and the highest value obtained is close to 6 dB. The curves show that the impact of the radii sizes fluctuations on the backscattering gain is important. However, from the results obtained, the impact is globally positive. Even for the worst case scenario, the backscattering gain remains positive at the coat size of interest.

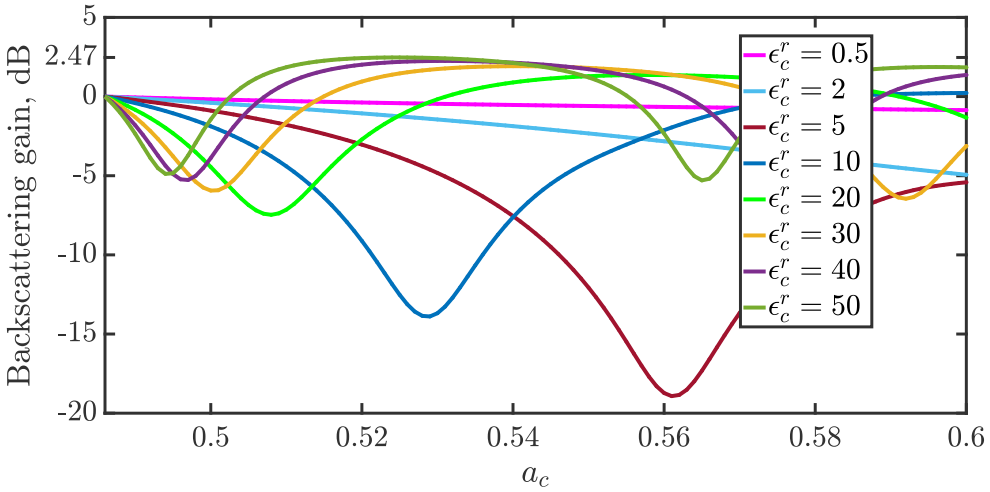

FIGURE 4.26 – Backscattering gain (in dB) of a four-layered cylinder emulating a human core versus coat radius a_c for different values of $\epsilon_c^r = 0.5, 2, 5, 10, 20, 30, 40$ and 50

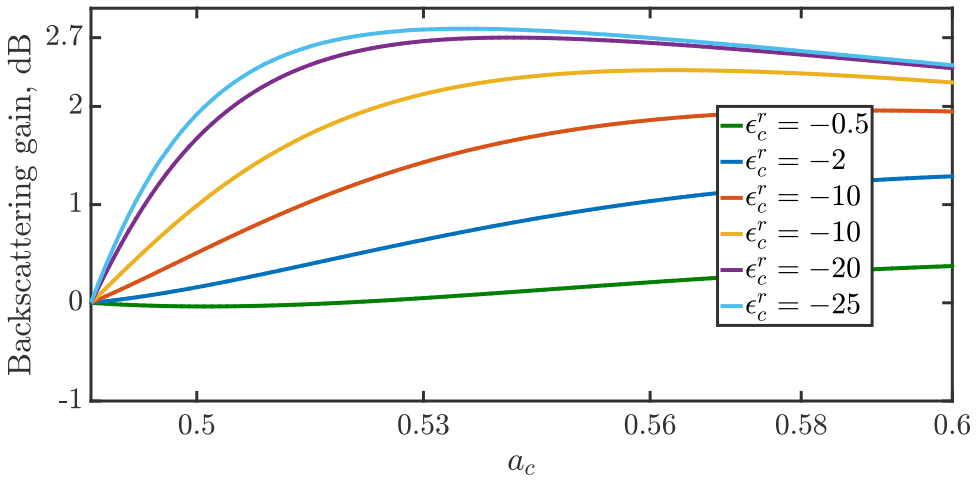

FIGURE 4.27 – Backscattering gain (in dB) of a four-layered cylinder emulating a human core versus coat radius a_c for different values of $\epsilon_c^r = -0.5, -2, -5, -10, -20$ and -25

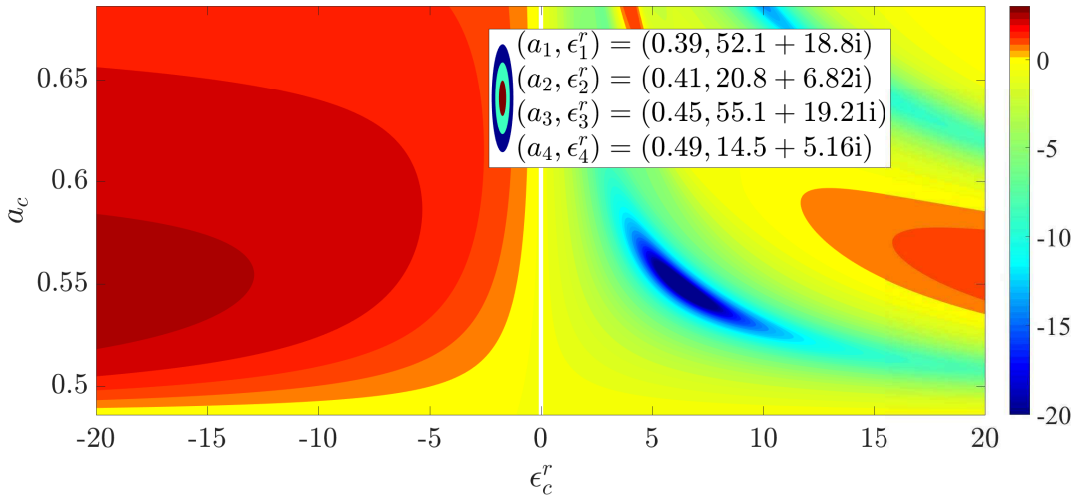

FIGURE 4.28 – Contour plot of the backscattering gain (in dB) of a four-layered cylinder emulating a human core versus the coat permittivity ϵ_c and outer radius a_c

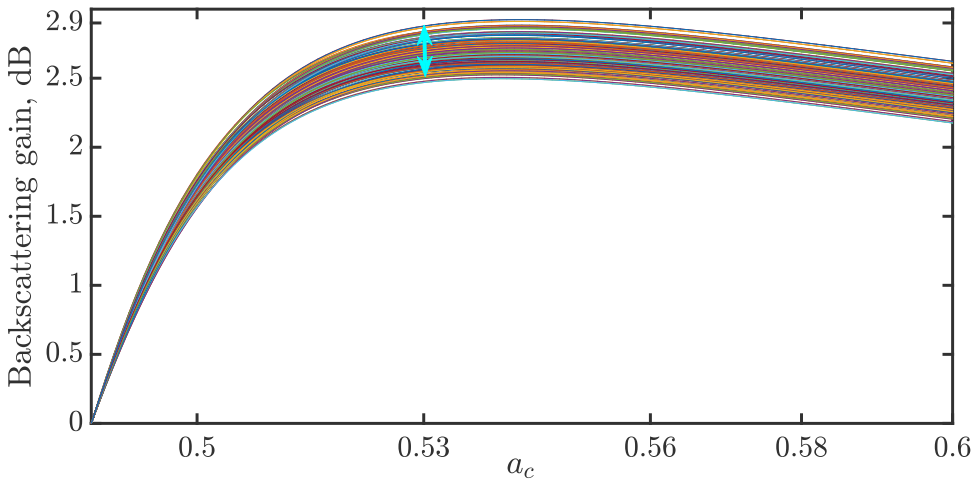

FIGURE 4.29 – Plot of the backscattering gain (in dB) of all the possible fluctuation combinations of the layers dielectric complex permittivity values versus the outer radius a_c

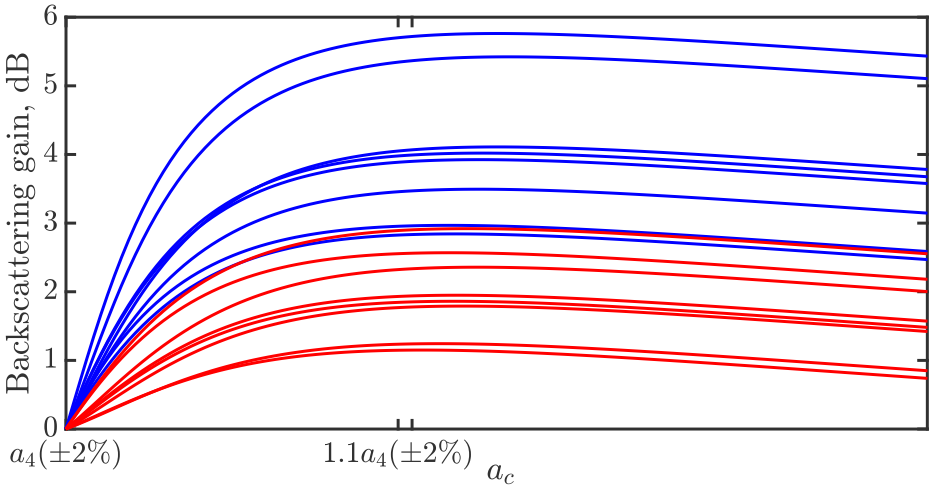

FIGURE 4.30 – Plot of the backscattering gain (in dB) of all the possible fluctuation combinations of the layers radii sizes versus the outer radius a_c

4.6.7 Summary

In this section, the possibility of enhancing the backscattering by a multi-layered cylinder emulating a human core has been investigated. The human core model has been simplified as a circular cylinder of four tissue layers. The tissue dielectric properties have been obtained using well-known models in the literature.

From the analytical study performed on the backscattering gain using positive and negative coats, the following points have been concluded :
1. The backscattering by a cylinder emulating a human core can be enhanced by up to 3 dB using thin coats ($a_c < 1.1a_4$) of high negative value ($\epsilon_c^r < -20$).
Considering the theoretical model used here as an infinite cylinder, it is expected that a thinly coated finite cylinder would produce higher backscattering due to the scattering by the edges. The results also show that this enhancement cannot be achieved using thin coats of simple positive dielectric media, but rather thin coats of very high positive permittivity values are required to accomplish the feat.
2. The analysis showed that the dielectric material fluctuations do not have a major impact on the backscattering gain. Thus, the backscattering gain using a specific coat profile is not sensitive to the tissues variation from one individual to the other.
3. The impact of the layers radii fluctuations is significant. The margin between the lowest gain obtained by a fluctuation combination and the highest one is about 5 dB. In the best case scenario, the gain increased by 3 dB more than the nominal gain value. In the worst case scenario, the gain has dropped by nearly 1.5 from the nominal case value. Even though, the backscattering gain in any case remains positive.

4.7 Conclusion

In this chapter, the enhancement of the backscattering by an infinitely long dielectric cylinder emulating a human core using a dielectric coat was investigated. The second section of the chapter provided the reader with an alerting qualitative taste about the scattering problem. In the third section, the mathematical derivation of the Mie solution of the scattering problem by single and coated cylinders was rigorously presented. Based on the obtained scattering coefficients, scattering and backscattering widths, efficiencies and gains have been defined. To compute those metrics as a function of the core cylinder and coat permittivity (ϵ^r and ϵ_c^r respectively) and size (a and a_c respectively), a numerical model has been coded. In section 4, the results obtained using this model were validated by examples found in literature for both of the cases of single and double-layered cylinder.

In section 5, a comprehensive study was conducted on the backscattering enhancement of cylinders of dielectric media ranging from simple and lossless to highly lossy. This study aimed to help understand how coats of positive and negative permittivity materials affect the backscattering by a cylinder of medium of certain dielectric properties. It was concluded that the backscattering by a highly lossy cylinder as that of permittivity $\epsilon^r = 15 + 5\mathrm{i}$ can only be enhanced using thin coats of negative material. Such complex medium actually resembles the dielectric medium of a human skin-fat layer at 870 MHz.

In section 6, the case of a multi-layered cylinder emulating a human core was considered. The human model was simplistically assumed as an infinitely long circular four-layered cylinder (outer radius $R_4 = 16.75cm \approx 0.49\lambda_0$). The layers tissues (internal organs, bone, muscle and fat-skin) were characterized at 870 MHz using dielectric properties libraries found in literature. By extending our numerical model, it became possible to obtain the scattering coefficients for the case of multi-layered cylinder. Based on those coefficients, the backscattering gain of a coated multi-layered cylinder was formulated in a similar fashion to that of a double-layered cylinder.

The results showed that using a coat of thickness 0.7 cm and permittivity $\epsilon^r = -25$ it is possible to obtain nearly 3 dB of backscattering gain. Also, using coat permittivity values of higher negativity, the same gain level can be achieved using much thinner coats. Using coats of positive dielectric material, such enhancement can only achieved using thicker coats and high permittivity values.

The results obtained in this chapter will serve as guidelines for the design of a coat that enhances the backscattering by a finite multi-layered lossy dielectric cylinder emulating a human core. The theoretical results obtained in this chapter for infinite cylinder will be thus validated in the following chapter using full-wave numerical simulation of finite cylinder.

Chapter 5

Enhancement of the Backscattering by a finite lossy multi-layered cylinder emulating a human core

5.1 Introduction

The work detailed in this chapter is the first step towards enabling a more realistic implementation of a metamaterial coat on a cylinder. To this end, several challenges need to be addressed namely. Indeed, a 3-D full-wave numerical model is required to ensure that the metamaterial coat can be directly simulated later on prior to considering any experimental implementation. A mere comparison of the analytical model (proposed in chapter 4 for cloaking a dielectric cylinder) to a numerical one requires extension to finite cylinders.

In this chapter, the theoretical work in the previous chapter on the infinite cylinder is hence extended here to the case of finite cylinder. The backscattering enhancement of the finite lossy multi-layered cylinder emulating a human core is thus studied.

Guidelines for the design of a coat that enhances the backscattering by a finite multi-layered lossy cylinder emulating a human core will be confirmed. The methodology followed in this chapter is to progressively complicate the problem just as has been done in the previous chapter, with the last section covering the problem of backscattering by a multi-layered finite cylinder model emulating a human torso.

In the first section, an extension of the 2D cross section formula for the infinite cylinder to a 3D cross section for the infinite cylinder is proposed. The theoretical formulation can then be validated by full-wave simulations. A simple single-layered finite cylinder is first considered. Based on this formulation, the theoretical backscattering gain is defined as the difference between the backscatter RCS of the coated and non-coated cylinders of finite length. This will be termed the corrected backscattering gain.

In the next section, the problem of single-layered cylinder is considered. Full wave simulations are performed to obtain the backscattering by single and coated cylinders. The simulated and theoretical backscattering gain profiles are then compared. Using this information, the ability of the proposed theoretical model in providing information on the backscatter enhancing coat profile is discussed.

In the last section, the multi-layered cylinder case is considered. The layers of the cylinder are the biological tissues the human torso is made of : internal organs, bone, muscles, skin. The tissues dielectric properties are obtained at 870 MHz using the library of Gabriel ([98]). The cylinder is coated with negative dielectric material upon which a theoretical solution of the backscattering gain is given. Full wave simulations are then performed. The information extracted from both the theoretical and simulated gain profiles are used to form guidelines for the design of a coat that enhances the backscattering by a cylinder emulating a human core.

5.2 Analytical formulation of the backscatter Radar cross section by a finite cylinder

5.2.1 Proposed approximations

Analytically, no exact solution for the scattering by finite dielectric cylinder exists. Thus, only approximative solutions exist in literature. The main concept behind those approximations is based on the infinite model of cylinder. The electric field inside the finite cylinder is approximated by the internal electric field of an infinite cylinder. The latter can be analytically obtained as explained in the previous chapter. Now, it is possible to obtain the scattering by a finite cylinder by applying the field equivalence principle[105]. The infinite cylinder is first truncated by the length of the finite cylinder. The approximated internal electric field inside this truncation is transformed into either volume or surface current [106]. The approach based on the surface current can be used for the simpler cases where rough approximations can be made, specifically speaking, when the electrical size of the radius is very small compared to the cylinder length. The approach based on the volume current offers more accuracy and generalization. In the work published in [107], it has been shown that for the case where the incidence is oblique on the axis of the cylinder, both approaches were not accurate regarding finding the forward and back scattering.

5.2.2 3D cross section approximated formulation based on Knott 2D cross section formulation

5.2.2.1 RCS formulation for cylinders of finite length

In this part, we propose to use an extended formulation of 2D scattering width into 3D RCS cross section. The extension is based on the approximation suggested by Knott ([18]). For the case of a cylinder normally illuminated by a plane wave, the backscatter

RCS can be written as following :

$$\sigma_{3D} = \frac{4L^2}{\pi} \sum_{n=-\infty}^{+\infty} |b_n|^2 \tag{5.1}$$

where L is the cylinder length and b_n is the scattering coefficient obtained for the TM case.

The significance of this formulation is that it only depends on the scattering coefficient obtained in the previous chapter. This makes it a simple and handful metric to use.

In this section, we discuss the validity of this formulation for the case of a finite lossy dielectric cylinder. The validation method is based on comparing the analytical formulation with results obtained using the numerical full wave simulations. The procedure is decomposed into three stages where the cylinder dielectric loss is progressively intensified. This should give a primary view on the validity of this formulation for the case of a finite lossy dielectric cylinder.

5.2.2.2 Geometry description and simulation setup

In the previous section, an analytical formulation of the backscatter RCS of a finite lossy dielectric cylinder has been proposed. In this section, backscatter RCS is obtained numerically by performing full-wave simulations. Hence, a comparative study on the validity of the analytical formulation can be conducted based on those obtained results.

The simulated structure is composed of a finite cylinder of certain relative permittivity ϵ^r, radius R and length L. The cylinder is place in a vacuum box. The box itself has its sides assigned radiation boundary conditions. The solver combines the finite elements method (FEM) with the integral equation (IE) method for efficient solving of the scattering problem. The new so-called FEBI hybrid method uses the IE to reduce the computational space as compared to the FEM while preserving its solving accuracy based on volume-discretization.

For further reduction of simulation time, the cylinder size is reduced to its half size (L/2) and symmetry condition is used on the radial plane at the middle of the cylinder.

The cylinder is normally illuminated by a plane wave whose electric field is aligned along the cylinder axis. An illustration is given in Fig. 5.1.

5.2.2.3 Validation of the approximated formulation discussed using results obtained from numerical simulations

In this part, the full wave simulation results of the RCS backscatter are presented and plotted with respect to the length to radius ratio (L/R). Those results are compared to their counterparts obtained using the theoretical formulation defined earlier.

For the simulations in this section, the cylinder is assigned the following geometrical parameters : $R = 0.2\lambda_0$ ($a = R/\lambda_0 = 0.2$) at frequency of operation 5 GHz ; L=10R. Fig. 5.2 shows the plot of backscatter RCS for the case where the cylinder dielectric medium is lossless : $\epsilon^r = 3$. The results show a good agreement between the simulation

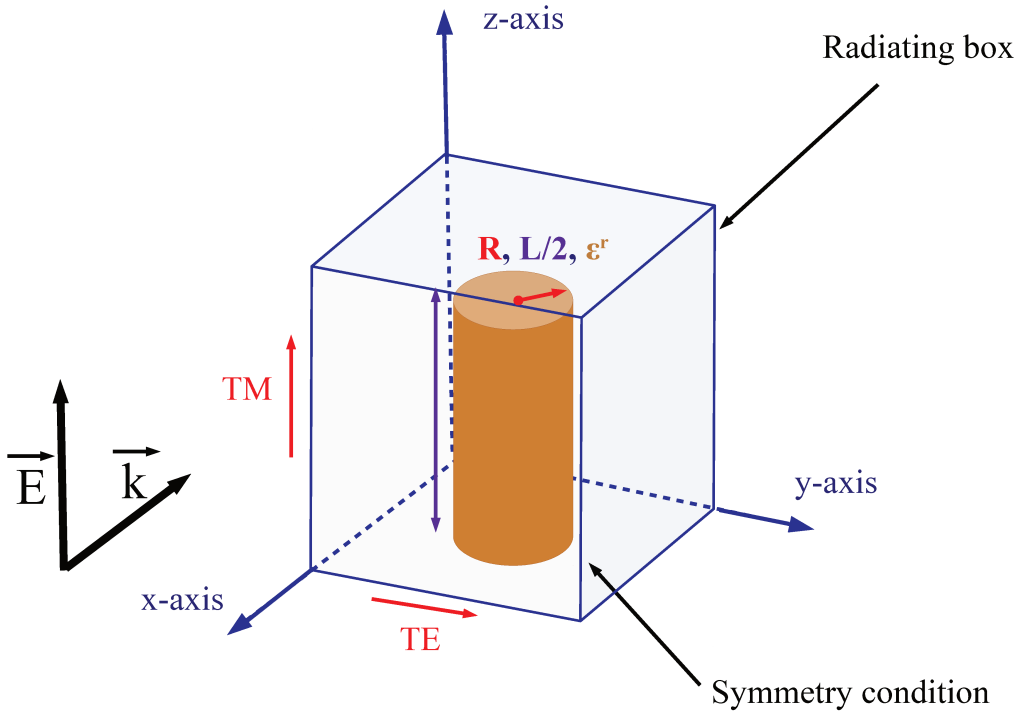

FIGURE 5.1 – A sketch showing the simulation setup for the computation of the backscatter RCS of a single cylinder : the backscatter energy is sensed in the opposite direction of incidence (- x-axis)

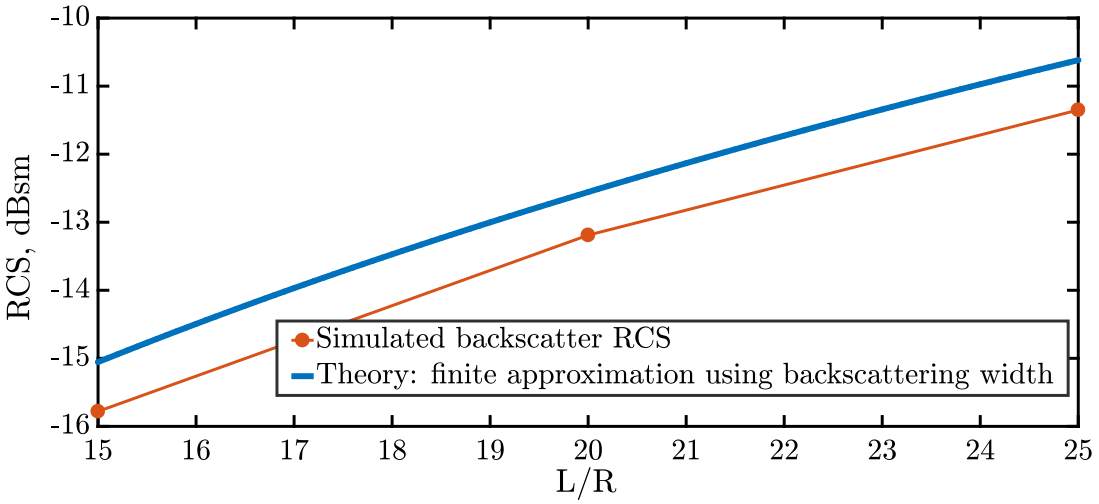

FIGURE 5.2 – Comparison between the theoretical and simulated RCS (in dBsm) for a single finite cylinder of radius $a = 0.2$ and permittivity $\epsilon^r = 3$ versus the cylinder length to radius ratio at the operation frequency 5 GHz

results and the theoretical formulation. For all L/R values, the largest difference between the simulated and theoretical RCS does not exceed 1.3%. Also, the curves profiles show remarkable consistency at such low levels of energy.

Now, the medium is considered lossy with a loss tangent delta $\delta = 1/30$, in other words, the dielectric permittivity is equal to $\epsilon^r = 3 + 0.1\mathrm{i}$. Fig. 5.3 shows the plot of the backscatter RCS for a range of L/R values. Similar to the lossless case, the results show good agreement between the simulated and theoretical profiles. The highest relative difference between the two curves does not exceed 3% for any L/R value. Again, the curve profiles seem consistent over the L/R range.

The medium losses are now intensified to the extent that delta tangent $\delta = 1/3$. From Fig. 5.4, it is deduced that the maximum relative RCS difference is less than 4%. This means that even for a highly lossy medium, the simulated and theoretical backscatter RCS curves remain in good agreement.

From the comparisons performed in this part, the results seem very promising. It is using only a simple formulation based on the scattering coefficient that we were capable of predicting the backscatter RCS of a normally illuminated finite lossy dielectric cylinder.

5.2.2.4 Corrected backscattering gain

For single cylinders, the backscatter RCS metric can be be used to assess its backscattering intensity. However, in our work, the aim is to evaluate how a dielectric coat affects the backscattering by a coated cylinder, in other words, how much RCS enhancement or reduction can be obtained after adding the coat. This can be well-described using the backscatter gain metric. In the previous chapter, the theoretical backscatter gain of an

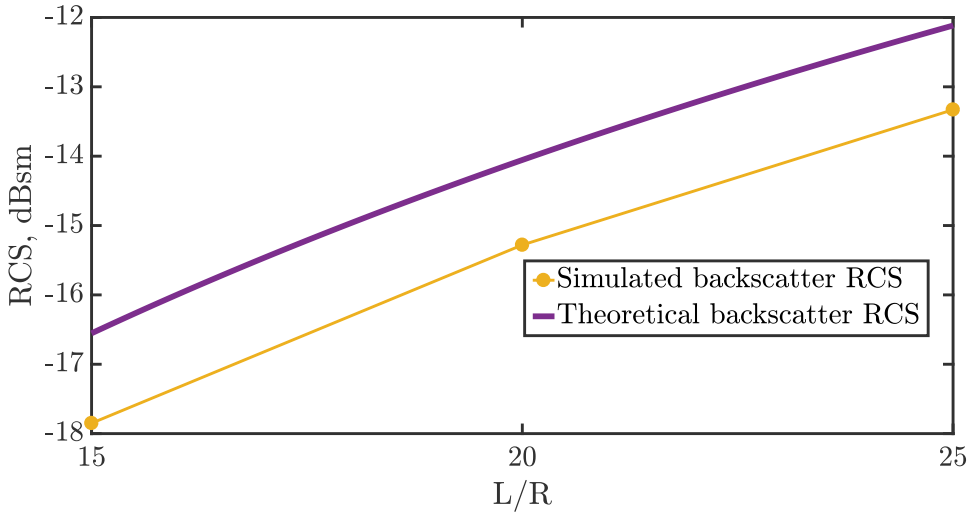

FIGURE 5.3 – Comparison between the theoretical and simulated RCS (in dBsm) for a single finite cylinder of radius $a = 0.2$ and permittivity $\epsilon^r = 3 + 0.1\mathrm{i}$ versus the cylinder length to radius ratio at the operation frequency 5 GHz

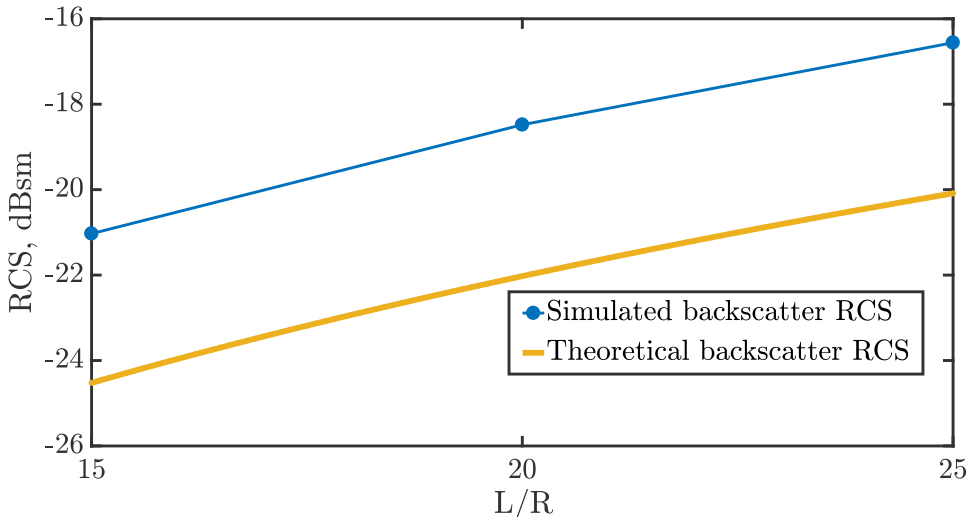

FIGURE 5.4 – Comparison between the theoretical and simulated RCS (in dBsm) for a single finite cylinder of radius $a = 0.2$ and permittivity $\epsilon^r = 3 + \mathrm{i}$ versus the cylinder length to radius ratio at the operation frequency 5 GHz

infinite cylinder was defined as the ratio of the efficiency of the coated cylinder as compared to the non-coated. A correction factor is introduced in this chapter to account for the finiteness of the cylinder. The corrected backscatter gain is defined as the difference in dB of the backscatter RCS of the coated cylinder with respect to the non-coated as following :

$$Gain = \sigma_{3D}^{coated} - \sigma_{3D}^{non-coated} \tag{5.2}$$

. Extracted from the above formula, the corresponding correction factor becomes ${a_c}^2 a^2$. Hence, for a finite cylinder, the gain increases by a value of $\log {a_c}^2 a^2$ (in dB) with respect to that of the infinite. This increase can be physically interpreted by the additional scattering produced at the edges of the cylinder. Considering that the corrected gain still depends on the scattering width of an infinite cylinder, such a correction can be considered as rough as simple.

5.3 Full wave numerical solution of the scattering problem : the challenge of negative permittivity medium

In the previous part, the simulation problem was limited to a single and electrically large dielectric cylinder of positive permittivity. Ansys HFSS solver based on finite element method can handle such problems. However, in the next parts, the cylinder will be coated by a layer of a medium of negative permittivity. Here, the full wave simulation problem becomes complicated. The wave inside such a medium has an imaginary wave number. Also, our structure that is composed of thin arched layer makes the problem even more complicated. The choice of the permittivity is going to be very critical. Choosing a coat of negatively low values (-2 or -5) makes it **impossible** for the solver to converge based even on a relaxed energy delta constraint. It will be seen that the permittivity chosen is of negatively high values (-15) and that is to reduce the propagation inside the medium and by so simplifying the problem.

5.4 Full wave simulation results on the backscattering gain by a coated cylinder using metamaterial coat

5.4.1 Introduction

In this section, the enhancement of the backscatter RCS of a coated cylinder is investigated. The main theme of this section is to study how the theoretical predictions based on the scattering coefficient compare to the full wave simulation results. This will give a basic insight on the ability to predict the characteristics of the coat profile provoking the enhancement of the backscatter of a finite cylinder. The whole study can be seen as a transitional step towards investigating the backscatter enhancement by a multi-layered cylinder emulating a real-scenario human core.

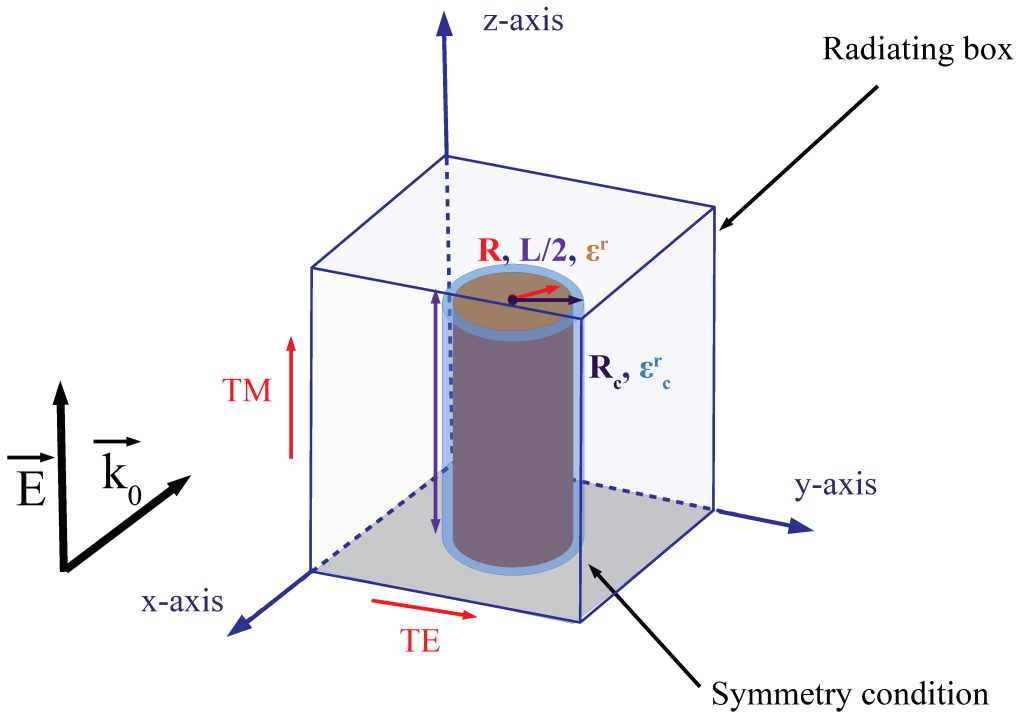

FIGURE 5.5 – A sketch of the simulation setup of a coated cylinder : the backscatter energy is sensed in the opposite direction of incidence (- x-axis)

5.4.2 Geometry description and simulation setup

In this section, two structures are going to be simulated. The first is the single cylinder as described in the previous section, while the second is the coated cylinder as depicted in Fig. 5.5. Similar simulation setup to that of the single cylinder is used for the case of coated cylinder. Transposing into the electrically moderate size, the cylinder electric size will be fixed to $a = 0.5$ throughout this section. As will be seen later, this is actually similar to the electrical size of the human core at the chosen frequency of operation.

Similar to the previous section, the core cylinder has a relative permittivity of $\epsilon^r = 3$. The simulation results will be obtained for cases of different loss intensity. The shell thickness will be made to vary while fixing the shell permittivity to $\epsilon_c^r = -15$. The reason behind choosing such a relatively high negative permittivity relates to the simulation time and complexity. In fact, as the medium is more negative, the less the propagation is inside it and this leads to the simplification of the problem. The less negative the medium is, the more the propagation is inside the medium. This leads to increased computational

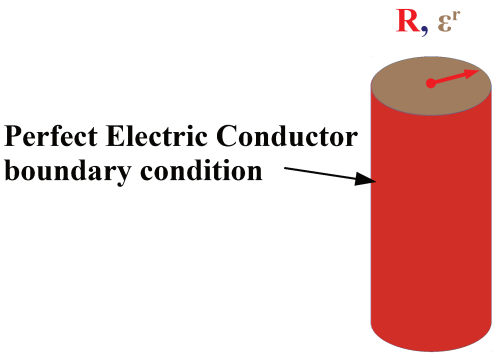

FIGURE 5.6 – Sketch of a cylinder coated with a perfectly conducting layer

complexity and the requirement of very dense meshing to obtain convergent results.

5.4.3 Backscatter RCS reference value : a dielectric cylinder coated by a metallic coat

In this part, we try to envisage the level of backscatter RCS that can be obtained using a totally reflective coat. Consider a single dielectric cylinder of permittivity $\epsilon^r = 3$ and L/R ratio equal to 10. The cylinder is simulated using the setup shown in Fig. 5.5. The results obtained show a backscatter RCS of -9.32 dBsm. In a second simulation, the cylinder outer surface is then assigned a perfectly conducting boundary condition as shown in Fig. 5.6. Now, the outer surface is totally reflecting, the backscatter RCS obtained is -4.92 dBsm. This means that a 4.4 dB gain can been obtained using an extremely thin conducting coat. This sets the standard value for the rest of our study based on coating using negative dielectric medium. It would be then possible to know what coat permittivity and thickness is needed so that to obtain the same standard gain value of 4.4 dB.

5.4.4 Backscatter RCS results for single dielectric cylinders of $\epsilon^r = 3$, $\epsilon^r = 3 + 0.1\mathrm{i}$ and $\epsilon^r = 3 + \mathrm{i}$ of cylinder size $0.5\lambda_0$ at 5 GHz

In this section, the case of a cylinder of different losses intensity is considered as following : $\epsilon^r = 3$, $3 + 0.1\mathrm{i}$ and $3 + \mathrm{i}$. The three scenarios are simulated using similar simulation setups. The backscatter RCS obtained are summarized in Tab. 5.1. As expected, the results in the table show that less backscattering occurs as the losses increase and this accounts to the absorption phenomenon occurring inside the cylinder medium.

TABLE 5.1 – The simulated backscatter RCS obtained for different losses intensities

scenario	σ_{3D}(dBsm)
$\epsilon^r = 3$	-9.3
$\epsilon^r = 3 + 0.1\mathrm{i}$	-12.7
$\epsilon^r = 3 + \mathrm{i}$	-21.7

5.4.5 Backscattering gain of various coated cylinders of a coat permittivity $\epsilon_c^r = -15$

5.4.5.1 Dielectric cylinder of core of $\epsilon^r = 3$ and coat permittivity $\epsilon_c^r = -15$

The cylinder is now coated with a coat of negative dielectric medium and certain thickness. The main point here is that it is not possible to obtain backscattering enhancement using very thin metamaterial shells. In fact, such ultra thin shells have been used to reduce the overall scattering by cylinders of positive permittivity medium. This is accounted for the scattering cancellation phenomenon that occurs on the level of two mediums of opposite polarizabilities[73].

In our work, however, the aim is to form a negative-positive coupled medium that upon interacting with a plane wave is capable of producing resonances or result in an enhancement in the backscattering.

The coat permittivity is fixed to $\epsilon_c^r = -15$ for computational reasons as declared previously. In fact, it has been theoretically predicted in the previous chapter that even choosing a negatively higher value would not impact the level of backscatter peak in dB. On the other hand, using higher negative dielectrics, coats of thinner thickness are sufficient to produce the same backscatter peak.

The backscatter RCS of a single non-coated has been shown in Tab. 5.1. Now, the simulated backscatter RCS of the coated cylinder is obtained using similar simulation setup for a defined range of outer radius $a_c = [0.5, 0.6]$. In other words, the thickness varies from null to 0.1 λ_0. The simulated backscatter gain results are hence compared to the theoretical backscatter gain of the finite and infinite models.

Fig. 5.7 shows the corresponding plots. As theoretically predicted, the gain remains relatively low for coats of very thin thickness with respect to wavelength (less than 0.005 λ_0). Remarkably, the simulated and theoretical gain profiles (based on both finite and infinite models) show excellent agreement regarding the coat thickness producing the peak gain. This proves that it is possible to predict the maximum gain coat profile characteristics using the theoretical model we proposed.

In other terms, by comparing the simulated gain profiles for the cases of $L/R = 10$ and 15, it is observed that the peak gain value for the case of $L/R = 15$ is closer to the theoretical gain than that of $L/R = 10$. This is in agreement with the fact that the theory is based on the infinite cylinder model.

Adding the previously defined correction factor to account for the finiteness of the cylinder results in a gain profile better comparable to the simulated one. The violet and red curves representing the $L/R = 15$ simulated and theoretical have similar profiles over

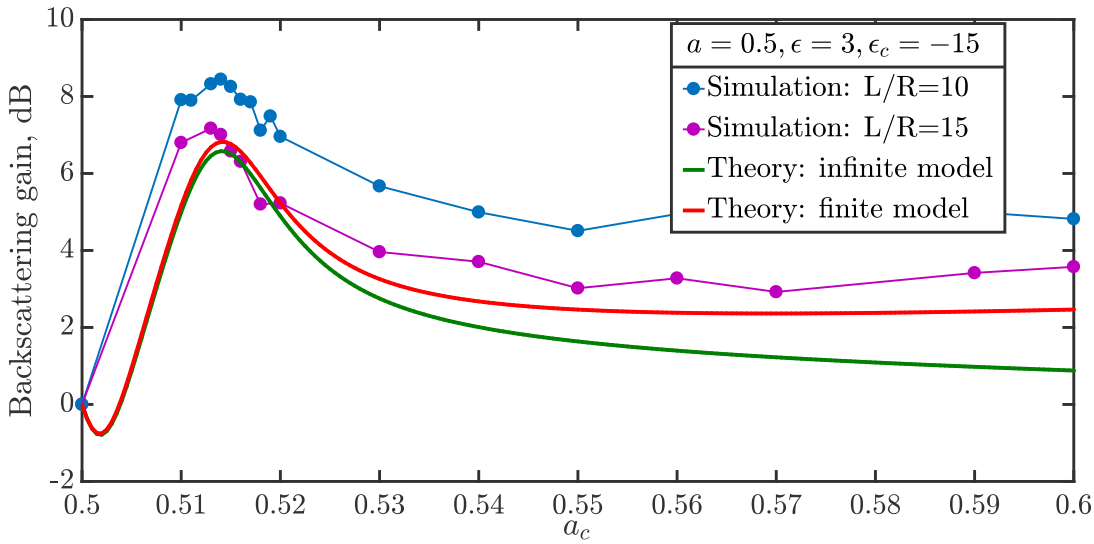

FIGURE 5.7 – Comparison between the theoretical and simulated backscattering gain (in dB) for a coated finite single-layered cylinder of size $a = 0.5$ and permittivity $\epsilon^r = 3$ and a coat of permittivity $\epsilon_c^r = -15$ versus the outer radius of the coat at a frequency of 5 GHz

the a_c range. It is expected that the simulated gain profiles of higher L/R ratios would be even closer to the profile of the theoretical gain.

It is worth noting that for the simulations, the negative dielectric medium has been defined to have a loss tangent of 0.001. Adding those light losses to the medium is for the aim of having a more stable computational process and hence better convergent results. Theoretically, adding those very light losses won't affect the theoretical gain profile at all. Figures . 5.8 and . 5.9 shows the azimuth E field distribution plots corresponding to the cases of the lossless and lossy coats. The E-field distributions are nearly identical for both cases. No intense field concentrations can be seen to indicate an additional energy losses inside the coat.

5.4.5.2 Backscattering gain results for coated dielectric cylinders of core of $\epsilon^r = 3 + 0.1\mathrm{i}$

In this part, the core cylinder is considered to have a dielectric permittivity equal to $\epsilon^r = 3 + 0.1\mathrm{i}$. Fig. 5.10 plots the simulated and theoretical gain profiles for this case. The theoretical gain profile is similar to that in the lossless case, with the most significant difference is having a smoother peak. Second of all, the simulated gain profile is actually in good agreement with the theoretical one. Again, the difference in the levels can be accounted for the finiteness of the cylinder.

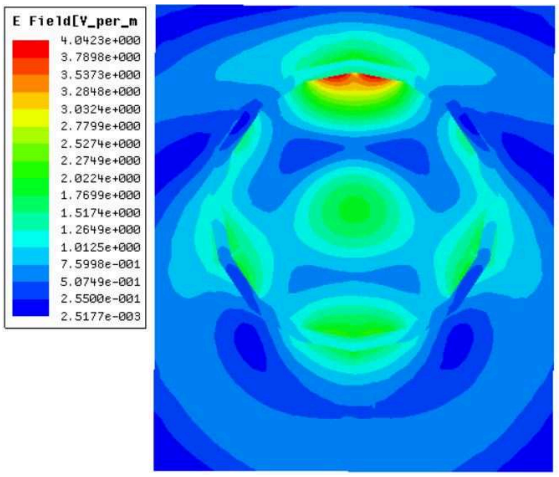

FIGURE 5.8 – Plot of the electric field distribution on the azimuth plane traversing the cylinder for the case where the coat medium is lossless

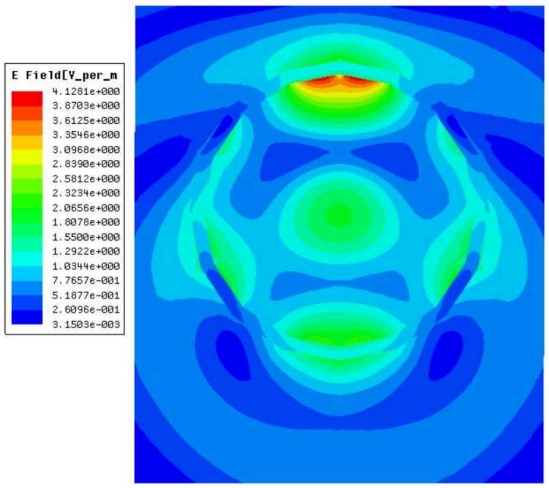

FIGURE 5.9 – Plot of the electric field distribution on the azimuth plane traversing the cylinder for the case where the coat medium is lossy : loss tangent $\delta = 0.001$

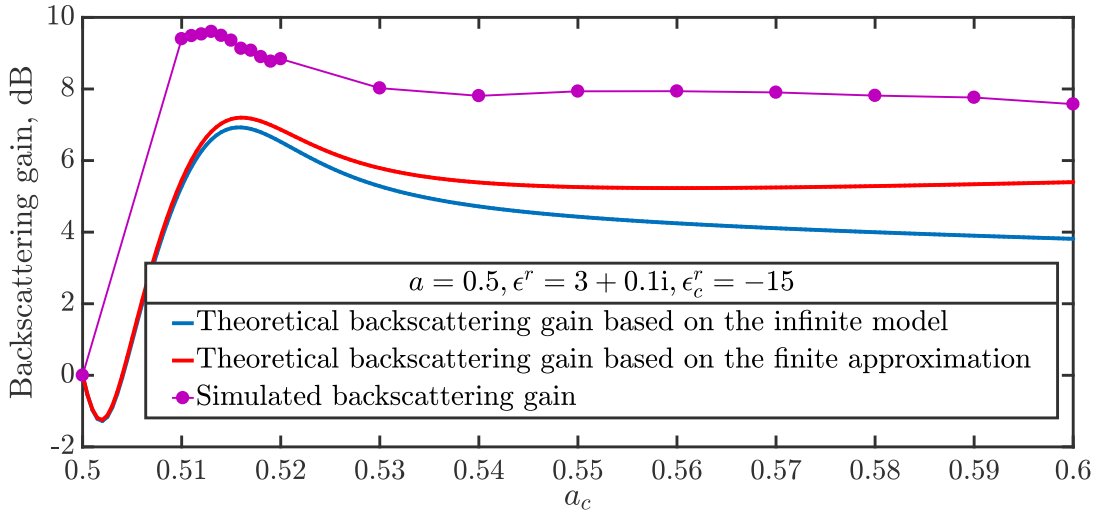

FIGURE 5.10 – Comparison between the theoretical and simulated backscattering gain (in dB) for a coated finite cylinder of size $a = 0.5$, $L/R = 10$ and permittivity $\epsilon^r = 3 + 0.1\mathrm{i}$ and a coat of permittivity $\epsilon_c^r = -15$ versus the outer radius of the coat at a frequency of 5 GHz

5.4.5.3 Backscattering gain results for coated dielectric cylinders of core of $\epsilon^r = 3 + \mathrm{i}$

Now, the loss tangent is equal to 1/3. As stressed in the previous chapter, this is a case of certain significance because the human tissue layers usually have similar loss tangent values. Therefore, the results obtained here can be seen as introductory to the problem of the human model.

Fig. 5.11 plots the corresponding gain profiles which show major difference from those of the lossless and slightly lossy cases. In fact, for the heavily lossy case, there's no gain peak at all. The theoretical gain increases monotonically and then starts a quasi-asymptotic behavior at radius $a_c = 0.53$. As for previous cases, the simulation results agree well with the theoretical one. The simulated gain profile show similar monotonic behavior. In this case here, there is no peak gain and after radius $a_c = 0.53$ the gain value does not increase that much. This means that the optimum coat profile is the one whose radius is still thin enough while still producing the required backscatter gain.

Understandably, the simulated backscatter gain is always higher than that of the predicted theoretical one. This is due to the truncation effect in which the edges scatter in all directions and significantly contribute in the backscatter as well. Those findings are convincing enough to suggest that the proposed theoretical model can guide to the desired coat profile. The same methodology is hence followed in the case of multi-layered cylinder in the aim of enhancing the backscattering by a human core. .

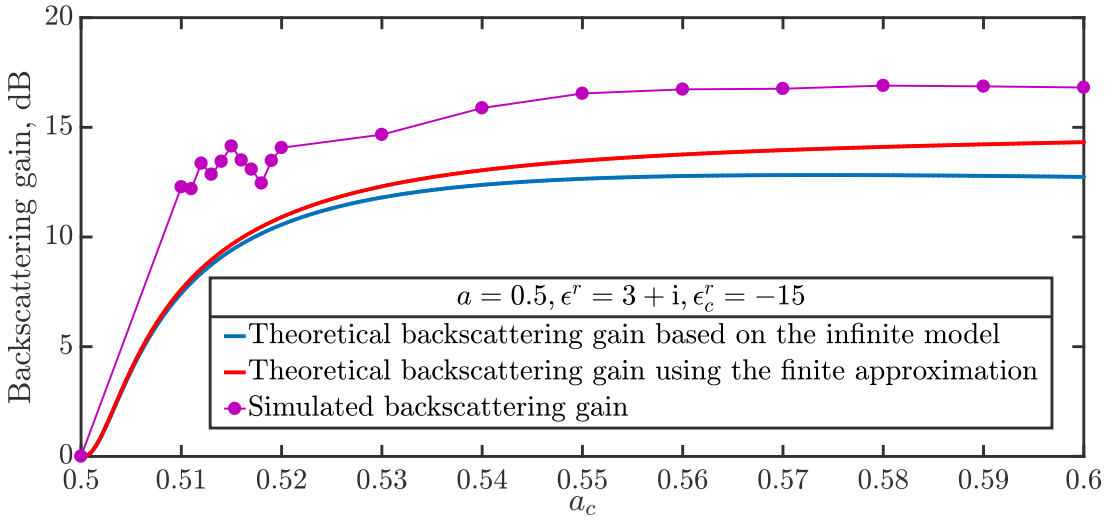

FIGURE 5.11 – Comparison between the theoretical and simulated backscattering gain (in dB) for a coated finite cylinder of size $a = 0.5$, $L/R = 10$ and permittivity $\epsilon^r = 3 + \mathrm{i}$ and a coat of permittivity $\epsilon_c^r = -15$ versus the outer radius of the coat at a frequency of 5 GHz

5.5 Backscattering gain of a coated multi-layered cylinder emulating a human core at 870 MHz

5.5.1 Introduction

In the previous section, we have proven that our methodology based on the theoretical formulation of the backscatter gain can lead to the prediction of the optimum coat profile that enhances the backscattering by the cylinder. The simulation results obtained for the case of a relatively long cylinder validated those theoretical predictions. In this section, similar methodology is carried on for the purpose of obtaining the coat profile that theoretically enhances the backscattering by a multi-layered cylinder emulating a human core. The study starts dealing with the case of a long cylinder ($L/R = 10$), and concentrates in the next section on the real case scenario of a human core where $L/R \approx 2.4$. The study presented in this section can be seen as the first needed step towards the realization of a wearable metamaterial capable of enhancing the detection of cyclists by the Radar.

5.5.2 Backscatter gain based on the finiteness correction factor

Fig. 5.12 plots the contour of the corrected backscatter gain of a coated human multi-layered cylinder model. For better comparison, Fig. 5.13 plots the difference between the corrected and non-corrected gains which is equal to $10\log({a_c}^2{a_4}^2)$ as previously defined in part 5.2.2.4. Obviously, the correction factor is positive and is linearly dependent on

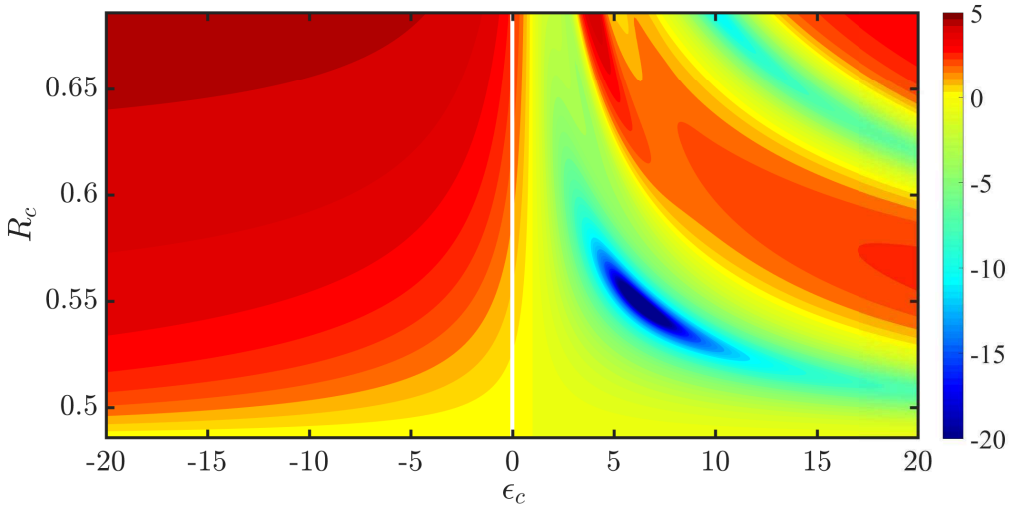

FIGURE 5.12 – Contour plot of the backscatter gain in dB versus the coat radius and permittivity for the case of multi-layered cylinder emulating a human core based on the corrected formulation taking into account the cylinder finiteness

the coat radius. The larger the coat radius is the more the correction factor impact is significant on the backscatter of the coated cylinder.

5.5.3 Simulation setup

The simulation setup used for the simulations in this part is similar to the one proposed in the previous parts. As stated in the previous chapter, the electrical size of the human core (radius of torso) is nearly half of the wavelength at a frequency of operation 870 MHz. The coat permittivity chosen is -20 which is close to the one used in the previous part. The cylinder is simulated by a plane wave of wavelength $\lambda_0 \approx 34.48cm$.

5.5.4 Simulation results for long finite cylinder emulating a human core ($L/R = 10$)

In this part, the case of a long multi-layered cylinder ($L/R = 10$) emulating human core tissues is considered (Fig. 5.14). Fig. 5.15 shows the comparison between the simulated and theoretical gains versus the coat thickness($R_c - R$) where R_c is the coat radius and R is the radius of the outer layer of the human core. There are several talking points to reveal. First, the theoretical gain profiles are monotonic and strictly positive. They resemble the gain profiles of the case of a single cylinder of permittivity $\epsilon^r = 3 + \mathrm{i}$. This means that theoretically, even using very thin coats, still a positive gain would be obtained. This takes us to the next point, to the case of the simulated gain obtained for the very thin coats. In this range there is a relative disagreement between the theoretical and simulated gains. For example, a coat of thickness 0.1 cm produces a negative gain

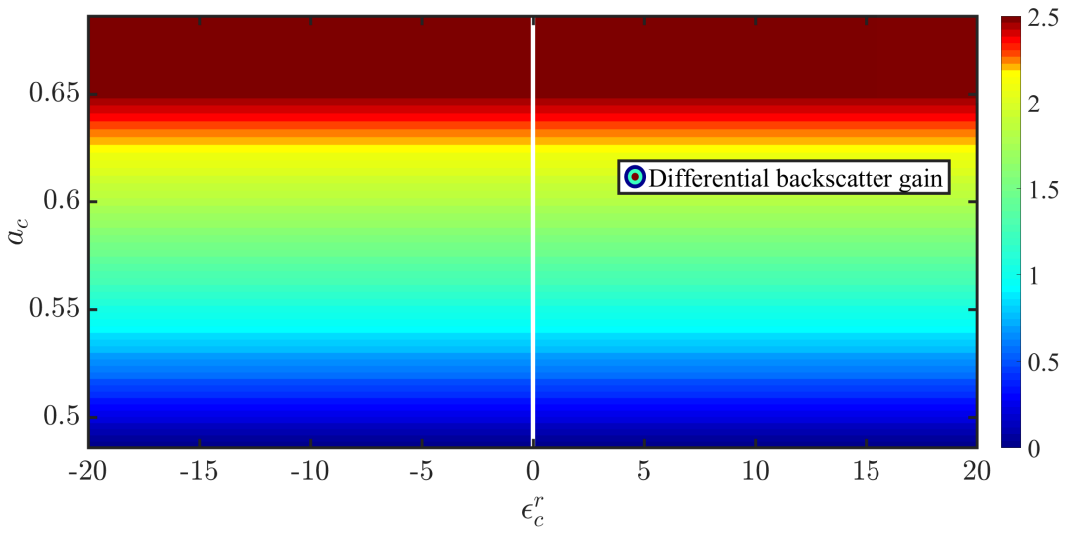

FIGURE 5.13 – Contour plot showing the difference in dB between the corrected and non-corrected backscatter gains

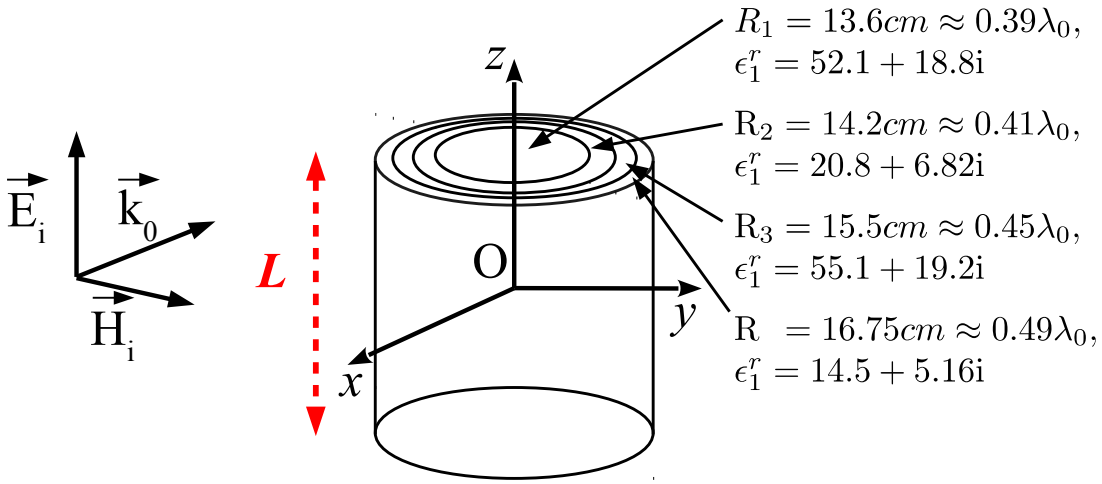

FIGURE 5.14 – A sketch of a finite multi-layered cylinder of length L emulating a human torso radial size and dielectric properties

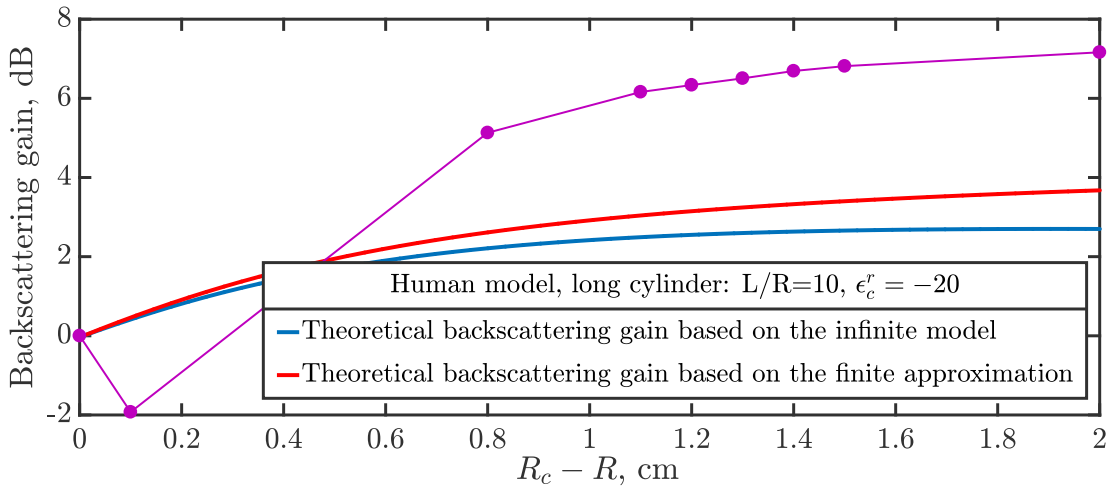

FIGURE 5.15 – Plot of the theoretical and simulated backscattering gain (in dB) obtained for the case of a multilayered cylinder emulating a human core of length to ratio $L/R = 10$ and a coat of permittivity $\epsilon_c^r = -20$ versus the coat thickness at frequency 870 MHz

of -2 dB which is lower than theoretical gain by about 2.5 dB. However, this error is rapidly corrected and this dip is largely overcame before the coat gets significantly thicker. Specifically speaking, the simulated gain curve catches the theoretical for a thickness of nearly 0.5 cm. Beyond this thickness, the simulated gain level rises above that theoretical steadily until the difference level stabilizes at about 3.5 dB.

The difference in the simulated and theoretical backscattering behavior for very thin coats can be related to the finiteness of the cylinder and also to its complexity as it constitutes of four different layers of lossy dielectric media.

Now, the proposed model provided the required guidelines for the design of the desired coat. We pass to the real case scenario with two main guidelines to follow. The first is that we are looking for a coat of negative permittivity to enhance the backscattering by a human torso. The second, as predicted in the previous chapter, is that the thinness of the coat depends on the negativity of the coat. The higher the negativity is the thinner the coat that can be obtained.

5.6 Simulation results for the real life scenario of an average sized human core ($L = 40cm, L/R \approx 2.4$)

Now, the cylinder height is set to L=40 cm which is the average length of a human male torso. The cylinder is hence considered short having $L/R \approx 2.4$. Thus, the problem becomes even more complicated and interesting at the same time.

Fig. 5.16 shows the gain profiles for coats of permittivity $\epsilon_c^r = -20$, -30 and -40 versus the coat thickness. First to notice is that the obtained simulated gain profile for

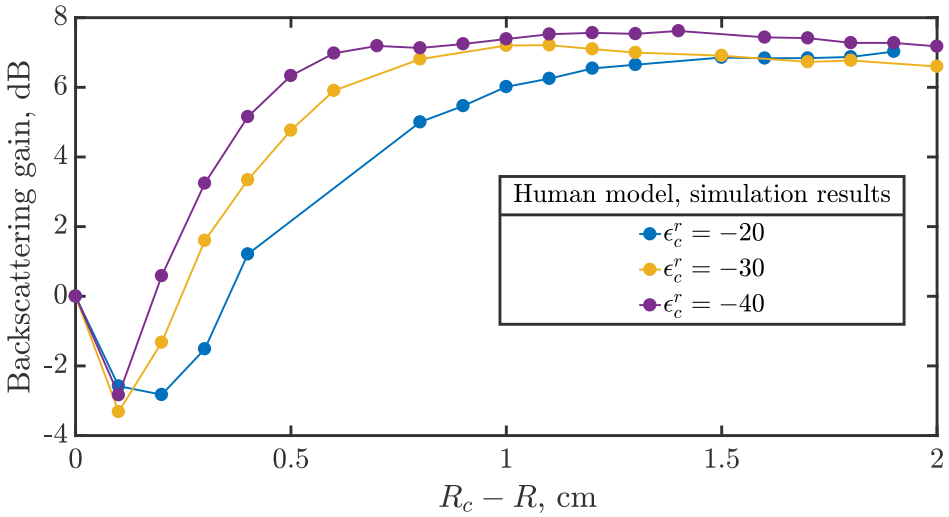

FIGURE 5.16 – Study on the coat permittivity : Plot of the simulated backscattering gain (in dB) obtained for the case of a multi-layered cylinder emulating a human core of length $L = 40$ cm and coats of permittivity $\epsilon_c^r = -20$, -30 and -40 versus the coat thickness at a frequency of 870 MHz

$\epsilon_c^r = -20$ is quite comparable to that obtained for the case of $L/R = 10$. In particular, using a coat of permittivity $\epsilon_c^r = -20$ and thickness equal to 0.6 cm, a gain of more than 3 dB can be obtained.

To obtain such a gain utilizing thinner coats, it would be then necessary to negatively increase the permittivity of the coat. The results obtained prove the point. As the coat negativity increases, the dip in backscatter gain profile tends to sharpen and recover faster. It becomes sufficient to choose a coat of thickness of 3 mm and permittivity $\epsilon_c^r = -40$ to reach the mark of 3 dB gain.

However, the maximum gain obtained using negative coats does not reach the benchmark set using an extremely thin metallic coat. By wrapping the same human cylinder model with a perfectly conducting materials, the obtained simulation results showed 8 dB backscatter gain that could not be achieved even using relatively thick coats.

5.7 Conclusion

In this chapter, the possibility of enhancing the backscattering of a human core cylinder model using a dielectric coat was investigated. Based on the theoretical solution of the scattering problem by infinite cylinder, a simple formula to predict the RCS was proposed to take into account the finiteness of the cylinder. This theoretical formulation was validated using simulations of simple coated single-layered cylinders. By comparing the theoretical and simulated backscatter gain profiles, it was validated that a coat of negative permittivity enhances the backscattering by a single dielectric cylinder. Moreo-

ver, by considering the shape of the gain profile for the cases of lossless and slightly lossy media, our theoretical model was able to predict the optimum coat profile corresponding to the maximum gain possible or peak gain.

Capitalizing on those promising results, we passed to the case of multi-layered cylinder emulating a human core. By observing the gain profile obtained for the case of single highly lossy dielectric cylinder, it was clear that the gain profile of the multi-layered cylinder would be different from the ones of single lossless and slightly lossy cylinders. In the multi-layered cylinder, there will be no peak gain, but rather a monotonic profile with respect to the coat thickness. It was shown based on the simulation results that a trade-off is required between the backscatter gain level and the coat thickness. For a specific gain level, the coat thickness can be reduced by choosing negatively higher dielectric coats.

Finally, this work provided guidelines in the aim of enhancing the backscattering by a human torso. It has been demonstrated that a coat of negative permittivity can enhance the backscattering by cylinder emulating the human core. The thinness of the coat depends on the negativity of the permittivity. The more the negative the coat permittivity is the thinner the coat can be obtained. Those findings are interesting and can help in the realization of jacket that improves the detectability of cyclists by Radars.

General Conclusion

This thesis tackled the problem of RCS enhancement of weakly reflective objects with a foreseen application to the bicycle-cyclist system on the road. Two approaches inspired from reflectarrays and metamaterials have been thoroughly investigated to assess their applicability in a real life scenario.

Reflectarrays

In the first part of the thesis, we have performed a novel analysis on the retrodirective mechanism of a flattened dihedral inspired by reflectarrays. The global retrodirective phase law have first been derived as a function of the incidence angle and the geometrical parameters of the structure. This derivation has opened the door for analyzing the different aspects of this design, mainly speaking about the impact of the flattening and the incidence angle sensitivity on the overall retrodirective performance. This has been made possible by defining complementary formulations to quantitatively assess those aspects.

However, before heading further, there was a need to distinguish between the ideal and attainable cases. The ideal case has been defined as when the phasing cells can obey the phase law corresponding to any incidence angle, i.e., senseless to incidence angle. The attainable case, which is the only one that can be implemented, has been defined as when the phasing cells are designed to obey the phase law for a unique incidence angle. The study on the impact of the flattening degree has shown that this geometrical parameter directly affects the visible range of the dihedral. For a unit cell periodicity $p = \lambda/3$, it has been shown that the visible range of a dihedral of $\alpha = 10°$ theoretically ranges from $-2.6°$ to $+2.6°$. For a flattening degree $\alpha = 22.5°$, the visible range theoretically measures from $-13°$ to $+13°$. Such results show that as the dihedral gets flatter, its performance regarding the visible range further deteriorates. For the attainable case, three modes of operation have been distinguished. The first is when both forward and reverse configurations operate simultaneously. The second and the third describe when only one of the configurations is operating.

Finally, by performing a study on the impact of the phase law inaccuracies on the retrodirective performance, it has been shown that only a tolerable deviation from the retrodirective direction results from such inaccuracies. Those theoretical predictions serve

as guidelines to follow for the design of a retrodirective flattened dihedral.

To validate this study, a design of flattening degree $\alpha = 22.5°$ and operating at 24 GHz was designed. The full-wave simulation results showed good agreement with the theoretical predictions. Furthermore, a simple trick in the Floquet setup-based unit cell study produced an improvement in the retrodirective performance at the nominal angle of incidence.

This prototype has been fabricated and tested. The measurement results have shown good agreement with the simulation ones validating by that our theoretical study and the improvement method that we have proposed.

Metamaterials

In the second part, a theoretical model has been proposed in the aim to enhance the backscattering by a multi-layered cylinder emulating a human core. To the knowledge of the authors, no one before had attempted to analytically obtain the backscattering by the human torso. What makes this work novel is the methodology followed in applying the classical theory of scattering and combining it with the modern advances in metamaterials for the purpose of enhancing the backscattering by a human core.

We have presented the exact mathematical solution of the problem of scattering by an infinite cylinder. Based on this solution, we constructed a numerical model to solve the problem of double-layered cylinders and validated it using examples found in literature. Afterwards, we have extended this numerical model to account for the solution of a multi-layered lossy dielectric cylinder. By characterizing those layers with the appropriate human tissue dielectric properties, we have obtained the backscattering efficiency of a long human torso. To enhance this backscattering, we have coated the human torso model with a dielectric layer. We have found that it is theoretically possible to enhance the backscattering of a human torso using negative dielectric coats of relatively thin thickness. Those results were seen as useful guidelines to follow in the design of the optimum backscattering-enhancing coat.

The work has been afterwards focused on the problem of finite cylinder. We have introduced first an approximate 3D RCS formula as a function of the scattering coefficients obtained from the infinite cylinder solution. Then, we have validated this formula using full-wave simulations of a finite single-layered dielectric cylinder. As a consequence, we have proposed a backscattering gain formulation which is the difference between the 3D RCS's of the coated and non-coated cylinders. By fixing the coat permittivity and varying the thickness, a comparison has been performed between the resulting theoretical and simulated backscattering gains. The results were in good agreement and prove that it is possible to predict the optimum coat profile using our theoretical model.

By extending this theoretical model to the multi-layered cylinder case, we have pro-

duced useful design guidelines to follow for enhacing the backscattering the human torso. Using full-wave simulations, we have shown that it is possible to enhance the backscattering of a human core using negative dielectric coats. The coat thickness can be reduced by using materials of higher negativity permittivity. Those promising results can be subject for further tuning so that to be more adaptive to the real-case scenario of the human core. At the end, we have proven that the methodology we have followed based on the cylinder scattering model has provided us with the needed guidelines to design a coat capable of enhancing the backscattering by a human torso.

Perspectives

Both approaches based on reflectarray and metamaterial have shown to offer promising solutions for the problem of RCS enhancement. However, still, further prospective studies could be performed in the future to improve the aspects of the work already done.

For the case of reflectarray-inspired reflector, several points could be considered :

Reflector-bicycle test

A reflector mountable on a bicycle is now fabricated and tested. Next step would be to test the backscattering behavior of the reflector-bicycle system in different real life road scenarios to observe the overall level of backscattering enhancement obtained.

77-79 GHz prototype

More automotive Radar systems are being designed to operate at 77-79 GHz frequency band to follow the regulations. Hence, it would be interesting to work on an extension of the flattened dihedral to operate in this frequency range.

Dual-band reflector

Another interesting perspective would be to design a reflector whose cells can operate on dual band frequencies 24 GHz and 77-79 GHz.

Regarding the metamaterial inspired solution, the next considerations can be seen as interesting potential prospective studies :

Negative coat synthesis using metamaterials

The results obtained showed that it is possible to enhance the backscattering using a negative permittivity coat. Going further, the following step would be to synthesize the coat in the nature of metamaterials. This synthesis can be done using metallo-dielectric periodic arrays. By carefully tuning the array cell geometry dimensions, the required medium effective permittivity could be synthesized.

Textiles

At a very applicative level, it would be very interesting to investigate the possibility of using flexible wearable conducting textiles instead of the metallic parts of the metamaterial. The resulting performance and reflectivity of such a wearable textile can finally indicate how effective is the methodology we have proposed in the aim of enhancing the RCS of a cyclist and hence improving his safety on the road.

Cyclist-reflector-bicycle test

Finally, after fabricating those devices, it would be possible to test the backscattering behavior of the cyclist-reflector-bicycle system and compare the measured RCS levels to those corresponding to the other vehicles on roads for validation. The information on this RCS signature will be very helpful for implementations in the radar systems.

List of Figures

List of Tables

Bibliography

[1] Mariusz Ptak and Krystian Konarzewski. Numerical Technologies for Vulnerable Road User Safety Enhancement. Advances in Intelligent Systems and Computing, pages 355–364. Springer, Cham, 2015.

[2] J R. Treat, N S. Tumbas, S T. McDonald, David Shinar, R D. Hume, R E. Mayer, R L. Stansifer, and N J. Castellan. Tri-level study of the causes of traffic accidents : final report. Executive summary. April 2018.

[3] Alex LAFONT, Joceline ROGE, and Jean-Michel Boucheix. Driver's emotional state and vulnerable road user detection. page 2 p, PARIS, France, March 2017.

[4] George Platzer. The Geometry of Automotive Rearview Mirrors - Why Blind Zones Exist and Strategies to Overcome Them. SAE Technical Paper, SAE Technical Paper, Warrendale, PA, February 1995.

[5] Dr Eun-Ha Choi and U. S. Department of Transportation National Highway Traffic Safety Administration. *Crash Factors in Intersection-Related Crashes : An On-Scene Perspective*. CreateSpace Independent Publishing Platform, September 2010.

[6] David Gerónimo, David Vázquez, Arturo de la Escalera, Antonio M. López, Atsushi Imiya, Tomas Pajdla, and Jose M. Álvarez. Vision-Based Advanced Driver Assistance Systems. In *Computer Vision in Vehicle Technology*, pages 100–121. John Wiley & Sons, Ltd, 2017.

[7] David Geronimo and Antonio M. Lopez. *Vision-based Pedestrian Protection Systems for Intelligent Vehicles*. SpringerBriefs in Computer Science. Springer-Verlag, New York, 2014.

[8] Xiaofei Li, F. Flohr, Yue Yang, Hui Xiong, M. Braun, S. Pan, Keqiang Li, and D. M. Gavrila. A new benchmark for vision-based cyclist detection. In *2016 IEEE Intelligent Vehicles Symposium (IV)*, pages 1028–1033, June 2016.

[9] Tong Li, X. Cao, and Yanwu Xu. An effective crossing cyclist detection on a moving vehicle. In *2010 8th World Congress on Intelligent Control and Automation*, pages 368–372, July 2010.

[10] TN. DENSO develops world's smallest vision sensor for ADAS, July 2012.

[11] K. Saleh, M. Hossny, A. Hossny, and S. Nahavandi. Cyclist detection in LIDAR scans using faster R-CNN and synthetic depth images. In *2017 IEEE 20th International Conference on Intelligent Transportation Systems (ITSC)*, pages 1–6, October 2017.

[12] T. Ogawa, H. Sakai, Y. Suzuki, K. Takagi, and K. Morikawa. Pedestrian detection and tracking using in-vehicle lidar for automotive application. In *2011 IEEE Intelligent Vehicles Symposium (IV)*, pages 734–739, June 2011.

[13] Velodyne LiDAR Announces Puck Hi-Res™ LiDAR Sensor, Offering Higher Resolution to Identify Objects at Greater Distances, September 2016.

[14] V. Jain, F. Tzeng, L. Zhou, and P. Heydari. A Single-Chip Dual-Band 22 #x2013 ;29-GHz/77 #x2013 ;81-GHz BiCMOS Transceiver for Automotive Radars. *IEEE Journal of Solid-State Circuits*, 44(12) :3469–3485, December 2009.

[15] V. Jain, B. Javid, and P. Heydari. A BiCMOS Dual-Band Millimeter-Wave Frequency Synthesizer for Automotive Radars. *IEEE Journal of Solid-State Circuits*, 44(8) :2100–2113, August 2009.

[16] J. Hasch, E. Topak, R. Schnabel, T. Zwick, R. Weigel, and C. Waldschmidt. Millimeter-Wave Technology for Automotive Radar Sensors in the 77 GHz Frequency Band. *IEEE Transactions on Microwave Theory and Techniques*, 60(3) :845–860, March 2012.

[17] sR-1200e - 24 GHz FMCW Radar Module.

[18] Eugene F. Knott, John F. Schaeffer, and Michael T. Tulley. *Radar Cross Section*. SciTech Publishing, 2004. Google-Books-ID : j7hdXhgwws4C.

[19] T. Griesser and C. Balanis. Backscatter analysis of dihedral corner reflectors using physical optics and the physical theory of diffraction. *IEEE Transactions on Antennas and Propagation*, 35(10) :1137–1147, October 1987.

[20] K. Geary, J. S. Colburn, A. Bekaryan, S. Zeng, B. Litkouhi, and M. Murad. Automotive radar target characterization from 22 to 29 GHz and 76 to 81 GHz. In *2013 IEEE Radar Conference (RadarCon13)*, pages 1–6, April 2013.

[21] E. Knott. RCS reduction of dihedral corners. *IEEE Transactions on Antennas and Propagation*, 25(3) :406–409, May 1977.

[22] W. J. Liao, Y. C. Hou, C. C. Tsai, T. H. Hsieh, and H. J. Hsieh. Radar Cross Section Enhancing Structures for Automotive Radars. *IEEE Antennas and Wireless Propagation Letters*, 17(3) :418–421, March 2018.

[23] Corner reflector, May 2018. Page Version ID : 839674542.

[24] Paul Saville. Review of Radar Absorbing Materials. Technical report, DEFENCE RESEARCH AND DEVELOPMENT ATLANTIC DARTMOUTH (CANADA), DEFENCE RESEARCH AND DEVELOPMENT ATLANTIC DARTMOUTH (CANADA), January 2005.

[25] K. J. Vinoy and R. M. Jha. *Radar Absorbing Materials : From Theory to Design and Characterization*. Springer US, 1996.

[26] F. Qin and C. Brosseau. A review and analysis of microwave absorption in polymer composites filled with carbonaceous particles. *Journal of Applied Physics*, 111(6) :061301, March 2012.

[27] Q. Gao, Y. Yin, D. B. Yan, and N. C. Yuan. Application of metamaterials to ultra-thin radar-absorbing material design. *Electronics Letters*, 41(17) :936–937, August 2005.

[28] JOON TAE Hwang, SUK YOON Hong, JEE HUN Song, and HYUN WUNG Kown. Analysis of radar cross section for advanced naval ships with wide-band metamaterials, December 2017.

[29] Anusha Eldo and Balamati Choudhury. Design Optimization of Broadband Radar Absorbing Structures. pages 149–173. Springer, Singapore, 2017.

[30] P. Salonen, Y. Rahmat-Samii, and M. Kivikoski. Wearable antennas in the vicinity of human body. In *IEEE Antennas and Propagation Society Symposium, 2004.*, volume 1, pages 467–470 Vol.1, June 2004.

[31] P. S. Hall and Y. Hao. Antennas and propagation for body centric communications. In *2006 First European Conference on Antennas and Propagation*, pages 1–7, November 2006.

[32] P. Schilingovski, V. Vulfin, S. Sayfan-Altman, and R. Shavit. Wearable antennas design for wireless communication. In *2017 IEEE International Conference on Microwaves, Antennas, Communications and Electronic Systems (COMCAS)*, pages 1–3, November 2017.

[33] Javier R. Flores-Cuadras, Jose L. Medina-Monroy, Ricardo A. Chavez-Perez, and Humberto Lobato-Morales. Flexible thin antenna solution for wearable ankle bracelet applications with GNSS and BLE connectivity. *Microwave and Optical Technology Letters*, 60(5) :1239–1245, May 2018.

[34] R. Y. Miyamoto and T. Itoh. Retrodirective arrays for wireless communications. *IEEE Microwave Magazine*, 3(1) :71–79, March 2002.

[35] A. Zamora, R. T. Iwami, T. F. Chun, and W. A. Shiroma. An overview of recent advances in retrodirective antenna arrays. In *2010 IEEE International Conference on Wireless Information Technology and Systems*, pages 1–4, August 2010.

[36] D. S. Goshi, K. M. K. H. Leong, and T. Itoh. Recent advances in retrodirective system technology. In *2006 IEEE Radio and Wireless Symposium*, pages 459–462, October 2006.

[37] E. Sharp and M. Diab. Van Atta reflector array. *IRE Transactions on Antennas and Propagation*, 8(4) :436–438, July 1960.

[38] C. Pon. Retrodirective array using the heterodyne technique. *IEEE Transactions on Antennas and Propagation*, 12(2) :176–180, March 1964.

[39] V. Fusco, Chee Binn Soo, and N. Buchanan. Analysis and characterization of PLL-based retrodirective array. *IEEE Transactions on Microwave Theory and Techniques*, 53(2) :730–738, February 2005.

[40] Shyh-Jong Chung, Shing-Ming Chen, and Yang-Chang Lee. A novel bi-directional amplifier with applications in active Van Atta retrodirective arrays. *IEEE Transactions on Microwave Theory and Techniques*, 51(2) :542–547, February 2003.

[41] Z. W. Miao, Z. C. Hao, and Q. Yuan. A Passive Circularly Polarized Van Atta Reflector For Vehicle Radar Applications. *IEEE Antennas and Wireless Propagation Letters*, 16 :2254–2257, 2017.

[42] C. Luxey and J. M. Laheurte. A retrodirective transponder with polarization duplexing for dedicated short-range communications. *IEEE Transactions on Microwave Theory and Techniques*, 47(9) :1910–1915, September 1999.

[43] K. M. K. H. Leong, Yuanxun Wang, and T. Itoh. A full duplex capable retrodirective array system for high-speed beam tracking and pointing applications. *IEEE Transactions on Microwave Theory and Techniques*, 52(5) :1479–1489, May 2004.

[44] L. D. DiDomenico and G. M. Rebeiz. Digital communications using self-phased arrays. *IEEE Transactions on Microwave Theory and Techniques*, 49(4) :677–684, April 2001.

[45] P. D. H. Re, S. K. Podilchak, S. Rotenberg, G. Goussetis, and J. Lee. Retrodirective antenna array for circularly polarized wireless power transmission. In *2017 11th European Conference on Antennas and Propagation (EUCAP)*, pages 891–895, March 2017.

[46] S. Lee, Y. Zeng, and R. Zhang. Retrodirective Multi-User Wireless Power Transfer With Massive MIMO. *IEEE Wireless Communications Letters*, 7(1) :54–57, February 2018.

[47] I. Krikidis. Retrodirective Large Antenna Energy Beamforming in Backscatter Multi-User Networks. *IEEE Wireless Communications Letters*, pages 1–1, 2018.

[48] O. Malyuskin and V. Fusco. Antenna terminals based on ultra-compact retrodirective antenna arrays. *Antennas Propagation IET Microwaves*, 11(15) :2185–2193, 2017.

[49] Yang Luo, Lian-Xing He, Shou-Zheng Zhu, Helen L.W. Chan, and Yu Wang. Flattening of conic reflectors via a transformation method. *Physical Review A*, 84(2) :023843, August 2011.

[50] Shuai Xiong, Yijun Feng, Tian Jiang, and Junming Zhao. Designing retrodirective reflector on a planar surface by transformation optics. *AIP Advances*, 3(1) :012113, January 2013.

[51] H. Haddad, R. Loison, R. Gillard, A. Jrad, and A. Harmouch. Compression technique for retrodirective reflectors using transformation optics. In *2016 IEEE Middle East Conference on Antennas and Propagation (MECAP)*, pages 1–4, September 2016.

[52] H. Haddad, R. Loison, R. Gillard, A. Harmouch, and A. Jrad. A combination of transformation optics and surface impedance modulation to design compact retrodirective reflectors. *AIP Advances*, 8(2) :025114, February 2018.

[53] Nanfang Yu, Patrice Genevet, Mikhail A. Kats, Francesco Aieta, Jean-Philippe Tetienne, Federico Capasso, and Zeno Gaburro. Light Propagation with Phase Discontinuities : Generalized Laws of Reflection and Refraction. *Science*, 334(6054) :333–337, October 2011.

[54] Yiguo Chen, Xiong Li, Yannick Sonnefraud, Antonio I. Fernández-Domínguez, Xiangang Luo, Minghui Hong, and Stefan A. Maier. Engineering the Phase Front of Light with Phase-Change Material Based Planar lenses. *Scientific Reports*, 5 :8660, March 2015.

[55] Yinghui Guo, Lianshan Yan, Wei Pan, and Liyang Shao. Scattering engineering in continuously shaped metasurface : An approach for electromagnetic illusion. *Scientific Reports*, 6 :30154, July 2016.

[56] Benoit B. Mandelbrot. *The Fractal Geometry of Nature*. 1997, August 1982.

[57] A. R. Chandran, M. Gopikrishna, C. K. Aanandan, P. Mohanan, and K. Vasudevan. Radar cross-section enhancement of dihedral corner reflector using fractal-based metallo-dielectric structures. *Electronics Letters*, 42(20) :1135–1136, September 2006.

[58] M. J. Gans. A General Proof of Floquet's Theorem (Correspondence). *IEEE Transactions on Microwave Theory and Techniques*, 13(3) :384–385, May 1965.

[59] John Huang and Jose Antonio Encinar. *Reflectarray Antennas*. John Wiley & Sons, November 2007. Google-Books-ID : JNwYCzFt8Z0C.

[60] A. Valentino and P. Toulios. Fields in the focal region of offset parabolic antennas. *IEEE Transactions on Antennas and Propagation*, 24(6) :859–865, November 1976.

[61] A. W. Rudge and N. A. Adatia. Offset-parabolic-reflector antennas : A review. *Proceedings of the IEEE*, 66(12) :1592–1618, December 1978.

[62] Robert C. Hansen. *Phased Array Antennas*. John Wiley & Sons, November 2009. Google-Books-ID : vVtnDPhi43YC.

[63] D. Lipuma, S. Meric, and R. Gillard. RCS enhancement of flattened dihedral corner reflector using reflectarray approach. *Electronics Letters*, 49(2) :152–154, January 2013.

[64] Viktor G Veselago. The electrodynamics of substances with simultaneously negative values of and μ. *Soviet physics uspekhi*, 10(4) :509, 1968.

[65] R. A. Shelby, D. R. Smith, S. C. Nemat-Nasser, and S. Schultz. Microwave transmission through a two-dimensional, isotropic, left-handed metamaterial. *Applied Physics Letters*, 78(4) :489–491, January 2001.

[66] Split-ring resonator, January 2018. Page Version ID : 822363956.

[67] B. Zhou and T. J. Cui. Directivity Enhancement to Vivaldi Antennas Using Compactly Anisotropic Zero-Index Metamaterials. *IEEE Antennas and Wireless Propagation Letters*, 10 :326–329, 2011.

[68] N. I. Landy, S. Sajuyigbe, J. J. Mock, D. R. Smith, and W. J. Padilla. Perfect Metamaterial Absorber. *Physical Review Letters*, 100(20) :207402, May 2008.

[69] N. Fang and Xiang Zhang. Imaging properties of a metamaterial superlens. In *Proceedings of the 2nd IEEE Conference on Nanotechnology*, pages 225–228, 2002.

[70] I. Al-Naib. Biomedical Sensing With Conductively Coupled Terahertz Metamaterial Resonators. *IEEE Journal of Selected Topics in Quantum Electronics*, 23(4) :1–5, July 2017.

[71] J. B. Pendry, D. Schurig, and D. R. Smith. Controlling Electromagnetic Fields. *Science*, 312(5781) :1780–1782, June 2006.

[72] Chen Pai-Yen, Soric Jason, and Alù Andrea. Invisibility and Cloaking Based on Scattering Cancellation. *Advanced Materials*, 24(44) :OP281–OP304, November 2012.

[73] Andrea Alù and Nader Engheta. Achieving transparency with plasmonic and metamaterial coatings. *Physical Review E*, 72(1) :016623, July 2005.

[74] Steven A. Cummer, Bogdan-Ioan Popa, David Schurig, David R. Smith, and John Pendry. Full-wave simulations of electromagnetic cloaking structures. *Physical Review E*, 74(3) :036621, September 2006.

[75] Sergei Tretyakov, Pekka Alitalo, Olli Luukkonen, and Constantin Simovski. Broadband Electromagnetic Cloaking of Long Cylindrical Objects. *Physical Review Letters*, 103(10) :103905, September 2009.

[76] Shakeel Ahmed and Q. A. Naqvi. Electromagnetic scattering from a perfect electromagnetic conductor circular cylinder coated with a metamaterial having negative permittivity and/or permeability. *Optics Communications*, 281(23) :5664–5670, December 2008.

[77] Yuping Shang, Zhongxiang Shen, and Keming Feng. Enhancement of backscattering by a conducting cylinder coated with gradient metasurface. *Journal of Applied Physics*, 120(4) :045109, July 2016.

[78] H. Rajagopalan, S. Xu, and Y. Rahmat-Samii. On Understanding the Radiation Mechanism of Reflectarray Antennas : An Insightful and Illustrative Approach. *IEEE Antennas and Propagation Magazine*, 54(5) :14–38, October 2012.

[79] S. D. Targonski and D. M. Pozar. Analysis and design of a microstrip reflectarray using patches of variable size. In *Proceedings of IEEE Antennas and Propagation Society International Symposium and URSI National Radio Science Meeting*, volume 3, pages 1820–1823 vol.3, June 1994.

[80] HUGO Human Body Model.

[81] Constantine A. Balanis. *Antenna Theory : Analysis and Design*. John Wiley & Sons, December 2012. Google-Books-ID : v1PSZ48DnuEC.

[82] Steven L. Jacques. Optical properties of biological tissues : a review. *Physics in Medicine & Biology*, 58(11) :R37, 2013.

[83] Arthur L. Aden and Milton Kerker. Scattering of Electromagnetic Waves from Two Concentric Spheres. *Journal of Applied Physics*, 22(10) :1242–1246, October 1951.

[84] Craig F. Bohren and Donald R. Huffman. *Absorption and scattering of light by small particles*. Wiley, 1983. Google-Books-ID : S1RCZ8BjgN0C.

[85] Hendrik Christoffel Hulst and H. C. van de Hulst. *Light Scattering by Small Particles*. Courier Corporation, 1957. Google-Books-ID : PlHfPMVAFRcC.

[86] M. Kerker and E. Matijević. Scattering of Electromagnetic Waves from Concentric Infinite Cylinders*. *JOSA*, 51(5) :506–508, May 1961.

[87] Gustav Mie. Beiträge zur Optik trüber Medien, speziell kolloidaler Metallösungen. *Annalen der Physik*, 330(3) :377–445, January 1908.

[88] Helge Kragh. Ludvig Lorenz and nineteenth century optical theory : the work of a great Danish scientist. *Applied Optics*, 30(33) :4688–4695, November 1991.

[89] Andrea Alù, David Rainwater, and Aaron Kerkhoff. Plasmonic cloaking of cylinders : finite length, oblique illumination and cross-polarization coupling. *New Journal of Physics*, 12(10) :103028, 2010.

[90] Andrea Alù and Nader Engheta. Polarizabilities and effective parameters for collections of spherical nanoparticles formed by pairs of concentric double-negative, single-negative, and or double-positive metamaterial layers. *Journal of Applied Physics*, 97(9) :094310, April 2005.

[91] M. A. Karam, A. K. Fung, and Y. M. M. Antar. Electromagnetic wave scattering from some vegetation samples. *IEEE Transactions on Geoscience and Remote Sensing*, 26(6) :799–808, November 1988.

[92] Y. Shang and Z. Shen. Polarization-Independent Backscattering Enhancement of Cylinders Based on Conformal Gradient Metasurfaces. *IEEE Transactions on Antennas and Propagation*, 65(5) :2386–2396, May 2017.

[93] Erdinc Irci and Vakur B. Ertürk. Achieving transparency and maximizing scattering with metamaterial-coated conducting cylinders. *Physical Review E*, 76(5) :056603, November 2007.

[94] Samel Arslanagic, Richard W. Ziolkowski, and Olav Breinbjerg. Excitation of an electrically small metamaterial-coated cylinder by an arbitrarily located line source. *Microwave and Optical Technology Letters*, 48(12) :2598–2606, December 2006.

[95] Ruey-Bing Hwang and Hsien-Tung Huang. Scattering characteristics of cylindrical metamaterials. *AIP Advances*, 6(3) :035107, March 2016.

[96] Hai-Ying Yao, Le-Wei Li, and Cheng-Wei Qiu. Electromagnetic scattering properties in a multilayered metamaterial cylinder. In *MELECON 2006 - 2006 IEEE Mediterranean Electrotechnical Conference*, pages 246–249, May 2006.

[97] Pai-Yen Chen, Jason Soric, and Andrea Alù. Invisibility and Cloaking Based on Scattering Cancellation. *Advanced Materials*, 24(44) :OP281–OP304, November 2012.

[98] C. Gabriel, S. Gabriel, and E. Corthout. The dielectric properties of biological tissues : I. Literature survey. *Physics in Medicine & Biology*, 41(11) :2231, 1996.

[99] D. Fiala, K. J. Lomas, and M. Stohrer. A computer model of human thermoregulation for a wide range of environmental conditions : the passive system. *Journal of Applied Physiology (Bethesda, Md. : 1985)*, 87(5) :1957–1972, November 1999.

[100] K. G. Zhu and M. Popovic´. Spectral response of a multi-layered sphere applied in microwave breast imaging. In *Proceedings of the Fourth European Conference on Antennas and Propagation*, pages 1–4, April 2010.

[101] G. Marrocco. RFID Antennas for the UHF Remote Monitoring of Human Subjects. *IEEE Transactions on Antennas and Propagation*, 55(6) :1862–1870, June 2007.

[102] Maciej Klemm and G. Troester. EM Energy Absorption in the Human Body Tissues Due to UWB Antennas. *Progress In Electromagnetics Research*, 62 :261–280, 2006.

[103] S. Dumanli. Challenges of wearable antenna design. In *2016 46th European Microwave Conference (EuMC)*, pages 1350–1352, October 2016.

[104] Milton Kerker. *The Scattering of Light and Other Electromagnetic Radiation*. Elsevier, June 2016. Google-Books-ID : FqhmDAAAQBAJ.

[105] S. R. Rengarajan and Y. Rahmat-Samii. The field equivalence principle : illustration of the establishment of the non-intuitive null fields. *IEEE Antennas and Propagation Magazine*, 42(4) :122–128, Aug 2000.

[106] L. Tsang, C.H. Chan, J.A. Kong, and J. Joseph. Polarimetric signatures of a canopy of dielectric cylinders based on first and second order vector radiative transfer theory. *Journal of Electromagnetic Waves and Applications*, 6(1-4) :19–51, 1992.

[107] P. de Matthaeis and R. H. Lang. Comparison of Surface and Volume Currents Models for Electromagnetic Scattering From Finite Dielectric Cylinders. *IEEE Transactions on Antennas and Propagation*, 57(7) :2216–2220, July 2009.

INSA de RENNES
Service des Formations

AVIS DU JURY SUR LA REPRODUCTION DE LA THESE SOUTENUE

Titre de la thèse:
Investigation of RCS-enhancement devices inspired from reflectarrays and metamaterials

Nom Prénom de l'auteur : SROUR HUSSEIN

Membres du jury :
- Madame SEETHARAMDOO Divitha
- Monsieur GUINVARC'H Régis
- Monsieur LHEURETTE Eric
- Monsieur GILLARD Raphaël
- Monsieur DAUVIGNAC Jean-Yves
- Monsieur MERIC Stéphane

Président du jury : Jean-Yves DAUVIGNAC

Date de la soutenance : 29 Juin 2018

Reproduction de la these soutenue

☒ Thèse pouvant être reproduite en l'état
☐ Thèse pouvant être reproduite après corrections suggérées

Fait à Rennes, le 29 Juin 2018

Signature du président de jury

Jean-Yves Dauvignac

Le Directeur,

M'hamed DRISSI

INSTITUT NATIONAL des SCIENCES APPLIQUÉES - RENNES

Titre : Etude sur les dispositifs d'amélioration de SER inspirés des reflectarrays et des métamatériaux

Mots clés : Sécurité routière, Cyclistes, Radar, SER, Reflectarrays, Métamatériaux

Résumé : Aujourd'hui, la sécurité des cyclistes sur les routes est une préoccupation majeure. Les statistiques d'accidents montrent une augmentation de 12% des décès de cyclistes depuis 2010. L'objectif du projet national français CYCLOPE est d'améliorer la sécurité des cyclistes grâce à des dispositifs électroniques innovants. Dans le cadre de ce projet, ces travaux de thèse se concentrent sur l'amélioration de la détectabilité du cycliste par un véhicule équipé d'un radar anticollision. L'objectif est d'augmenter la réflexion du système vélo-cycliste pour que le niveau d'énergie rétrodiffusé soit suffisant pour provoquer une alarme.

Pour atteindre cet objectif, deux approches sont étudiées dans cette thèse. La première approche vise à concevoir un réflecteur rétrodirectif inspiré des techniques utilisées pour les antennes réseaux réflecteurs. Ce réflecteur est destiné à être placé sur le vélo, comme un catadioptre. Le réflecteur utilise deux panneaux imprimés formant un dièdre aplati, dans un souci de compacité. L'utilisation des motifs imprimés permet de réaliser une loi de phase sur les panneaux et, par ce biais, de restaurer le comportement rétrodirectif mis à mal par l'applatissement. Une étude théorique du mode de fonctionnement de cette structure complexe est proposée, permettant de dégager ces potentialités mais également ces limitations. Finalement, une conception complète est menée pour un prototype à 24 GHz. Sa fabrication et sa caractérisation montrent sa capacité à améliorer la surface radar d'un cycliste.

Dans la deuxième approche, le dispositif réfléchissant est destiné à équiper le cycliste lui-même, comme un gilet fluorescent. Le torse humain est modalisé sous la forme d'un cylindre multi-couches diélectriques avec pertes. En revêtant ce cylindre d'une couche de nature réfléchissante, il est possible d'améliorer sa rétrodiffusion. Le travail se concentre donc sur la recherche du profil de revêtement optimal. Pour ce faire, un modèle numérique basé sur la solution mathématique exacte du cylindre infini multi-couches est proposé. En utilisant ce modèle, on constate que la couche requise doit être réalisée par des matériaux à permittivité négative, synthétisables grâce à des métamatériaux. L 'étude est ensuite étendue au cas d'un cylindre fini, plus représentatif de la réalité. Des comparaisons sont menées avec une simulation électromagnétique rigoureuse.

Title : Investigation of RCS-enhancement devices inspired by reflectarrays and metamaterials

Keywords : Road safety, Cyclists, Radar, RCS, Reflectarrays, Metamaterials

Abstract: A cyclist safety nowadays on roads is a major concern. Accident statistics show an increase of 12 % of deaths of cyclists since 2010. In the French national project CYCLOPE, the aim is improve the safety of cyclists by developing innovative electronic devices. In the context of this project, the work in this thesis is concerned with enhancing the detectability of the cyclist by a vehicle equipped with an anti-collision radar. The objective hence is to enhance the reflection by the bicycle-cyclist system so that the backscattered energy level would be sufficient to cause an alarm.

In order to attain this objective, two approaches are investigated in the thesis. In the first, the design of a retrodirective reflector inspired by reflectarrays is studied. This device is going to be attached to the bicycle to operate as a retroreflector. The reflector is formed of two panels attached and flattened till a certain degree. Equipping each of the two panels with printed phasing cells permits for the construction of a phase law that restores the retrodirective behavior of the corner dihedral after it being flattened. A theoretical study performed on the retrodirective mechanism permits to uncover the potentials as well as limits of such reflector. Finally, a prototype operating at 24 GHz is realized. Its performance validates its capacity to enhance the RCS of a bicycle-cyclist.

In the second approach, the possibility of enhancing the backscattering by the cyclist body using a reflective jacket is discussed. The human torso can be modeled as a multi-layered lossy dielectric cylinder. By coating this cylinder with a layer of reflective nature, it is possible to enhance its backscattering. The work hence concentrates on finding the corresponding optimum coat profile. Therefore, a numerical model based on the exact mathematical solution of the multilayered infinite cylinder is proposed. Using this model, it is found that the required coat should be made of negative permittivity materials, synthesizable using metamaterials. The study then is concentrated on the case of a finite cylinder which more accurately represents the real case scenario. Finally, Electromagnetic full-wave simulations are performed to compare the infinite-based numerical model to the finite-based simulation results.